Theoretical studies of frustrated magnets with dipolar interactions

by

Paweł Stasiak

A thesis
presented to the University of Waterloo
in fulfillment of the
thesis requirement for the degree of
Doctor of Philosophy
in
Physics

Waterloo, Ontario, Canada, 2009

I hereby declare that I am the sole author of this thesis. This is a true copy of the thesis, including any required final revisions, as accepted by my examiners.

I understand that my thesis may be made electronically available to the public.

Abstract

Several magnetic materials, in the first approximation, can be described by idealised theoretical models, such as classical Ising or Heisenberg spin systems, and, to some extent, such models are able to qualitatively expose many experimentally observed phenomena. But often, to account for complex behavior of magnetic matter, such models have to be refined by including more terms in Hamiltonian.

The compound $LiHo_xY_{1-x}F_4$, by increasing concentration of nonmagnetic yttrium can be tuned from a diluted ferromagnet to a spin glass. $LiHoF_4$ is a good realisation of the transverse field Ising model, the simplest model exhibiting a quantum phase transition. In the pure case the magnetic behaviour of this material is well described by mean-field theory. It was believed that when diluted, $LiHo_xY_{1-x}F_4$ would also manifest itself as a diluted transverse field Ising model which continue to be well described by mean-field theory, and, at sufficient dilution, at zero temperature, exhibit a quantum spin-glass transition. The experimental data did not support such a scenario, and it was pointed out that, to explain physics of $LiHo_xY_{1-x}F_4$ in transverse magnetic field, the effect of a transverse-field-generated longitudinal random field has to be considered. We explore this idea further in local mean-field studies in which all three parameters: temperature, transverse field and concentration can be consistently surveyed, and where the transverse-field-generated longitudinal random field is explicitly present in the effective spin-1/2 Hamiltonian.

We suggest other materials that are possible candidates for studying quantum criticality in the transverse field Ising model, and in the diluted case, for studying the effects of transverse and longitudinal random fields. The compounds we consider are $RE(OH)_3$, where RE are the rare earth ions Tb^{3+}, Dy^{3+} and Ho^{3+}. Using mean-field theory, we estimate the values of the transverse magnetic field that, at zero temperature, destroy ferromagnetic order to be B_x^c =4.35 T, B_x^c =5.03 T and B_x^c =54.81 T for $Ho(OH)_3$, $Dy(OH)_3$ and $Tb(OH)_3$, respectively. We confirm that $Ho(OH)_3$ and $Tb(OH)_3$, similarly to $LiHoF_4$, can be described by an effective spin-1/2 Hamiltonian. In the case of $Dy(OH)_3$ there is a possibility of a first order phase transition at transverse field close to B_x^c, and $Dy(OH)_3$ cannot be described by a spin-1/2 effective Hamiltonian.

While diluted dipolar Ising spin glass has been studied experimentally in $LiHo_xY_{1-x}F_4$

and in numerical simulations, there are no studies of the Heisenberg case. Example materials that are likely candidates to be realisations of the diluted dipolar Heisenberg spin glass are $(Gd_xY_{1-x})_2Ti_2O_7$, $(Gd_xY_{1-x})_2Sn_2O_7$ and $(Gd_xY_{1-x})_3Ga_5O_{12}$. To stimulate interest in experimental studies of these systems we present results of Monte of Carlo simulations of the diluted dipolar Heisenberg spin glass. By performing finite-size scaling analysis of the spin-glass correlation length and the spin-glass susceptibility, we provide a compelling evidence of a thermodynamical spin-glass transition in the model.

Frustrated pyrochlore magnets, depending on the character of single ion anisotropy and interplay of different types of interaction over a broad range of energy scales, exhibit a large spectrum of exotic phases and novel phenomena. The pyrochlore antiferromagnet $Er_2Ti_2O_7$ is characterised by a strong planar anisotropy. Experimental studies reveal that $Er_2Ti_2O_7$ undergoes a continuous phase transition to a long-range ordered phase with a spin configuration that, in this thesis, is referred to as the Champion-Holdsworth state. Such results are not in agreement with the theoretical prediction that the ground state of the pyrochlore easy-plane antiferromagnet with dipolar interactions complementing the nearest neighbour exchange interactions, is not the Champion-Holdsworth state but the so-called Palmer-Chalker state. On the other hand, Monte Carlo simulations of the easy-plane pyrochlore antiferromagnet indicate a thermal order-by-disorder selection of the Champion-Holdsworth state. To answer the question of whether order-by-disorder selection can be the mechanism at play in $Er_2Ti_2O_7$, we performed Monte Carlo simulations of the easy-plane pyrochlore antiferromagnet with weak dipolar interactions. We estimate the range strengths of the dipolar interaction such that order-by-disorder selection of the Champion-Holdsworth state is not suppressed. The estimated value of the allowed strength of the dipolar interactions indicates that the model studied is likely insufficient to explain the physics of $Er_2Ti_2O_7$ and other types of interactions or quantum effects should be considered.

Acknowledgements

First of all, I would like to express my sincere gratitude to Prof. Michel J. P. Gingras of the Department of Physics and Astronomy at University of Waterloo, who has been my academic supervisor and mentor. His guidance has been instrumental in ensuring my academic and professional growth. He provided me with many helpful suggestions, important advice and constant encouragement during the course of this work.

I would like to thank my Ph.D. advisory committee Prof. Jeff Chen, Prof Tom Devereaux, Prof. Rob Hill, Prof. Roger Melko and Prof. Marcel Nooijen for their guidance during my studies.

I would like to express my appreciation to Prof. Byron W. Southern of the Department of Physics and Astronomy at University of Manitoba for agreeing to be the external examiner, and I would like to thank my Ph.D. thesis examining committee Prof. Michel Gingras, Prof. Rob Hill, Prof. Roger Melko and Prof. Marcel Nooijen.

I enjoyed insightful discussions with my colleagues and friends, fellow students and postdocs in the condensed matter theory group: Mahmoud Ghaznavi, Taoran Lin, Dr. Paul McClarty, Dr. Hamid Molavian, Dr. Mohammad Moraghebi, Jeffrey Quilliam, Dr. Ali Tabei, Sattar Taheri, Dr. Ka-Ming Tam, Jordan Thompson, Dr. Martin Weigel and Dr. Taras Yavorsk'ii.

In particular, I acknowledge collaboration with Dr. Paul McClarty in the study of the easy-plane pyrochlore antiferromagnet, discussions with Dr. Ali Tabei on the topics related to the physics of $LiHoF_4$ and discussions with Dr. Ka-Ming Tam on topics related to spin glasses.

I would like to thank Dr. Paul McClarty and Dr. Ka-Ming Tam for reading the manuscript of my thesis and for their helpful suggestions.

I am indebted to my former mentors, who sparked my interest in scientific research: my M.Sc. thesis advisor, Prof. Andrzej Pękalski of the University of Wrocław, Prof. Mark Matsen of the University of Reading and Dr. Zygmunt Petru of the University of Wrocław.

Finally, I would like to express my special gratitude to my dearest, Kasia Wcisłowska for her love, support in difficult times, and her patience during our parting while this work was being done.

I acknowledge the permission of Prof. Michel Gingras to reproduce in this thesis the

content of the article he co-authored (P. Stasiak and M. J. P. Gingras, Phys. Rev. B 78, 224412 (2008)). I acknowledge the permission from The American Physical Society to reproduce the content of the article published in Physical Review B, P. Stasiak and M. J. P. Gingras, Phys. Rev. B 78, 224412 (2008).

In memory of my beloved Mother, Aleksandra Stasiak

Contents

List of Figures

List of Tables

Chapter 1

Introduction

The study of magnetic materials plays an important role in exploring the physics of systems with many interacting degrees of freedom. It offers more than just an understanding of magnetism in matter as such. Some general conclusion may be extended to nonmagnetic systems and shed some light on the more fundamental issues in condensed matter. Often, in the study of magnetism, phenomena can be identified that are analogous to phenomena occurring in systems of a totally different nature; e.g. in this thesis magnetic phases will be mentioned that are referred to as a spin ice, spin liquid or spin glass, which, in some sense, are analogues of these non magnetic systems from which they take their names. A salient example of research where the study of magnetism extends our understanding of a much broader class of phenomena is the study of phase transitions and criticality. Magnetic systems are quite convenient to study experimentally and to describe theoretically; thus, many major advances in the study of complex and interacting systems were made in studies of models related to crystalline magnetic solids. An important model, that was proposed in the context of magnetism, and turned out to bring an important contribution to the understanding of physics of many interacting degrees of freedom, is the famous Ising model [4], describing the classical magnetic moments that can point in two directions, either up or down, interacting via nearest-neighbour ferromagnetic or antiferromagnetic exchange. The Ising model in two dimensions was the first model to be solved exactly [5] that exhibits a phase transition at finite temperature.

Among magnetic materials are systems that can be quite well approximated by

relatively simple model Hamiltonians. An important group among such materials are some compounds containing rare earth elements playing the role of interacting magnetic ions. One of the materials that falls into this category, that is widely known and the subject of extensive research, is the Ising ferromagnetic compound $LiHoF_4$ [6–21]. When a magnetic field is applied perpendicular to the Ising direction, $LiHoF_4$ is a realisation of the transverse-field Ising model, that is regarded as the simplest model exhibiting a quantum phase transition [22, 23]. When magnetically diluted, $LiHo_xY_{1-x}F_4$ creates an opportunity for experimental studies of the physics of spin glass [7, 8, 19]. When both diluted and subject to transverse magnetic field, an effective longitudinal random field appears [24–26]. Other materials with similar properties can be identified. In this work we propose $Ho(OH)_3$ and $Dy(OH)_3$ as candidates for studies of quantum criticality and glassiness in diluted dipolar ferromagnets [27].

A very interesting class of magnetic materials is that of *geometrically frustrated* rare earth pyrochlores [28]. In this group of materials, systems with different types and strengths of local anisotropy can be investigated and compared. One can find Ising-like materials (spin ice), i.e. $Dy_2Ti_2O_7$, $Ho_2Ti_2O_7$ and $Ho_2Sn_2O_7$ [28–32], Heisenberg-like $Gd_2Sn_2O_7$ or $Gd_2Ti_2O_7$ [28, 33, 34], and XY-like $Er_2Ti_2O_7$ [28, 35–37]. Frustrated magnets display a broad array of phenomena and new states of matter that are not observed in conventional magnets. Their behaviour is often very difficult to predict and depends on the interplay of multiple types of interactions over a broad range of energy scales.

In most cases, the leading interaction in insulating magnetic matter is a short range exchange, and indeed some phenomena occurring in magnetic solids can be captured in models considering only the nearest-neighbour exchange interaction. But besides the short range exchange other interactions are also present in physical systems, of which the most important is the dipolar interaction. The magnetostatic interaction between magnetic dipolar moments is usually weaker than the exchange interaction. Nevertheless, it can profoundly affect the physics of the magnetic materials. An important example, where the dipolar interaction deeply changes the behaviour of the system is domain formation in ferromagnets. The dipolar interaction often plays an important role in rare earth magnetism because in rare earth compounds, due to the screening of the partially filled $5f$ electron shell by the external shells, the exchange interaction is relatively weak and thus of comparable magnitude to the dipolar coupling.

An important group of systems where interactions weaker than the leading nearest-neighbour exchange play also an important role are systems where the nearest-neighbour exchange interaction is geometrically frustrated, such that, if only nearest-neighbour exchange is considered, the ground state would be extensively degenerate and such system would not order at the temperature corresponding to the energy scale of the exchange interaction, an example of such system are classical Heisenberg spins placed on the pyrochlore lattice [38–40]. At sufficiently low temperature, other interactions, such as dipole-dipole interaction, may then bring about ordering in such system. Examples of geometrically frustrated magnets, where the dipolar interaction is often important in understanding the physics at play, are the aforementioned rare-earth pyrochlores [28].

Another type of frustration that also leads to interesting physics is random frustration that is induced by random disorder in the system in question. While the simplest models of magnetic matter describe ideally periodic and spatially homogeneous systems, all experimentally accessible samples contain chemical impurities and crystal dislocations. Besides considering the effect of disorder as a correction to a model pure system, there are instances where strong disorder takes control of the system's properties causing completely new physics to emerge. Such a situation occurs in spin glasses. In the canonical spin-glass materials, the magnetic element appears as an impurity in an otherwise nonmagnetic crystal [41, 42]. In the case of a strongly spatially varying interaction between impurities, the spatial disorder leads to random frustration. Such a system does not order down to zero temperature but freezes in an apparently random, disordered configuration. The canonical spin glasses are metallic systems with magnetic ions interacting via the isotropic RKKY interaction [43–45] that varies with the inter-ion distance, r, like $\cos(k_F r)/r^3$, where k_F is the Fermi wavevector of the conduction electrons. Other systems in which spin glass physics arises are systems of spatially disordered dipoles. The dipolar interaction, similarly to the RKKY interaction, decreases with distance like $1/r^3$, but the strong spatial fluctuations are not distance-dependent, as in the RKKY interaction, but angle-dependent. Specifically, the sign of the dipolar coupling depends on the relative direction of the vector connecting the interacting moments.

This thesis contains four independent but related research projects. The common theme is the presence of the long-range dipolar interaction and the motivation of the

work we have undertaken is largely to make comparison with experimental data or to suggest interesting systems and phenomena that can be suitable for experimental studies. In Chapter 2, mean-field approximation and Monte Carlo methods, applied in the studies presented in the subsequent chapters, are briefly introduced. In Chapter 3, in the framework of local mean-field theory, a transverse-field diluted dipolar Ising model is studied in the context of the magnetic compound $LiHoF_4$. In Chapter 4, a preliminary, mean-field study of other magnetic materials - rare-earth hydroxides - is conducted with the aim of assessing their validity for experimental studies of transverse field induced quantum criticality. In Chapter 5, a diluted dipolar Heisenberg spin glass is studied using Monte Carlo methods. And finally, in Chapter 6, a Monte Carlo investigation of the effect of the dipolar interaction on the order-by-disorder transition in an easy-plane antiferromagnet is presented. A short conclusion is provided in Chapter 7. In the remaining part of this Introduction, the topics briefly mentioned in the above preface are further discussed, with the objective of introducing the motivation of the work presented in the following chapters.

1.1 Geometrical frustration

Interest in geometrically frustrated magnets dates back to the study of an antiferromagnetic Ising model on the triangular lattice by Wannier in 1950 [46]. It was observed that the Ising antiferromagnet on the triangular lattice dramatically differs in its properties from ferromagnets or antiferromagnets on bipartite lattices. Bipartite lattices can be separated into two identical interpenetrating lattices; examples of bipartite lattices are the square or simple cubic lattice. On bipartite lattices, antiferromagnetic Ising spins can form a long-range ordered Néel state. Formation of a Néel state is not possible in the Ising antiferromagnet on a triangular lattice. The ground state of such system is disordered and the system possesses a finite zero-temperature entropy. A three dimensional model with quite similar properties, that is an extensive degeneracy of a ground state and a lack of long-range order down to zero temperature, was studied by Anderson [47]. In the context of magnetic properties of ferrites he studied a system of antiferromagnetic Ising spins on the octahedral sites of normal spinels. This lattice structure is now often referred to as the pyrochlore lattice and is frequently occurring

in studies of frustrated magnetism. The problem of antiferromagnetic Ising spins on the pyrochlore lattice is especially interesting due to the connection to the topic of proton ordering in hexagonal water ice (I_h) [48]. The oxygen atoms in water ice are surrounded by four protons and in this structure each proton is shared between two oxygen atoms. The protons are placed on the pyrochlore structure of corner-sharing tetrahedra. Each proton is bound to one of the oxygen atoms by a covalent bond and form a hydrogen bond with the other. This creates an Ising-like, two value, "in" or "out", degree of freedom. In his seminal paper in 1935 Linus Pauling showed [48] that such proton arrangement allows for an extensive number of ground states, with proton configurations on each tetrahedron described by the so-called *ice rules*, i.e. two covalent and two hydrogen bonds on each oxygen atom or "two-in/two-out" configuration, and explains a finite zero-temperature entropy measured in I_h ice [49, 50]. A global easy-axis direction of Ising spins on pyrochlore lattice, like in the model considered by Anderson, cannot occur due to symmetry. But pyrochlore magnetic systems with spins pointing in local Ising directions, "in" or "out" of the tetrahedron, exactly like protons in water ice, were identified. In the first work, investigating one of such magnets, $Ho_2Ti_2O_7$, for its analogy to water ice, Harris *et al.* coined the term *spin ice* to refer to such frustrated magnetic systems [29].

1.1.1 The concept of frustration

Frustration occurs when a Hamiltonian contains terms that cannot be simultaneously satisfied. It means that the minimum of total energy does not correspond to the minimum of each term in the Hamiltonian separately. The concept of frustration was introduced for the first time by Toulouse [51] in the context of spin-glass systems. Real materials are often frustrated due to the presence of several types of interactions, but usually the energy scale of different couplings is different. For example a nearest-neighbour exchange can dominate and dictate the type of ordering in the system, while weaker interactions like a next-nearest-neighbour exchange, that may be of different sign, or a dipolar interaction are also present. Another example of frustrated but ordered systems are magnetic dipoles placed on a lattice. Such systems choose a long-range ordered Néel state that minimizes the energy [52], e.g. an antiferromagnetic state on the simple cubic lattice and a ferromagnetic state on the face centered cubic

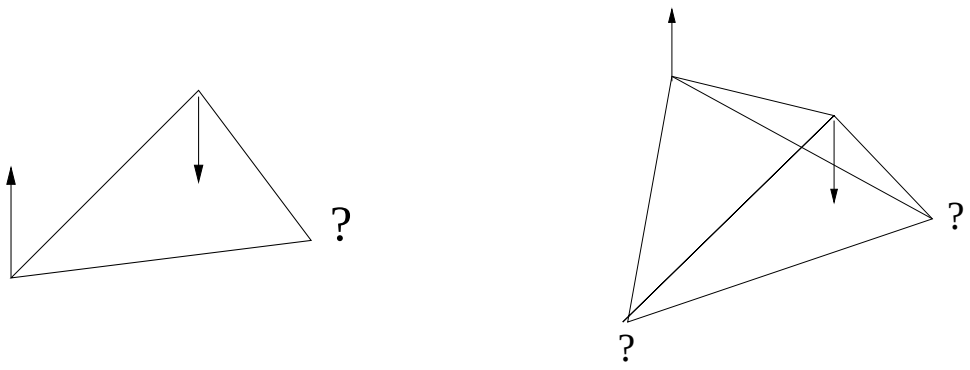

Figure 1.1: Frustrated plaquettes of Ising spins.

or body centered cubic lattice, but in such configurations some interaction still remain unsatisfied.

An interesting case of frustration is when it is the geometry of the system that leads to frustration and degeneracy of the ground state. A simple example is the triangular plaquette containing three antiferromagnetically coupled Ising spins as shown in Fig. 1.1. Anti-parallel alignment minimizes the energy. In triangular geometry at most two bonds can be satisfied. While two spins are anti-parallel, the third spin, regardless of its direction, stays parallel to one of the remaining two; the lowest energy state is that of two spins pointing up and one spin pointing down. Among all $2^3 = 8$ possible configurations 6 satisfy this condition; hence, the lowest energy state is highly degenerate. A similar argument can be provided for the three dimensional system of four antiferromagnetic Ising spins residing on the vertices of a tetrahedron, shown in Fig. 1.1. Among the $2^4 = 16$ possible configurations there are 6 degenerate lowest energy states. These ground states consist of two spins pointing up and two spins pointing down. In such a configuration, each spin has two bonds satisfied - pointing to antiparallel spins, and one bond not satisfied - pointing to the parallel spin. These two cases are examples of geometrical frustration that occurs solely due to the lattice geometry. It should be distinguished from random frustration, that occurs when interaction between spins varies randomly [41, 42].

1.1.2 Cubic pyrochlore oxides and pyrochlore lattice

Geometrical frustration occurs for lattices consisting of frustrated units like triangles or tetrahedra. In two dimensions, the most obvious example is the triangular lattice. Another instance is the kagome lattice of corner-sharing triangles. In three dimensions, the most often studied is the pyrochlore lattice of corner-sharing tetrahedra; numerous instances of extensively studied frustrated magnetic materials are a realisation of this structure [28]. The pyrochlore lattice is depicted in Fig. 1.2. A different example of a three-dimensional frustrated system is the corner sharing triangle structure of garnets; among them an interesting example is gadolinium gallium garnet (GGG) [53–55].

The cubic pyrochlore oxides, $A_2B_2O_7$ have attracted a significant amount of attention in the context of frustrated magnetism. Either one or both of the A and B elements can carry a magnetic moment. The elements A and B reside on two interpenetrating pyrochlore lattices. It is a non-Bravais lattice with a basis of four ions. The pyrochlore structure can be viewed as a system of tetrahedra placed in the sites of FCC lattice. In Fig. 1.2, the faces of these tetrahedra are colored in red. Another set of "inverted" tetrahedra that are connecting the red tetrahedra is colored in blue. Often a cubic unit cell is considered, containing 16 sites and 4 tetrahedra. In the case of antiferromagnetic classical Heisenberg spins residing on the pyrochlore lattice, the system is geometrically frustrated and the ground state is macroscopically degenerate [30, 38, 40, 56].

1.1.3 Experimental measure of frustration

As was explained in the previous section, the geometrical frustration of antiferromagnetic interactions between spins on the pyrochlore lattice prevents the system from exhibiting long-range order. Experimentally, a frustration is visible in the temperature dependence of magnetic susceptibility. According to the Curie-Weiss law, the susceptibility, χ, above the ordering temperature is given by the expression

$$\chi = \frac{1}{T - \theta_{\mathrm{CW}}}, \tag{1.1}$$

where the Curie-Weiss constant, θ_{CW}, determines the sign and the strength of interaction. θ_{CW} is positive in ferromagnets and negative in antiferromagnets. In an

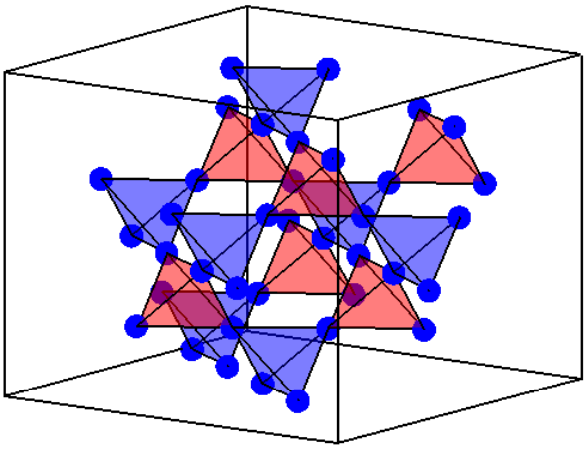

Figure 1.2: The pyrochlore lattice of corner sharing tetrahedra. The lattice can by constructed by placing the tetrahedral four atom basis on the body centered lattice. These tetrahedra are colored in red. Another set of inverted tetrahedra, connecting the red tetrahedra, is colored in blue.

antiferromagnetic system without frustration, if the phase transition from a paramagnetic to an ordered Néel state occurs, it happens in the proximity of θ_{CW}, and it is signalled by a cusp in a plot of χ vs T. In the case of geometrically frustrated systems such features are either not present, or, more often, postponed to much lower temperatures, where interaction other than the frustrated nearest-neighbour exchange, give rise to long-range order or spin-glass freezing. A convenient measure of frustration is the so-called frustration index [57]

$$f \equiv \frac{|\theta_{\mathrm{CW}}|}{T^*}, \tag{1.2}$$

where T^* is the ordering temperature, T_c for a ferromagnet, T_N for an antiferromagnet or freezing temperature, T_g, in the case of a spin glass.

In the ideal spin liquid system the frustration index is infinite, i.e. there is no ordering even at T=0. But in the real materials some perturbations are present. Such systems may stay in a spin liquid state down to a very low temperature, but finally, at the temperature of the energy scale set by the perturbing interaction, they order, as "directed" by the perturbing interactions.

1.1.4 Ground state degeneracy in the classical Heisenberg pyrochlore antiferromagnets - classical spin liquid

It will be shown that in the case of purely nearest-neighbour Heisenberg antiferromagnetic interaction the lowest energy state of a single tetrahedron is continuously degenerate, and furthermore on the pyrochlore lattice, there is an extensive degeneracy and the system stays dynamically disordered at all temperatures.

A lattice can be separated into a number of clusters or plaquettes. For example, in the case of the triangular or kagome lattices they are triangles, or in the case of the pyrochlore lattice they are tetrahedra. If all the plaquettes have their energy separately minimized it is also a ground state of the whole lattice. But one has to bear in mind that the problem is more difficult than it initially sounds, because the plaquettes are usually not independent. What is a ground state of a frustrated antiferromagnetic plaquette? The Hamiltonian for one plaquette can be written as [38–40]

$$\mathcal{H} = -\frac{J}{2}\sum_{i\neq j}^{q} \boldsymbol{S}_i \boldsymbol{S}_j = -\frac{J}{2}\left[\left(\sum_{i}^{q} \boldsymbol{S}_i\right)^2 - \sum_{i}^{q} \boldsymbol{S}_i \cdot \boldsymbol{S}_i\right], \tag{1.3}$$

where q is the number of spins in the plaquette. The second term in the square bracket is a constant, and for spins of unit length it is equal q. The first term is just the square of the total magnetic moment on the plaquette; hence, for $J < 0$, the condition of minimum energy is that of minimum total magnetic moment. The Hamiltonian for the whole lattice can be written in the form [38–40]

$$\mathcal{H} = -\frac{J}{2}\sum_{\alpha}^{N_\alpha} \boldsymbol{L}_\alpha^2 - \frac{J}{2} N_\alpha q, \tag{1.4}$$

where N_α is the number of plaquettes, and $\boldsymbol{L}_\alpha$ is a magnetic moment on a plaquette,

$$\boldsymbol{L}_\alpha = \sum_{i}^{q} \boldsymbol{S}_i^\alpha. \tag{1.5}$$

In the case of Heisenberg spins on the pyrochlore lattice the ground state is such

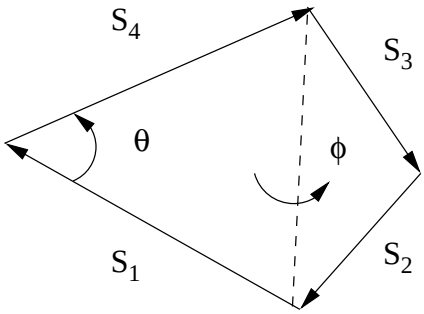

Figure 1.3: A configuration of four spins such that their total magnetic moment reduces to zero.

that the total magnetic moment on each tetrahedron is zero,

$$\boldsymbol{L} = \boldsymbol{S}_1 + \boldsymbol{S}_2 + \boldsymbol{S}_3 + \boldsymbol{S}_4 = 0. \tag{1.6}$$

It can be realised in many ways. A diagram of a configuration of four spins that has zero total magnetic moment is shown in Fig. 1.3. The rotation of the system as a whole can be described using three Euler angles. In addition to these three rotational degrees of freedom of the whole system, that is due to the symmetry of the Hamiltonian, there are also two internal degrees of freedom, θ and ϕ. The question of how this degeneracy of the ground state on a single plaquette extends to the whole lattice can be understood using a Maxwellian counting argument [38–40]. We determine the number of degrees of freedom in the ground state, D, by subtracting the number of constraints that the system must satisfy to stay in the ground state, K, from the total number of degrees of freedom, F. There are 2 degrees of freedom for each of N Heisenberg spins; hence, the total number of degrees of freedom is $F = 2N$. The condition for a tetrahedron to be in the ground state is given by three equations, one for each of the Cartesian directions. Each spin is shared between two tetrahedra, and the number of all tetrahedra is $N_\alpha = N/2$, where N is the number of all spins. This gives $K = 3/2N$ for the number of the ground state constraints. Finally, we obtain $D = F - K = N/2$, that is the number of degrees of freedom in the ground state and it is extensive. This argument can underestimate D if the ground state constraints are not linearly independent, but it was shown [38–40] that in the case of the pyrochlore lattice any corrections to D cannot be extensive. i.e. they are proportional N^ν with $\nu < 1$, and

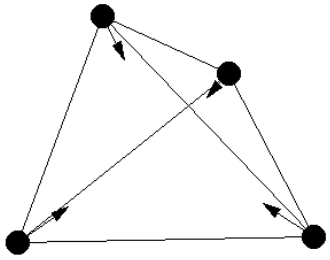

Figure 1.4: Local <111> directions.

they vanish in the thermodynamic limit. An important conclusion of this section is that due to the extensive ground state degeneracy the pyrochlore antiferromagnet does not order down to zero temperature but stays in a so-called collective paramagnetic or classical spin liquid state.

1.1.5 Ising antiferromagnet on the pyrochlore lattice - spin ice

In the previous section, the subject of the pyrochlore Heisenberg antiferromagnet was discussed. Here the case of Ising spins is considered. To start, consider Ising spins on the vertices of a tetrahedron, as shown in the right panel of Fig. 1.1. The case with spins interacting via ferromagnetic exchange interaction is trivial: the ground state is ferromagnetically ordered; all the spins point in the same direction. In the antiferromagnetic case the system is frustrated as discussed in Sec. 1.1.1. Such a situation when the spins point along a global Ising easy axis is unphysical for the cubic pyrochlore lattice. In a real material, the crystal field will tend to select local <111> direction: that is, on each of the vertices of a tetrahedron, the spins point along the lines connecting each vertex with the center of the opposite face, as illustrated in Fig. 1.4. The discussion below shows that the global easy-axis model with ferromagnetic interactions maps to antiferromagnetic interaction in the local <111> easy-axis model, and vice versa.

Consider a Hamiltonian

$$\mathcal{H} = -\frac{J}{2}\sum_{\langle i,j\rangle}^{N} \boldsymbol{S}_i \boldsymbol{S}_j, \tag{1.7}$$

where for J>0 the interaction is ferromagnetic and for J<0 the interaction is antiferromagnetic. The Ising easy axes lie along the local <111> direction; hence, the spins can only point "in", into the tetrahedron, toward the centre of the opposite plane, or in the opposite direction, "out" of the tetrahedron. For such spins, the Hamiltonian can be rewritten as

$$\mathcal{H} = -\frac{J}{2}\sum_{\langle i,j\rangle}^{N} (\hat{z}_i \cdot \hat{z}_j) S_i^z S_j^z, \tag{1.8}$$

where $\hat{z}_i$ and $\hat{z}_j$ are the local easy axes, and $\hat{z}_i \cdot \hat{z}_j = -\frac{1}{3}$. Hence, for ferromagnetic global interaction the system maps onto an effective frustrated Ising antiferromagnet. This spin ice model with Ising spins that are pointing in or out and are effectively coupled by antiferromagnetic exchange is equivalent to a system of antiferromagnetic spins on tetrahedron with a global easy axis, as illustrated in Fig. 1.1.

In the antiferromagnetic case, J<0, the effective interaction between the local <111> Ising spins is ferromagnetic, $-\frac{1}{3}J > 0$, and the ground state in not frustrated. It consists of all the spins pointing "in" or all spins pointing "out". In the pyrochlore lattice in Fig. 1.2, this means that all the spins on the red tetrahedra point "in" and, consequently, all the spins on the blue tetrahedra are point "out", or the reverse.

For a ferromagnetic interaction, J>0, the pyrochlore Ising system is frustrated. Analogously to the discussion of Sec. 1.1.4, the Hamiltonian (1.8) can be written in the form:

$$\mathcal{H} = \frac{J}{6}\sum_{\alpha}^{N_\alpha} L_\alpha^2 - \frac{J N_\alpha q}{6}, \tag{1.9}$$

where

$$L = S_1 + S_2 + S_3 + S_4. \tag{1.10}$$

The condition for the ground state of a single tetrahedron is that L=0. Such a requirement is satisfied if there are two spins pointing in and two spins pointing out. Six of all $2^4 = 16$ possible spin configurations satisfy this condition. To determine the lattice ground state degeneracy, we use the argument introduced by Pauling in the context of proton ordering in water ice [48]. Note that for the pyrochlore lattice there

are two types of tetrahedra that are related by inversion symmetry; in Fig. 1.2 they are distinguished by color. Each site is shared between a red and blue tetrahedron. Considering only the blue tetrahedra, there are 6 possible ground-state configurations per each tetrahedron. The total number of configurations in the lattice would be then $6^{N/4}$, where $N/4$ is the number of blue tetrahedra. But, the red tetrahedra have to satisfy the "two-in/two-out" condition as well. The probability that a given red tetrahedron satisfies the "two-in/two-out" ice rule is $6/16$. For the whole lattice we have to multiply $6^{N/4}$ states, that satisfy ice rules for the blue tetrahedra, by the probability that all red tetrahedra are satisfied, that is $(6/16)^{N/4}$. This gives the ground-state degeneracy $\Omega = 6^{N/4}\,(6/16)^{N/4} = (3/2)^{N/2}$. Consequently, in the ground state there is a zero-temperature entropy of $S_0 = k_{\mathrm{B}} \ln \Omega_0 = \frac{1}{2} N k_{\mathrm{B}} \ln (3/2)$.

The magnetic phenomena occurring in ferromagnetically coupled <111> Ising spins on the pyrochlore lattice was termed spin ice [29] in relation to a similar phenomenon of finite zero-temperature entropy that was observed for the first time in water ice [48].

1.1.6 Order by disorder

In a system where degeneracy is not just a consequence of symmetry, as is the case in frustrated magnets, the fluctuations around different ground states can be different. Some of them can be characterized by higher density of zero modes in the Brillouin zone. Being able to fluctuate in a larger number soft modes, such states are characterized by the highest entropy while the energy is kept close to the minimal, ground-state value. Hence, a system has a tendency to stay in the region of the ground-state manifold with the largest number of soft modes available, and paradoxically more ordered configuration is selected in the presence of fluctuations. The fluctuations enhance order instead of suppressing it, and because of that, such selection of ordered configuration is referred to as order-by-disorder [58]. Order-by-disorder selection can be induced both by thermal or quantum fluctuations.

The idea of order-by-disorder, or in other words entropic, selection can be illustrated with the aid of a cartoon diagram [40] shown in Fig. 1.5. In the left panel a schematic view of phase space is shown. The solid line represents the ground state manifold. At low temperature only a narrow band of states around the ground state

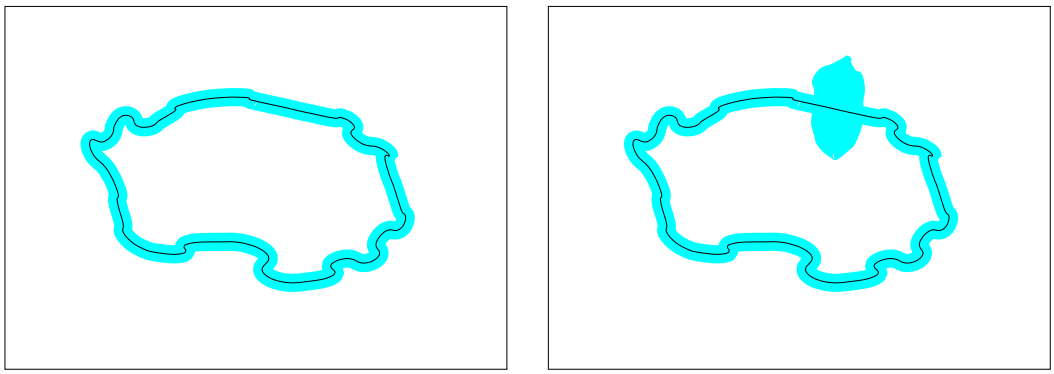

Figure 1.5: Cartoon diagram of the phase space of a frustrated magnet [40]. In the left panel the case of frustrated magnet where order-by-disorder does not occur. In the right panel a situation where entropic selection is likely to occur.

manifold is accessible. In the right panel order-by-disorder selection takes place. In a particular region of the ground-state manifold there is a bulge of accessible states. This is the place where soft modes allow low energy excitations from the ground state and this region of phase space is entropically selected.

1.1.7 XY-pyrochlore antiferromagnet

In the previous sections the cases of frustrated Heisenberg and Ising spins on the pyrochlore lattice were discussed. No less interesting is the case of the XY pyrochlore antiferromagnet in which the spins are confined to easy planes. The easy planes are perpendicular to the local <111> directions, as illustrated in Fig. 1.6. The study of such a model with both a nearest-neighbour exchange and weak dipolar interaction is the topic of Chapter 6.

In Sec. 1.1.4 a ground state manifold of antiferromagnetic Heisenberg spins on a tetrahedron was discussed. Here confinement of the spins to their easy planes decreases the number of spin degrees of freedom. The ground state of the XY model is just the subset of the ground-state manifold in Heisenberg case, chosen such that the the spins remain in the easy-planes. The Heisenberg spins on a tetrahedron have 5 degrees of freedom in their ground state (see Sec. 1.1.4). With the 4 constraints confining the spins to the planes, there is still one continuous degree of freedom per tetrahedron. Considering the whole lattice, it can be shown that there is a macroscopic degeneracy

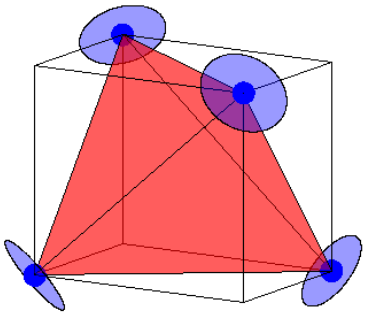

Figure 1.6: The easy-planes on the pyrochlore lattice.

of the ground state [59–61].

It was found in Monte Carlo simulations that in the pyrochlore XY-antiferromagnet there is an order-by-disorder selection of a particular set of 6 symmetry-related ground states [59–61], and it was confirmed by a spin-wave calculation that these states are characterised by the existence of soft modes that induce entropic selection [60, 61].

1.2 The various faces of geometrical frustration in real materials

The study of geometrically frustrated magnetism is a very rich topic [28, 62]. Here only a short introduction is provided and a very restricted selection from a large number of frustrated magnetic materials is discussed, to set some of the background for the study of the pyrochlore dipolar XY antiferromagnet in the context of $Er_2Ti_2O_7$ presented in Chapter 6.

1.2.1 $Gd_2Ti_2O_7$ and $Gd_2Sn_2O_7$

A good examples of geometrically frustrated materials that do not order down to very low temperatures relative to their Curie-Weiss constants, θ_{CW}, are $Gd_2Ti_2O_7$ and $Gd_2Sn_2O_7$. Gd^{3+} magnetic ions reside on the vertices of the pyrochlore lattice.

Gd^{3+} has a half-filled $4f$-shell. The ground state manifold is ${}^8S_{7/2}$ and Gd^{3+} has no orbital momentum. $Gd_2Ti_2O_7$ and $Gd_2Sn_2O_7$ [28, 33, 34] are strongly frustrated Heisenberg pyrochlore antiferromagnets and in these materials Gd^{3+} is a very good approximation of the classical Heisenberg spin. While the Curie-Weiss temperature is about $\theta_{\rm CW} \sim -10$ K, due to frustration, both compounds stay disordered down to $T \sim 1$ K [33, 63]. Theoretically, the extensive ground-state degeneracy in the pyrochlore nearest-neighbour Heisenberg antiferromagnet prevents ordering down to zero temperature [64, 65](see Sec. 1.1.4), and the low temperature order in the materials $Gd_2Ti_2O_7$ and $Gd_2Sn_2O_7$ is induced by other, weaker interactions that are specific to each of these compounds. One of the interactions at play below 1 K is the dipolar interaction. Indeed, in the case of $Gd_2Sn_2O_7$, the spin configuration in the ordered state was found [66] to be the ground state of a pyrochlore antiferromagnet with dipolar interactions, termed here the Palmer-Chalker state [67]. Unlike $Gd_2Sn_2O_7$, $Gd_2Ti_2O_7$ does not order to the Palmer-Chalker state [68, 69]. It was suggested that small differences in further nearest-neighbour exchange couplings, are responsible for the differences between the titanate and stannate [66, 70]. In $Gd_2Ti_2O_7$, below the first phase transition at 1 K there is another one at 0.7 K [63], and in the both phases the material orders with ordering vector $k = \left[\frac{1}{2}\ \frac{1}{2}\ \frac{1}{2}\right]$ [68, 69].

Beside being good materials to study geometrical frustration, $Gd_2Ti_2O_7$ and $Gd_2Sn_2O_7$ will be mentioned later in this Introduction (Sec. 1.5.2), and in Chapter 5 in a different context - their magnetically diluted forms: $(Gd_xY_{1-x})_2Ti_2O_7$ and $(Gd_xY_{1-x})_2Sn_2O_7$ are good candidates for the study of the diluted dipolar Heisenberg spin glass.

1.2.2 Spin ice materials $Ho_2Ti_2O_7$ and $Dy_2Ti_2O_7$

Both $Ho_2Ti_2O_7$ and $Dy_2Ti_2O_7$ are spin ices; the spin ice state was described in Sec. 1.1.5 [56]. The Curie-Weiss temperature is $\theta_{\rm CW} \approx +1.9$ K [29] and $\theta_{\rm CW} \approx +0.5$ K [71] for $Ho_2Ti_2O_7$ and $Dy_2Ti_2O_7$, respectively; thus the interaction is ferromagnetic overall. Magnetic ions, Ho^{3+} or Dy^{3+}, are located on the vertices of the pyrochlore lattice. The strong axial crystal field acting on the Ho^{3+} or Dy^{3+} ion in the local <111> direction makes the ground-state doublet a very good realisation of an Ising spin. The ground states are separated from the higher crystal-field levels by hundreds of Kelvin [72, 73]; hence, admixing of the ground state doublet with higher

levels is negligible in the temperature range of interest [56, 72, 73].

The discovery of a spin ice initiated an extensive research in the field of frustrated magnetism. Spin ice physics was first observed in $Ho_2Ti_2O_7$ by Harris *et al.* [29], who also coined the term *spin ice* in analogy to the proton ordering in water ice [48]. Despite a θ_{CW} of the order of 2 K, muon spin relaxation experiments (μSR) indicate that $Ho_2Ti_2O_7$ does not order down to a temperature of 0.05 K [29, 36].

The most direct indication of spin ice state is the presence of a residual entropy. From the specific heat data measured in the both systems [71, 74], a residual entropy was obtained close to the value $S_0 = \frac{1}{2}Nk_B \ln(3/2)$ [48], calculated in Sec. 1.1.5.

The above values of Curie-Weiss temperature, θ_{CW}, contain both the contribution of the exchange and dipolar interaction. The dipolar moment of magnetic ions Ho^{3+} and Dy^{3+} in $Ho_2Ti_2O_7$ and $Dy_2Ti_2O_7$ is very large, around $10\mu_B$ [28]. The dipolar interaction in both materials is estimated to be +2.4 K [30]; hence, the ferromagnetic dipolar interaction is larger than the Curie-Weiss constant, and the dipolar interaction is the leading coupling in the system, while the exchange interaction is smaller and negative [28]. As the exchange is antiferromagnetic, a naive interpretation suggest that $Ho_2Ti_2O_7$ and $Dy_2Ti_2O_7$ should exhibit all-in/all-out long-range order rather than the spin ice phenomenology, as discussed in Sec. 1.1.5.

To explain the spin ice physics in $Ho_2Ti_2O_7$ and $Dy_2Ti_2O_7$, a dipolar spin ice model has to be considered. The nearest-neighbour Hamiltonian (1.8) must be "upgraded" by the inclusion of dipolar coupling

$$\mathcal{H} = -J\sum_{\langle i,j\rangle}^{N} \boldsymbol{S}_i \cdot \boldsymbol{S}_j + Dr_{\mathrm{nn}}^3 \sum_{i>j} \frac{\boldsymbol{S}_i \cdot \boldsymbol{S}_j}{|\boldsymbol{r}_{ij}|^3} - \frac{3\,(\boldsymbol{S}_i \cdot \boldsymbol{r}_{ij})\,(\boldsymbol{S}_j \cdot \boldsymbol{r}_{ij})}{|\boldsymbol{r}_{ij}|^5}. \tag{1.11}$$

Again, the rescaling of the interaction constant in the projection onto local <111> spin direction takes place, and, as in Sec. 1.1.5, from geometry of the system $J_{\mathrm{nn}} = -\frac{1}{3}J$, and for the nearest-neighbour dipolar interaction, observing that $\hat{z}_i \cdot \hat{z}_j = -\frac{1}{3}$ and $(\hat{z}_i \cdot \boldsymbol{r}_{ij})(\hat{z}_j \cdot \boldsymbol{r}_{ij}) = \frac{2}{3}\boldsymbol{r}_{nn}^2$ one gets $D_{\mathrm{nn}} = \frac{5}{3}D$. Thus, for $\frac{5}{3}D > -\frac{1}{3}J$ the effective interaction between Ising spins is antiferromagnetic an spin ice physics emerges.

In the early Monte Carlo simulations of the dipolar spin ice model, the dipolar interactions were truncated to a certain number of nearest neighbours [35, 71, 75]. The conclusion was that the spin ice state can exist for $Dy_2Ti_2O_7$, while for $Ho_2Ti_2O_7$

a partially ordered state was obtained. In subsequent simulations [31], with a more careful treatment of the dipolar interaction via the use of the Ewald summation technique [76–79](see Appendix D), no ordered phases were found and the residual entropy was obtained to be within a few percent of Pauling's residual entropy, $\frac{1}{2}Nk_{\mathrm{B}}\ln(3/2)$. In further Monte Carlo studies of the dipolar spin ice model [80], using a new, designed to speed up equlibration in the spin ice state, loop algorithm, it was found that below the lacking long-range correlations spin ice state, at very low temperature a long range ordered spin ice phase, so-called Melko phase exist [80]. The Melko phase has not been found in experiments and it is under debate if this low temperature long-range ordered phase occurs in the spin ice materials, $Dy_2Ti_2O_7$ and $Ho_2Ti_2O_7$ [80].

1.2.3 $Gd_3Ga_5O_{12}$ (GGG)

Another interesting geometrically frustrated antiferromagnet is $Gd_3Ga_5O_{12}$, gadolinium gallium garnet (GGG). The lattice structure of this material is not the pyrochlore structure of corner sharing tetrahedra but the cubic garnet structure of corner sharing triangles. This system is not directly related to the frustrated pyrochlores discussed here, but it is mentioned in the context of discussed later, in Sec. 1.5.2 and in Chapter 5, dipolar spin glasses. While the Curie-Weiss temperature is $\theta_{\mathrm{CW}} = 2$ K, the frustration postpones ordering down to 0.18 K [81]. The rich low temperature physics of GGG is still not fully understood, but recently some insight was gained from dynamic magnetization studies, revealing that in the low temperature phase, there is a long range-order coexisting with spin liquid behaviour [55]. In the framework of mean-field theory, it was shown that the dipolar interaction plays an important role in the ordering in GGG [54], and that the neutron scattering [53] data can be reproduced with a proper treatment of the dipolar interactions [54]. Analogously to $(Gd_xY_{1-x})_2Ti_2O_7$ and $(Gd_xY_{1-x})_2Sn_2O_7$, at sufficient dilution, $(Gd_xY_{1-x})_3Ga_5O_{12}$ may be expected to exhibit, at low temperature, a dipolar spin-glass phase.

1.3 $Er_2Ti_2O_7$ - pyrochlore XY antiferromagnet

The calculations in Chapter 6 are motivated by the puzzling properties observed in the rare earth pyrochlore $Er_2Ti_2O_7$. The electronic configuration of Er^{3+} is $4f^{11}$ and

it gives rise to a $^4I_{15/2}$ (L=6, S=3/2) single ion ground-state configuration. The crystal field on Er^{3+} in $Er_2Ti_2O_7$ is characterised by a strong uni-axial anisotropy. This results in a weak magnetic moment of $0.12\mu_B$ along local <111> direction, while in the plane perpendicular to the local easy axis it is $3.8\mu_B$, that is over 30 times larger; hence, $Er_2Ti_2O_7$ can be recognised as an easy-plane system [35, 36]. The Curie-Weiss temperature is $\theta_{\rm CW} = -15.9$ K [82], thus suggesting that the exchange interaction is antiferromagnetic. Being an odd electron system, the crystal field energy level structure of Er^{3+} in $Er_2Ti_2O_7$ consists of Kramers doublets. The first doublet is separated from the ground-state doublet by the energy gap of 74.1 K, and the next doublet is 85.8 K above the ground-state doublet [37].

Measurements of the specific heat of $Er_2Ti_2O_7$ reveal a sharp peak at 1.2 K [35, 83] that signals a phase transition. The powder neutron scattering experiments indicate that the transition is to a long-range ordered phase with propagation vector q=[000] [37, 61]. Zero propagation vector means that each tetrahedron has the same spin configuration. The magnetic ordering was determined in spherical neutron polarimetry studies [84]. The observed spin configuration in the ordered state is referred to as ψ_2 state in Ref. [37] and Ref. [84]; later in this thesis, we will refer to this ψ_2 configuration as the Champion-Holdsworth state [60, 61]. The spin configuration in the Champion-Holdsworth state is shown in the left panel of Fig. 1.7. This configuration is in agreement with that found in Monte Carlo simulations on the easy-plane pyrochlore antiferromagnet [60, 61].

The agreement of the configuration found in the experiments on $Er_2Ti_2O_7$ and in the simulation of the easy-plane pyrochlore antiferromagnet is only superficially satisfactory, and in fact it constitutes a puzzle that is not yet solved. Energetically, the isotropic exchange XY model has continuous degeneracy. The Monte Carlo simulations show that there is a first order thermally-driven order-by-disorder phase transition selecting the Champion-Holdsworth state. That the phase transition is first order is in disagreement with neutron scattering data [60, 61] that suggest a second order transition. At T_N the scattering intensity vanishes like $I(T) \propto (T_N - T)^{2\beta}$ with $\beta \approx 0.33$, that is characteristic of 3D XY model [37, 61].

Furthermore, in $Er_2Ti_2O_7$, besides the nearest-neighbour antiferromagnetic exchange, a sizable dipolar interaction is present. The dipolar interaction breaks the degeneracy of the ground-state manifold, and selects a discrete set of states, that is

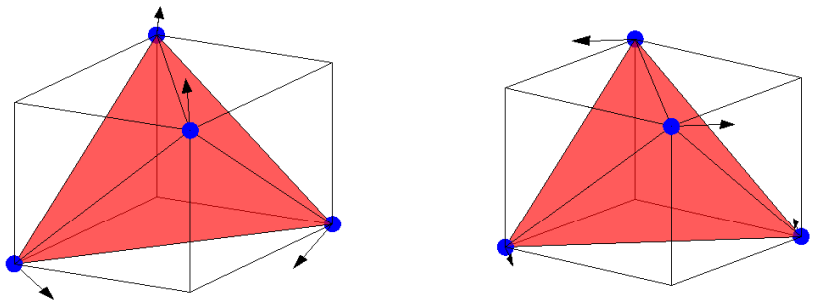

Figure 1.7: The Champion-Holdsworth, ψ_2, state (left) and the Palmer-Chalker state (right).

different from the thermally selected Champion-Holdsworth state. The ground state configuration of the XY antiferromagnet with the dipolar interaction is six-fold degenerate. The ground-state spin configurations consist of two perpendicular pairs of antiparallel spins that are parallel to the opposite plane of the tetrahedron [67], as depicted in the right panel of Fig. 1.7. In this thesis, this state will be referred to as the Palmer-Chalker state [67].

In Chapter 6, the range of dipolar interaction coupling over which order-by-disorder selection of the Champion-Holdsworth state persists is investigated. It turns out that the dipolar interaction must be very weak, much weaker than the dipolar interaction in $Er_2Ti_2O_7$, relative to the exchange coupling, for thermal selection of the Champion-Holdsworth state.

McClarty *et al.* [85] studied the effect of interaction-induced admixing of the ground doublet with excited crystal field levels. They show that such admixing may induce a six-fold anisotropy, that is consistent with the six-fold modulation of the Champion-Holdsworth state, and, in principle, could induce an energetic selection of the Champion-Holdsworth state. But, the energy level splitting is much larger than the energy scale of the interaction, and the six-fold anisotropy created by the interaction-induced admixing of the ground doublet with excited crystal field levels is very weak relatively to the strength of the dipolar coupling. Moreover, if the ordering in the Champion-Holdsworth state were driven by this effect alone, the transition temperature would have to be much lower than the experimental T_c.

1.4 Random frustration and spin glasses

1.4.1 Classical spin glass theories

Our current theoretical understanding of the spin-glass (SG) phase is mostly based on the replica symmetry breaking (RSB) picture set by the Parisi solution [86, 87] of the infinite-dimensional Sherrington-Kirkpatrick model [88]. As the upper critical dimension (UCD) of SG models is large (d_{UCD}=6) [42], such a mean-field description is likely to be insufficient to understand the physics of real materials exhibiting glassy behaviour. An alternative description of the SG phase in finite dimension is given by the phenomenological droplet picture [89], which has been found to possibly characterize better three dimensional (3D) SG [90]. But it remains an open debate what is the proper theory describing SG systems in real (finite) dimensions.

1.4.2 Simulations of Edwards-Anderson model

The theoretical studies of 3D SG models are almost entirely limited to numerical simulations, but the slow relaxation characterizing spin-glass systems makes the numerical studies very difficult. Most of the work has concentrated on the Edwards-Anderson (EA) model [91] of n-component spins interacting via a nearest-neighbour random exchange interaction, J_{ij}, where both ferromagnetic or antiferromagnetic couplings are present. The cases n=1 and n=3 refer to Ising and Heisenberg SG, respectively. The probability distribution of the random bonds, $P(J_{ij})$, is usually taken to be Gaussian or bimodal [41, 42].

The greater part of all numerical studies on SG have been devoted to the minimal EA model, the one-component Ising SG. Due to severe technical difficulties, only a very limited range of system sizes was accessible in the early simulations, while scaling corrections in SG systems are large. The existence of a finite temperature SG transition in 3D Ising SG model remained under debate for a long time [92–96]. The early MC studies strongly supported the finite-temperature SG transition, but a zero-temperature transition could not be definitively ruled out [92, 93, 97]. Only quite recently, in the course of large-scale Monte Carlo studies, has the existence of a thermodynamic phase transition in the Ising case been established [94] and the universality among systems with different bond distributions been confirmed [95, 96].

The case of the Heisenberg SG is somewhat more controversial than the Ising SG. Originally, it was believed that the lower critical dimension (LCD) for the Heisenberg SG is $d_{\mathrm{LCD}} \geq 3$, and that the small anisotropies present in the real system are responsible for the SG behaviour observed in experiments [98, 99]. But no indication of a crossover from the Heisenberg to the Ising SG universality class caused by a weak anisotropy has been observed in experiments [99]. It was suggested that in the Heisenberg EA SG a finite-temperature transition occurs in the chiral sector [99, 100], while a SG transition in the spin sector occurs at zero temperature [101, 102]. The chirality is a multi-spin variable representing the handedness of the noncolinear or noncoplanar spin structures [99, 100]. At that point, the SG phase in the Heisenberg SG materials was attributed to the spin-chirality coupling induced by small anisotropies. Later simulations indicated the existence of a nonzero-temperature SG transition [103, 104]. The most recent work on the 3D Heisenberg SG shows either that the SG transition is decoupled from occurring at slightly higher temperature chiral glass (CG) transition [105, 106], or that a common transition temperature may exist [107].

1.4.3 Spin-glass materials

On the experimental side there do exist some SG materials with a strong, Ising-like uni-axial anisotropy, but the majority of experimental studies of SG focus on nearly isotropic, Heisenberg-like systems. A well studied Ising SG material is $Fe_{0.5}Mn_{0.5}TiO_3$ [108, 109], and other examples of Ising SGs $Eu_{0.5}Ba_{0.5}MnO_3$ [110] and $Cu_{0.5}Co_{0.5}Cl_2$-$FeCl_3$ [111, 112] can be mentioned. Considering $Fe_{0.5}Mn_{0.5}TiO_3$, the leading coupling is a nearest-neighbour exchange, and both base compounds: $FeTiO_3$ and $MnTiO_3$, are antiferromagnets. In both cases, the nearest-neighbour exchange interactions within the hexagonal layers is antiferromagnetic. The magnitude of the intralayer coupling is substantially larger than the interlayer coupling. The SG nature of the mixture, $Fe_{0.5}Mn_{0.5}TiO_3$, originates from the fact that the coupling between the layers is ferromagnetic in $FeTiO_3$ but antiferromagnetic in $MnTiO_3$ [108]; hence, in the mixture, random frustration occurs. For the Heisenberg case, some short-range SG compounds are also available, for example insulating $Eu_xSr_{1-x}S$. In the Eu-rich case, this material is a ferromagnet; the nearest-neighbour exchange interaction between Eu ions is ferromagnetic and the next-nearest-neighbour exchange is weaker and antiferro-

magnetic [113]. When magnetic Eu is randomly substituted with nonmagnetic Sr, a random frustration of the ferromagnetic and antiferromagnetic bonds arises. But the most often studied SG [41, 42] are nearly anisotropic (Heisenberg) metallic systems interacting via the long-range Ruderman-Kittel-Kasuya-Yoshida (RKKY) [43–45] interaction, in which the interaction between localized magnetic moments is mediated by conduction electrons. In this category, the classical systems are the alloys of noble metals as Ag, Au, Cu or Pt, diluted with a transition metal, such as Fe or Mn, often labeled as canonical SGs [41, 42]. In the large $\boldsymbol{r}$ approximation, the RKKY interaction varies with $\boldsymbol{r}$ as $\cos(2k_F r)/r^3$, where k_F is the Fermi wavevector; hence it is anisotropic and long range.

1.5 Dipolar spin glass

An another class of SG materials consist of systems of spatially disordered magnetic dipoles. The dipolar interaction has either ferromagnetic or antiferromagnetic character depending on the relative position of the interacting dipoles. In the presence of positional disorder, it gives rise to random frustration and the presence of a SG phase at low temperature and sufficiently high level of disorder is expected.

1.5.1 Studies of dipolar Ising spin glasses

A number of Ising dipolar SG materials have been identified and related models have been studied numerically. In the context of nanosized magnetic particles dispersed in a frozen nonmagnetic solvent [114], a system of Ising dipoles with randomly oriented easy axes has been simulated [115, 116]. In three dimensions, a spin-glass transition has been confirmed, both in the diluted and undiluted case [115, 116]. A well known physical realization of a diluted dipolar Ising model and a dipolar SG is $\mathrm{LiHo}_x\mathrm{Y}_{1-x}\mathrm{F}_4$ [117–120]. The early numerical studies of diluted Ising dipoles on the simple cubic (SC) lattice and in the lattice geometry corresponding to $\mathrm{LiHo}_x\mathrm{Y}_{1-x}\mathrm{F}_4$ did not find a spin-glass transition [121, 122]. A more recent work confirms the existence of a spin-glass phase in a model approximating $\mathrm{LiHo}_x\mathrm{Y}_{1-x}\mathrm{F}_4$ [120]; although, as in the previous works, crossing of the spin-glass Binder ratio plots was not found, but a finite size scaling of the spin-glass correlation length provided compelling evidence

for a thermodynamical phase transition [120]. Apparently, the corrections to scaling are large for the system sizes studied, and they are much more pronounced in the Binder ratio, while the SG correlation length is somewhat less affected.

1.5.2 Diluted dipolar Heisenberg spin glass

The case of the dipolar Heisenberg SG might be even more interesting, but to the extent of our knowledge such systems have not been studied yet. In the presence of spatial disorder, the off-diagonal terms in the dipolar interaction destroy the rotational symmetry of the ground state. Thus, the dipolar Heisenberg SG is expected to be in the Ising universality class [98, 123]. As mentioned in the discussion of the existence of a SG phase in the Heisenberg EA SG model, a crossover from the Heisenberg SG universality class to the Ising SG universality class induced by small anisotropies has not been observed in experiments. In this context, it is interesting to study a SG system where anisotropic and long-range interactions, i.e. dipolar interactions, dominate. Finding in such a system critical exponents that are consistent with the exponents of the Ising SG universality class would further confirm universality in SG.

In anticipation of eventual experimental studies of dipolar SG, e.g. diluted Gd compounds, we performed numerical studies of the SG transition in a diluted dipolar Heisenberg model. This work is presented in Chapter 5. Experimentally, a diluted dipolar spin glass can be realised by sufficiently diluting magnetic dipoles with a non-magnetic substituent, to the point that a short-range exchange interaction becomes insignificant, and a long-range dipolar interaction dominates. The best candidate materials are those compounds containing rare earth magnetic ions, because, as a result of the screening of the partially filled $4f$ shell by outer shells, the exchange interaction is relatively weak among the rare earths, while their magnetic moments can be large. In this group, the Gd^{3+} ion has a half-filled $4f$-shell. The ground state manifold is $^8S_{7/2}$ and Gd^{3+} has no orbital momentum. Gd^{3+} a very good approximation of a classical Heisenberg spin. A good example of materials that can be considered as candidates for Heisenberg diluted dipolar spin glasses are $(Gd_xY_{1-x})_2Ti_2O_7$ and $(Gd_xY_{1-x})_2Sn_2O_7$. The physics of the pure case $Gd_2Ti_2O_7$ and $Gd_2Sn_2O_7$ was presented in Sec. 1.2.1. Another frustrated antiferromagnet, mentioned in Sec. 1.2.3, gadolinium gallium garnet, $Gd_3Ga_5O_{12}$, in a diluted form, $(Gd_xY_{1-x})_3Ga_5O_{12}$, similarly to $(Gd_xY_{1-x})_2Ti_2O_7$

and $(Gd_xY_{1-x})_2Sn_2O_7$, may be expected to exhibit, at low temperature, a dipolar SG phase.

1.6 Experimental realisations of transverse field Ising model[1]

1.6.1 Transverse field Ising model

Quantum phase transitions occur near zero temperature and are driven by quantum mechanical fluctuations associated with the Heisenberg uncertainty principle and not by thermal fluctuations as in the case of classical temperature-driven phase transitions [124, 125]. There is accumulating evidence that the exotic behaviour exhibited by several metallic, magnetic and superconducting materials may have its origin in underlying large quantum fluctuations and proximity to a quantum phase transition. For this reason, huge efforts are currently being devoted to understanding quantum phase transitions in a wide variety of condensed matter systems.

Perhaps the simplest model that embodies the phenomenon of a quantum phase transition is the transverse field Ising model (TFIM) [22, 23], first proposed by de Gennes to describe proton tunneling in ferrolectric materials [126]. The spin Hamiltonian for the TFIM reads:

$$\begin{aligned} H_{\mathrm{TFIM}} &= -\frac{1}{2}\sum_{(\boldsymbol{r}_i,\boldsymbol{r}_j)} J_{ij}(|\boldsymbol{r}_j-\boldsymbol{r}_i|)S_i^z(\boldsymbol{r}_i)S_j^z(\boldsymbol{r}_j) \\ &\quad -\Gamma\sum_{(\boldsymbol{r}_i)} S_i^x(\boldsymbol{r}_i). \end{aligned} \tag{1.12}$$

The $\boldsymbol{S}_i$ ($S = 1/2$) quantum spin operators reside on the lattice sites $\boldsymbol{r}_i$ of some $d-$dimensional lattice. The $\boldsymbol{S}_i$ operators are related to the Pauli spin matrices by $\boldsymbol{S}_i = \frac{1}{2}\boldsymbol{\sigma}_i$ (here we set $\hbar = 1$). The components of $\boldsymbol{S}_i$ obey the commutation relations $[S_i^\alpha, S_j^\beta] = i\epsilon_{\alpha\beta\gamma}S_i^\gamma\delta_{ij}$ where α, β and γ indicate x, y and z spin components, δ_{ij} and $\epsilon_{\alpha\beta\gamma}$ are the Kronecker delta and fully antisymmetric tensor, respectively. Γ is the

[1]The content of Section 1.6 is reproduced with permission from P. Stasiak and M. J. P. Gingras, Phys. Rev. B 78, 224412 (2008). Copyright 2008, The American Physical Society.

effective transverse field along the x direction, perpendicular to the Ising z axis. As described below, the effective transverse field Γ does not correspond one-to-one to the applied physical field B_x. Rather, Γ in Eq. (1.12) is a function of the real physical field B_x. In fact, J_{ij} is also a function of B_x [1, 26, 127]. If the spin interactions, J_{ij}, possess translational invariance, the system displays for $\Gamma = 0$ conventional long range magnetic order below some critical temperature, T_c. In the simplest scenario, where $J_{ij} > 0$, the ordered phase is ferromagnetic and the order parameter is the average magnetization per spin, $m_z = (1/N)\sum_i \langle S_i^z \rangle$, where N is the number of spins. Since S_i^x and S_i^z do not commute, nonzero Γ causes quantum tunneling between the spin-up, $|\uparrow\rangle$, and spin-down, $|\downarrow\rangle$, eigenstates of S_i^z. By increasing Γ, T_c decreases until, ultimately, $T_c(\Gamma)$ vanishes at a *quantum critical point* where $\Gamma = \Gamma_c$. On the $T = 0$ temperature axis, the system is in a long-range ordered phase for $\Gamma < \Gamma_c$ while it is in a quantum paramagnetic phase for $\Gamma > \Gamma_c$. The phase transition between the paramagnetic and long range ordered phase at Γ_c constitutes the quantum phase transition [22, 23].

One can also consider generalizations of the $H_{\rm TFIM}$ where the J_{ij} are quenched (frozen) random interactions. Of particular interest is the situation where there are as many ferromagnetic $J_{ij} > 0$ and antiferromagnetic $J_{ij} < 0$ couplings. This causes a high level of random frustration and the system, provided it is three dimensional, freezes into a spin-glass state via a true thermodynamic phase transition at a spin-glass critical temperature T_g [41, 128]. Here as well, one can investigate how the spin-glass transition is affected by a transverse field Γ. As in the previous example, $T_g(\Gamma)$ decreases as Γ is increased from zero until, at $\Gamma = \Gamma_c$, a quantum phase transition between a quantum paramagnet and a spin-glass phase ensues. Extensive numerical studies have found the quantum phase transition between a quantum paramagnet and a spin-glass phase [129–131] to be quite interesting due to the occurrence of Griffiths-McCoy singularities [132, 133]. These Griffiths-McCoy singularities arise from rare spatial regions of disorder which may, for example, resemble the otherwise non-random (disorder-free) version of the system at stake. As a result, Griffiths-McCoy singularities can lead to singularities in various thermodynamic quantities away from the quantum critical point.

1.6.2 $LiHo_xY_{1-x}F_4$

On the experimental side, most studies aimed at exploring the phenomena associated with the TFIM have focused on the insulating $LiHo_xY_{1-x}F_4$ Ising magnetic material [6–21]. In this system, the Ho^{3+} Ising spin direction is parallel to the c axis of the body-centered tetragonal structure of $LiHo_xY_{1-x}F_4$. The random disorder is introduced by diluting the magnetic Ho^{3+} ions by non-magnetic Y^{3+}. Crystal field effects lift the degeneracy of the $^5I_8$ electronic manifold, giving an Ising ground doublet $|\Phi_0^{\pm}\rangle$ and a first excited $|\Phi_e\rangle$ singlet at approximately 11 K above the ground doublet [16]. The other 14 crystal field states lie at much higher energies [16]. Quantum spin flip fluctuations are introduced by the application of a magnetic field, B_x, perpendicular to the Ising c axis. B_x admixes $|\Phi_e\rangle$ with $|\Phi_0^{\pm}\rangle$, splitting the latter and producing an effective TFIM with $\Gamma(B_x) \propto B_x^2$ for small B_x [127].

The properties of pure $LiHoF_4$ in a transverse B_x are now generally qualitatively well understood [127]. Indeed, a recent quantum Monte Carlo study [127] found general agreement between experiments and a microscopic model of $LiHoF_4$. However, some quantitative discrepancies between Monte Carlo and experimental data, even near the classical paramagnetic to ferromagnetic transition where B_x/T_c is small, do exist [1, 127]. One noteworthy effect at play in $LiHo_xY_{1-x}F_4$ at low temperatures is the significant enhancement of the zero temperature critical B_x, B_x^c, caused by the strong hyperfine nuclear interactions in Ho^{3+}-based materials [10, 15, 127, 134].

$LiHo_xY_{1-x}F_4$ in a transverse B_x and $x < 1$ has long been known to display paradoxical behaviours, both in the ferromagnetic (FM) ($0.25 < x < 1.0$) and spin-glass (SG) ($x < 0.25$) regimes. In the FM regime, a mean-field behaviour $T_c(x) \propto x$ for the PM to FM transition is observed when $B_x = 0$ [11]. However, in nonzero B_x, the rate at which $T_c(B_x)$ is reduced by $B_x > 0$ increases faster than mean-field theory predicts as x is reduced [12, 17]. In the high Ho^{3+} (SG) dilution regime (e.g. $LiHo_{0.167}Y_{0.833}F_4$), $LiHo_xY_{1-x}F_4$ has long been [7, 8, 19][2] argued to display a conventional SG transition for $B_x = 0$ signalled by a nonlinear magnetic susceptibility, χ_3, diverging at T_g as $\chi_3(T) \propto (T - T_g)^{-\gamma}$ [128]. However, $\chi_3(T)$ becomes less singular as B_x is increased from $B_x = 0$, suggesting that no quantum phase transition between a

[2] A recent experimental study suggest that there might not even be a spin-glass transition in $LiHo_xY_{1-x}F_4$ for $x \leq 0.16$, even in zero B_x. See Ref. [19] and the discussions in Refs. [20, 21].

PM and a SG state exists as $T \to 0$ [8, 9]. Recent theoretical studies [24–26] suggest that for dipole-coupled Ho^{3+} in a diluted sample, nonzero B_x generates longitudinal (along the Ising $\hat{z}$ direction) random fields that (i) lead to a faster decrease of $T_c(B_x)$ in the FM regime [12, 17, 25] and (ii) destroy the PM to SG transition for samples that otherwise show a SG transition when $B_x = 0$ [8, 9, 19, 21, 24–26], or, at least, lead to a disappearance of the χ_3 divergence as B_x is increased from zero [8, 9, 25].

Perhaps most interesting among the phenomena exhibited by $LiHo_xY_{1-x}F_4$ is the one referred to as *antiglass* and which has been predominantly investigated in $LiHo_{0.045}Y_{0.955}F_4$ [6, 13, 14, 19, 135]. The reason for this name comes from AC susceptibility data on $LiHo_{0.045}Y_{0.955}F_4$ which show that the distribution of relaxation times *narrows* upon cooling below 300 mK [6, 13, 14]. This behaviour is quite different from that observed in conventional spin glasses where the distribution of relaxation times broadens upon approaching a spin-glass transition at $T_g > 0$ [41, 128]. The antiglass behaviour has been interpreted as evidence that the spin-glass transition in $LiHo_xY_{1-x}F_4$ disappears at some nonzero $x_c > 0$. Results from more recent experimental studies on $LiHo_{0.165}Y_{0.835}F_4$ ($x = 16.5\%$) and $LiHo_{0.045}Y_{0.955}F_4$ ($x = 4.5\%$) suggest an absence of a genuine spin-glass transition, even for a concentration of Ho as large as 16.5% [19]. In particular, it is in stark contrast with theoretical arguments [136] which predict that, because of the long-ranged $1/r^3$ nature of dipolar interactions, classical dipolar Ising spin glasses should have $T_g(x) > 0$ for all $x > 0$. However, even more recent work asserts that there is indeed a thermodynamic SG transition for $x = 16.5\%$ [20], but that the behaviour found in $LiHo_{0.045}Y_{0.955}F_4$ is truly unconventional [20].

Two very different scenarios for the failure of $LiHo_{0.045}Y_{0.955}F_4$ to show a spin-glass transition have been put forward [14, 137–139]. Firstly, it has been suggested that the (small) off-diagonal part of the dipolar interactions lead to virtual crystal field excitations that admix $|\Phi_0^{\pm}\rangle$ with $|\Phi_e\rangle$ and give rise to non-magnetic singlets for spatially close pairs of Ho^{3+} ions. The formation of these singlets would thwart the development of a spin-glass state. This mechanism is analogous to the one leading to the formation of the random singlet state in dilute antiferromagnetically coupled $S = 1/2$ Heisenberg spins [140]. However, a recent study [141] shows that the energy scale for this singlet formation is very low ($\sim 10^0$ mK) and that the random singlet mechanism [14] may not be very effective at destroying the spin-glass state in $LiHo_{0.045}Y_{0.955}F_4$ [14]. Hence the proposed formation of an entangled state in $LiHo_{0.045}Y_{0.955}F_4$ may, if it re-

ally exist, perhaps proceed via a more complex scheme than that proposed in Ref. [14]. Also, the low-temperature features observed in the specific heat in Ref. [14] have not been observed in a more recent study [135]. Secondly, and from a completely different perspective, early numerical simulations of *classical* Ising dipoles found that the spin-glass transition temperature, T_g appears to vanish for a concentration of dipoles below approximately 20% of the sites occupied [137–139]. However, a more recent Monte Carlo studies found compelling evidence that there is a thermodynamical spin-glass transition at Ho^{3+} concentration $x = 0.0625$ and $x = 0.125$ [120].

As another possible and yet unexplored scenario, we note here that since Ho^{3+} is an even electron system (i.e. a non-Kramers ion), the Kramers' theorem is inoperative and the ground state doublet can be split by random (electrostatic) crystal field effects that compete with the collective spin-glass behaviour. For example, random strains, which may come from the substitution of $Ho^{3+} \rightarrow Y^{3+}$, break the local tetragonal symmetry and introduces (random) crystal fields operators (e.g. $O_2^{\pm 2}$) which have nonzero matrix elements between the two states $|\Phi_0^+\rangle$ with $|\Phi_0^-\rangle$ of the ground doublet, splitting it, and possibly destroying the spin-glass phase at low Ho^{3+} concentration. Indeed, such random transverse fields have been identified in samples with very dilute Ho^{3+} in a $LiYF_4$ matrix [142, 143]. Also, very weak random strains, hence effective random transverse fields, arise from the different (random) anharmonic zero point motion of ^6Li and ^7Li in Ho:$LiYF_4$ samples with natural abundance of ^6Li and ^7Li [144]. Finally, there may be intrinsic strains in the crystalline samples that do not arise from the Ho^{3+}/Y^{3+} or $^6Li/^7Li$ admixture [142]. However, using available estimates [142–144], calculations suggests that strain-induced random fields at play in $LiHo_{0.045}Y_{0.955}F_4$ may be too small [$< O(10^1$ mK)] to cause the destruction of the spin-glass phase in this system [145]. Nevertheless, the point remains that, in principle, the non-Kramers nature of Ho^{3+} does offer a route for the destruction of the spin-glass phase in $LiHo_xY_{1-x}F_4$ outside strictly pairwise, quantum [14, 141] or classical [137–139], magnetic interaction mechanisms. At this stage, this is clearly a matter that needs to be investigated experimentally further. One notes that, because of Kramers' theorem, the destruction of a SG phase via strain-induced effective random transverse fields would not occur for an odd-electron (Kramers) ion such as Dy^{3+} or Er^{3+}. In that context, one might think that a comparison of the behaviour of $LiDy_xY_{1-x}F_4$ or $LiEr_xY_{1-x}F_4$ with that of $LiHo_xY_{1-x}F_4$ would be interesting. Unfortunately, while

$LiHo_xY_{1-x}F_4$ is an Ising system, the Er^{3+} and Dy^{3+} moments in $LiEr_xY_{1-x}F_4$ and $LiDy_xY_{1-x}F_4$ are XY-like [146, 147]. Hence, one cannot compare the $LiEr_xY_{1-x}F_4$ and $LiDy_xY_{1-x}F_4$ XY compounds with the $LiHo_xY_{1-x}F_4$ Ising material on the same footing.

From the above discussion, it is clear that there are a number of fundamental questions raised by experimental studies of $LiHo_xY_{1-x}F_4$, both in zero and nonzero transverse field B_x, that warrant systematic experimental investigations in other similar diamagnetically-diluted dipolar Ising-like magnetic materials. Specific questions are:

1. How does the quantum criticality of a transverse field Ising material with much smaller hyperfine interactions than Ho^{3+} in $LiHo_xY_{1-x}F_4$ manifest itself [10, 15, 134] ?

2. Is the theoretical proposal of transverse-induced random longitudinal fields in diluted dipolar Ising materials [24–26] valid and can it be explored and confirmed in materials other than $LiHo_xY_{1-x}F_4$ [17]? In particular, are the phenomena observed in Ref. [17] and ascribed to Griffiths singularities observed in other disordered dipolar Ising systems subject to a transverse field?

3. Does the antiglass phenomenon [6, 13, 14] occur in other diluted dipolar Ising materials? If yes, which, if any, of the aforementioned theoretical proposals for the destruction of the spin-glass state at small spin concentration is correct?

1.6.3 $RE(OH)_3$ materials

As mentioned above, these questions cannot be investigated with the $LiEr_xY_{1-x}F_4$ and $LiDy_xY_{1-x}F_4$ materials isotructural to the $LiHo_xY_{1-x}F_4$ Ising compound since they are XY-like systems. However, we note in passing that it would nevertheless be interesting to explore the topic of induced random fields [24–26] and the possible existence of an XY dipolar spin glass and/or antiglass state in $LiEr_xY_{1-x}F_4$ and $LiDy_xY_{1-x}F_4$. The $LiTb_xY_{1-x}F_4$ material is of limited use in such investigations since the single ion ground state of Tb^{3+} in this compound consists of two separated singlets [148], and local moment magnetism on the Tb^{3+} site disappears at low Tb concentration [149]. In this paper, we propose that the $RE(OH)_3$ (RE=Ho, Dy) compounds may offer

themselves as an attractive class of materials to study the above questions. Similarly to the $LiHoF_4$, the $RE(OH)_3$ materials possess the following interesting properties:

1. They are insulating rare earth materials.
2. Their main spin-spin couplings are magnetostatic dipole-dipole interactions.
3. The $RE(OH)_3$ materials are stable at room temperature.
4. Both pure $RE(OH)_3$ and $LiHoF_4$ are colinear (Ising-like) dipolar ferromagnets with the Ising direction along the c axis of a hexagonal unit cell ($RE(OH)_3$) or body-centered tetragonal unit cell ($LiHoF_4$). In both cases there are two magnetically equivalent ions per unit cell.
5. In $RE(OH)_3$, the Kramers (Dy^{3+}) and non-Kramers (Ho^{3+}) variants possess a common crystalline structure and both have similar bulk magnetic properties in zero transverse magnetic field B_x.
6. The critical temperature of the pure $RE(OH)_3$ compounds is relatively high, $\sim$ 3 K. This would make possible the study of Y$-$substituted Dy and Ho hydroxides down to quite low concentration of rare earth while maintaining the relevant magnetic temperature scale above the lowest attainable temperature with a commercial dilution refrigerator.
7. Finally, and this is a key feature that motivated the present study, the first excited crystal field state in the $Ho(OH)_3$ and $Dy(OH)_3$ compounds is low-lying, hence allowing a possible transverse-field induced admixing and, possibly, a transverse field Ising model description.

To the best of our knowledge, it appears that the $RE(OH)_3$ materials have so far not been investigated as potential realization of the TFIM. The purpose of the work presented in Chapter 4 is to explore (i) the possible description of these materials as a TFIM, (ii) obtain an estimate of what the zero temperature critical transverse field B_x^c may be and, (iii) assess if any new interesting phenomenology may occur, even in the pure compounds, in nonzero transverse field B_x.

We note, however, that there are so far no very large single crystals of $RE(OH)_3$ available [3]. For example, their length typically varies between 3 mm and 17 mm

and their diameter between 0.2 and 0.6 mm. The lack of large single crystals would make difficult neutron scattering experiments. However, possibly motivated by this work and by a first generation of bulk measurements (e.g. susceptibility, specific heat), experimentalists and solid state chemists may be able to conceive ways to grow larger single crystals of $RE(OH)_3$. Also, in light of the fact that most experiments on $LiHo_xY_{1-x}F_4$ that have revealed exotic behaviour are bulk measurements [6–8, 11, 13, 14, 135], we hope that at this time the lack of availability of large single crystals of the $RE(OH)_3$ series is not a strong impediment against pursuing a first generation of bulk experiments on $RE(OH)_3$.

1.7 Outline of the thesis

The rest of the thesis is organised as follows. In Chapter 2, the techniques used in the thesis are discussed, i.e Weiss mean-field theory and Monte Carlo methods. The application of the mean-field approximation to the transverse-field Ising model is introduced. The discussion of the Monte Carlo methods includes subsections on the Metropolis algorithm, thermal parallel tempering, overrelaxation method and heat-bath algorithm.

In Chapter 3, local mean-field studies of $LiHo_xY_{1-x}F_4$ are described. Local mean-field equations are solved iteratively. In the presence of dilution, the spatial disorder gives rise to random frustration. The free energy landscape of randomly frustrated systems is complicated and characterised by the existence of many local minima. To find low-lying solutions, ideally the global minimum, and to estimate the number of local free energy minima, the iterative procedure is repeated starting from different initial configurations. That way, multiple solutions are obtained, corresponding to different local free energy minima. A phase diagram for concentration, x, vs temperature for different values of transverse magnetic field, B_x, is obtained. To locate the phase boundary two methods are used. The first method is based on calculation of the order parameters for ferromagnetic and spin-glass phases. In the second method, the location of the spin-glass phase is found by locating the region in parameter space that is characterised by a large number of local free energy minima.

In Chapter 4, studies of the rare earth hydroxides: $Ho(OH)_3$, $Dy(OH)_3$ and $Tb(OH)_3$

are presented. The aim of that work is to assess the suitability of these Ising-like magnetic materials for experimental studies of quantum criticality and quantum phase transitions. A mean-field approximation is used to estimate the values of the critical transverse field, B_x^c, for each of these compounds. $Ho(OH)_3$ is found to be a good realization of the transverse-field Ising model, with an experimentally accessible value of the critical transverse field, B_x^c. $Tb(OH)_3$ can also be described by an effective transverse-field Ising model Hamiltonian, but the estimated value of B_x^c is too large for experimental studies. As opposed to the two materials discussed above, $Dy(OH)_3$ cannot by described by an effective spin-1/2 Hamiltonian. The value of the transverse magnetic field that is inducing the zero-temperature phase transition is experimentally accessible, but the transition in high transverse field, B_x, is first order. The first-order transition in $Dy(OH)_3$ is studied in the framework of Ginzburg-Landau theory.

In Chapter 5, numerical studies of a diluted dipolar Heisenberg spin glass are presented. A system of Heisenberg spins interacting via dipolar interactions, randomly placed on the simple cubic lattice is simulated. Two values of dipole concentrations are considered: x=0.125 and x=0.0625. The Metropolis Monte Carlo method with thermal parallel tempering is used. Finite-size scaling analysis of the Binder ratio, spin-glass correlation length and spin-glass susceptibility is performed. The finite-size scaling of the spin-glass correlation length and the spin-glass susceptibility strongly indicates a thermodynamical phase transition to a spin-glass phase. Critical exponents ν and η are computed and compared with the exponents obtained in experiments and simulations of different models.

In Chapter 6, the results of Monte Carlo simulations of the easy-plane pyrochlore antiferromagnet with dipolar interaction are discussed. The model is studied in the context of the physics of $Er_2Ti_2O_7$. The aim of the study is to estimate the range of the dipolar interaction strength for which, in the transition from the paramagnetic state, the order-by-disorder selection is not suppressed, and for which the Champion-Holdsworth state is selected, and not the Palmer-Chalker state that is the actual ground state of the easy-plane pyrochlore antiferromagnet with dipolar interactions. It is found that a very weak dipolar interaction, when compared with the exchange interaction, is sufficient to destroy the entropic selection of the Champion-Holdsworth state. This suggests that the explanation of the experimentally observed selection of Champion-Holdsworth state in $Er_2Ti_2O_7$ should be sought among other phenomena

than thermal order-by-disorder; for example, other types of interactions and quantum effects might be considered.

Chapter 7 contains a short conclusion.

Chapter 2

Methods

2.1 Local mean-field theory for transverse-field Ising model

Only few models can be solved exactly. Even Ising model, considered simple, is not solved exactly in dimensionality higher that two. Powerful but difficult in practical calculations renormalization group techniques require development of new methods almost for each problem considered. Hence, crude but easy to apply mean-field approximation is often the first method chosen to study critical phenomena in new models. In the most cases, mean-field approximation allows qualitative exploration of the phase diagram.

2.1.1 Weiss molecular field theory

The concept and the most intuitive formulation of mean-field theory is due to Pierre Weiss (1907). The basic idea is that the interaction is replaced by the molecular field that captures the effect of interaction with all other particles. Consider Ising Hamiltonian

$$\mathcal{H} = -\frac{1}{2}\sum_{i,j} J_{ij}\sigma_i^z\sigma_j^z - h\sum \sigma_i^z, \tag{2.1}$$

where σ_i^z is a classical Ising spin and $\sigma_i^z = \pm 1$, and the summation is carried over all spin pairs i,j. To calculate the thermal average of spin σ_i^z we need to perform a

difficult summation

$$\langle \sigma_i^z \rangle = \sum_{\{\sigma_i^z\}} \sigma_i^z e^{-\beta(-\frac{1}{2}\sum_{i,j} J_{ij}\sigma_i^z\sigma_j^z - h\sum \sigma_i^z)} / \sum_{\{\sigma_i^z\}} e^{-\beta(-\frac{1}{2}\sum_{i,j} J_{ij}\sigma_i^z\sigma_j^z - h\sum \sigma_i^z)}. \tag{2.2}$$

The difficulty here is that the Hamiltonian (2.1) cannot be separated into parts depending on a single spin, σ_i. To alleviate this problem, to be able to conveniently factorize the Boltzmann probability term, and calculate $\langle \sigma_i^z \rangle$ in Eq. (2.2), we make an assumption that all other spins are fixed and equal to their thermal average values. By doing so, we neglect the effect of thermal fluctuations. The summation reduces to the summation over the two states of the spin σ_i^z,

$$\langle \sigma_i^z \rangle = \sum_{\sigma_i^z=\pm 1} \sigma_i^z e^{-\beta\left(-\sum_j J_{ij}\langle \sigma_j^z\rangle - h\right)\sigma_i^z} / \sum_{\sigma_i^z=\pm 1} e^{-\beta\left(-\sum_j J_{ij}\langle \sigma_j^z\rangle - h\right)\sigma_i^z}, \tag{2.3}$$

and one obtains

$$\langle \sigma_i^z \rangle = \tanh\left(\beta\left(\sum_j J_{ij}\langle \sigma_j^z\rangle + h\right)\right). \tag{2.4}$$

In a slightly different approach, σ_i^z in Hamiltonian (2.1) is replaced with an equivalent expression $\langle \sigma_i^z \rangle + (\sigma_i^z - \langle \sigma_i^z \rangle)$, and the fluctuation term $(\sigma_i^z - \langle \sigma_i^z \rangle)\left(\sigma_j^z - \langle \sigma_j^z \rangle\right)$ is neglected, to obtain

$$\begin{aligned} \mathcal{H} &= -\frac{1}{2}\sum_{i,j} J_{ij}\left[\langle \sigma_i^z\rangle\left(\sigma_j^z - \langle \sigma_j^z\rangle\right) + \langle \sigma_j^z\rangle\left(\sigma_i^z - \langle \sigma_i^z\rangle\right) + \langle \sigma_i^z\rangle\langle \sigma_j^z\rangle\right] - h\sum_i \sigma_i^z \\ &= -\sum_{i,j} J_{ij}\langle \sigma_j^z\rangle \sigma_i^z - h\sum \sigma_i^z + \frac{1}{2}\sum_{i,j} J_{ij}\langle \sigma_i^z\rangle\langle \sigma_j^z\rangle. \end{aligned} \tag{2.5}$$

All thermodynamical quantities can be calculated from the partition function, Z. To compute Z in Weiss mean-field theory one writes:

$$\begin{aligned} Z &= e^{-\frac{1}{2}\beta\sum_{i,j} J_{ij}\langle \sigma_i^z\rangle\langle \sigma_j^z\rangle} \prod_i \sum_{\sigma_i=\pm 1} e^{-\beta\left(-\sum_j J_{ij}\langle \sigma_j\rangle - h\right)\sigma_i} \\ &= e^{-\frac{1}{2}\beta\sum_{i,j} J_{ij}\langle \sigma_i^z\rangle\langle \sigma_j^z\rangle} \prod_i 2\cosh\left[\beta\left(\sum_j J_{ij}\langle \sigma_j\rangle + h\right)\right]. \end{aligned} \tag{2.6}$$

The free energy, $F = -k_{\mathrm{B}}T \ln Z$, reads

$$F = -k_{\mathrm{B}}T \sum_i \ln \left\{ 2\cosh \left[\beta \left(\sum_j J_{ij} \langle \sigma_i \rangle + h \right) \right] \right\} + \frac{1}{2} \sum_{i,j} J_{ij} \langle \sigma_i^z \rangle \langle \sigma_j^z \rangle . \tag{2.7}$$

2.1.2 Transverse field Ising model and mean-field solution

The above argument can be extended for the case of transverse-field Ising model. We consider the Hamiltonian

$$\mathcal{H} = -\frac{1}{2} \sum_{i,j} J_{ij} \sigma_i^z \sigma_j^z - \Gamma \sum_i \sigma_i^x . \tag{2.8}$$

In the mean-field approximation, one gets

$$\mathcal{H} = -\sum_{i,j} J_{ij} \langle \sigma_j^z \rangle \sigma_i^z - \Gamma \sum_i \sigma_i^x + \frac{1}{2} \sum_{i,j} J_{ij} \langle \sigma_i^z \rangle \langle \sigma_j^z \rangle , \tag{2.9}$$

or, denoting $P_i = \sum_{,j} J_{ij} \langle \sigma_j^z \rangle$ and $\Gamma_i = \Gamma$,

$$\mathcal{H} = \frac{1}{2} \sum_{i,j} J_{ij} \langle \sigma_i^z \rangle \langle \sigma_j^z \rangle - \sum_i P_i \sigma_i^z - \sum_i \Gamma_i \sigma_i^x . \tag{2.10}$$

The partition function is of the form

$$Z = C \prod_i \mathrm{Tr} \exp \left[\beta \left(P_i \sigma_i^z + \Gamma_i \sigma_i^x \right) \right] , \tag{2.11}$$

where $C = \exp \left[-\frac{1}{2} \beta \sum_{i,j} J_{ij} \langle \sigma_i^z \rangle \langle \sigma_j^z \rangle \right]$. The eigenvalues of the 2×2 matrix

$$P_i \sigma_i^z + \Gamma_i \sigma_i^x = \begin{pmatrix} P_i & \Gamma_i \\ \Gamma_i & -P_i \end{pmatrix} \tag{2.12}$$

are $\pm |\lambda_i|$, where $|\lambda_i| = \sqrt{(P_i)^2 + (\Gamma_i)^2}$, and the partition function reads

$$Z = C \prod_i \left(e^{-|\lambda_i|} + e^{|\lambda_i|} \right) = C \prod_i \left[2\cosh \left(\beta |\lambda_i| \right) \right] . \tag{2.13}$$

The free energy, $F = -k_{\mathrm{B}}T \ln Z$, takes the following form

$$F = -k_{\mathrm{B}}T \sum_i \ln \left[2\cosh \left(\beta \sqrt{(P_i)^2 + (\Gamma_i)^2} \right) \right] + \frac{1}{2} \sum_{i,j} J_{ij} \left\langle \sigma_i^z \right\rangle \left\langle \sigma_j^z \right\rangle . \tag{2.14}$$

The local magnetization, $m_i^z = \langle \sigma_i^z \rangle$, can be expressed as the derivative of the partition function

$$m_i^x = \frac{\partial F}{\partial \Gamma_i}, \; m_i^z = \frac{\partial F}{\partial P_i}, \tag{2.15}$$

and one obtains

$$\begin{aligned} m_i^x &= \frac{\Gamma_i}{\sqrt{(P_i)^2 + (\Gamma_i)^2}} \tanh \left[\beta \sqrt{(P_i)^2 + (\Gamma_i)^2} \right], \\ m_i^z &= \frac{P_i}{\sqrt{(P_i)^2 + (\Gamma_i)^2}} \tanh \left[\beta \sqrt{(P_i)^2 + (\Gamma_i)^2} \right]. \end{aligned} \tag{2.16}$$

2.2 The Monte Carlo method

Another class of techniques used to tackle problems that cannot be solved exactly are Monte Carlo methods [150, 151]. The term "Monte Carlo method" refers to a wide class of numerical algorithms based on statistical sampling. In statistical physics it applies almost exclusively to Metropolis algorithm [150–152] and its derivatives.

2.2.1 Metropolis Algorithm

We consider here the canonical ensemble that is representing a system that can exchange energy with a heat reservoir, thus it is isothermal. The probability of a microstate k, characterized by energy E_k, is given by Boltzmann distribution

$$w_B(E_k) = \frac{1}{Z} e^{-E_k/k_B T}, \tag{2.17}$$

where T is the temperature and k_B is Boltzmann constant, $k_B = 1.38 \cdot 10^{-23}\mathrm{J} \cdot \mathrm{K}^{-1}$. The normalization constant

$$Z = \sum_k e^{-E_k/k_B T}, \tag{2.18}$$

is the partition function. The summation is carried over all configurations, k. The aim of a simulation is to sample the configurations with a statistical weight $w_B(E_k)$. The most straightforward approach is to sample configurations from a uniform probability distribution. The estimator for the expected value of physical observable, O, is given by the formula

$$\bar{O} = \sum_k w_B(E_k) O_k, \tag{2.19}$$

where O_k is the value of observable O in the microstate k. In practice such "simple-sampling" is prohibitively inefficient. The statistical weight, $w_B(E_k)$, of the majority of drawn configuration is very small and the statistically important configuration would be likely missed. To alleviate this problem, the sampling can be performed from an arbitrary probability distribution, $w(E_k)$, that would promote sampling of statistically important configurations. The estimator for the expected value of observable O from such "importance-sampling" is

$$\bar{O} = \sum_k \frac{w_B(E_k)}{w(E_k)} O_k. \tag{2.20}$$

In the case of sampling from Boltzmann distribution, $w_B(E_k)$, the average is just the arithmetic mean

$$\bar{O} = \frac{1}{N} \sum_k O_k, \tag{2.21}$$

where N is the number of sampled configurations, k. In practice it may be difficult to generate random configurations with arbitrary distribution function, $w(E_k)$. The particular difficulty of sampling configurations form Boltzmann distribution (2.17) is that the partition function, Z, is not known. The solution to this problem is the Markov chain Monte Carlo. A Markov chain is a stochastic process having a property that the future state is dependent only on the present state, and does not depends on the previous states. The Markov chain is described by a transition matrix (transition probability), P. P_{ij} is the probability of the transition from state i to state j. It is not difficult to create a Markov chain that has an arbitrary probability distribution as its equilibrium distribution. The necessary conditions that must be satisfied by the transition matrix are ergodicity and detailed balance. By ergodicity we understand

the condition that any possible state can be reached from any other state in a finite number of elementary moves. The detailed balance is given by the equation

$$P_{ij}w_i = P_{ji}w_j, \tag{2.22}$$

where w_i and w_j is are the equilibrium probabilities of being in states i and j, respectively, and P_{ij} is the probability of transition from state i to state j.

A popular method for generating a Markov chain with such properties is known as Metropolis-Hastings algorithm [150–152]. The method is based on generating small random changes of the configuration and accepting or rejecting them with probability

$$P_{\text{accept}} = \min(1, \frac{w_j}{w_i}), \tag{2.23}$$

where w_i and w_j are the probabilities of the current configuration, i, and proposed new configuration, j, respectively. In the case of the Boltzmann distribution, $w_B(E_k)$ of Eq. (2.17), the acceptance probability is

$$P_{\text{accept}} = \min(1, e^{-\Delta E/T}), \tag{2.24}$$

where $\Delta E = E_j - E_i$, is the change of energy that follows the configuration change from state i to state j; E_i and E_j are the energies of the configurations i and j, respectively.

2.2.2 Parallel Tempering

In simulations of slowly equilibrating systems such as spin glasses the parallel tempering, also known as replica exchange method was found to substantially improve the performance [153, 154]. The technique is intended for simulating systems with large energy barriers. In parallel tempering Monte Carlo a number of temperatures is simulated simultaneously. In addition to standard Metropolis local updates configuration swaps between different temperatures, so-called thermal replicas, are performed. At high temperatures updates associated with large energy changes are more likely to happen than in low temperatures. Hence, when temperature is high, a simulation explore a large volume of phase space, while at low temperatures a narrow local region

of phase space space is sampled, and the system can be easily trapped in a local energy minima. Performing configuration exchanges with thermal replicas at higher temperature allows a low temperature system to travel between local free energy minima that are separated by energy barriers that local update alone would be very unlikely to overcome.

The probability of configuration swaps are chosen such that the detailed balance (2.22) is satisfied. The system of M thermal replicas can be formally treated as an extended ensemble. Let the replicas be associated with a set of temperatures T_m, where $m = 1, 2, \ldots, M$. The state of the extended ensemble, X, is specified by the configurations of all M replicas, $X = \{X_1, X_2, \ldots, X_M\}$ and the partition function is

$$Z = \prod_{m=1}^{M} Z_m, \tag{2.25}$$

where Z_m is the partition function of the replica at temperature T_m. The probability of a configuration X reads

$$W(X) = \prod_{m=1}^{M} w(X_m, T_m), \tag{2.26}$$

where

$$w(X_m, T_m) = \frac{1}{Z_m} e^{-\frac{\mathcal{H}(X_m)}{k_B T_m}} \tag{2.27}$$

is the probability of configuration X_m in temperature T_m. Let

$$X = \{X_1, \ldots, X_k, \ldots, X_l, \ldots, X_M\}$$

and

$$X' = \{X_1, \ldots, X_l, \ldots, X_k, \ldots, X_M\},$$

thus the extended ensemble configuration change, $X|X'$, consist of swapping the configurations between replicas k and l. A transition matrix $P(X|X')$ is defined. For convenience we write

$$P_{kl \to lk} = P(\{X_1, \ldots, X_k, \ldots, X_l, \ldots, X_M\} | \{X_1, \ldots, X_l, \ldots, X_k, \ldots, X_M\}), \tag{2.28}$$

and

$$W_{kl} = W(\{X_1, \ldots, X_k, \ldots, X_l, \ldots, X_M\}). \tag{2.29}$$

The detailed balance condition take the form

$$P_{kl\to lk} W_{kl} = P_{lk\to kl} W_{lk}. \tag{2.30}$$

Like in the case of local updates, we compute

$$\frac{W_{lk}}{W_{kl}} = \frac{e^{-\frac{\mathcal{H}(X_k)}{k_B T_l} - \frac{\mathcal{H}(X_l)}{k_B T_k}}}{e^{-\frac{\mathcal{H}(X_k)}{k_B T_k} - \frac{\mathcal{H}(X_l)}{k_B T_l}}} = e^{-[\mathcal{H}(X_l) - \mathcal{H}(X_k)]\left[\frac{1}{k_B T_k} - \frac{1}{k_B T_l}\right]}, \tag{2.31}$$

and a possible choice of the probability of swapping the configurations between k and l replicas, satisfying the detailed balance condition, is Metropolis-Hastings formula (2.23), that gives here

$$P_{\text{accept}} = \min(1, e^{-\Delta}), \tag{2.32}$$

where

$$\Delta = [\mathcal{H}(X_l) - \mathcal{H}(X_k)] \left[\frac{1}{k_B T_k} - \frac{1}{k_B T_l}\right]. \tag{2.33}$$

The difference between the simulated temperatures, ΔT, must be small enough for the configuration swap to happen. Each of the replicas is sampled with the Boltzmann probability characteristic for the relevant temperature, T_m. The energy of a new configuration, to be accepted, must be in the energy range characteristic for the sampled temperature. If the configurations of thermal replicas k and l are to be exchanged, there must be overlap between the probability distributions for the temperatures T_k and T_l, or, in other words, the configurations sampled at $T = T_k$ must be also likely to appear at $T = T_l$. As the probability of a configuration exchange decreases with increasing temperature difference, the configuration swaps are usually performed between adjacent replicas. The probability of configuration exchange should reasonably large and uniform among the replicas. For this to happen, Δ (2.33) should be small, and uniform for considered temperatures. One can write

$$\Delta = \frac{\mathcal{H}(X_l) - \mathcal{H}(X_k)}{T_l - T_k} \frac{(T_l - T_k)^2}{T_l T_k} \approx C_V(T) \frac{(\Delta T)^2}{T^2}, \tag{2.34}$$

where $T = (T_k + T_l)/2$, and $C_V(T) \approx \frac{\mathcal{H}(X_l)-\mathcal{H}(X_k)}{T_l-T_k}$. That means that the difference between the temperatures should be

$$\Delta T \propto \frac{T}{\sqrt{C_v}} = \frac{T}{\sqrt{c_v N}}, \tag{2.35}$$

where c_V is the specific heat per particle in the simulation cell. Hence, for a fixed temperature range, the number of thermal replicas should increase with the system size, N, as $\frac{1}{\sqrt{N}}$.

2.2.3 Overrelaxation

It has been reported that, in simulations of Heisenberg spin systems, such as the model considered in Chapter 5, supplementing canonical Metropolis spin updates with "overrelaxation" steps, computationally inexpensive, zero energy transformations, can substantially reduce autocorrelation times [155, 156]. Unfortunately, this technique does not provide performance improvement in the case of long-range interactions and cannot be used when periodic boundary condition are imposed on a system characterized by dipolar interaction with non-cubic lattice symmetry.

In overrelaxation update, a new spin direction, $\boldsymbol{S}_i'$, is obtained by performing a reflection of the spin at site i, $\boldsymbol{S}_i$, around the local dipolar field vector, $\boldsymbol{H}_i$,

$$\boldsymbol{S}_i' = -\boldsymbol{S}_i + 2\frac{\boldsymbol{S}_i \cdot \boldsymbol{H}_i}{H_i^2}\boldsymbol{H}_i. \tag{2.36}$$

The local dipolar field is given by Eq. (5.5),

$$\boldsymbol{H}_k = \sum_{j \neq k} \hat{L}_{kj}\boldsymbol{S}_j, \tag{2.37}$$

where the tensor $\hat{L}_{kj}$ stands for dipolar interaction. Using Eq. (2.37) the Hamiltonian can be written in the form

$$\mathcal{H} = -\frac{1}{2}\sum_k \boldsymbol{S}_k\boldsymbol{H}_k - \frac{1}{2}\sum_k \boldsymbol{S}_k\hat{L}_{kk}\boldsymbol{S}_k. \tag{2.38}$$

Let the energy of a spin configuration be written in the form

$$E = -\frac{1}{2}\boldsymbol{S}_i\boldsymbol{H}_i - \frac{1}{2}\sum_{k\neq i}\boldsymbol{S}_k\boldsymbol{H}_k - \frac{1}{2}\sum_{k}\boldsymbol{S}_k\hat{L}_{kk}\boldsymbol{S}_k. \tag{2.39}$$

After changing spin $\boldsymbol{S}_i$ to $\boldsymbol{S}'_i$, according to Eq. (2.36), we have

$$E' = -\frac{1}{2}\boldsymbol{S}'_i\boldsymbol{H}_i - \frac{1}{2}\sum_{k\neq i}\boldsymbol{S}_k\boldsymbol{H}'_k - \frac{1}{2}\sum_{k}\boldsymbol{S}'_k\hat{L}_{kk}\boldsymbol{S}'_k, \tag{2.40}$$

where $\boldsymbol{H}'_k$ are updated dipolar fields; $\boldsymbol{H}'_i = \boldsymbol{H}_i$ and for $k \neq i$:

$$\boldsymbol{H}'_k = \boldsymbol{H}_k + \hat{L}_{ki}(\boldsymbol{S}'_i - \boldsymbol{S}_i). \tag{2.41}$$

Eqs. (2.36), (2.39), (2.40) and (2.41) give

$$E' - E = \frac{1}{2}\left(\boldsymbol{S}'_i\hat{L}_{ii}\boldsymbol{S}'_i - \boldsymbol{S}_i\hat{L}_{ii}\boldsymbol{S}_i\right). \tag{2.42}$$

The energy does not change only if $\boldsymbol{S}'_i\hat{L}_{ii}\boldsymbol{S}'_i - \boldsymbol{S}_i\hat{L}_{ii}\boldsymbol{S}_i = 0$. It is the case when, for each μ,ν, $L^{\mu\nu}_{ii} = 0$, or for diagonal $\hat{L}_{ii}$, $L^{\mu\nu}_{ii} = L_{ii}\delta_{\mu\nu}$, what is satisfied in the case of cubic lattice symmetry (see Appendix C).

In simulations discussed in Chapter 5 we do not use the overrelaxation method. For the model considered in Chapter 5, the fact that we do not use the overrelaxation method does not cause a large decrease of efficiency in our simulation. In the case of long-range interaction, the reflection (2.36) would have to be followed by the recalculation of dipolar field, $\boldsymbol{H}'_k$, of Eq. (2.41). A similar lattice sums have to be performed in the case of Metropolis updates.Most of the computation time is spent on doing such lattice sums; hence, here the overrelaxation move would be practically as computationally expensive as a Metropolis update.

2.2.4 Heatbath algorithm

In the original Metropolis algorithm a random configuration update is attempted and it is accepted with the probability depending on the change of the energy that follows such configuration change. The updates lowering the energy are always accepted,

while if the energy was going to increase, the acceptance probability is

$$P(\Delta E) = \exp(-\beta \Delta E), \tag{2.43}$$

where $\beta = 1/k_{\mathrm{B}}T$. The probability exponentially decreases with increase of the energy change, ΔE. Thus, to obtain a sufficient acceptance rate the attempted moves have to be sufficiently small. Usually the configuration update is chosen in such way that the acceptance rate is close to 50%. In many applications a better way of performing a local spin updates is the "heatbath" algorithm [157–159], where the new direction of a spin is drawn from suitable probability distribution, such that the new configuration energy is distributed according to a Boltzmann weight. In the case of isotropic (O(3)) Heisenberg model, the distribution of angle θ between the local dipolar field, $\boldsymbol{H}_i$, and the spin vector $\boldsymbol{S}_i$ can be calculated analytically [157–159]. In such isotropic case, the Hamiltonian that can be written as

$$\mathcal{H} = -\frac{1}{2} \sum_i \boldsymbol{S}_i \boldsymbol{H}_i \tag{2.44}$$

where $\boldsymbol{H}_i$ is the interaction field and $\boldsymbol{H}_i$ does not depend on spin $\boldsymbol{S}_i$. In the case of long-range interaction we write

$$\boldsymbol{H}_i = \sum_{j \neq i} \hat{L}_{ij} \boldsymbol{S}_j \tag{2.45}$$

It is convenient to describe spin $\boldsymbol{S}_i$ in the polar coordinates, θ and ϕ , with the polar axis along the local dipolar field, $\boldsymbol{H}_i$. The energy of spin i in the field of other spins is,

$$E_i = -\boldsymbol{S}_i \boldsymbol{H}_i = -H_i \cos(\theta), \tag{2.46}$$

where θ is the polar angle defined as the angle between $\boldsymbol{S}_i$ and $\boldsymbol{H}_i$. We wish to randomly choose $\boldsymbol{S}_i$ such that the probability distribution of the energy (2.46) given by Boltzmann distribution. The energy does not depend on the azimuthal angle, ϕ; hence, ϕ is randomly chosen from the uniform distribution on the interval $[0, 2\pi]$. The

polar angle, θ, is chosen such that $x = \cos(\theta)$ is given by the probability distribution

$$P(x) = \frac{e^{\beta H_i x}}{\int_{-1}^{1} dx e^{\beta H_i x}} = \frac{\beta H_i}{2 \sinh \beta H_i} e^{\beta H_i x}, \tag{2.47}$$

where $\beta = 1/T$. To obtain random variable x drawn from distribution (2.47), we calculate the cumulative distribution

$$F(x) = \int_{-1}^{x} P(x')dx' = \frac{e^{\beta H_i x} - e^{-\beta H_i}}{e^{\beta H_i} - e^{-\beta H_i}} \tag{2.48}$$

and we reverse $r = F(x)$, where $r \in [0, 1]$ is a uniformly distributed random number. We obtain [157–159]

$$x = \frac{1}{\beta H_i} \ln \left[1 + r \left(e^{2\beta H_i} - 1\right)\right] - 1. \tag{2.49}$$

Having chosen ϕ and θ we need to compute the vector components of the spin and rotate them to the global coordinate system. Let ϕ_H and θ_H denote azimuthal and polar angle of vector $\boldsymbol{H}_i$ in global coordinates. One of possible choices of the local coordinates $\hat{x}'$, $\hat{y}'$ and $\hat{z}'$, having $\hat{z}'$ axis along $\boldsymbol{H}_i$ is

$$\begin{aligned}
\hat{x}' &= \cos(\theta_H)\cos(\phi_H)\hat{x} + \cos(\theta_H)\sin(\phi_H)\hat{y} - \sin(\theta_H)\hat{z} \\
\hat{y}' &= -\sin(\phi_H)\hat{x} + \cos(\phi_H)\hat{y} \\
\hat{z}' &= \sin(\theta_H)\cos(\phi_H)\hat{x} + \sin(\theta_H)\sin(\phi_H)\hat{y} + \cos(\theta_H)\hat{z}.
\end{aligned} \tag{2.50}$$

The new spin, $\boldsymbol{S}_i$, in local coordinates is

$$\boldsymbol{S}_i = \sin(\theta)\cos(\phi)\hat{x}' + \sin(\theta)\sin(\phi)\hat{y}' + \cos(\theta)\hat{z}', \tag{2.51}$$

and finally, combining Eq. (2.50) and Eq. (2.51), we get

$$\begin{aligned}
S_x &= \Theta\cos(\phi_H) - \sin(\theta)\sin(\phi)\sin(\phi_H), \\
S_y &= \Theta\sin(\phi_H) + \sin(\theta)\sin(\phi)\cos(\phi_H), \\
S_z &= -\sin(\theta)\cos(\phi)\sin(\theta_H) + \cos(\theta)\cos(\theta_H),
\end{aligned} \tag{2.52}$$

where

$$\Theta = \sin(\theta)\cos(\phi)\cos(\theta_H) + \cos(\theta)\sin(\theta_H). \tag{2.53}$$

Hamiltonian (2.44) with dipolar field (2.45) does not include self-interaction term. In the case of dipolar interaction with periodic boundary condition we have to include self-interaction and we write

$$\mathcal{H} = -\frac{1}{2}\sum_i \left(\boldsymbol{S}_i\boldsymbol{H}_i + \boldsymbol{S}_i\hat{L}_{ii}\boldsymbol{S}_i\right). \tag{2.54}$$

For Hamiltonian (2.54), as opposite to Hamiltonian (2.44), in the general case, cumulative distribution (2.48) could not be integrated and reversed analytically. For cubic symmetry self-interaction term is of the form $L_{ii}^{\mu\nu} = L_{ii}\delta_{\mu\nu}$ and Eq. (2.54) reduces to

$$\mathcal{H} = -\frac{1}{2}\sum_i \left(\boldsymbol{S}_i\boldsymbol{H}_i + L_{ii}\right); \tag{2.55}$$

hence, it is of the form (2.44) with just an independent of spin configuration constant added and the heatbath method can be applied.

In principle, for the model discussed in Chapter 5 the heatbath algorithm could be used, because a cubic lattice is considered. Nevertheless, we decided to use a method generally applicable for any lattice symmetry, to obtain results that are directly comparable with simulations for other lattice geometries, and we do not use heatbath.

2.3 Summary

In this chapter, the mean field approximation and Monte Carlo methods were discussed. The mean-field theory is used in Chapter 3 and 4 to study $LiHo_xY_{1-x}F_4$ and rare earth hydroxides, $RE(OH)_3$, respectively. The Monte Carlo simulations are used in Chapter 5 and 6 to study diluted dipolar Heisenberg spin glass and dipolar pyrochlore easy-axis antiferromagnet.

In the next chapter, local mean-field method is used to study $LiHo_xY_{1-x}F_4$ [6–21]. In zero transverse magnetic field, depending on the concentration, x, $LiHo_xY_{1-x}F_4$ is a diluted dipolar Ising ferromagnet or diluted dipolar Ising spin glass [7, 8, 120]. The effect of the transverse field on the pure $LiHoF_4$ ferromagnet-paramagnet phase

diagram, with a quantum critical point at T=0 was studied using quantum Monte Carlo simulations [127]. At large dilution, in the classical, $B_x = 0$, case, the spin glass transition was also investigated, using Monte Carlo simulations [120]. It is difficult or impossible to consider together in a Monte Carlo simulation the effect of transverse magnetic field and dilution, especially in the high dilution regime, where frustration would lead to severe sign problem in quantum Monte Carlo simulation. For that reason local mean-field approximation is used. It was shown that in a diluted, spatially disordered, $LiHo_xY_{1-x}F_4$ the transverse field gives rise to a longitudinal random field [24–26]. The longitudinal random field suppress the spin-glass phase and affects the ferromagnet-paramagnet phase boundary. Used in the following chapter, local mean-field theory allows in quite a direct way to analyse the effect of the random field on both ferromagnetic and spin glass phases.

Chapter 3

Mean-field studies of $LiHo_xY_{1-x}F_4$ in transverse magnetic field

In this chapter, the effect of transverse-field-induced longitudinal random field in $LiHo_xY_{1-x}F_4$ is studied. In the pure case, $LiHoF_4$ is a dipolar Ising ferromagnet with a Curie temperature $T_c = 1.53$ K [160]. The magnetic moments of Ho^{3+} in the perfect crystalline environment of $LiHoF_4$ are characterized by a strong Ising anisotropy [161]. The first excited state is ~ 11 K above the ground state doublet [16]. At the temperatures of interest, $T < T_c = 1.53$ K, $LiHoF_4$ is well described by a spin-1/2 effective Ising Hamiltonian [162]. The exchange interactions between Ho^{3+} ions are relatively weak and the long-range dipolar interactions play the leading role [117].

Subject to a magnetic field perpendicular to the Ising easy-axis direction, B_x, $LiHoF_4$ is a realization of the transverse-field Ising model [22, 23, 126]. The transverse magnetic field admixes the ground state doublet with the excited states and splits the ground-state doublet. The energy gap created between the states of the ground doublet plays the role of a transverse magnetic field, Γ, in the effective transverse field Ising Hamiltonian

$$\mathcal{H} = -\frac{1}{2}\sum_{i,j} J_{ij}\sigma_i^z\sigma_j^z - \Gamma\sum_i \sigma_i^x, \tag{3.1}$$

where σ_i^μ ($\mu = x,\ z$) denotes spin operators given by Pauli matrices and J_{ij} is the effective dipolar interaction, rescaled by the transverse field, B_x. The transverse-field Ising model is the simplest model that exhibits a quantum phase transition [22, 23];

$LiHoF_4$ and its diluted variant $LiHo_xY_{1-x}F_4$ have long been used to study the effects of tunable quantum fluctuations and quantum criticality [6–21]. For the classical phase transition in an Ising system with dipolar interactions, the upper critical dimension is $d_U = 3$, and not $d_U = 4$ as in the case of short range interactions [163, 164]. Thus, one expects mean-field-like critical behaviour with logarithmic corrections [163]. The quantum criticality is expected to be mean-field like as a quantum phase transition in d dimensions can be identified with a classical phase transition in $d+1$ dimensions [165].

Bitko *et al.* [10] obtained an experimental B_x vs T phase diagram for $LiHoF_4$. In the high transverse field regime, the critical transverse field, B_x^c, is pushed up [10]. This feature is due to the hyperfine interaction and it was reproduced in a mean-field calculation [10]. Stochastic series expansion [127] and perturbative [1] quantum Monte Carlo simulation studies of B_x vs T phase diagram for $LiHoF_4$ were performed. Qualitative agreement between the experimental and numerical phase diagrams have been obtained [127], but there is a significant discrepancy in the vicinity of the classical critical point [1, 127], and it was shown that the discrepancy cannot be resolved just by more careful treatment of the long-range dipolar interactions [1].

Many interesting phenomena can be explored in magnetically diluted $LiHo_xY_{1-x}F_4$, where some of the magnetically active Ho^{3+} ions are randomly replaced with nonmagnetic Y^{3+}. The temperature vs concentration, x, phase diagram for $LiHo_xY_{1-x}F_4$ that was proposed by Reich *et al.* [117] is shown in Fig. 3.1. As mentioned before, in the pure case, $x = 1$, the system undergoes a continuous phase transition from the paramagnetic to the ferromagnetic phase at $T_c = 1.53$ K. Upon decreasing the concentration, x, of the magnetic Ho^{3+} ions the critical temperature, $T_c(x)$, is depressed. In agreement with analytical predictions [136, 166], down to $x \sim 0.5$, $T_c(x)$ vs x is given by a linear, mean-field form $T_c(x) = xT_c(x = 1)$ [11, 12, 17]. The linear dependency, $T_c(x) = xT_c(x = 1)$ was also found in Monte Carlo simulations [138]. The dipolar interactions can have either ferromagnetic or antiferromagnetic character, depending on the spatial arrangement of the dipoles; hence, in the presence of spatial disorder, random frustration occurs. Upon dilution below $x = 0.5$, the antiferromagnetic component of the dipolar interaction becomes more prominent and the paramagnet-ferromagnet transition temperature is depressed at a higher rate than linearly, and finally, around $x \simeq 0.25$, the long-range order vanishes and gives way to a spin-glass phase. For $x = 0.167$, a signature of a spin-glass transition was via a diver-

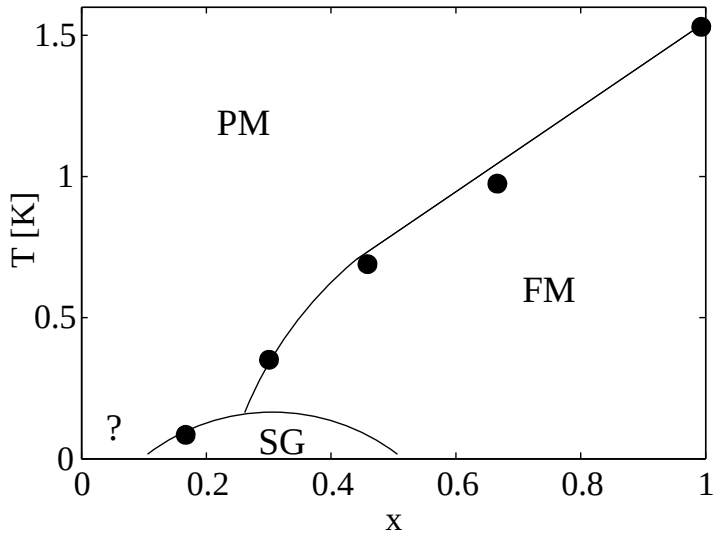

Figure 3.1: The phase diagram for $LiHoF_4$. PM, FM and SG denote paramagnetic phase, ferromagnetic phase and spin glass, respectively; and '?' shows "anti-glass" state [117].

gence in the nonlinear susceptibility, χ_3, and by the imaginary part of the linear AC susceptibility, $\chi''(f)$, that shows critical behaviour broadening as the temperature is lowered [7, 8]. Theory predicts that either spin-glass or ferromagnetic ordering persist down to x=0 [136, 166], but in early experimental studies, it was found that at the concentration $x = 0.045$, the system exhibits unusual glassy behaviour [13, 14, 117]. In contrast to the conventional spin-glass response, the imaginary part of the linear AC susceptibility, $\chi''(f)$, does not exhibits broadening but rather narrowing when the temperature is decreased. Because of this behaviour, the state of matter in this regime was named the anti-glass phase. Contradictory results were obtained in recent measurements of specific heat [135] and susceptibility [119], which clearly indicate that there is a spin-glass transition for x=0.045.

Interesting phenomenology occurs when transverse magnetic field, B_x, and dilution are considered simultaneously. Naively, one would expect that such system provides a framework to study the physics of the transverse field Ising model when the system is either a diluted ferromagnet or a spin glass, and hence possibly to observe a quantum phase transition in a strongly disordered system. In fact, the physics of $LiHo_xY_{1-x}F_4$

in a transverse magnetic field turns out to be more complex. The transverse field induces quantum fluctuations which suppress the spontaneous magnetic order, and the critical temperature decreases. In the experiments, with increasing B_x, the critical temperature decreases faster than is predicted by mean-field theory [12], which suggest that the transverse field becomes more efficient in destroying long-range order [12]. The spin-glass transition is signaled by a divergence in the nonlinear susceptibility, χ_3. If the transverse field Ising model is considered, the transverse field would be expected to reduce the spin-glass transition temperature, T_g, and, at $T = 0$, a quantum phase transition between a spin-glass and quantum paramagnet would occur, that would be signalled by a divergence of χ_3 as a function of the transverse field, B_x [167, 168]. In $LiHo_{0.167}Y_{0.833}F_4$, a completely different behaviour was observed. Upon decreasing temperature, the character of χ_3 becomes progressively less singular, suggesting that there is no quantum spin-glass transition at $T = 0$ [8].

In an attempt to explain these two observations: the increasing of the rate of depressing of T_c with dilution in transverse field and the suppression of the spin-glass phase by the transverse field, it was observed that in the presence of transverse field and dilution, when the effective spin-1/2 Hamiltonian is considered, not only does the effective transverse field term $\Gamma\sigma_i^x$ occur, as in Eq. (3.1), but also other terms mixing longitudinal and transverse spin operators and, due to the spatial disorder, an effective longitudinal random field appear [24–26]. Tabei *et al.* analysed the effective spin-1/2 Hamiltonian for $LiHo_xY_{1-x}F_4$ [26] and demonstrated in finite-lattice mean-field calculations [25] that the paramagnet-ferromagnet transition temperature gets suppressed when the random field term is included. Also, using the replica trick and imaginary time formalism in a toy model where a Gaussian distribution of fields and interactions is used, they showed that the longitudinal random field suppresses the divergence in the nonlinear susceptibility, χ_3.

Here, we would like to extend the existing mean-field study to consistently survey range of macroscopic parameters: T, B_x and x, to produce a complete phase boundary including both the spin glass and ferromagnetic phases. The effect of the longitudinal random field on the spin-glass phase was investigated using an infinite dimensional toy model [25]. The computational method used herein allows us to study a realistic model of $LiHoF_4$. In the case of experimental studies of other, similar materials, e.g. $Ho(OH)_3$ that is discussed in the next chapter, it is reasonable to believe that

our theoretical method may be able to capture eventual difference between magnetic properties observed in $LiHo_xY_{1-x}F_4$ and $Ho_xY_{1-x}(OH)_3$.

Considering disorder substantially increases computational complexity of the problem, because of the need to compute disorder average and because of rugged free energy landscape and our attempts to estimate a number of free energy minima. Hence, we decided to not include the hyperfine interaction and perform the calculation using a spin-1/2 effective Hamiltonian rather than diagonalising 136×136 matrices that would be required for the hyperfine interaction to be included [10]. Besides substantially decreasing the the complexity of calculations, a benefit of using the effective spin-1/2 Hamiltonian is that the transverse-field-generated longitudinal random field is explicitly present in the effective spin-1/2 Hamiltonian. The effect of hyperfine interactions is pronounced at high B_x only [10]; hence our calculations for moderate B_x should not lose too much in accuracy in respect to the case when the hyperfine interaction is considered.

We use a local mean-field theory to study the effect of transverse-field-induced longitudinal random fields on the phase diagram of $LiHo_xY_{1-x}F_4$, considering both the transverse field, temperature and dilution as the variable parameters. We derive a low energy spin-1/2 Hamiltonian that includes the effect of the transverse field and dilution. Within a mean-field approximation, a system of equations is derived which describes the local magnetizations at all the lattice sites occupied by magnetic ions for a given realisation of disorder at the considered dilution. This set of equations amounts to a condition for a local free energy minima. Random frustration in the system gives rise to a rugged free energy landscape with many local minima; hence, multiple solutions to each set of equations are found and they are counted to estimate the complexity of the free energy landscape. A range of temperatures, T, transverse field, B_x, and concentration, x, is surveyed. For each value of the macroscopic parameters: T, B_x and x, a number of realisations of disorder is considered and, in the glassy phase, for each realisation of disorder, multiple solutions of the local mean-field equations are found.

Two methods for locating the phase boundaries are used. In the first method we calculate a relevant order parameter: the magnetization for a ferromagnet and the Edwards-Anderson order parameter for a spin-glass, and estimate the transition temperature by looking for inflection points in plots of the order parameter vs con-

centration, x. To locate the spin-glass phase, we also estimate the complexity of the free energy landscape by counting the solutions of the mean field equations. The second method of locating the spin-glass phase is superior to the inflection point method for the Edwards-Anderson order parameter, because it allows one to locate not only the paramagnet-spin-glass boundary but also the boundary between the ferromagnetic and spin-glass phases. In zero transverse field, the phase diagram obtained is qualitatively similar to the phase diagram shown in Fig. 3.1. In an applied transverse field, the estimated number of local free energy minima, in the regime where the spin-glass phase is expected, is considerably reduced, indicating a quenching of the spin-glass phase, while the magnitude of the local magnetizations does not vanish - suggesting that the spins are aligned with the local random longitudinal field.

Our original aim was to use the local mean-field theory to compute the nonlinear susceptibility, χ_3. We hoped to reproduce the smearing of the χ_3 divergence at the spin-glass transition with decreasing temperature in χ_3 vs B_x plots, as it was obtained in experimental work of Wu *et al.* [8]. Unfortunately, we found that it is not possible to calculate the nonlinear susceptibility, χ_3, in the framework of local mean-field theory because of local singularities that occur in the model.

This chapter is organised as follows. In Section 3.1, we discuss the material properties of $LiHoF_4$ or equivalently its diluted version $LiHo_xY_{1-x}F_4$. We consider the effect of transverse magnetic field on the single ion crystal field Hamiltonian and we examine the interactions present in the system. In Section 3.2, the mean-field Hamiltonian is derived and a projection to the Ising, spin-1/2 subspace is discussed. In Section 3.3, the system of mean-field equations for local magnetizations is presented, and the iterative procedure for obtaining and counting solutions is discussed. Section 3.4 is devoted to a discussion of the results, both in the case of zero transverse field and for nonzero transverse field, where the effect of random field is observed. The chapter is concluded by a short summary.

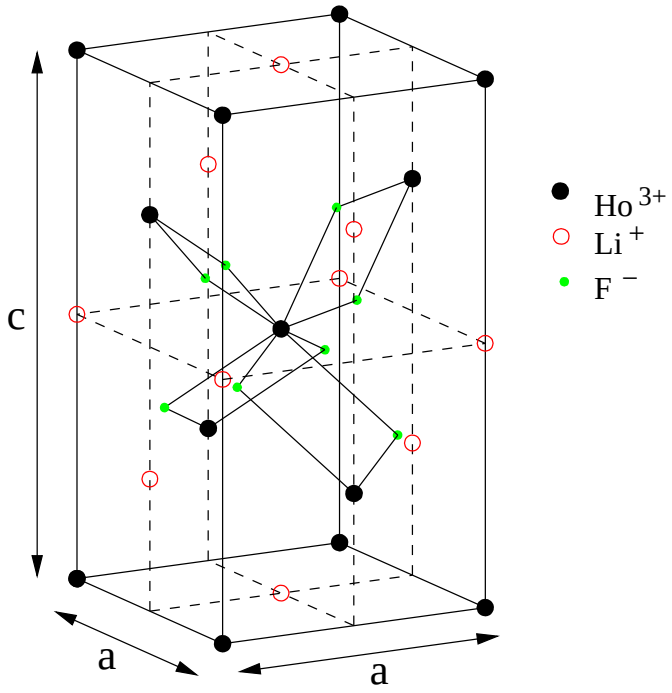

Figure 3.2: The crystal structure of $LiHoF_4$.

3.1 Material properties

3.1.1 Crystal structure and crystal field Hamiltonian

$LiHoF_4$ forms tetragonal crystals with lattice constants a=b=5.175 Å and c=10.75 Å [169]. The magnetic properties of $LiHoF_4$ originate from Ho^{3+} cations. $LiHoF_4$ is an Ising ferromagnet with the easy axis pointing along the crystallographic c direction. There are 4 Ho^{3+} ions in a unit cell, at the positions: (0,0,1/2), (0,1/2,3/4), (1/2,1/2,0) and (1/2,0,1/4) [169]. The crystal structure of $LiHoF_4$ is shown in Fig. 3.2. The black dots in the figure represent the Ho^{3+} ions. The red circles mark the positions of Li^+ ions. The F^- ions are drawn as small green dots. For clarity, only the four nearest-neighbour and the four next-nearest-neighbour F^- ions, surrounding the Ho^{3+} central ion, are shown. The lines connecting the central Ho^{3+} ion with the F^- ions and then with the other Ho^{3+} ions indicate exchange pathways between nearest-neighbour Ho^{3+} cations [169].

The electronic configuration of Ho^{3+} is $4f^{10}$. Because the $4f$ orbital is screened

by $5s$, $5p$ and $5d$ shells the exchange interaction in $LiHoF_4$ is relatively weak, and the dipolar interaction plays a dominant role [127]. The ground state configuration of Ho^{3+} is ${}^5I_8(S{=}2,L{=}6,J{=}8)$. The energy gap between the ground-state, ${}^5I_8$, manifold and the first excited state, ${}^5I_7$, is around 7400 K [170]. The ground state is a 17-fold degenerate multiplet. The Ho^{3+} ions in $LiHoF_4$ are subject to a strong crystal electric field from the F^- and Li^+ ions. The crystal field partially lifts the degeneracy of the ground-state manifold. The crystal field ground state is a non-Kramers doublet, i.e. that degeneracy is coincidental, as opposite to Kramers multiplets that originate from time reversal symmetry in odd electron systems. The first excited state is a singlet, located around 11 K above the ground doublet. There are no J_x and J_y matrix elements between the states of the ground doublet; hence, to the first order in applied transverse magnetic field, the transverse susceptibility vanishes and Ho^{3+} ions in $LiHoF_4$ are characterised by a strong Ising anisotropy.

The crystal field Hamiltonian for the ground-state manifold can be expressed in terms of Stevens' "operator equivalents" [171, 172][1]. The Stevens' operators, O_n^m, are conveniently expressed in terms of vector components of angular momentum operator, $\boldsymbol{J}$. The crystal field Hamiltonian can be written in the form

$$\mathcal{H}_{\text{cf}} = \sum_{nm} B_n^m O_n^m, \tag{3.2}$$

where O_n^m are Stevens' "operator equivalents", and B_n^m are crystal field parameters[2]. From angular momentum algebra, we know that in the case of f electrons, we need to consider only $n = 0, 2, 4, 6$ in the sum (3.2) [172]. The choice of B_n^m coefficients in Hamiltonian (3.2) that do not vanish and have nonzero corresponding matrix elements is dictated by the point symmetry group of the crystalline environment. The point symmetry group at the Ho^{3+} site in $LiHoF_4$ is S_4, and the crystal-field Hamiltonian reads

$$\mathcal{H}_{\text{cf}}(\boldsymbol{J}_i) \;=\; B_2^0 O_2^0(\boldsymbol{J}_i) + B_4^0 O_4^0(\boldsymbol{J}_i) + B_6^0 O_6^0(\boldsymbol{J}_i)$$

[1] Ref. [172] contains a comprehensive review of the method and conventions used to express crystal field Hamiltonians

[2] Writing Hamiltonian (3.2) we assume that B_n^m include Stevens multiplicative factors [172], θ_n. In Chapter 4 a different convention for writing a crystal field Hamiltonian is used - θ_n are written explicitly.

	Ref. [16, 127]	Ref. [142]
B_2^0	-0.696 K	-0.609 K
B_4^0	4.06×10^{-3} K	3.75×10^{-3} K
B_6^0	4.64×10^{-6} K	6.05×10^{-6} K
B_4^{4c}	4.18×10^{-2} K	3.15×10^{-2} K
B_4^{4s}	0 K	2.72×10^{-2} K
B_6^{4c}	8.12×10^{-4} K	6.78×10^{-4} K
B_6^{4s}	1.137×10^{-4} K	4.14×10^{-4} K

Table 3.1: Crystal field parameters for $LiHoF_4$ from Ref. [16, 127], used in the calculations of this chapter, and from Ref. [142], given just for comparison.

$$+B_4^{4c}O_4^{4c}(\boldsymbol{J}_i) + B_4^{4s}O_4^{4s}(\boldsymbol{J}_i) + B_6^{4c}O_6^{4c}(\boldsymbol{J}_i) + B_6^{4s}O_6^{4s}(\boldsymbol{J}_i). \tag{3.3}$$

The CFP are usually determined by fitting the crystal-field Hamiltonian to experimental data, for example electron paramagnetic resonance [142], inelastic neutron scattering [16] or magnetic susceptibility measurements [161]. In the calculations presented in this chapter we use values of the crystal field parameters proposed by Rønnow *et al.* [16]. These crystal field parameters were obtained from fitting the results of random phase approximation calculations to neutron scattering data [16]. Taking into account a rather qualitative character of mean-field calculations, we do not attempt to study rather subtle differences between the results obtained when using different estimations of the crystal field parameters, and we stick to the crystal field parameters of Ref. [16, 127]. But for comparison, the values of crystal field parameters collected in Table 3.1, besides the used here crystal field parameters from Ref. [16], include also the values given in Ref. [142].

3.1.2 Transverse field spectrum

To derive an effective spin-1/2 Hamiltonian we start from considering the effect of transverse field on single Ho^{3+} ion [127]. A transverse magnetic field, B_x, applied in the direction perpendicular to the direction of the Ising easy axis splits the degeneracy of the ground doublet. In a transverse field, the Hamiltonian of a single Ho^{3+} ion consist of the crystal-field and Zeeman term,

$$\mathcal{H}_0 = \mathcal{H}_{\rm cf}(\boldsymbol{J}_i) - g\mu_{\rm B}B_xJ_x. \tag{3.4}$$

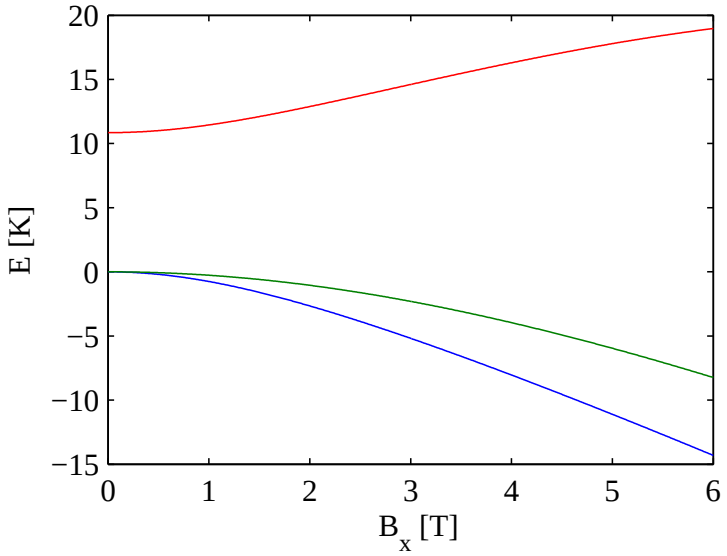

Figure 3.3: The lowest energy levels in $LiHoF_4$ in transverse field, B_x.

Diagonalizing Hamiltonian (3.4), the transverse field dependence of the energy levels is obtained, and for the three lowest levels it is shown in Fig. 3.3[3]. As will be discussed in Section 3.2.1 the transverse-field-induced energy gap between the states of the ground doublet plays the role of a transverse magnetic field in the effective spin-1/2 model.

3.1.3 Interaction Hamiltonian

The low-energy Hamiltonian for $LiHoF_4$, containing the crystal-field term, Zeeman term, and magnetic interaction terms, can be written in the form

$$\begin{aligned} \mathcal{H} &= \sum_i \mathcal{H}_{\rm cf}(\boldsymbol{J}_i) - g\mu_{\rm B}\sum_i B_x J_{i,x} \\ &+ \frac{1}{2}\sum_{ij}\sum_{\mu\nu}\mathcal{L}_{ij}^{\mu\nu}J_{i,\mu}J_{j,\nu} + \frac{1}{2}\mathcal{J}_{\rm ex}\sum_{i,\rm nn}\boldsymbol{J}_i\cdot\boldsymbol{J}_{\rm nn}. \end{aligned} \tag{3.5}$$

$\mathcal{L}_{ij}^{\mu\nu}$ are the anisotropic dipole-dipole interaction constants of the form $\mathcal{L}_{ij}^{\mu\nu} = \frac{\mu_0(g\mu_{\rm B})^2}{4\pi a^3}L_{ij}^{\mu\nu}$, where $\mu,\nu = x,y,z$; a is a lattice constant and μ_0 is the permeability of vacuum. $L_{ij}^{\mu\nu}$

[3]A similar plot was originally shown in Ref. [127]

are dimensionless dipolar interaction coefficients,

$$L_{ij}^{\mu\nu} = \frac{\delta^{\mu\nu} \left|\boldsymbol{r}_{ij}\right|^2 - 3 \left(\boldsymbol{r}_{ij}\right)^{\mu} \left(\boldsymbol{r}_{ij}\right)^{\nu}}{\left|\boldsymbol{r}_{ij}\right|^5}, \tag{3.6}$$

where $\boldsymbol{r}_{ij} = \boldsymbol{r}_j - \boldsymbol{r}_i$, with $\boldsymbol{r}_i$ the lattice position of magnetic moment $\boldsymbol{J}_i$, expressed in units of the lattice constant, a. $\mathcal{J}_{\text{ex}}$ is the antiferromagnetic ($\mathcal{J}_{\text{ex}} > 0$) exchange interaction constant, which can be recast as $\mathcal{J}_{\text{ex}} = \frac{\mu_0 (g\mu_{\text{B}})^2}{4\pi a^3} J_{\text{ex}}$, where J_{ex} is now a dimensionless exchange constant that can be directly compared with dipolar interaction $L_{ij}^{\mu\nu}$. The label nn in Eq. (3.5) denotes the nearest-neighbour sites of site i. The value of nearest-neighbour exchange, J_{ex}, is not exactly known. In the calculations presented in this chapter we use $J_{\text{ex}} = 0.75$ [1]. For simplicity, the dipolar and exchange interaction coefficients can be combined together, and the Hamiltonian is written,

$$\mathcal{H} = \sum_i \mathcal{H}_{\text{cf}}(\boldsymbol{J}_i) - g\mu_{\text{B}} \sum_i B_x J_{i,x} + \frac{1}{2} \sum_{ij} \sum_{\mu\nu} D_{ij}^{\mu\nu} J_{i,\mu} J_{j,\nu}, \tag{3.7}$$

where $D_{ij}^{\mu\nu}$ includes both dipolar and exchange interaction, $\mathcal{L}_{ij}^{\mu\nu}$ and $\mathcal{J}_{\text{ex}}$.

Periodic boundary conditions are imposed. For each considered spin, an array of its periodic images, repeated outside the simulation cell, is considered. To compute the effect of the periodic images, the Ewald summation technique is used [76–79]. The Ewald method is described in Appendix D.

3.2 Mean-field Hamiltonian and projection to spin-1/2 subspace

3.2.1 Projection to Ising spin-1/2 subspace

We construct an effective Ising Hamiltonian, following the method of Refs. [1, 26, 127]; a similar method is used in Chapter 4. We diagonalize exactly the non-interacting Hamiltonian, $\mathcal{H}_0$ of Eq. (3.4), for each value of the transverse field, B_x. We denote the two lowest states by $|\alpha(B_x)\rangle$ and $|\beta(B_x)\rangle$ and their energies by $E_\alpha(B_x)$ and $E_\beta(B_x)$, respectively. A transverse field enforces a unique choice of basis, in which the states can be interpreted as $|{\rightarrow}\rangle$ and $|{\leftarrow}\rangle$ in the Ising subspace. We introduce a new $|{\uparrow}\rangle$ and

$|\downarrow\rangle$ basis, in which the J_z matrix elements are diagonal, by performing a rotation

$$\begin{aligned} |\uparrow\rangle &= \tfrac{1}{\sqrt{2}}(|\alpha(B_x)\rangle + \exp(i\theta)\,|\beta(B_x)\rangle), \\ |\downarrow\rangle &= \tfrac{1}{\sqrt{2}}(|\alpha(B_x)\rangle - \exp(i\theta)\,|\beta(B_x)\rangle). \end{aligned} \tag{3.8}$$

In this basis, the effective single ion Hamiltonian, describing the two lowest states, is of the form

$$\mathcal{H}_T = E_{\rm CM}(B_x) - \frac{1}{2}\Delta(B_x)\sigma^x, \tag{3.9}$$

where $E_{\rm CM}(B_x) = \frac{1}{2}(E_\alpha(B_x) + E_\beta(B_x))$ and $\Delta(B_x) = E_\beta(B_x) - E_\alpha(B_x)$. Thus the splitting of the ground state doublet plays the role of a transverse magnetic field, $\Gamma \equiv \frac{1}{2}\Delta(B_x)$ in Eq. (1). The energies $E_\alpha(B_x)$ and $E_\beta(B_x)$ are plotted in Fig. 3.3.

To include the interaction terms in our Ising Hamiltonian, we expand the matrix elements of J_x, J_y and J_z operators in terms of the σ^ν ($\nu = x, y, z$) Pauli matrices and a unit matrix, $\sigma^0 \equiv \mathbb{1}$,

$$J_{i,\mu} = C_\mu \mathbb{1} + \sum_{\nu=x,y,z} C_{\mu\nu}(B_x)\sigma_i^\nu. \tag{3.10}$$

The coefficients, C_μ and $C_{\mu\nu}$, are defined as

$$\begin{aligned} C_\mu &= \frac{1}{2}\left[\langle\uparrow|\mathrm{J}^\mu|\uparrow\rangle + \langle\downarrow|\mathrm{J}^\mu|\downarrow\rangle\right], \\ C_{\mu x} &= \frac{1}{2}\left[\langle\uparrow|\mathrm{J}^\mu|\downarrow\rangle + \langle\downarrow|\mathrm{J}^\mu|\uparrow\rangle\right], \\ C_{\mu y} &= \frac{1}{2i}\left[\langle\uparrow|\mathrm{J}^\mu|\downarrow\rangle - \langle\downarrow|\mathrm{J}^\mu|\uparrow\rangle\right], \\ C_{\mu z} &= \frac{1}{2}\left[\langle\uparrow|\mathrm{J}^\mu|\uparrow\rangle - \langle\downarrow|\mathrm{J}^\mu|\downarrow\rangle\right]. \end{aligned} \tag{3.11}$$

The states $|\uparrow\rangle$ and $|\downarrow\rangle$ are obtained from diagonalization of the transverse-field Hamiltonian (3.4) thus they are B_x-dependent, and so are the coefficients $C_{\mu\nu}$. There are 12 coefficients, 5 of them: C_{xz}, C_{yz}, C_{zx}, C_{zy} and C_z are equal zero. The remaining 7 are plotted vs. transverse field, B_x, in Fig. 3.4. The coefficients C_y, C_{xy} and C_{yx} are small and they are neglected in the calculations presented below.

To obtain the effective low-energy Hamiltonian, J_x, J_y and J_z operators in the Hamiltonian (3.7) are replaced by their spin-1/2 projections (3.10). In the case of zero transverse field, $B_x = 0$, only the C_{zz} coefficient has a non-zero value, and the effective

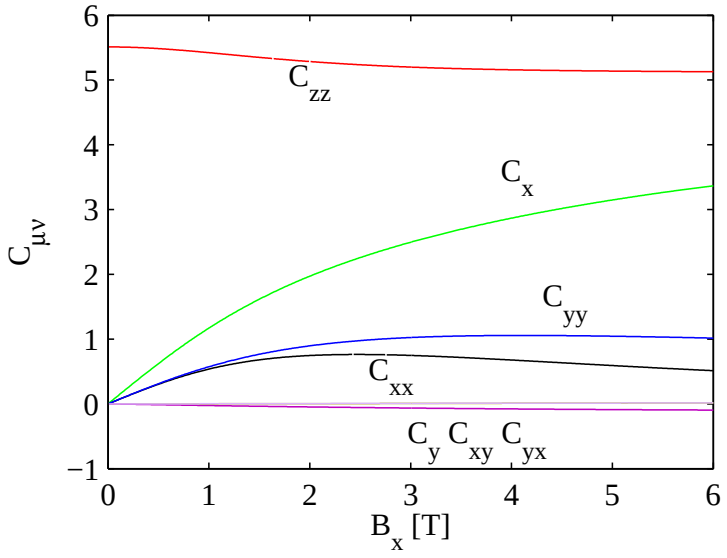

Figure 3.4: The dimensionless $C_{\mu\nu}$ coefficients vs B_x for $LiHoF_4$. Analogous calculation was performed in Ref. [1].

spin-1/2 Hamiltonian takes a simple form

$$\mathcal{H} = \frac{1}{2}\sum_{ij} A_{ij}^{zz}\sigma_i^z\sigma_j^z, \tag{3.12}$$

where $A_{ij}^{zz} = D_{ij}^{zz}\, C_{zz}{}^2$. To further simplify the form of the effective Hamiltonian, we also define: $A_{ij}^{xx} = D_{ij}^{xx}\, C_{xx}{}^2$, $A_{ij}^{xz} = 2D_{ij}^{xz}C_{xx}C_{zz}$, $A_{ij}^{x} = 2D_{ij}^{xx}C_xC_{xx}$ and $A_{ij}^{z} = 2D_{ij}^{xz}C_xC_{zz}$. The magnetization in $\hat{y}$ direction vanishes, and for simplicity, we neglect the terms containing σ_i^y operators. Using $A_{ij}^{\mu\nu}$ coefficients, the effective Hamiltonian is written in the form:

$$\begin{aligned}\mathcal{H} &= E_0 + \frac{1}{2}\sum_{ij} A_{ij}^{zz}\sigma_i^z\sigma_j^z + \frac{1}{2}\sum_{ij} A_{ij}^{xx}\sigma_i^x\sigma_j^x + \sum_{ij} A_{ij}^{xz}\sigma_i^x\sigma_j^z \\ &\quad + \sum_i A_i^x\sigma_i^x + \sum_i A_i^z\sigma_i^z.\end{aligned} \tag{3.13}$$

The coefficients $A_{ij}^{\mu\nu}$ depend on B_x via the coefficients $C_{\mu\nu}$, and on the spatial arrangement of the spins via the dipolar coupling, $D_{ij}^{\mu\nu}$.

3.2.2 Mean-field Hamiltonian

Using the mean-field approximation as shown in Sec. 2.1.1 of Chapter 2 one can write

$$\frac{1}{2}\sum_{ij} A_{ij}^{zz}\sigma_i^z\sigma_j^z \cong \sum_i \left(\sum_j A_{ij}^{zz} m_j^z\right)\left(\sigma_i^z - \frac{1}{2}m_i^z\right) \tag{3.14}$$

$$\frac{1}{2}\sum_{ij} A_{ij}^{xx}\sigma_i^x\sigma_j^x \cong \sum_i \left(\sum_j A_{ij}^{xx} m_j^x\right)\left(\sigma_i^x - \frac{1}{2}m_i^x\right) \tag{3.15}$$

$$\begin{aligned}\sum_{ij} A_{ij}^{xz}\sigma_i^x\sigma_j^z \cong & \sum_i \left[\left(\sum_j A_{ij}^{xz} m_j^x\right)\sigma_i^z + \left(\sum_j A_{ij}^{xz} m_j^z\right)\sigma_i^x\right] \\ & - \sum_{i,j} A_{ij}^{xz} m_j^x m_i^z,\end{aligned} \tag{3.16}$$

where $m_i^x = \langle\sigma_i^x\rangle$ and $m_i^z = \langle\sigma_i^z\rangle$. Finally, the mean-field Hamiltonian can be written as

$$\mathcal{H}_{\mathrm{MF}} = E_0 + \sum_i P_i\sigma_i^z + \sum_i \Gamma_i\sigma_i^x - \frac{1}{2}\sum_{ij} A_{ij}^{xx} m_i^x m_j^x - \frac{1}{2}\sum_{ij} A_{ij}^{zz} m_i^z m_j^z - \frac{1}{2}\sum_{ij} A_{ij}^{xz} m_i^x m_j^z, \tag{3.17}$$

where P_i is the local longitudinal mean field,

$$P_i = \sum_j A_{ij}^{zz} m_j^z + \sum_j A_{ij}^{xz} m_j^x + A_i^z, \tag{3.18}$$

and Γ_i is the local transverse field,

$$\Gamma_i = \sum_j A_{ij}^{xx} m_j^x + \sum_j A_{ij}^{xz} m_j^z + A_i^x. \tag{3.19}$$

3.3 Local mean-field equations and iterative solutions

Having defined the effective spin-1/2 Hamiltonian (3.17), in terms of B_x- and disorder-dependent coefficients $A_{ij}^{\mu\nu}$, we want to compute disorder-averaged macroscopic observables such as magnetization or Edwards-Anderson spin-glass order parameters. A set of self-consistent equations describing the local magnetizations, m_i, is derived. The self-consistent equations are solved iteratively for a number of different disor-

der realizations. As the number of local free energy minima, that are defined by the self-consistent equations, is increasing upon entering the spin-glass phase. The self-consistent solutions, found for different initial conditions, are counted, where solutions are regarded as different if their free energy differs, and their number is treated as an estimation of the number of local free energy minima.

3.3.1 Local mean-field equations

Using Hamiltonian (3.17), the free energy is calculated as described in Sec. 2.1.2, and one obtains

$$\begin{aligned} F &= E_0 - \frac{1}{2}\sum_{ij} A_{ij}^{xx} m_i^x m_j^x - \frac{1}{2}\sum_{ij} A_{ij}^{zz} m_i^z m_j^z - \frac{1}{2}\sum_{ij} A_{ij}^{xz} m_i^x m_j^z \\ &\quad - \sum_i k_{\mathrm{B}} T \ln\left[2\cosh\left(\beta\sqrt{(P_i)^2 + (\Gamma_i)^2}\right)\right], \end{aligned} \tag{3.20}$$

where P_i and Γ_i are given by Eqs. (3.18) and (3.19). Referring to Sec. 2.1.2 one finds that the $\hat{x}$ and $\hat{z}$ vector components of local magnetization are

$$\begin{aligned} m_i^x &= \frac{\Gamma_i}{\sqrt{(P_i)^2 + (\Gamma_i)^2}} \tanh\left[\beta\sqrt{(P_i)^2 + (\Gamma_i)^2}\right], \\ m_i^z &= \frac{P_i}{\sqrt{(P_i)^2 + (\Gamma_i)^2}} \tanh\left[\beta\sqrt{(P_i)^2 + (\Gamma_i)^2}\right]. \end{aligned} \tag{3.21}$$

3.3.2 Iterative procedure

The solution to Eqs. (3.21) is obtained by starting from random initial values of m_i^x and m_i^z taken from the uniform probability distribution on the interval (-1,1) and iterating the equations, i.e. evaluating m_i^x and m_i^z as a function of other local magnetizations, m_j^x and m_j^z, until convergence is reached. The local magnetizations are updated "in place", that means that once a new value for a single site is calculated it replaces the old value and is instantaneously used in subsequent calculation for the other sites [4]. The order in which the local magnetizations, m_i^x and m_i^z, are updated

[4]The alternative way, such that whole N component vectors $\boldsymbol{m}^{\mu(\mathrm{new})}$, $\mu = x, z$,where N is the number of sites, are calculated using the old vectors, $\boldsymbol{m}^{\mu(\mathrm{old})}$, i.e. after $m_k^{\mu(\mathrm{new})}$ was computed,

is chosen randomly for each sweep over all the sites, i.

The iteration procedure is stopped when the relative change of the free energy, F of Eq. (3.20) is smaller than $\epsilon = 10^{-6}$,

$$\left|\left(F_n - F_{n-1}\right)/F_n\right| < \epsilon. \tag{3.22}$$

In presence of a disorder, the free energy landscape is complicated and the iterative procedure may yield different solutions when started from different initial configurations (set of m_i^x and m_i^z values). Eqs. (3.21) are the condition for local minimum of the free energy; hence, in the presence of many local minima, many solutions to Eqs. (3.21) exist. To find a solution with a possibly lowest value of the free energy, the procedure is repeated multiple times, each time starting from a different random initial configuration. The value of F for each solution is compared against the lowest value obtained in the previous attempts that used different initial conditions. If a solution with lower F than the previous best solution is found, it is taken as the new best solution.

To estimate the number of solutions, and to establish a terminating condition of the solution counting loop, the following procedure is used. The obtained values of the free energy, F, are grouped into bins of width $\Delta = 10^{-4}F_k$, where F_k is the center of the k-th bin. If a new value, F_l, satisfies the condition: $|F_l - F_k| < \Delta = 10^{-4}F_k$ for any of the existing bins, k, than it is added to that bin (the counter of the bin is incremented). In the opposite case, or trivially, if it is the first attempt, a new bin, with the center F_l, is created. The binning procedure is stopped when the bin corresponding to the lowest free energy contains at least 5 counts or if the number of bins reaches 100. These numbers are arbitrarily chosen to cut off the computational power to be employed for a given solution search. To illustrate the solution counting procedure with an example, in the case when there is only one solution, the iteration is repeated 5 times; in the case when there is exactly 10 solutions (and if all of them are found), the iteration is repeated at least 50 times. The number of bins is an estimate of the number of solutions or the complexity of the free energy landscape. At the boundary of the spin-glass phase, an exponential increase of the number of local

$m_l^{\mu(\text{new})}$ is computed using $m_k^{\mu(\text{old})}$ and not $m_k^{\mu(\text{new})}$, was also attempted. When iterating Eqs. (3.21) that way, the iteration converged very slowly or a convergence has not been reached.

minima occurs, and the increase of the number of solutions is one of the determinants of the of onset glassiness in the model.

To perform the disorder average, the procedure described above is repeated for 1000 samples of random dilution and a mean value is computed for all the calculated quantities.

3.3.3 Calculated quantities

As described in the preceding section, for a given realisation of disorder a set of local magnetizations, m_i, is obtained. The total magnetization of the sample in $\hat{z}$ direction is computed

$$m_z^{\text{sample}} = \left| \frac{1}{N} \sum_{i=1}^{N} m_i^z \right|, \tag{3.23}$$

where N is the number of spins, and absolute value was taken to avoid random alteration of sign of the total (macroscopic) magnetization. The expression for the disorder-averaged magnetization reads

$$m_z = \left[\left| \frac{1}{N} \sum_{i=1}^{N} m_i^z \right| \right]_{\text{dis}} \tag{3.24}$$

where $[\ldots]_{\text{dis}}$ denotes the disorder average. In a similar way, the Edwards-Anderson spin-glass order parameter, q, is computed

$$q = \left[\frac{1}{N} \sum_{i=1}^{N} (m_i^z)^2 \right]_{\text{dis}}. \tag{3.25}$$

An order parameter, $q_{|m|}$, that also indicates "spin freezing", i.e. that there are nonzero thermally averaged local magnetizations, m_i, and which is equal to the magnetization in the ferromagnetic phase is also calculated,

$$q_{|m|} = \left[\frac{1}{N} \sum_{i=1}^{N} |m_i^z| \right]_{\text{dis}}. \tag{3.26}$$

Finally, to detect whether spins are aligned with longitudinal random field, an order parameter q_A is defined,

$$q_A = \left[\frac{1}{N} \sum_{i=1}^{N} m_i^z \text{sign}(A_i^z) \right]_{\text{dis}}, \tag{3.27}$$

where A_i^z is the effective transverse-field-induced longitudinal random field (see Eq. (3.13)). For $q_{|m|}$and q_A, the inequality $q_{|m|} \leq q_A$ is always satisfied, and in the case when all the spin are aligned with random field, q_A is equal to $q_{|m|}$.

Due to finite-size effects, the order parameters do not vanish rapidly at the transition from an ordered phase to the paramagnetic phase, as it would happen in an infinite system. A finite-size tail is present in the order parameter vs concentration, x, plots, and the phase boundary cannot be straightforwardly located by looking for the order parameter to decrease to zero. In Monte Carlo simulation finite-size effects at the critical point can be taken into account by using the finite-size scaling methods. Here, for the local mean-field calculation, finite-size scaling techniques in the form known from Monte Carlo cannot be applied. Having in mind the fact that the mean-field approximation already introduces a large systematic error to the calculations, looking for sophisticated methods to analyze finite size data would not improve the accuracy of the results. For that reason only one system size (L=6, i.e with $N = 4 \cdot 6^3 = 864$ lattice sites) is simulated. The phase boundary, separating the paramagnetic phase form the ferromagnetic or spin glass phase, is taken to be at the inflection point of the plot of magnetization, m_z, or Edwards-Anderson order parameter, q, respectively.

3.4 Results

The aim of this work is to study the effect of transverse-field-induced longitudinal random fields on the paramagnet-ferromagnet phase boundary and on the presence of the spin-glass phase. For completeness, and to have a reference data to compare with, the finite B_x results, we start from the case of $B_x = 0$. When analysing the case of zero transverse field, we show the intermediate results such as magnetisation plots vs temperature and concentration, x, to illustrate how the method is used to obtain the phase boundaries. The same technique is used to computer the phase boundaries in

the $B_x > 0$ case. To study the effect of transverse field, some order parameter plots are also shown for $B_x = 1.5$ T, but for other values $B_x > 0$ we show only the final results, i.e the phase boundaries.

3.4.1 Graphical presentation of $B_x = 0$ results and the procedure of calculating the critical concentration, x_c

In this section, while presenting the data for zero transverse field, the details of the method used to find the critical temperature is discussed. We consider one system size, L=6, that gives $4 \cdot 6^3 = 864$ lattice sites. In order to vary the concentration, x, the number of occupied sites, N, is varied between 50 and 850. For completeness, a pure system, with $N = 864$, is also considered.

To start, in Fig. 3.5 the magnetization, m_z^{sample} of Eq. (3.23), vs magnetic ion fraction, x, for three simulation runs, at T=0.6 K is shown. In one simulation run, the concentration x, or in practice the number of ions, is varied by starting from a system with the maximal number of ions and reducing x by randomly, gradually removing ions. Hence, some correlation between subsequent values of x is present. Such correlation is visible especially at the right, large x, side of the plots in Fig. 3.5.

The choice of x as the parameter that is densely sampled to search for the inflection point, instead of temperature or transverse field, may seem peculiar at first. But, as it will be explained later, it is the best way to consistently identify the phase boundary from the inflection point of order parameter plot, when one wants to explore a three dimensional parameter space consisting of x, T and B_x.

From this point, all presented data are averaged over 1000 disorder samples. Disorder averaged magnetization, m_z, vs x for T=0.1, 0.6, 1.1 and 1.6K is shown in Fig. 3.6. The error bars are calculated based on the disorder sample to sample fluctuation. As the estimate of the critical concentration, x_c, the inflection point of the magnetization plot is taken. The inflection points on the magnetization plots in Fig. 3.6 are marked with red squares. To locate the inflection point a cubic spline interpolation of the disorder-averaged data is computed. The cubic spline interpolation is differentiated and the maximum of its derivative is found. To calculate the statistical error of the critical concentration, x_c, the 1000 disorder samples is divided into 10 sets, 100 samples each. From each set, n, x_c^n is computed and the fluctuation of x_c^n is used as

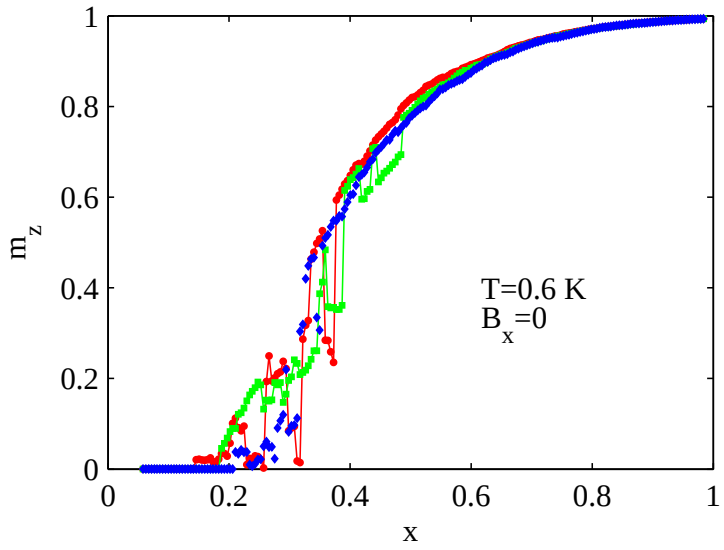

Figure 3.5: Example plots of m_z^{sample} vs x for 3 disorder realisations, T=0.6K and B_x=0.

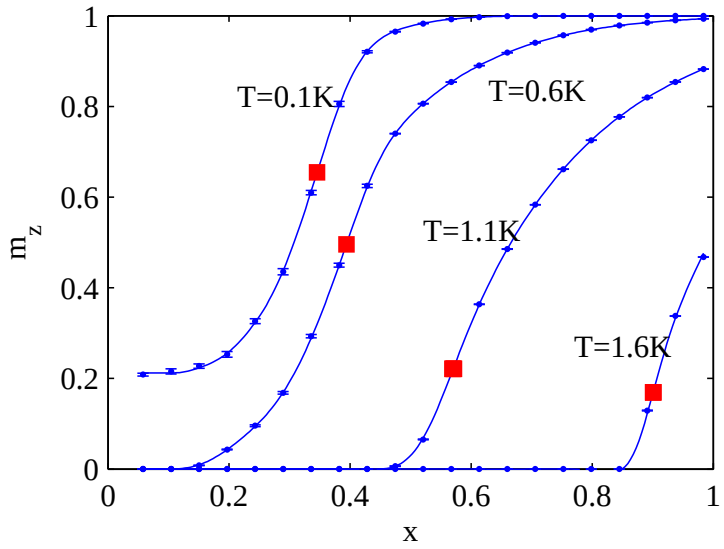

Figure 3.6: Disorder-averaged magnetization, m_z vs x, for T=0.1, 0.6, 1.1 and 1.6 K, B_x=0. The red squares mark the inflection points.

the measure of the statistical uncertainty of x_c. In Fig. 3.6 the horizontal error bars for x_c are smaller than the marker size.

In Fig. 3.7 magnetization vs x and T is presented in a three dimensional plot. The plot consist of m_z vs x blue lines for a number of temperatures separated by intervals of 0.1K. Each of the lines has the inflection point marked with a red square marker, similar to the plots in Fig. 3.6. The projections of the inflection points on the (T,x) plane determines the phase boundary $T_c(x)$, or technically, $x_c(T)$, and is marked in the (T,x) plane with red stars connected by a red line. At the low T side a thick finite-size tail in m_z vs x plots is present, extending down to x=0. This large finite-size tail is suggesting the presence of a spin-glass phase. Additionally, in Fig. 3.7, m_z vs T plot for $x = 1$ is shown with a green line. A similar method is used to obtain the spin-glass phase boundary from the inflection points in the plots of Edwards-Anderson spin-glass order parameter, q, vs x. In Fig. 3.8 a three dimensional plot of q vs x and T is shown. The Edwards-Anderson order parameter has a nonzero value also in a ferromagnetic phase. T_g, found that way is meaningful only for $x < x_c$, where x_c is the critical value of x below which the ferromagnetic phase ceases to exist, $T_c(x_c) = 0$. Computed that way, the T_g vs x dependency, together with ferromagnetic phase boundary, $T_c(x)$, for both zero and nonzero B_x, is presented in the next section, in Fig. 3.9.

Visualization of the magnetization vs T and x in Fig. 3.7 shows why the critical temperature was defined as the inflection point of m_z vs x plot and not m_z vs T or m_z vs B_x. There is a finite-size tail in m_z vs x plots at low temperature (and low B_x). In the thermodynamic limit, the magnetization vanishes abruptly at the boundary between a spin-glass and ferromagnetic phase. In a finite-size system, the magnetic moments of randomly frozen spins do not average out to zero exactly, and a finite magnetization in the spin-glass phase persist. Nevertheless an abrupt decrease of magnetization from a large value at the ferromagnetic phase to a smaller finite-size value in the spin-glass regime is present, and the transition can be located at the inflection point. One can imagine that, in the opposite case, if the inflection point in a plot of m_z vs T was chosen as the estimation of T_c, T_c vs x plot would bend towards lower x, into the spin-glass part of the phase diagram, due to the fact that on the finite-size tail m_z vs T dependency still could be plotted, and an inflection point would be found, erroneously identifying paramagnet to ferromagnet transition, in the part of the phase diagram that should be recognised as a spin-glass phase. From a

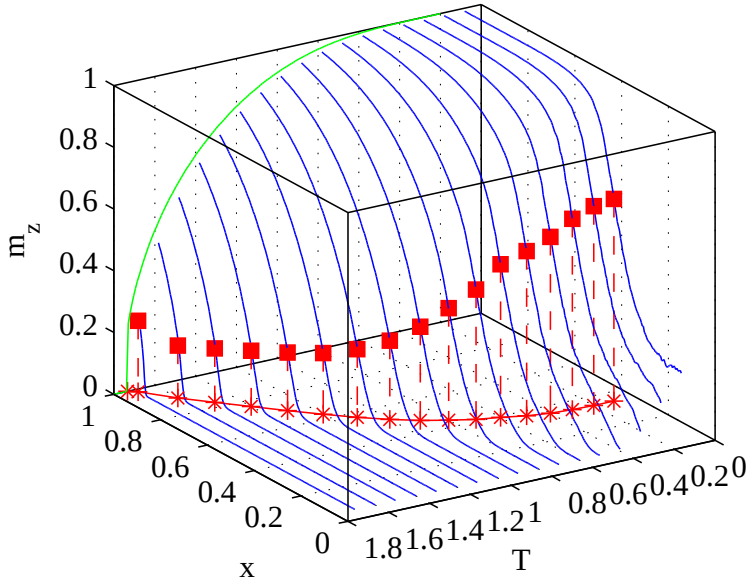

Figure 3.7: Magnetization m_z vs T and x for B_x=0. The red squares mark the inflection points. The projection of the inflection points onto (T,x) plane marks the phase boundary $T_c(x)$.

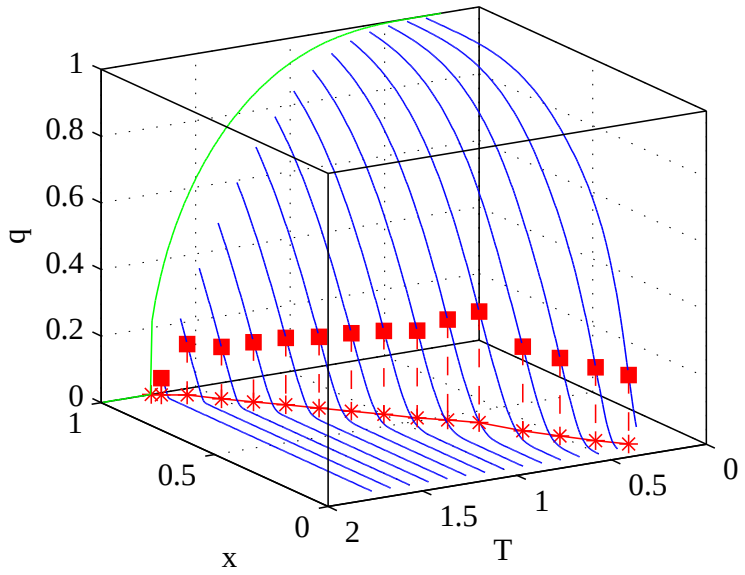

Figure 3.8: Edwards-Anderson order parameter, q, vs T and x for B_x=0. The red squares mark the inflection points. The projection of the inflection points onto (T,x) plane marks the phase boundary, $T_g(x)$.

slightly different perspective, the difference of looking for the phase boundary when going along x axis with T constant, or when going along T axis with x constant can be understood when looking at Fig. 3.9 shown in the next section. The phase boundary between the ferromagnetic and spin-glass phase is almost parallel to the T axis and thus finding the phase boundary would be very difficult in the proximity of x_c, while when going parallel to the x axis, perpendicular to the phase boundary, the feature indicating the transition is fairly sharp. It is visible in Fig. 3.8 that a large finite size tail is not present in the spin glass region of the (T,x) plane, in the q vs x plots. The finite-size magnetization in the spin-glass phase will be discussed further in Section 3.4.3.

3.4.2 The effect of transverse field on T vs x phase diagram

In Fig. 3.9, the phase boundaries T_c vs x for B_x=0, 1.5, 2.0, 2.5, 2.8 and 3.0 T are shown with blue lines. For B_x=0 and B_x=1.5T, the T_g vs x dependence is illustrated with red lines. The way of obtaining such phase boundaries was discussed in the previous section, and for $B_x = 0$ illustrated in Fig. 3.7 for T_c, and in Fig. 3.8 for T_g. At $B_x = 0$, the ferromagnetic phase vanishes at $x_c = 0.35$. Below that value of x_c the red line obtained from inflection points in q vs x plots marks the paramagnet to spin glass phase boundary. The plots for B_x=1.5T show that there is no spin glass phase. As will be argued later, at finite B_x the spin glass is suppressed by the longitudinal random fields. It will be argued that for $B_x > 0$, in an intermediate range of B_x, a disordered state with spins aligned along the random fields occurs.

The Edwards-Anderson order parameter, q, differs from the magnetization m_z in the ferromagnetic phase. It is of interest to analyze also a quantity that is equal to magnetization in the ferromagnetic phase and does not vanishes in the spin glass-phase. Such order parameter, $q_{|m|}$, is defined in Eq. (3.26). $q_{|m|}$ is better suited to indicate the state with the spins aligned with the random fields than is the parameter q. In Fig. 3.10 $q_{|m|}$ instead of q is used to locate the phase boundary of a "frozen state". Surprisingly, now, below x_c=0.44, where the ferromagnetic phase vanishes, a region with a nonzero $q_{|m|}$ is present. The explanation of the existence of this region may the presence of a state with the spins aligned with the transverse-field-generated longitudinal random fields. This issue is disscussed further in Section 3.4.3.

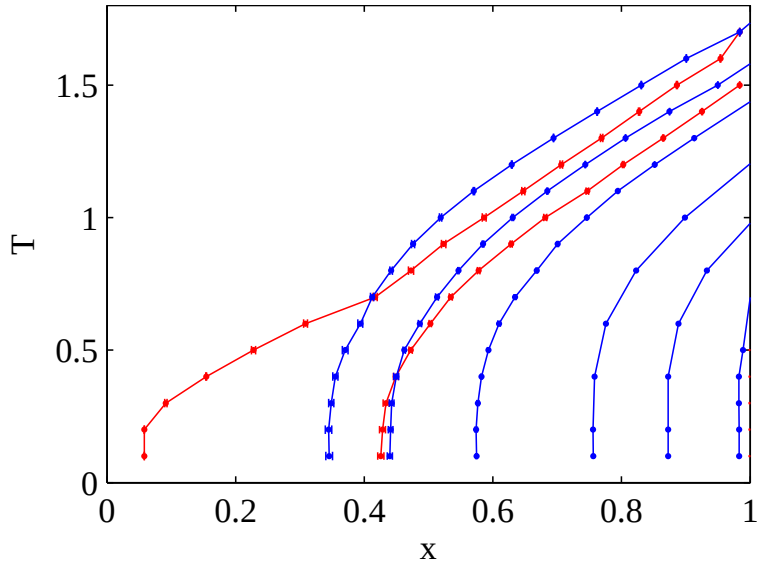

Figure 3.9: T_c (blue lines) and T_g (red lines) vs x for different values of transverse field, B_x. Starting from left and progressing to the right B_x=0, 1.5, 2.0, 2.5, 2.8 and 3.0 T. Obtaining T_c vs x and T_g vs x for B_x=0 was illustrated in Fig. 3.7 and Fig. 3.8, respectively.

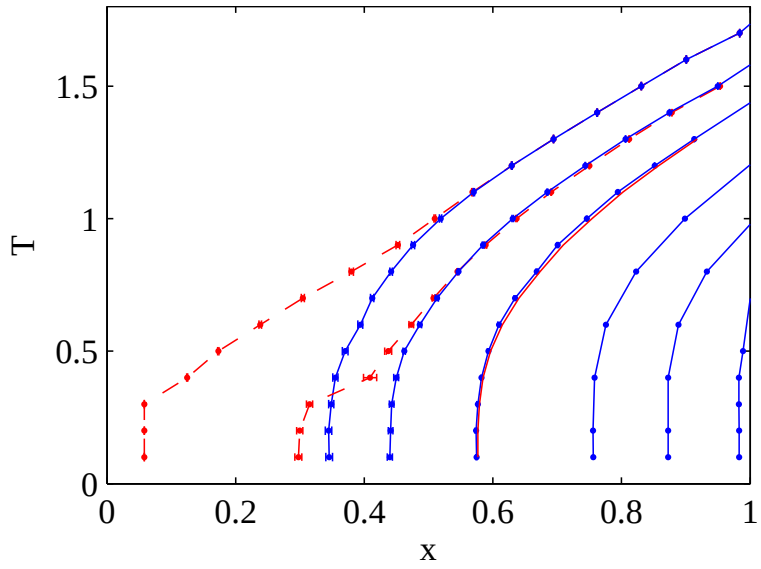

Figure 3.10: T_c (blue lines) and $T_{|m|}$ (red lines) vs x for different values of transverse field, B_x. Starting from left and progressing to the right B_x=0, 1.5, 2.0, 2.5, 2.8 and 3.0 T.

To understand why this state was not indicated when inflection point was sought in the plots of q, one needs to take into account how the square in the definition of q affects the location of the inflection point. In both cases, in $q_{|m|}$ vs x or q vs x plot, a thick tail is present. The square of local magnetizations that is taken to compute q sharpens the features of q vs x curve relative to the $q_{|m|}$ vs x plot. The inflection point in the q vs x plot is to the left from the inflection point of the $q_{|m|}$ vs x plot because in the case of q, the tail decreases sooner. Three-dimensional plots of q and $q_{|m|}$ for $B_x = 1.5$ T are shown in Figs. 3.11 and 3.12, respectively.

An alternative method to detect glassiness is to study the complexity of the free energy landscape or to count the number of local free energy minima. Using this method one can easily distinguish a spin glass from the state characterized by the spins aligned with the local longitudinal random fields. While in the spin-glass phase the number of "solutions" is large, in the case when the spins are aligned with the random field the unique ground state exists and it is easily found with the used here iterative procedure. In Fig. 3.13, for B_x=0, together with the "inflection point based" phase boundaries repeated from Fig. 3.9, the number of solutions, found as described in Sec. 3.3.2, is shown in the form of a color plot. Note that the maximum number of solutions shown in Fig. 3.13 is 100 because the solution counting loop is stopped at this value. There is a clear indication of a spin-glass phase and the obtained phase diagram is very similar, perhaps even semi-qualitatively, to the experimental phase diagram proposed in Ref. [117] and reproduced in Fig. 3.1. On the left side from x_c, the phase boundary where the number of solution drops to zero is in quite good agreement with the phase boundary obtained from Edwards-Anderson parameter, q.

Figure 3.14 shows a color plot of the number of solutions vs x and T for B_x=1.5 T. The spin-glass phase is clearly suppressed; there is no large increase of the number of solutions reaching the limiting value of 100, as was the case at $B_x = 0$. Instead, there is only a very small region where the number of solutions reaches around 40. In the state with a nonzero local magnetizations, below the boundary of ferromagnetic phase at x_c=0.44, that is marked by the red line obtained from $q_{|m|}$, as discussed above, there are not many solution. In the next section, it is shown that nonzero local magnetizations in this regime are due to the alignment of the spin with the random field rather than due to the frustrated interaction between the spins and the spin-glass freezing.

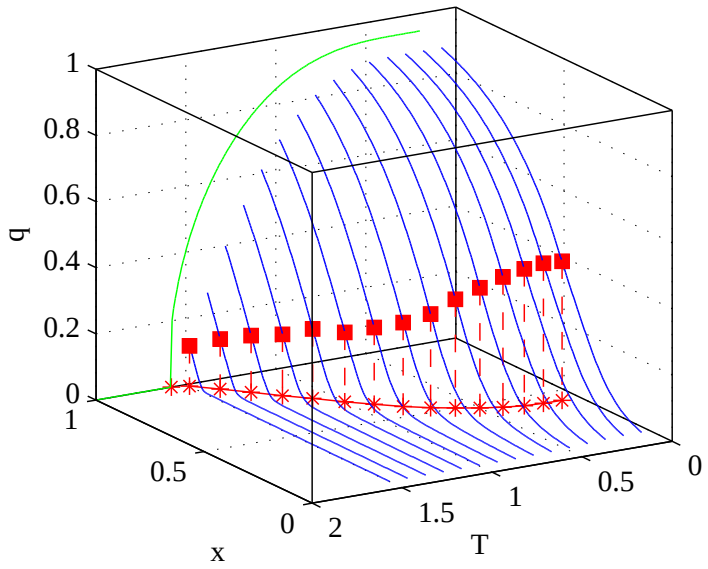

Figure 3.11: Edwards-Anderson order parameter, q, vs T and x for B_x=1.5 T. The red squares mark the inflection points. The projection of the inflection points onto (T,x) plane marks the phase boundary, $T_g(x)$.

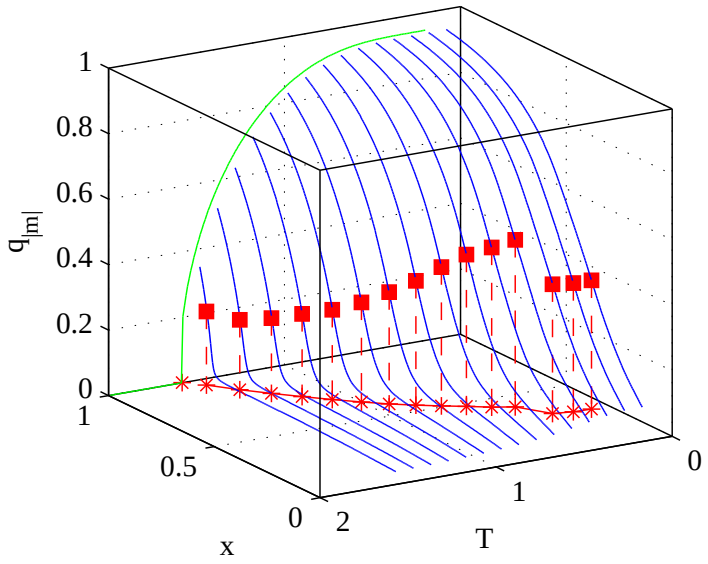

Figure 3.12: Order parameter, $q_{|m|}$, vs T and x for B_x=1.5 T. The red squares mark the inflection points. The projection of the inflection points onto (T,x) plane marks the phase boundary.

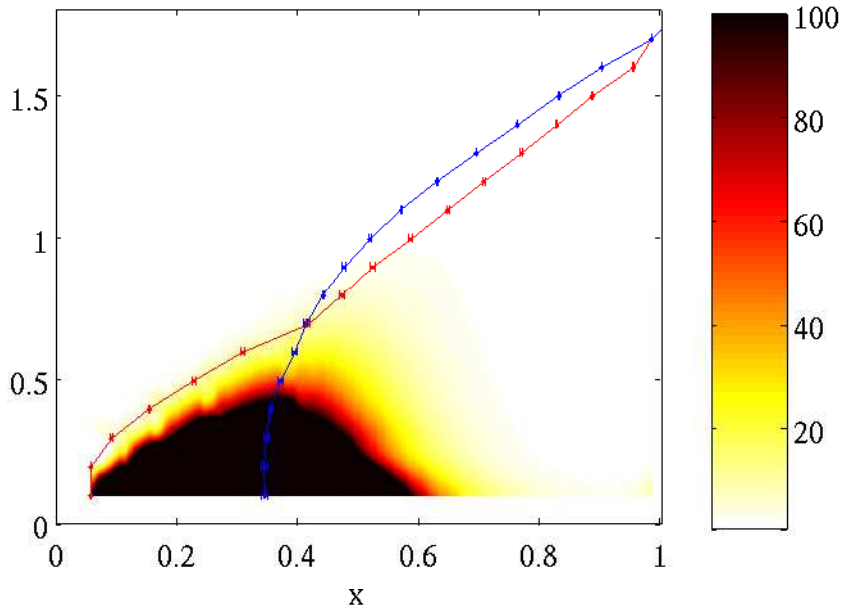

Figure 3.13: Color plot of number of solutions vs T and x at B_x=0. The blue and the red line show T_c vs x and T_g vs x phase boundaries, respectively.

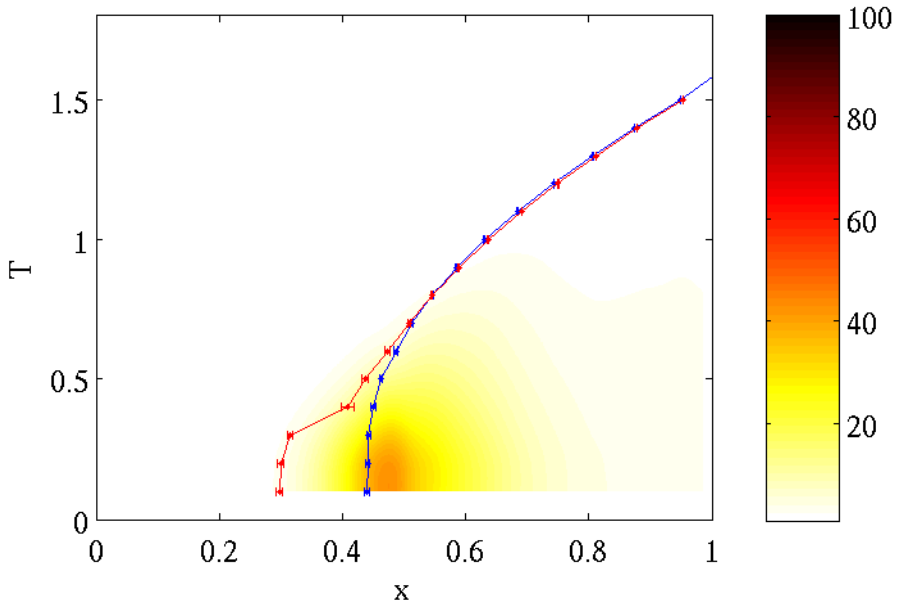

Figure 3.14: Color plot of number of solutions vs T and x at B_x=1.5T. The blue and the red line show T_c vs x and $T_{|m|}$ vs x phase boundaries, respectively.

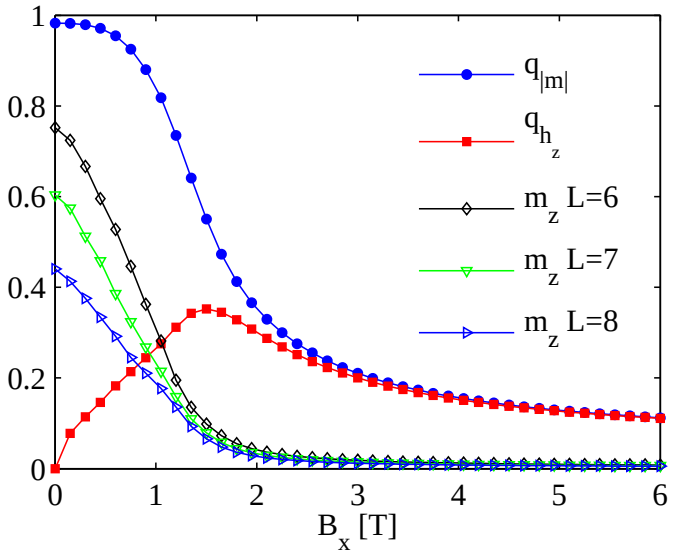

Figure 3.15: Order parameters m_z, $q_{|m|}$ and q_{h_z} vs B_x.

3.4.3 The alignment with longitudinal random field and finite-size effects

In this section, we analyse transverse field dependence of various order parameters at the concentration, $x = 0.4$, which for $B_x = 0$ is in the spin-glass phase and for $B_x > 0$ is in a frozen state that is controlled by the transverse-field-induced random field. In the previous section we reported only results obtained for one system size, $L = 6$. Here, we directly compare numerical values of different order parameters. To able to distinguish the physical behavior from finite size effects we consider a range of system sizes between $L = 4$ and $L = 8$.

In Fig. 3.15 we show the effect of transverse-field-generated longitudinal random field. We look at the transverse field dependence of the local magnetization order parameter, $q_{|m|}$, the random field projection order parameter, q_A and magnetization, m_z. The magnetization, m_z, is plotted for three system sizes: L=6, 7 and 8. m_z systematically decreases with increase of system size, L, suggesting that for this concentration, $x = 0.4$, at $B_x = 0$, magnetization likely is reduced to zero in the thermodynamical limit, as expected in a spin-glass phase. For L=6, the finite size magnetization at $x = 0.4$ and $B_x = 0$ is very large, $m_z \simeq 0.8$. This explain why the deflection point

method does not provide correct phase boundary separating the spin glass and ferromagnetic phases. This large value of the finite-size magnetization can be attributed to formation of ferromagnetic clusters that are small in comparison with spin-glass correlation length, such that their effect is significant only in small system sizes.

Finite-size effects are practically absent in the order parameters $q_{|m|}$ and q_A. If plots $q_{|m|}$ and q_A for the considered system sizes, L=6, 7 and 8, would be shown, there is no visible difference between plots for different L; hence, only single plots of $q_{|m|}$ and q_A are shown. The order parameter q_A indicates that spins are frozen and aligned with longitudinal random field, A_z. The order parameter $q_{|m|}$ indicates that the spins are froze, i.e. the local magnetization are nonzero, but it does not distinguish between spins aligned along random field and spins oriented in directions independent on the directions of random field. Both $q_{|m|}$ and q_A are reduced due to the transverse-field-induced admixing of spin-up and spin-down states. To see if the spin are aligned with random field q_A should be compared with $q_{|m|}$. Clearly, at weak B_x, q_A is much smaller than $q_{|m|}$ which is indicating that the spins are mostly oriented to satisfy the inter-spin interactions rather that the random field. Upon increasing B_x, $q_{|m|}$ decreases due to the transverse-field-induced admixing, but, for some intermediate value of B_x, q_A increases because the strength of the random field increases with B_x. Around $B_x = 1.5$ T, q_A has a maximum and a value quite close to $q_{|m|}$. This is the value of B_x where random field effects are the strongest. Upon further increasing of B_x, both $q_{|m|}$ and q_A decrease due to transverse-field-induced admixing.

3.5 Summary

In this chapter, the suppression of the spin-glass phase by the transverse-field-induced longitudinal random field was shown[5]. A plausible argument for the vanishing of the spin-glass phase when a transverse field is applied is provided by analysing the number of solutions of the local mean-field equations. At the intermediate values of the transverse field, B_x=1.5, there is a region in the (x,T) plane, outside of the boundaries

[5]We also made an attempt to use local mean-field theory to calculate nonlinear susceptibility in order to reproduce the effect where the divergence of nonlinear susceptibility become less singular with increase of transverse field, B_x [8]. We found that it is not possible to calculate nonlinear susceptibility in the framework of local mean-field theory.

of the ferromagnetic phase, where there are nonzero local magnetizations m_z^i. As the counting of the number of local minima of the free energy is excluding a spin-glass phase, the spins in this regime are expected be aligned with the local longitudinal random fields. With the increase of B_x the random-field-aligned state vanishes, i.e in Fig. 3.10, at $B_x = 2$, $T_{|m|}(x)$ boundary is overlapping with $T_c(x)$ and there is no indication of nonzero local magnetization m_i below the concentration, x_c, where the ferromagnetic phase vanishes. This happens because the ratio of the longitudinal and transverse random field terms in the Hamiltonian depends on the concentration, x. The random field depends on the inter-spin distance, r, and at some point the effect of quantum fluctuations induced by the applied field, B_x, is stronger than the effect of longitudinal random field.

At $B_x = 0$, T_c is approximately proportional to x, $T_c(x) \propto x$. At high concentration regime, the effect of transverse-field-induced longitudinal random field is indicated by the increase of the rate at which the critical temperature decreases with decreasing concentration, x. It happens because the random field increase with the transverse field, B_x, and with the dilution, x.

It would be interesting to study other magnetic materials that have properties similar to $LiHo_xY_{1-x}F_4$. Example systems that can be useful for such studies are rare earth hydroxides: $Ho(OH)_3$, $Dy(OH)_3$ and $Tb(OH)_3$. These three magnetic materials, similarly to $LiHoF_4$, are characterised by a strong Ising anisotropy; in a transverse magnetic field, B_x, they are likely to be an experimental realisation of the transverse field Ising model and, at T=0, to exhibit a quantum phase transition induced by the magnetic field applied in the direction perpendicular to the direction of the Ising easy axis. Like in $LiHo_xY_{1-x}F_4$, the rare earth atoms in the rare earth hydroxides can be randomly replaced by nonmagnetic yttrium and possibly the effects of transverse-field-induced random field may be observed. In the next chapter, we use a simple mean-field theory to investigate the validity of the mentioned hydroxides for experimental studies of quantum criticality. We estimate the values of critical transverse field, B_x, that, at T=0, induces a quantum phase transition from the ferromagnetic to quantum paramagnetic phase. We find that $Ho(OH)_3$ can be a good candidate to study quantum criticality while the critical transverse field for $Tb(OH)_3$ is too large to be produced in a laboratory. In the case of $Dy(OH)_3$, we find that in the model studied, at high B_x, there is a first order phase transition, but the occurrence of the first order phase

transition is strongly dependent on the microscopic parameters and may, but do not have to, occur in the real material.

Chapter 4

Mean-field study of $RE(OH)_3$ Ising-like Magnetic Materials[1]

The $LiHo_xY_{1-x}F_4$ Ising magnetic material subject to a magnetic field, B_x, perpendicular to the Ho^{3+} Ising direction has shown over the past twenty years to be a host of very interesting thermodynamic and magnetic phenomena [6–21]. Unfortunately, the availability of other magnetic materials other than $LiHo_xY_{1-x}F_4$ that may be described by a transverse field Ising model remains very much limited. It is in this context that we use here mean-field theory to investigate the suitability of the $Ho(OH)_3$, $Dy(OH)_3$ and $Tb(OH)_3$ insulating hexagonal dipolar Ising-like ferromagnets for the study of the quantum phase transition induced by a magnetic field, B_x, applied perpendicular to the Ising spin direction. Experimentally, the zero field critical (Curie) temperatures are known to be $T_c \approx 2.54$ K, $T_c \approx 3.48$ K and $T_c \approx 3.72$ K, for $Ho(OH)_3$, $Dy(OH)_3$ and $Tb(OH)_3$, respectively [2, 3]. From our calculations we estimate the critical transverse field, B_x^c, to destroy ferromagnetic order at zero temperature to be B_x^c =4.35 T, B_x^c =5.03 T and B_x^c =54.81 T for $Ho(OH)_3$, $Dy(OH)_3$ and $Tb(OH)_3$, respectively. We find that $Ho(OH)_3$, similarly to $LiHoF_4$, can be quantitatively described by an effective $S = 1/2$ transverse field Ising model (TFIM). This is not the case for $Dy(OH)_3$ due to the strong admixing between the ground doublet and first excited doublet induced by the dipolar interactions. Furthermore, we find that the paramagnetic (PM) to

[1]The content of this chapter is reproduced with permission from P. Stasiak and M. J. P. Gingras, Phys. Rev. B 78, 224412 (2008). Copyright 2008, The American Physical Society.

ferromagnetic (FM) transition in $Dy(OH)_3$ becomes first order for strong B_x and low temperatures. Hence, the PM to FM zero temperature transition in $Dy(OH)_3$ may be first order and not quantum critical. We investigate the effect of competing antiferromagnetic nearest-neighbour exchange and applied magnetic field B_z along the Ising spin direction $\hat{z}$ on the first order transition in $Dy(OH)_3$. We conclude from these preliminary calculations that $Ho(OH)_3$ and $Dy(OH)_3$, and their Y^{3+} diamagnetically diluted variants, $Ho_xY_{1-x}(OH)_3$ and $Dy_xY_{1-x}(OH)_3$, are potentially interesting systems to study transverse-field induced quantum fluctuations effects in hard axis (Ising-like) magnetic materials.

This chapter is organized as follows. In Section 4.1, we review the main single ion magnetic properties of $RE(OH)_3$ (RE=Dy, Ho, Tb). In particular, we discuss the crystal field Hamiltonian of these materials and the dependence of the low-lying crystal field levels on an applied transverse field B_x. We present in Section 4.2 a mean-field calculation to estimate the B_x vs temperature, T, $T_c(B_x)$ phase diagram of these materials. In Section 4.3, we show that $Ho(OH)_3$ and $Tb(OH)_3$ can be described quantitatively well by a transverse field Ising model, while $Dy(OH)_3$ cannot. The Subsection 4.4.1, uses a Ginzburg-Landau theory to explore the first order paramagnetic (PM) to ferromagnetic (FM) transition that occurs in $Dy(OH)_3$ at low temperatures and strong B_x. The following Subsection 4.4.2 discusses the effect of nearest-neighbour antiferromagnetic exchange interaction and applied longitudinal (i.e. along the $\hat{z}$ axis) magnetic field, B_z, on the first order transition in $Dy(OH)_3$. A brief conclusion is presented in Section 4.5. Appendix A discusses how the excited crystal field states in $Dy(OH)_3$ play an important quantitative role on the determination of $T_c(B_x)$ in this material. [2]

4.1 $RE(OH)_3$: Material properties

4.1.1 Crystal properties

All the rare earth hydroxides form hexagonal crystals that that are iso-structural with $Y(OH)_3$. The lattice is described by translation vectors $\boldsymbol{a_1} = (0, 0, 0)$, $\boldsymbol{a_2} =$

[2]The content of this chapter is reproduced with permission from Phys. Rev. B 78, 224412 (2008). Copyright 2008, The American Physical Society.

$(-a/2, a\sqrt{3}/2, 0)$ and $\boldsymbol{a_3} = (0, 0, c)$. A unit cell consist of two Ho^{3+} ions at coordinates $(1/3, 2/3, 1/4)$ and $(2/3, 1/3, 3/4)$ in the basis of lattice vectors $\boldsymbol{a_1}$, $\boldsymbol{a_2}$ and $\boldsymbol{a_3}$. The coordinates of three O^{2-} and H^- ions, relative to the position of Ho^{3+}, are $\pm(x, y, 0)$, $\pm(-y, x-y, 0)$ and $\pm(y-x, -x, 0)$, where $\pm$ refers to the first and second Ho^{3+} in the unit cell, respectively [173]. The values of the parameters x and y are listed in Table 4.1. x=0.396, y=0.312 and for H^-: x=0.28, y=0.17 [174]. The lattice structure is depicted in Fig. 4.1. The lattice constants for $Tb(OH)_3$, $Dy(OH)_3$, $Ho(OH)_3$ and $Y(OH)_3$, from Beall *et al.* [174], are collected in Table 4.2. Each magnetic ion is surrounded by 9 oxygen atoms that create a crystalline field characterized by the point group symmetry C_{3h} [173].

	O^{2-}, x	O^{2-}, y	H^-, x	H^-, y
$Tb(OH)_3$	0.3952(7)	0.3120(6)	0.276(1)	0.142(1)
$Dy(OH)_3$	0.3947(6)	0.3109(6)	0.29(3)	0.15(2)
$Ho(OH)_3$	0.3951(7)	0.3112(7)	0.30(3)	0.17(3)
$Y(OH)_3$	0.3958(6)	0.3116(6)	0.28(1)	0.17(1)

Table 4.1: Position parameters of O^{2-} and H^- ions in rare earth hydroxides and $Y(OH)_3$ from Ref. [174] and Ref. [175] (see text in Section 4.1.1).

	a	c	c/a
$Tb(OH)_3$	6.315(4)	3.603(2)	0.570(5)
$Dy(OH)_3$	6.286(3)	3.577(1)	0.569(0)
$Ho(OH)_3$	6.266(2)	3.553(1)	0.567(0)
$Y(OH)_3$	6.261(2)	3.544(1)	0.566(0)

Table 4.2: Lattice constants for rare earth hydroxides and $Y(OH)_3$ (from Ref. [174]).

4.1.2 Single ion properties

The electronic configuration of the magnetic ions Tb^{3+}, Dy^{3+} and Ho^{3+} is, respectively, $4f^8$, $4f^9$ and $4f^{10}$. Magnetic properties of the rare earth ions can be described by the states of the lowest energy multiplet: the spin-obit splitting between the ground state J manifold and the first excited states is of order of few thousands K. The ground state manifolds can be found from Hund's rules and are $^7F_6$, $^6H_{15/2}$ and $^5I_8$ for Tb^{3+},

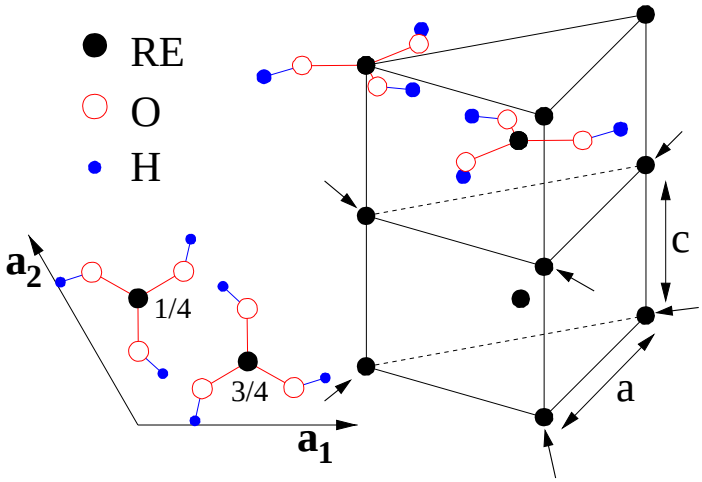

Figure 4.1: The lattice structure of rare earth hydroxides and $Y(OH)_3$. The arrows indicate the 6 nearest neighbours of the central ion in the lower prism. The lower left corner shows a projection of the unit cell onto the plane given by lattice vectors $\boldsymbol{a_1}$ and $\boldsymbol{a_2}$.

Dy^{3+} and Ho^{3+}, respectively. The Wigner-Eckart theorem gives the Landé g-factor equal to $\frac{3}{2}$, $\frac{4}{3}$ and $\frac{5}{4}$ for Tb^{3+}, Dy^{3+} and Ho^{3+}, respectively.

In a crystalline environment, an ion is subject to the electric field and covalency effects from the surrounding ions. This crystalline field effect partially lifts the degeneracy of the ground state multiplet. The low energy levels of Tb^{3+} in $Tb(OH)_3$ are a pair of singlets, that consist of the symmetric combination of $|\pm 6\rangle$ states with a small admixture of the $|0\rangle$ state and an antisymmetric combination 0.3 cm^{-1} above [176]. The next excited state is well separated from the lowest energy pair by an energy of 118 cm^{-1} [176] (1 $cm^{-1} \approx 1.44$ K). In the case of Dy^{3+} in $Dy(OH)_3$, the spectrum consist of 8 Kramers doublets with the first excited state 7.8 cm^{-1} above the ground state [177]. The low energy spectrum of Ho^{3+} in $Ho(OH)_3$ is composed of a ground state doublet and an excited singlet state 11.1 cm^{-1} above [173].

Due to the strong shielding of the $4f$ electrons by the electrons of the filled outer electronic shells, the exchange interactions for $4f$ electrons is weak and the crystal field can be considered as a perturbation to the fixed J manifold. Furthermore, because the strong spin-obit interaction yields a large energy gap between the ground state multiplet and the excited levels, we neglect all the excited electronic multiplets in the calculation.

According to arguments provided by Stevens [171], we express the matrix elements of the crystal field Hamiltonian for the ground state manifold in terms of operator equivalents. The details of the method and conventions for expressing the crystal field Hamiltonian can be found in the review by Hutchings [172]. On the basis of the Wigner-Eckart theorem, one can write the crystal field Hamiltonian in the form

$$\mathcal{H}_{\rm cf} = \sum_{nm} \theta_n B_n^m O_n^m, \tag{4.1}$$

where O_n^m are Steven's "operator equivalents", θ_n are constants called Stevens multiplicative factors and B_n^m are crystal field parameters (CFP)[3]. The CFP are usually determined by fitting experimental (spectroscopic) data. From angular momentum algebra, we know that in the case of f electrons, we need to consider only $n = 0, 2, 4, 6$ in the sum (4.1). The choice of B_n^m coefficients in Hamiltonian (4.1) that do not vanish and have nonzero corresponding matrix elements is dictated by the point symmetry group of the crystalline environment. The Stevens operators, O_n^m, are conveniently expressed in terms of vector components of angular momentum operator $\boldsymbol{J}$. In the case of the $RE(OH)_3$ materials, considered herein, the point-symmetry group is C_{3h}, and the crystal field Hamiltonian is of the form

$$\begin{aligned} \mathcal{H}_{\rm cf}(\boldsymbol{J}_i) &= \alpha_J B_2^0 O_2^0(\boldsymbol{J}_i) + \beta_J B_4^0 O_4^0(\boldsymbol{J}_i) \\ &\quad + \gamma_J B_6^0 O_6^0(\boldsymbol{J}_i) + \gamma_J B_6^6 O_6^6(\boldsymbol{J}_i). \end{aligned} \tag{4.2}$$

The Stevens multiplicative factors α_J, β_J and γ_J (θ_2, θ_4 and θ_6) are collected in Table. 4.3.

Ion	α_J	β_J	γ_J
Tb^{3+}	$-1/(3^2 \cdot 11)$	$2/(3^3 \cdot 5 \cdot 11^2)$	$-1/(3^4 \cdot 7 \cdot 11^2 \cdot 13)$
Dy^{3+}	$-2/(3^2 \cdot 5 \cdot 7)$	$-2^3/(3^3 \cdot 5 \cdot 7 \cdot 11 \cdot 13)$	$2^2/(3^3 \cdot 7 \cdot 11^2 \cdot 13^2)$
Ho^{3+}	$-1/(2 \cdot 3^2 \cdot 5^2)$	$-1/(2 \cdot 3 \cdot 5 \cdot 7 \cdot 11 \cdot 13)$	$-5/(3^3 \cdot 7 \cdot 11^2 \cdot 13^2)$

Table 4.3: Stevens multiplicative factors

[3]To be consistent with the source of crystal field parameters, in Chapter 3 a different convention for writing the crystal field Hamiltonian was used. Here the multiplicative factors, θ_n, are written explicitly, while in Chapter 3 B_n^m are already multiplied by the factor θ_n; hence, the Hamiltonian is of the form $\mathcal{H}_{\rm cf} = \sum_{nm} B_n^m O_n^m$.

Ref	Crystal	$B_2^0(\mathrm{cm}^{-1})$	$B_4^0(\mathrm{cm}^{-1})$	$B_6^0(\mathrm{cm}^{-1})$	$B_6^6(\mathrm{cm}^{-1})$
[173]	$Tb(OH)_3$*	207.9 ± 2.8	-69.0 ± 1.6	-45.3 ± 1.1	585 ± 10
[173]	$Tb{:}Y(OH)_3$	189.1 ± 2.6	-69.1 ± 1.5	-45.7 ± 1.0	606 ± 9
[173]	$Dy(OH)_3$*	209.4 ± 3.4	-75.5 ± 3.5	-40.1 ± 1.9	541.8 ± 26.5
[178]	$Ho(OH)_3$	200 ± 2.0	-57 ± 0.5	-40 ± 0.5	400 ± 5
[173]	$Ho{:}Y(OH)_3$*	246.0 ± 3.4	-56.7 ± 1.2	-39.8 ± 0.3	543.6 ± 3.3
[179]	$Dy(OH)_3$	215.9	-72.0	-42.0	515.3

Table 4.4: Crystal field parameters. Some of the calculation we performed with one set of crystal field parameters only. Crystal field parameters arbitrary chosen to be used in these calculations are marked by an asterisk.

For the sake of conciseness, and to illustrate the procedure, most of our numerical results below are presented for one set of CFP only. The qualitative picture that emerges from our calculations does not depend on the specific choice of CFP parameters. Only quantitative differences are found using the different sets of CFP. Ultimately, a further experimental determination of accurate B_n^m values would need to be carried out in order to obtain more precise mean-field estimates as well as to perform quantum Monte Carlo simulations of the $Re(OH)_3$ systems. According to our *arbitrary* choice[4], if not stated otherwise, we use in the calculations the CFP provided by Scott *et al.* [173, 176, 177, 180]. For $Ho(OH)_3$ and $Dy(OH)_3$ different values of CFP were proposed by Karmakar *et al.* [178, 179]. As one can see in Fig. 4.3, for $Ho(OH)_3$, the latter set of CFP yields a somewhat higher mean-field critical temperature and quite a bit higher critical value of the transverse magnetic field B_x^c =7.35 T, compared with B_x^c =4.35 T obtained using Scott *et al.*'s CFP [173] (see Fig. 4.3). Similarly, Karmakar *et al.*'s CFP [179] for $Dy(OH)_3$ give a much higher critical field of B_x^c =9.12 T, compared with B_x^c = 5.03 T when Scott 's *et al.*'s CFP [173, 177, 180] are used. From the two sets of CFP for $Tb(OH)_3$ we choose the one obtained from measurements on pure $Tb(OH)_3$ [173]. Using the CFP obtained for the system with a dilute concentration of Tb in a $Y(OH)_3$ matrix, $Tb{:}Y(OH)_3$ [173], makes only a small change to the value of critical transverse field; we obtained B_x^c =50.0 T and B_x^c =54.8 T calculated using $Tb{:}Y(OH)_3$ and $Tb(OH)_3$ CFP, respectively (see Fig. 4.3). Available values of the CFP are given in Table 4.4.

[4]By making this choice, we do not imply higher validity or better accuracy of the chosen sets of crystal field parameters.

Eigenstate	Energy (cm^{-1})
$Dy(OH)_3$	
$0.92\,\|\pm15/2\rangle - 0.15\,\|\pm3/2\rangle + 0.37\,\|\mp9/2\rangle$	
$0.40\,\|\pm15/2\rangle + 0.20\,\|\pm3/2\rangle - 0.90\,\|\mp9/2\rangle$	9.6
$Dy(OH)_3$ Karmakar *et al.*, Ref. [178, 179]	
$0.98\,\|\pm15/2\rangle - 0.09\,\|\pm3/2\rangle + 0.15\,\|\mp9/2\rangle$	
$0.17\,\|\pm15/2\rangle + 0.22\,\|\pm3/2\rangle - 0.96\,\|\mp9/2\rangle$	19.3
Ho:$Y(OH)_3$	
$0.94\,\|\pm7\rangle + 0.31\,\|\pm1\rangle + 0.15\,\|\mp5\rangle$	
$0.59\,\|6\rangle + 0.55\,\|0\rangle + 0.59\,\|-6\rangle$	12.7
$Ho(OH)_3$ Karmakar *et al.*, Ref. [178, 179]	
$0.97\,\|\pm7\rangle + 0.24\,\|\pm1\rangle + 0.09\,\|\mp5\rangle$	
$0.60\,\|6\rangle + 0.52\,\|0\rangle + 0.60\,\|-6\rangle$	23.6
$Tb(OH)_3$	
$0.71\,\|6\rangle + 0.05\,\|0\rangle + 0.71\,\|-6\rangle$	
$0.71\,\|6\rangle - 0.71\,\|-6\rangle$	0.49
$0.99\,\|\pm5\rangle + 0.13\,\|\mp1\rangle$	122.06
Tb:$Y(OH)_3$	
$0.71\,\|6\rangle + 0.06\,\|0\rangle + 0.71\,\|-6\rangle$	
$0.71\,\|6\rangle - 0.71\,\|-6\rangle$	0.58
$0.99\,\|\pm5\rangle + 0.16\,\|\mp1\rangle$	115.33

Table 4.5: Eigenstates and energy levels calculated with the crystal field parameters collected in Table 4.4.

We show in Table 4.5 the lowest eigenstates and eigenvalues of the crystal field Hamiltonian (4.2). The calculated energies are not in full agreement with the experimentally determined values because the CFP were fitted using all the observed optical transitions, including transitions between different $\boldsymbol{J}$ manifolds [173]. Furthermore, the fitting procedure used by Scott *et al.* [173] includes perturbative admixing between manifolds with the admixing incorporated into effective Stevens multiplicative factors α_J, β_J and γ_J that slightly differ from those given in Table 4.3.

Given the uncertainty in the CFP, which ultimately lead to an uncertainty of approximately $\sim$ 40% on B_x^c in $Ho(OH)_3$ and $Dy(OH)_3$, as well as the nature of the mean-field calculations that we use and which neglects thermal and quantum mechanical fluctuations, as well as for simplicity sake, we ignore here the effect of hyperfine coupling of the electronic and nuclear magnetic moments. However, as

shown for $LiHo_xY_{1-x}F_4$, the important role of hyperfine interactions for Ho^{3+} on the precise determination of B_x^c must eventually be considered [10, 15, 127, 134]. At this time, one must await results from further experiments and a precise set of CFP for $\mathcal{H}_c$ in order to go beyond the mean-field calculations presented below or to pursue quantum Monte Carlo calculations as done in Refs. [1, 127]. As suggested in Ref. [127], the accuracy of any future calculations (mean-field or quantum Monte Carlo) could be improved by the use of directly measured accurate values of the transverse field splitting of the ground state doublet instead of the less certain values calculated from CFP.

Since our main goal in this exploratory work is to estimate the critical transverse field, B_x^c, for the family of $RE(OH)_3$ compounds and to explore the possible validity of a transverse field Ising model description of these materials, we henceforth restrict ourselves to the $\mathcal{H}_{\rm cf}$ in Eq. (4.1) with the CFP (B_n^m parameter values) given in Table 4.4. These calculations could be revisited and quantum Monte Carlo simulations [1, 127] performed once experimental results reporting on the effect of B_x on $Dy(OH)_3$ and $Ho(OH)_3$ become available.

4.1.3 Single ion transverse field spectrum

A magnetic field, B_x, applied in the direction transverse to the easy axis splits the degeneracy of the ground state doublet in the case of $Ho(OH)_3$ and $Dy(OH)_3$, or increase the separation of the ground levels in the case of the already weakly separated singlets in $Tb(OH)_3$. By diagonalizing the single-ion Hamiltonian, $\mathcal{H}_0$, which consist of the crystal field and Zeeman term,

$$\mathcal{H}_0 = \mathcal{H}_{\rm cf}(\boldsymbol{J}_i) - g\mu_{\rm B}B_xJ_x, \tag{4.3}$$

we obtain the transverse field dependence of the single ion energy levels, plotted in Fig. 4.2. In the case of $Dy(OH)_3$, the two lowest energy levels splitting is too small to be clearly visible in the main panel of Fig. 4.2. Hence, we show the energy separation between the two lowest levels in the inset of Fig. 4.2 for $Dy(OH)_3$. Furthermore, the separation vanishes at $B_x = 3.92$ T, indicating that the two lowest states for this specific value of the transverse field, B_x, are degenerate.

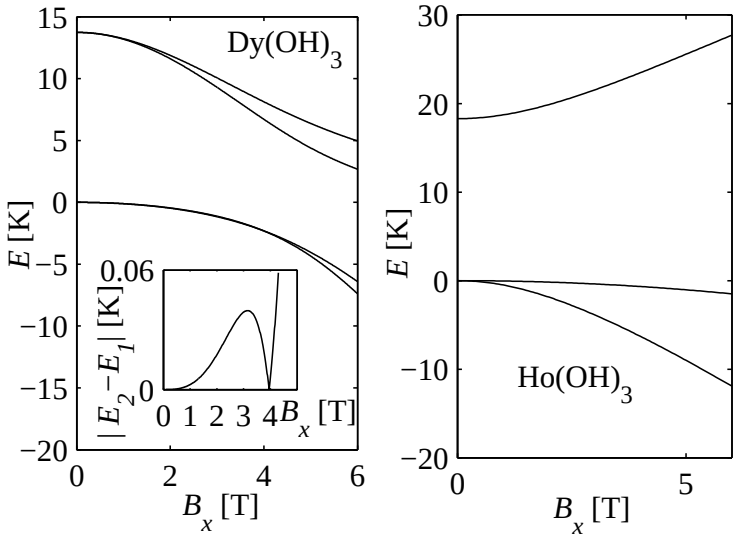

Figure 4.2: Energy levels as a function of applied transverse field for $Dy(OH)_3$ and $Ho(OH)_3$. The inset shows the separation of the lowest energy levels in $Dy(OH)_3$.

To calculate the transverse field dependence of the lowest energy levels up to the critical transverse field where dipolar ferromagnetism is destroyed, we do not have to include all the crystal field states since the B_x-induced admixing among the states decreases with increasing energy separation. We have tried how many energy levels have to be included in the calculation to obtain results that are visually overlaping with these of Fig. 4.2. In the case of $Ho(OH)_3$ we can reproduce the field dependence, B_x, of the lowest energy levels, E in Fig. 4.2 using only the four lowest levels. In the case of $Dy(OH)_3$, we have to retain the ground doublet and several of the lowest excited doublets.

4.2 Numerical solution

The collective magnetic properties of the considered rare earth hydroxides are mainly controlled by a long range dipolar interaction between the magnetic moments carried by the rare earth ions. The dipolar interaction is complemented by a short range exchange interaction. Adding the interaction terms to the single ion Hamiltonian

(3.4) gives a full Hamiltonian, $\mathcal{H}$, of the form

$$\begin{aligned}\mathcal{H} &= \sum_i \mathcal{H}_{\rm cf}(\boldsymbol{J}_i) - g\mu_{\rm B}\sum_i B_x J_{i,x} \\ &+ \frac{1}{2}\sum_{ij}\sum_{\mu\nu}\mathcal{L}_{ij}^{\mu\nu}J_{i,\mu}J_{j,\nu} + \frac{1}{2}\mathcal{J}_{\rm ex}\sum_{i,nn}\boldsymbol{J}_i\cdot\boldsymbol{J}_{nn}. \end{aligned} \tag{4.4}$$

$\mathcal{L}_{ij}^{\mu\nu}$ are the anisotropic dipole-dipole interaction constants of the form $\mathcal{L}_{ij}^{\mu\nu} = \frac{\mu_0(g\mu_{\rm B})^2}{4\pi a^3}L_{ij}^{\mu\nu}$, where $\mu,\nu = x,y,z$; a is a lattice constant (see Table 4.2) and μ_0 is the permeability of vacuum. $L_{ij}^{\mu\nu}$ are dimensionless dipolar interaction coefficients,

$$L_{ij}^{\mu\nu} = \frac{\delta^{\mu\nu}\left|\boldsymbol{r}_{ij}\right|^2 - 3\left(\boldsymbol{r}_{ij}\right)^{\mu}\left(\boldsymbol{r}_{ij}\right)^{\nu}}{\left|\boldsymbol{r}_{ij}\right|^5}, \tag{4.5}$$

where $\boldsymbol{r}_{ij} = \boldsymbol{r}_j - \boldsymbol{r}_i$, with $\boldsymbol{r}_i$ the lattice position of magnetic moment $\boldsymbol{J}_i$, expressed in units of the lattice constant, a. $\mathcal{J}_{\rm ex}$ is the antiferromagnetic ($\mathcal{J}_{\rm ex} > 0$) exchange interaction constant, which can be recast as $\mathcal{J}_{\rm ex} = \frac{\mu_0(g\mu_{\rm B})^2}{4\pi a^3}J_{\rm ex}$, where $J_{\rm ex}$ is now a dimensionless exchange constant that, when multiplied by the nearest neighbour coordination number, z=6, can be use to compare the relative strength of exchange vs the magnetic dipolar lattice sum (energies) collected in Table 4.6. The label nn in Eq. (4.4) denotes the nearest neighbour sites of site i.

The exchange interaction is expected to be of somewhat lower strength than the dipolar coupling [2, 3]. We therefore neglect it in most of the calculations, but we discuss its effect on the calculated B_x vs T phase diagram at the end of this section as well as explore its influence on the occurrence of a first order phase transition in $Dy(OH)_3$ in Section 4.4.2. Denoting $L_{\mu\nu} = \sum_j L_{ij}^{\mu\nu}$ and $\mathcal{L}_{\mu\nu} = \frac{\mu_0(g\mu_{\rm B})^2}{4\pi a^3}L_{\mu\nu}$, we write a mean-field Hamiltonian in the form

$$\begin{aligned}\mathcal{H}_{\rm MF} &= \mathcal{H}_c(\boldsymbol{J}) - g\mu_{\rm B}B_x J_x \\ &+ \sum_{\mu=x,y,z}\left(\mathcal{L}_{\mu\mu} + z\mathcal{J}_{\rm ex}\right)\left(J_\mu\left\langle J_\mu\right\rangle - \frac{1}{2}\left\langle J_\mu\right\rangle^2\right). \end{aligned} \tag{4.6}$$

with $z = 6$ the number of nearest neighbours. The last term in Eq. (4.6), $-\frac{1}{2}\left\langle J_\mu\right\rangle^2$, has no effect on the calculated thermal expectation values of the $\hat{x}$ and $\hat{z}$ components

of the magnetization, and can be dropped. The off-diagonal terms, $\mathcal{L}_{\mu\nu}$ with $\mu \neq \nu$, vanish due to the lattice symmetry. We employ the Ewald technique [76, 181–184] to calculate the dipole-dipole interaction, $L_{ij}^{\mu\nu}$, of Eq. (4.5). By summing over all sites j coupled to an arbitrary site i, we obtain the coefficients $L_{\mu\nu}$ listed in Table 4.6. The considered Ewald sums ignore a demagnetization term [184] and our calculations can therefore be interpreted as corresponding to a long needle-shape sample.

	L_{xx}	L_{yy}	L_{zz}
$Tb(OH)_3$	-11.43	-11.43	-28.01
$Dy(OH)_3$	-11.40	-11.41	-28.20
$Ho(OH)_3$	-11.38	-11.37	-28.45

Table 4.6: Dimensionless lattice sums calculated with the values of c/a taken from Table 4.2.

We diagonalize numerically $\mathcal{H}_{\rm MF}$ in Eq. (4.6), and calculate self-consistently the thermal averages of J_x and J_z operators, from the expression

$$\langle J_\mu \rangle = \frac{\text{Trace}[J_\mu \exp(-\mathcal{H}_{\rm MF}/T)]}{\text{Trace}[\exp(-\mathcal{H}_{\rm MF}/T)]}, \tag{4.7}$$

where μ stands for x and z. $\langle J_y \rangle = 0$ due to the lattice mirror symmetries and since $\boldsymbol{B}$ is applied along $\hat{x}$.

For a given B_x, we find the value of the critical temperature, $T_c(B_x)$, at which the order parameter, $\langle J_z \rangle$, vanishes. The resulting B_x vs T phase diagrams, obtained that way, using *all* sets of CFP from Table 4.4, are shown in Fig. 4.3. In the main panel, we plot the phase diagrams for $Ho(OH)_3$ and $Dy(OH)_3$, using Scott *et al.*'s CFP [173, 176, 177, 180]. The top inset shows the B_x vs T phase diagrams for $Tb(OH)_3$, using two available sets of CFP. This indicates that, for $Tb(OH)_3$, the critical field $B_x(T)$ reaches very quickly the upper limit of magnetic fields attainable with commercial magnets. The bottom inset shows the B_x vs T phase phase diagrams for $Ho(OH)_3$ and $Dy(OH)_3$ using Karmakar *et al.*'s CFP [178, 179]. Although the diagrams differ quantitatively for the two sets of CFP, the overall qualitative trend is the same for both sets. Table 4.7 lists the mean-field estimates of T_c and B_x^c together with the experimental values of T_c [2, 3, 185].

There are two contributing factors behind the difference between the experimental

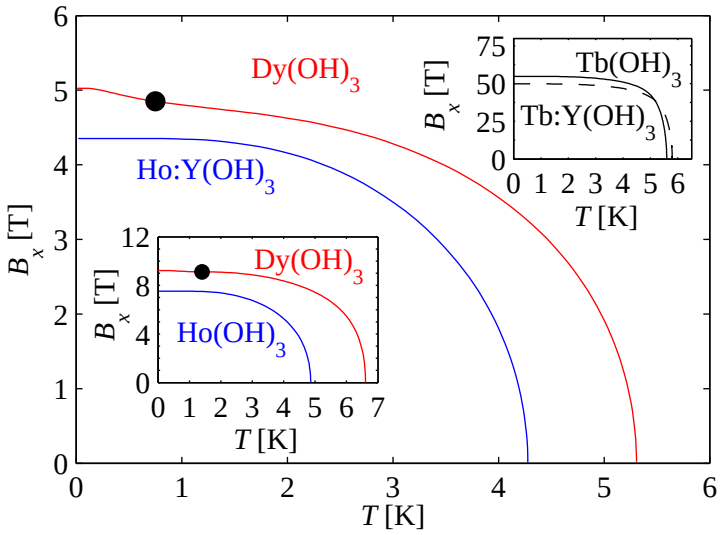

Figure 4.3: The main panel shows the phase diagrams for $Dy(OH)_3$ and $Ho{:}Y(OH)_3$ (crystal field parameters of Scott *et al.* [173, 177]). The dot indicates the location of the tricritical point for $Dy(OH)_3$. The transition is first order for temperatures below the temperature location of the tricritical point. The upper inset shows the phase diagram for $Tb(OH)_3$ (crystal field parameters of Scott *et al.* [173, 176, 180]). The lower inset shows the phase diagram for $Ho(OH)_3$ and $Dy(OH)_3$ calculated with the crystal field parameters of Karmakar *et al.* [178, 179].

and mean-field values of T_c in Table 4.7 and, presumably once they are experimentally determined, those for B_x^c. Firstly, in obtaining those mean-field values from Eq. (4.6) and Eq. (4.7), we neglected the (presumably) antiferromagnetic nearest-neighbour exchange $\mathcal{J}_{\rm ex}$ which would contribute to a depression of both the critical ferromagnetic temperature T_c and B_x^c. Secondly, mean-field theory neglects correlations in the thermal and quantum fluctuations which would also contribute to reduce T_c and B_x. From the comparison of mean-field theory [127] and quantum Monte Carlo [1, 127] for $LiHoF_4$, we would anticipate that our mean-field estimates of T_c and B_x are accurate within 20% to 40%, notwithstanding the uncertainty on the crystal field parameters.

By seeking a self-consistent solution for $\langle J_z \rangle$, starting from either the fully polarized or weakly polarized state, two branches of solutions are obtained at low temperature and large B_x for $Dy(OH)_3$. This suggests a first order PM to FM transition when using either set of CFP for this material. This result was confirmed by a more thorough investigation (see Section V below). The top right inset of Fig. 4.7 shows the behaviour

of the $\langle J_z \rangle$ as a function of B_x for $T = 0.3$ K, illustrating the transition field and the limits for the superheating and supercooling regime. The black dot in the main panel and inset of Fig. 4.3 shows the location of the tricritical point (see Section V). Note that the B_x value at the tricritical point is ~ 4.85 T using the CFP of Scott *et al.* (main panel of Fig. 4.3) [173, 176, 177, 180]. Hence, the occurrence of a first order transition here is not directly connected to the degeneracy occurring between the two lowest energy levels at $B_x = 3.92$ T using the same set of CFP (see inset of Fig. 4.2 for $Dy(OH)_3$). A zoom on the low temperature regime and the vicinity of the tricritical point for $Dy(OH)_3$ is shown in Fig. 4.7. The calculation details needed to obtain the phase diagram of Fig. 4.7 are described in Section 4.4.1. The existence of a first order transition at strong B_x in $Dy(OH)_3$ depends on the details of the chosen Hamiltonian in Eq. (4.4). For example, as discussed in Section 4.4.2, a sufficiently strong nearest-neighbour antiferromagnetic exchange, $\mathcal{J}_{\rm ex}$, eliminates the first order transition. We also discuss in Section 4.4.2 the role of a longitudinal field B_z (along c axis) on the first order transition. At this time, one must await experimental results to ascertain the specific low temperature behaviour that is at play for strong B_x in $Dy(OH)_3$.

Crystal	experimental T_c [K]	MFT T_c [K]	MFT B_x^c [T]
$Ho(OH)_3$	2.54	4.28	4.35
$Dy(OH)_3$	3.48	5.31	5.03
$Tb(OH)_3$	3.72	5.59	54.81

Table 4.7: Experimental values of critical temperatures T_c [2, 3] and mean-field theory (MFT) estimates for T_c and B_x^c.

We now briefly analyze the effect of a nonzero exchange interaction. The dependence of the critical temperature, T_c, and the critical transverse field, B_x^c, on the exchange constant, $J_{\rm ex}$, is plotted in Fig. 4.4. The dot on the B_x vs $J_{\rm ex}$ plot for $Dy(OH)_3$ indicates the threshold value of $J_{\rm ex}$, $J_{\rm ex}^{\rm 2nd}$=0.995, above which the first order transition ceases to exist. The dependence of the existence of the first order transition on $J_{\rm ex}$ is discussed in some detail in Section 4.4.2. For $J_{\rm ex} < J_{\rm ex}^{\rm 2nd}$, the thinner lines correspond to the boundary of the supercooling and superheating regime. In the mean-field theory presented here, $J_{\rm ex}$ simply adds to the interaction constant $\mathcal{L}_{\mu\mu}$ with $\mu = x, y, z$ in Eq. (4.6) (see Table 4.6). Hence, beyond a threshold value of $J_{\rm ex}$, the system no longer admits a long range ordered ferromagnetic phase. In the case of

$Dy(OH)_3$, B_x^c stays almost unchanged as a function of J_{ex}, until it drops very sharply when $\mathcal{L}_{zz} + z\mathcal{J}_{ex} = 0$ ($z = 6$). In the inset of Fig. 4.4, we focus on the regime where B_x^c vs J_{ex} plot sharply drops. The cusp at B_x =3.92 T is a consequence of the degeneracy of the lowest energy eigenstates (see Fig. 4.2). As will be shown in detail in the next section for the $Ho(OH)_3$ system, the energy gap separating transverse-field-split levels of the ground state doublet plays the role of an effective transverse field $\Gamma(B_x)$ acting on effective Ising spins.

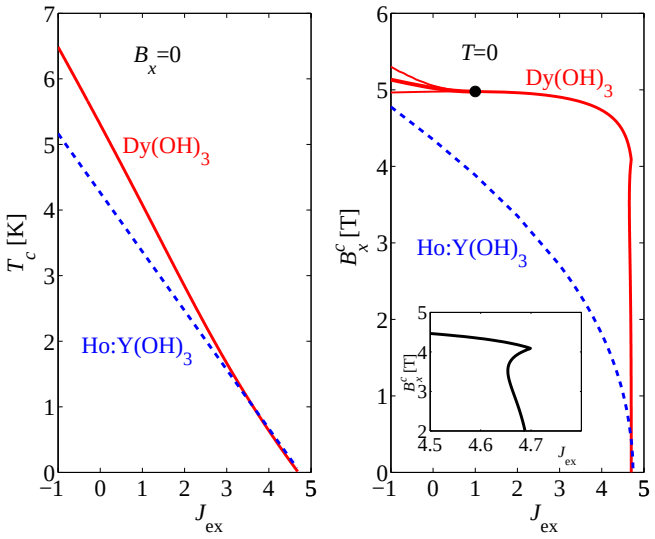

Figure 4.4: The effect of the value of the exchange constant on the phase boundary, T_c vs J_{ex} at B_x=0 (left) and B_x^c vs J_{ex} at $T = 0$ (right). Solid and dashed lines are used for $Dy(OH)_3$ and $Ho(OH)_3$, respectively. The inset of the right graph shows a focus on the features of the high J_{ex} regime in the $Dy(OH)_3$ plot. The dot in the right panel indicates the tricritical point. The two additional lines at the left side of the tricritical point mark the limits of superheating and supercooling regimes. In the calculations, the CFP of Ref. [173] were used.

4.3 Effective $S = 1/2$ Hamiltonian

In this section we show that $Ho(OH)_3$ and $Tb(OH)_3$ can be described with good accuracy by an effective TFIM Hamiltonian. On the other hand, although $Dy(OH)_3$ has been referred in the literature as an Ising material [2, 186], we find that it is not

possible to describe the magnetic properties of this material within the framework of an effective Ising Hamiltonian that neglects the effect of the excited crystal field states.

To be able to identify a material as a realization of an effective *microscopic* Ising model, the following conditions should apply [187]:

- There has to be a ground state doublet or a close pair of singlets that are separated from the next energy level by an energy gap that is large in comparison with the critical temperature. This ensures that at the temperatures of interest only the two lowest levels are significantly populated.

- To first order, there has to be no transverse susceptibility. It means that there should be no matrix elements of (J_x, J_y) operators between the two states of the ground doublet.

- Furthermore, the longitudinal (in the easy axis direction) susceptibility has to be predominantly controlled by the two lowest levels. In other words, there has to be no significant mixing of the states of the lowest doublet with the higher levels via the internal mean field along the Ising direction. In more technical terms, the van Vleck susceptibility should play a negligible role to the non-interacting (free ion) susceptibility near the critical temperature [188].

- In setting up the above conditions, one is in effect requesting that a material be describable as a TFIM from a microscopic point of view. However, one can, alternatively, ask whether the quantum critical point of a given material is in the same universality class as the relevant transverse field Ising model. In such a case, as long as transition is second order, then sufficiently close to the quantum critical point, a mapping to an effective TFIM is always in principle possible. However, it can be difficult to estimate the pertinent parameters entering the Ginzburg-Landau-Wilson theory describing the transition. From that perspective, the first and the third point above are always fulfilled sufficiently close to a second order quantum critical point[5].

The first condition is not satisfied in the case of $Dy(OH)_3$. The energy gap of 7.8 cm^{-1} $\approx$ 11.2 K is not much larger than the mean-field critical temperature $T_c \sim 5.31$ K.

[5]We thank an anonymous referee for his/her comments on this point.

Hence, at temperatures close to T_c, the first excited doublet state is also significantly populated. Furthermore, and most importantly, in the context of a field-induced quantum phase transition, the third condition above is also not satisfied. Hence, even at low temperatures, because of the admixing of the two lowest energy states with the higher energy levels that is induced via the internal (mean) field from the surrounding ions, $Dy(OH)_3$ cannot by described by an effective *microscopic* Ising model that solely considers the ground doublet and ignores the excited crystal field states. This effect and the associated role of nonzero J_z matrix elements between the ground state and higher crystal field levels is discussed in more detail in Appendix A. As an interesting consequence of this participation of the higher energy levels, we predict that, unlike in the TFIM of Eq. (1), a first order phase transition may occur at high transverse field in $Dy(OH)_3$ (see Section 4.4.1).

For $Ho(OH)_3$ and $Tb(OH)_3$ we construct an effective Ising Hamiltonian, following the method of Refs. [1, 26, 127]. We diagonalize exactly the noninteracting Hamiltonian, $\mathcal{H}_0$ of Eq. (3.4), for each value of the transverse field, B_x. We denote the two lowest states by $|\alpha(B_x)\rangle$ and $|\beta(B_x)\rangle$ and their energies by $E_\alpha(B_x)$ and $E_\beta(B_x)$, respectively. a transverse field enforces a unique choice of basis, in which the states can be interpreted as $|\rightarrow\rangle$ and $|\leftarrow\rangle$ in the Ising subspace. We introduce a new $|\uparrow\rangle$ and $|\downarrow\rangle$ basis, in which the J_z matrix elements are diagonal, by performing a rotation

$$\begin{aligned} |\uparrow\rangle &= \tfrac{1}{\sqrt{2}}(|\alpha(B_x)\rangle + \exp(i\theta)\,|\beta(B_x)\rangle), \\ |\downarrow\rangle &= \tfrac{1}{\sqrt{2}}(|\alpha(B_x)\rangle - \exp(i\theta)\,|\beta(B_x)\rangle). \end{aligned} \tag{4.8}$$

In this basis, the effective single ion Hamiltonian, describing the two lowest states, is of the form

$$\mathcal{H}_T = E_{\mathrm{CM}}(B_x) - \frac{1}{2}\Delta(B_x)\sigma^x, \tag{4.9}$$

where $E_{\mathrm{CM}}(B_x) = \frac{1}{2}(E_\alpha(B_x) + E_\beta(B_x))$ and $\Delta(B_x) = E_\beta(B_x) - E_\alpha(B_x)$. Thus the splitting of the ground state doublet plays the role of a transverse magnetic field, $\Gamma \equiv \frac{1}{2}\Delta(B_x)$ in Eq. (1). In the case of $Tb(OH)_3$, after performing the rotation (4.8), even at $B_x = 0$, a small transverse field term ($\Gamma = \frac{1}{2}\Delta(0) > 0$) is present in Hamiltonian (4.9). For $Dy(OH)_3$ and $Ho(OH)_3$, the splitting of the energy levels, obtained via exact diagonalization was already discussed at the end of Section 4.1 and is shown in Fig. 4.2. To include the interaction terms in our Ising Hamiltonian, we expand the matrix

elements of J_x, J_y and J_z operators in terms of the σ^ν ($\nu = x, y, z$) Pauli matrices and a unit matrix, $\sigma^0 \equiv \mathbb{1}$,

$$J_{i,\mu} = C_\mu \mathbb{1} + \sum_{\nu=x,y,z} C_{\mu\nu}(B_x)\sigma_i^\nu. \tag{4.10}$$

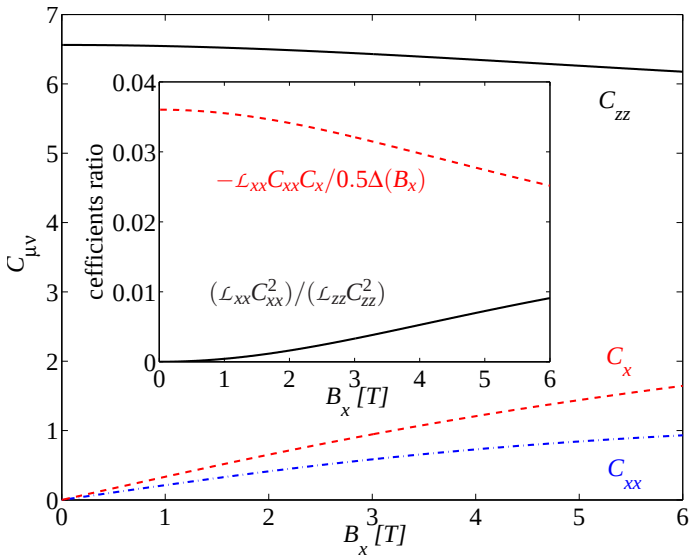

Figure 4.5: The coefficients in the projection of $\boldsymbol{J}$ operators onto the two dimensional Ising subspace for $Ho(OH)_3$. The inset shows the ratios of the coefficients present in Eq. (4.11).

By replacing all $J_{i,\mu}$ operators in the interaction term of Hamiltonian (4.4) by the two dimensional representation of Eq. (4.10), one obtains in general a lengthy Hamiltonian containing all possible combinations of spin-$\frac{1}{2}$ interactions. In the present case, the resulting Hamiltonian is considerably simplified by the crystal symmetries and the consequential vanishing of off-diagonal elements of the interaction matrix $\mathcal{L}_{\mu\nu}$. This would not be the case for diluted $Ho_xY_{1-x}F_4$ (see Ref. [26]). After performing the transformation in Eq. (4.8), we have $J_i^z = C_{zz}\sigma_i^z$, $J_i^y = C_{yy}\sigma_i^y$ and $J_i^x = C_{xx}\sigma_i^x + C_x\mathbb{1}$. Hence, we can rewrite the mean-field Hamiltonian (4.6) in the form

$$\begin{aligned}\mathcal{H}_{\rm MF} &= (\mathcal{L}_{zz} + z\mathcal{J}_{\rm ex})C_{zz}^2 m_z\sigma^z + \left(\mathcal{L}_{xx}C_xC_{xx} - \frac{1}{2}\Delta(B_x)\right)\sigma^x \\ &+ (\mathcal{L}_{xx} + z\mathcal{J}_{\rm ex})C_{xx}^2 m_x\sigma^x + (\mathcal{L}_{yy} + z\mathcal{J}_{\rm ex})C_{yy}^2 m_y\sigma^y,\end{aligned} \tag{4.11}$$

where $m_\nu \equiv \langle \sigma^\nu \rangle$ and $\langle \ldots \rangle$ denotes a Boltzmann thermal average.

The C_{zz}, C_{xx} and C_x coefficients for $Ho(OH)_3$ are plotted in Fig. 4.5. The inset shows a comparison of the terms in $\mathcal{H}_{\rm MF}$. In $Ho(OH)_3$, the coefficient $\mathcal{L}_{xx} {C_{xx}}^2$ (the fourth therm of $\mathcal{H}_{\rm MF}$) does not exceed 1.5% of the effective transverse field, $\Gamma = \mathcal{L}_{xx} C_x C_{xx} - \frac{1}{2}\Delta(B_x)$. In $Tb(OH)_3$, this ratio is even smaller, and we thus neglect it, further motivated by the fact that doing so decouples m_z from m_x and make the problem simpler. The term $\mathcal{L}_{yy} {C_{yy}}^2 m_y \sigma^y$ in Eq. 4.11 can be omitted, since due to symmetry $m_y \equiv \langle \sigma^y \rangle = 0$. The interaction correction, $\mathcal{L}_{xx} C_x C_{xx}$, to the effective transverse field, Γ, is of order of 3% of Γ and we retain it in our calculations. Thus, we finally write

$$\mathcal{H}_{\rm MF} = P\sigma^z + \Gamma\sigma^x, \tag{4.12}$$

where $P = \mathcal{L}_{zz} {C_{zz}}^2 m_z$ and $\Gamma = \mathcal{L}_{xx} C_x C_{xx} - \frac{1}{2}\Delta(B_x)$.

Diagonalizing the Hamiltonian (4.12) allows us to evaluate m_z and $m_x \equiv \langle \sigma^x \rangle$, giving well known formulae [23]:

$$\begin{array}{l} m_x = \frac{\Gamma}{\sqrt{P^2+\Gamma^2}} \tanh(\sqrt{P^2+\Gamma^2}/T), \\ m_z = \frac{P}{\sqrt{P^2+\Gamma^2}} \tanh(\sqrt{P^2+\Gamma^2}/T) \end{array}, \tag{4.13}$$

and the phase boundary,

$$T_c(B_x) = \frac{\Gamma(B_x)}{\mathrm{atanh}(\frac{\Gamma(B_x)}{\mathcal{L}_{zz} C_{zz}^2})}. \tag{4.14}$$

In Fig. 4.6, we show that Eq. (4.14) yields a phase diagram that only insignificantly differs from the one obtained from the full diagonalization of $\mathcal{H}_{\rm MF}$ in Eq. (4.6) shown in Fig. 4.3, in the case of $Ho(OH)_3$, and, in the case of $Tb(OH)_3$, the discrepancy is even smaller because the energy gap to the third crystal field state, 118 $\mathrm{cm}^{-1} \simeq 170$ K, is very large compared to $T_c^{\rm MF} = 5.59$ K.

As alluded to above, in the case of $Dy(OH)_3$, a description in terms of an effective Ising Hamiltonian method does not work because of the admixing between states of the two lowest doublets induced by the local mean-field that is proportional to $\langle J_z \rangle$ (see Appendix A). The dashed line in the last panel of Fig. 4.6 shows the incorrect phase diagram obtained for $Dy(OH)_3$ obtained using an effective spin-1/2 Hamiltonian constructed from only the ground doublet. It turns out that a form of the method of Section 4.3 can still be used. However, instead of keeping only two levels in the

interaction Hamiltonian, one needs to retain at least four states. In analogy with the procedure in Section 4.3, we diagonalize the single ion Hamiltonian $\mathcal{H}_0$ of Eq. (3.4) which consist of the crystal field Hamiltonian and the transverse field term. Next, we write an effective interaction Hamiltonian using the four (or six) lowest eigenstates of $\mathcal{H}_0$. The resulting effective Hamiltonian is then used in the self-consistent Eqs. (4.7). For example, for $B_x = 4.8$ T, proceeding by keeping only the four lowest eigenstates of $\mathcal{H}_0$ to construct the effective Hamiltonian, one finds a critical temperature that is only about 3% off compared to a calculation that keeps all 16 eigenstates of $\mathcal{H}_0$. This difference drops below 1% when keeping the 6 lowest eigenstates of $\mathcal{H}_0$.

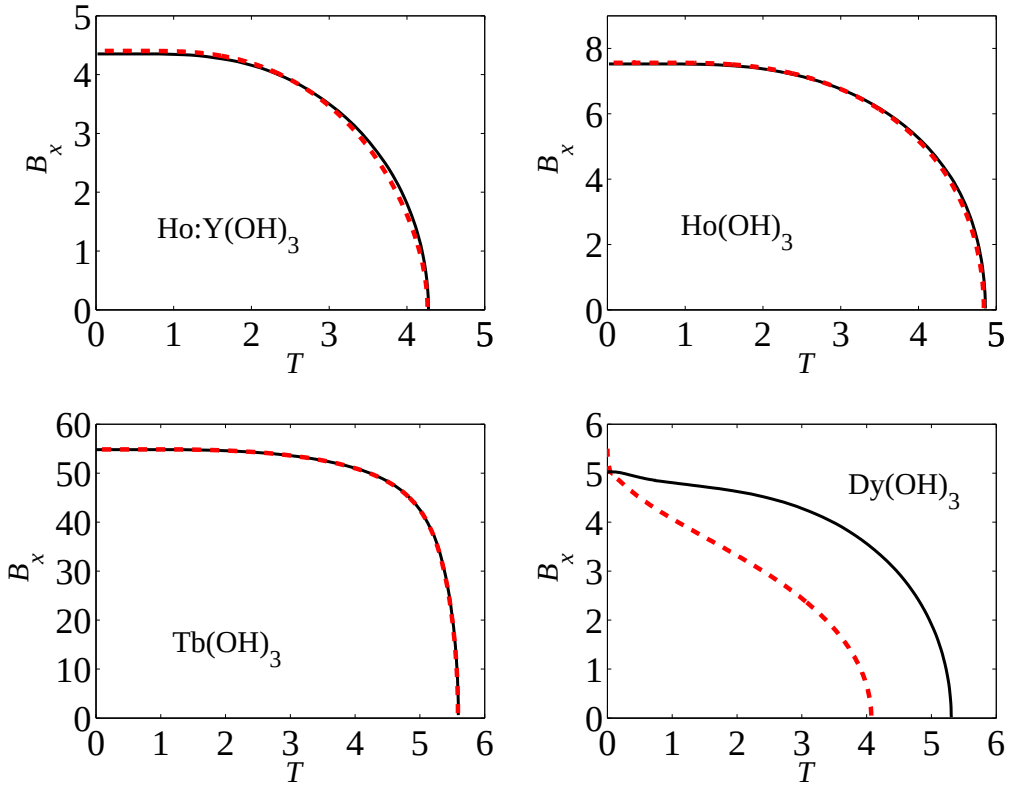

Figure 4.6: Comparison of the phase diagrams obtained with diagonalization of the full manifold (solid lines) and with effective spin-1/2 Hamiltonian (dashed lines). Calculation for $Ho(OH)_3$ were performed using the CFP of Karmakar *et al.* [178, 179].

Having explored the quantitative validity of the spin-1/2 TFIM description of

$Ho(OH)_3$ and $Tb(OH)_3$ in nonzero B_x, we now turn to the problem of the first order PM to FM transition at large B_x and low temperature in $Dy(OH)_3$, exposed in the numerical solution of the self-consistent equations comprised in Eq. (4.7) (with $\mu = x, z$).

4.4 First order transition

The first order transition in $Dy(OH)_3$ takes its origin in the sizable admixing among the four lowest levels induced by the the local mean-field that is proportional to $\langle J_z \rangle$. Under the right temperature and field conditions, two free-energy equivalent configurations can exist: an ordered state with some not infinitesimally small magnetization, $\langle J_z \rangle > 0$, and a state with zero magnetic moment, $\langle J_z \rangle = 0$. To simplify the argument, we consider how this occurs at $T = 0$. At first, let us look at the situation when the longitudinal internal mean field induces an admixing of the ground state with the first excited state only (as in the TFIM). In such a case, there is only a quadratic dependence of the ground state energy on the longitudinal mean field, B_z^{MF}, and, consequently, only one energy minimum is possible. Now, if there is an admixing of the ground state and at least three higher levels, the dependency of the ground state energy on B_z^{MF} is of fourth order and two energy minima are, in principle, possible. Thus, at a certain value of external parameters the system can acquire two energetically equivalent states, one with zero and the other with a non-zero magnetization. When passing through this point, either by varying the transverse field or the temperature, a first order phase transition characterized by a magnetization discontinuity occurs. To make this discussion more formal, we now proceed with a construction of the Ginzburg-Landau theory for $Dy(OH)_3$ for arbitrary B_x in the regime of B_x and T values where the paramagnetic to ferromagnetic transition is second order. This allows us to determine the the tricritical transverse field value above which the transition becomes first order.

4.4.1 Ginzburg-Landau Theory

To locate the tricritical point for $Dy(OH)_3$, we perform a Landau expansion of the mean-field free energy, $\mathcal{F}_{\mathrm{MF}}(\langle J_x \rangle, \langle J_z \rangle)$. Next, we minimize $\mathcal{F}_{\mathrm{MF}}$ with respect to $\langle J_x \rangle$,

leaving $\langle J_z \rangle$ as the only free parameter. The mean-field free energy can be written in the form

$$\begin{aligned} \mathcal{F}_{\mathrm{MF}}\left(\langle J_x \rangle, \langle J_z \rangle\right) &= -T \log Z\left(\langle J_x \rangle, \langle J_z \rangle\right) \\ &- \frac{1}{2}\left(\mathcal{L}_{xx} \langle J_x \rangle^2 + \mathcal{L}_{zz} \langle J_z \rangle^2\right), \end{aligned} \tag{4.15}$$

where $Z\left(\langle J_x \rangle, \langle J_z \rangle\right)$ is the partition function.

Just below the transition, in the part of the phase diagram where the transition is second order, $\langle J_z \rangle$ is a small parameter (i.e. has a small dimensionless numerical value). We therefore make an expansion for $\langle J_x \rangle$ as a function of $\langle J_z \rangle$, which we write it in the form:

$$\langle J_x \rangle = \langle J_x \rangle_0 + \delta(\langle J_z \rangle). \tag{4.16}$$

$\langle J_x \rangle_0$ is the value of $\langle J_x \rangle$ that extremizes $\mathcal{F}_{\mathrm{MF}}$ when $\langle J_z \rangle = 0$. $\delta(\langle J_z \rangle)$ is a perturbatively small function of $\langle J_z \rangle$, which we henceforth simply denote δ, and which is our series expansion small parameter for $\langle J_x \rangle$. Substituting expression (4.16) to $\mathcal{H}_{\mathrm{MF}}$ of Eq. (4.6), and setting $J_{\mathrm{ex}} = 0$ for the time being, we have

$$\begin{aligned} \mathcal{H} &= \mathcal{H}_{\mathrm{cf}}(\boldsymbol{J}_i) - g\mu_{\mathrm{B}} B_x J_x \\ &+ \mathcal{L}_{xx} J_x(\langle J_x \rangle_0 + \delta) + \mathcal{L}_{zz} J_z \langle J_z \rangle, \end{aligned} \tag{4.17}$$

or

$$\mathcal{H} = \mathcal{H}_0(B_x, \langle J_x \rangle_0) + \mathcal{L}_{xx} J_x \delta + \mathcal{L}_{zz} J_z \langle J_z \rangle, \tag{4.18}$$

where for brevity, as in Eq. (4.6), the constant term has been dropped because, again, it does not affect the expectation values needed for the calculation.

The power series expansion of the partition function, and then of the free energy (4.15), can be calculated from the eigenvalues of Hamiltonian (4.18). Instead of applying standard quantum-mechanical perturbation methods to Eq. (4.18), we obtain the expansion of energy levels as a perturbative, 'semi-numerical, solution to the characteristic polynomial equation

$$\det\left[\mathcal{H}_0 + \mathcal{L}_{xx} J_x \delta + \mathcal{L}_{zz} J_z \langle J_z \rangle - E_n\right] = 0. \tag{4.19}$$

We can easily implement this procedure by using a computer algebra method (e.g. Maple or Mathematica). To proceed, we substitute a formal power series expansion of the solution

$$E_n = E_n^{(0,0)} + E_n^{(0,1)}\delta + E_n^{(2,0)} \langle J_z \rangle^2 + E_n^{(2,1)} \langle J_z \rangle^2 \delta + \ldots, \tag{4.20}$$

to Eq. (4.19), containing all the terms of the form $E_n^{(\alpha,\beta)} \langle J_z \rangle^\alpha \delta^\beta$, where $\alpha + 2\beta \leq 6$, as will be justified below Eq. (4.23). To impose consistency of the resulting equation obtained from Eq. (4.19) and Eq. (4.20), up to sixth order of the expansion in $\langle J_z \rangle$ in), we need to equate to zero all the coefficient with the required order of $\langle J_z \rangle$ and δ, i.e. $\alpha + 2\beta \leq 6$. This gives a system of equations that can be numerically solved for the coefficients $E_n^{(k,l)}$, where $k, l > 0$. By $E_n^{(0,0)}$ we denote the eigenvalues of the Hamiltonian $\mathcal{H}_0(B_x, \langle J_x \rangle_0)$.

We use the perturbed energies, E_n, of Eq. (4.20) to calculate the partition function

$$Z(\delta, \langle J_z \rangle) = \sum_n e^{-E_n/T} \tag{4.21}$$

and substitute it in Eq. (4.15). We Taylor expand the resulting expression to obtain the numerical values of the expansion coefficients in the form

$$\mathcal{F}_{\text{MF}} = A^{(0,0)} + A^{(2,0)} \langle J_z \rangle^2 + A^{(0,1)}\delta + A^{(2,1)} \langle J_z \rangle^2 \delta + \ldots. \tag{4.22}$$

The free energy $\mathcal{F}_{\text{MF}}$ is a symmetric function of $\langle J_z \rangle$, so the expansion (4.22) contains only even powers of $\langle J_z \rangle$. We minimize $\mathcal{F}_{\text{MF}}$ in Eq. (4.22) with respect to δ. To achieve this, we have to solve a high order polynomial equation $d\mathcal{F}_{\text{MF}}/d\delta = 0$. Again, we do it by substituting to the equation a formal power series solution

$$\delta(\langle J_z \rangle) = D_2 \langle J_z \rangle^2 + D_4 \langle J_z \rangle^4 + \ldots \tag{4.23}$$

and then solve it for the values of the expansion parameters D_n. Due to symmetry, only even powers of $\langle J_z \rangle$ are present and, from the definition of δ, the constant $\langle J_z \rangle$-independent term is equal to zero. From the form of the expansion in Eq. (4.23), we see that to finally obtain the free energy expansion in powers of $\langle J_z \rangle$, up to n-th order, we need to consider only the terms $\langle J_z \rangle^\alpha \delta^\beta$ where $\alpha + 2\beta \leq n$. Finally, by

substituting δ from Eq. (4.23) into Eq. (4.22), we obtain the power series expansion of the free energy in the form:

$$\mathcal{F}_{\rm MF} = C_0 + C_2 \langle J_z \rangle^2 + C_4 \langle J_z \rangle^4 + C_6 \langle J_z \rangle^6 . \tag{4.24}$$

In the second order transition region, the condition $C_2 = 0$ with $C_4 > 0$ parametrizes the phase boundary. The equations $C_2 = C_4 = 0$ gives the condition for the location of the tricritical point. In the regime where $C_4 < 0$, the condition $C_2 = 0$ gives the supercooling limit. The first order phase transition boundary is located where the free energy has the same value at both local minima. Increasing the value of the control parameters, T and B_x, above the critical value, until the second (nontrivial) local minimum of $\mathcal{F}_{\rm MF}$ vanishes, gives the superheating limit.

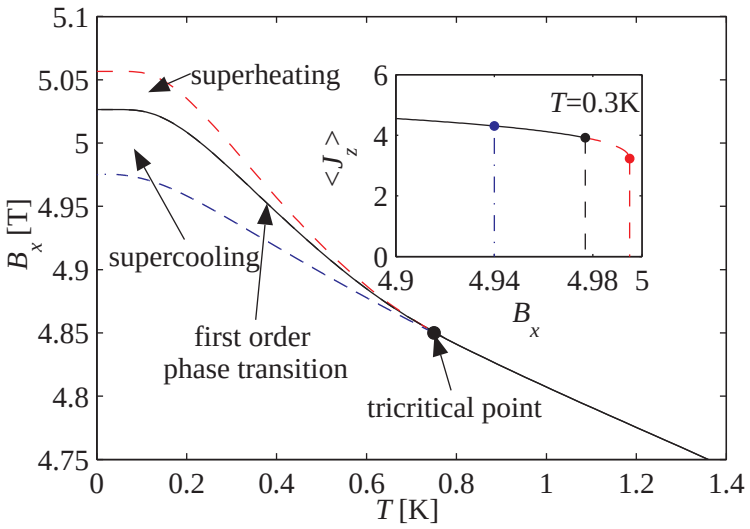

Figure 4.7: Tricritical behaviour of $Dy(OH)_3$. The continuous line marks the phase boundary. The dot indicates the location of the tricritical point. The upper and lower lines (dashed) are the limits of the superheating and supercooling regimes, respectively. As an example, the inset shows the order parameter $\langle J_z \rangle$ vs B_x, at the temperature T =0.3 K. For this temperature, the phase transition occurs at $B_x \approx 4.98$ T. The upper dashed extension of the solid line corresponds to the superheating limit. The dash-dotted line to the left of the tricritical point shows the transition at the supercooling limit.

The location of the tricritical point is $T_c^{\rm TCP}$ =0.75 K, $B_x^{\rm TCP}$ =4.85 T. We show in Fig. 4.7 the first and the second order transition phase boundary; the tricritical

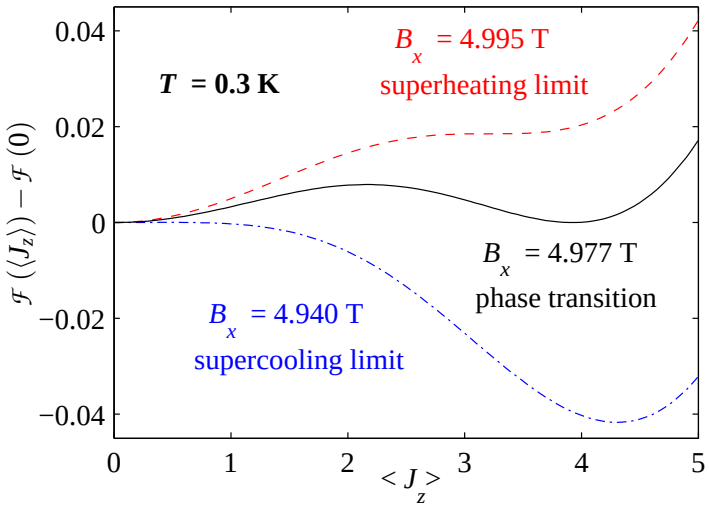

Figure 4.8: Free energy vs average magnetic moment $\langle J_z \rangle$ at the temperature of 0.3 K. The free energy at the first order phase transition is plotted with continuous line. The upper (dashed) line shows the free energy at the boundary of the superheating limit. The lower (dot-dashed) line shows the free energy when the system passes through the supercooling limit. All the plots show the free energy displaced by a constant chosen such that their shape can be compared.

point is marked with a dot. In the first order transition regime, the superheating and supercooling limits are also plotted. $\langle J_z \rangle$ ceases to be a small parameter for values of T and B_x 'away' from the tricritical point. Thus, the two upper curves in the phase diagram of Fig. 4.7 are determined from a numerical search for both local minima of the exact mean-field free energy in Eq. (4.15) without relying on a small $\langle J_z \rangle$ and $\delta(\langle J_z \rangle)$ expansion. The supercooling limit is calculated from the series expansion (4.24) and determined by the condition $C_2 = 0$.

In the inset of Fig. 4.7, we show the average magnetic moment, $\langle J_z \rangle$, as a function of the transverse field, at the temperature of 0.3 K. The dots and the dashed lines mark the supercooling limit, first order phase boundary and the superheating limit, in order of increasing B_x. The shape of the free energy at these three characteristic values of the magnetic field, B_x, at temperature of 0.3 K, is shown in Fig. 4.8.

In Fig. 4.8, we plot the free energy as a function of $\langle J_z \rangle$, where $\langle J_x \rangle$ is minimizing $\mathcal{F}_{\rm MF}$ as a function of $\langle J_z \rangle$ at $T = 0.3$ K. Free energy at the phase transition ($B_x \approx$ 4.977 T) is plotted with a continuous line. The dashed and dot-dashed plots show

free energy at the superheating and supercooling limits, at $B_x \approx 4.995$ T and $B_x \approx 4.940$ T, respectively. The free energy clearly shows the characteristic structure (e.g. barrier) of a system with a first order transition. It would be interesting to investigate whether the real $Dy(OH)_3$ material exhibits such a B_x-induced first order PM to FM transition at strong B_x. In the event that the transition is second order down to $T = 0$ and $B_x = B_x^c$, $Dy(OH)_3$ would offer itself as another material to investigate transverse field induced quantum criticality (see 4^{th} item in the list at the beginning of Section IV). However, a quantitative microscopic description at strong B_x would nevertheless require that the contribution of the lowest pairs of excited crystal field states be taken into account.

One may be tempted to relate the existence of a first order transition in $Dy(OH)_3$, on the basis of Eq. (4.22), with two expansion parameters $\langle J_z \rangle$ and δ, to the familiar problem where a free-energy function, $\mathcal{F}(m, \epsilon)$, of two order parameters m and ϵ,

$$\mathcal{F}(m, \epsilon) = \frac{a}{2}m^2 + \frac{|b|}{4}m^4 + \frac{|c|}{6}m^6 + \frac{K}{2}\epsilon^2 - g\epsilon m^2$$

displays a first order transition when $g^2/K > b/2$. However, we have found that this analogy is not useful and the mechanism for the first order transition is not trivially due to the presence of two expansion parameters, $\langle J_z \rangle$ and δ, in the expansion (4.22). It is rather the complex specific details of the crystal field Hamiltonian for $Dy(OH)_3$ that are responsible for the first order transition. For example, at a qualitative level, a first order transition still occurs even if $\delta(\langle J_z \rangle)$, in Eq. (4.16), is taken to be 0, for all values of $\langle J_z \rangle$.

4.4.2 The effect of longitudinal magnetic field and exchange interaction on the existence of first order transition in $Dy(OH)_3$

Having found that the PM to FM transition may be first order in $Dy(OH)_3$ at large B_x (low T), it is of interest to investigate briefly two effects of physical relevance on the predicted first order transition. Firstly, since the transition is first order from $0 \leq T \leq T^{\text{TCP}}$, one may ask what is the critical *longitudinal* field, B_z, required to push the tricritical point from finite temperature down to zero temperature. Focusing on

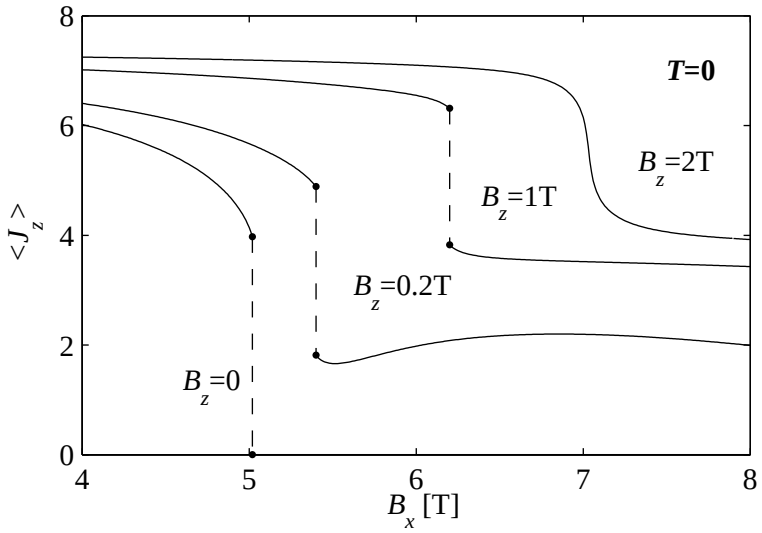

Figure 4.9: Average magnetic moment, $\langle J_z \rangle$, vs transverse magnetic field, B_x, at $T = 0$, $J_{\rm ex} = 0$, for different values of longitudinal magnetic field, B_z.

the CFP of Scott *et al.* from Refs. [173, 176, 177, 180], we find that a sufficiently strong magnetic field, B_z, applied along the longitudinal z direction destroys the first order transition, giving rise to an end critical point. We plot in Fig. 4.9 the magnetization, $\langle J_z \rangle$, as a function of B_x for different values of B_z at $T = 0$. We see that a critical value of B_z is reached between 1 T and 2 T, where the first order transition disappears, giving rise to an end critical point at $T = 0$. Hence, assuming that the low-temperature B_x-driven PM to FM transition is indeed first order in $Dy(OH)_3$, the results of Fig. (4.9) indicate that the critical longitudinal field for a quantum critical end point is easily accessible, using a so-called vector magnet (i.e. with tunable horizontal, B_x, and vertical, B_z, magnetic fields) [189].

It was discussed in Section 4.2 (Fig. 4.4) that the (yet undetermined) nearest-neighbour exchange interaction, $J_{\rm ex}$, affects the zero B_x critical temperature, T_c, and the zero temperature critical transverse field, B_x^c. It is also of interest to explore what is the role of $J_{\rm ex}$ on the location (temperature and transverse field) of the tricritical point in $Dy(OH)_3$.

We plot in Fig. 4.10 the temperature corresponding to the tricritical point (TCP) as a function of antiferromagnetic exchange and, in the upper inset, the location of the TCP on the phase diagram is presented. The location of the TCP was calculated using

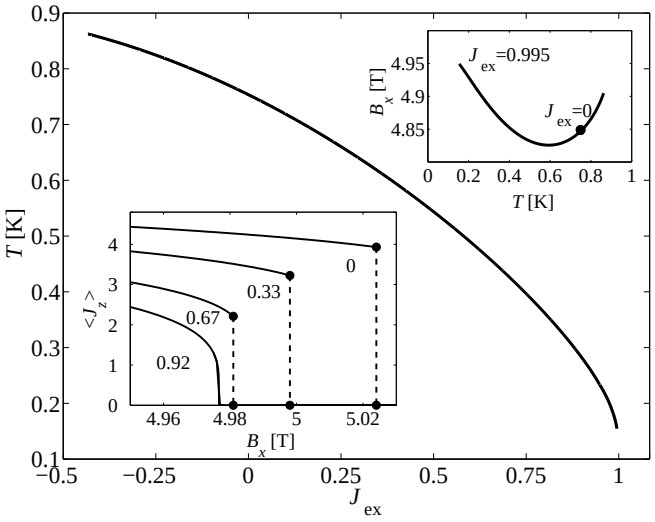

Figure 4.10: Temperature corresponding to the TCP as a function of nearest-neighbour exchange constant $J_{\rm ex}$. The upper inset shows position of the TCP in the phase diagram plane for the same range of exchange constant as in the main plot. For an exchange $J_{\rm ex} > J_{\rm ex}^{\rm 2nd}$, with $J_{\rm ex}^{\rm 2nd} = 0.995$, the tricritical point at $T > 0$ ceases to exist. The lower inset shows average magnetic moment $\langle J_z \rangle$ vs transverse field B_x at temperature T =0, for the shown values of exchange constant $J_{\rm ex}$.

the semi-analytical expansion described in Section 4.4.1. We found that the system ceases to exhibit a first order transition at nonzero temperature when the value of nearest neighbour exchange constant, $J_{\rm ex}$, exceeds $J_{\rm ex}^{\rm 2nd} = 0.995$. At B_x=0, the critical temperature calculated with the value of exchange constant $J_{\rm ex}$=0.995 is 4.09 K. In the lower inset of Fig. 4.10 we plot the average magnetic moment, $\langle J_z \rangle$, as a function of B_x at zero temperature, for different values of $J_{\rm ex}$. The top inset shows a parametric plot of the position of the TCP in the (T, B_x) plane as $J_{\rm ex}$ is varied.

4.5 Summary

We have presented a simple mean-field theory aimed at motivating an experimental study of transverse-field-induced phase transitions in the insulating rare-earth Ising $RE(OH)_3$ (RE=Dy, Ho) uniaxial dipolar ferromagnetic materials.

In setting out to perform the above calculations, we were mostly motivated in

identifying a new class of materials as analogous as possible to $LiHo_xY_{1-x}F_4$, where interesting phenomena, both in zero and nonzero applied transverse field B_x, have been observed. In particular, we were interested in finding compounds where a systematic comparison between a non-Kramers (e.g. Ho^{3+}) and a Kramers (e.g. Dy^{3+}) variant could be investigated. From our study, we are led to suggest that an experimental study of the $Dy_xY_{1-x}(OH)_3$ and $Ho_xY_{1-x}(OH)_3$ materials could bring new pieces of information on the physics that may be at play in $LiHo_xY_{1-x}F_4$ and to ascertain if that physics is unique to $LiHo_xY_{1-x}F_4$ or if it also arises in other diluted dipolar Ising ferromagnets.

Depending on the details of the Hamiltonian characterizing $Dy(OH)_3$, it may be that a first order transition occurs at low temperature (large B_x), due to the admixing between the ground doublet and the low-lying crystal field states that is induced by the spin-spin interactions. For the same reason, we find that $Dy(OH)_3$ is not well described by an effective microscopic transverse field Ising model (TFIM). On the other hand, $Ho(OH)_3$ appears to be very well characterized by a TFIM and, therefore, constitutes a highly analogous variant of $LiHoF_4$. $Tb(OH)_3$ is also very well described by a TFIM. Unfortunately, in that case, the critical B_x, B_x^c, appears prohibitively large to be accessed via in-house commercial magnets.

We hope that our work will stimulate future systematic experimental investigations of these materials and, possibly, help shed some light on the rather interesting problems that pertain to the fundamental nature of classical and quantum critical phenomena in disordered dipolar systems and which have been raised by nearly twenty years of study of $LiHo_xY_{1-x}F_4$.

The Ising diluted dipolar spin glass has been extensively studied experimentally, in $LiHo_xY_{1-x}F_4$ [7, 8, 19, 118], and numerically [120–122]. Similar studies can likely be in the context rare-earth hydroxides. It is surprising that the problem of Heisenberg diluted dipolar spin glass has not been investigated yet. A strong Ising anisotropy is quite rare in nature and many magnetic materials are well described by isotropic, Heisenberg Hamiltonians. Example Heisenberg materials that, sufficiently diluted, can be described by dipolar Heisenberg Hamiltonian and are likely to exhibit a spin-glass phenomenology are $(Gd_xY_{1-x})_2Ti_2O_7$, $(Gd_xY_{1-x})_2Sn_2O_7$ and $(Gd_xY_{1-x})_3Ga_5O_{12}$. In the next chapter we numerically study a diluted dipolar Heisenberg spin glass on the simple cubic lattice. At sufficient dilution, the lattice geometry is unimportant and

we believe that a similar result would obtained if different lattice is used, such as pyrochlore or garnet lattices that pertain to $(Gd_xY_{1-x})_2Ti_2O_7$ or $(Gd_xY_{1-x})_2Sn_2O_7$ and $(Gd_xY_{1-x})_3Ga_5O_{12}$, respectively. We perform a finite-size analysis of the spin-glass correlation length and spin-glass susceptibility. Our studies provide a compelling evidence of an equilibrium spin-glass transition. We estimate values of the critical exponents, ν and η, and we compare them with the exponents obtained in experimental and numerical studies of different spin-glass materials and models.

Chapter 5

Spin-Glass Transition in a Diluted Dipolar Heisenberg Model

In this chapter, by means of parallel tempering Monte Carlo simulation [153, 154], we study a system consisting of diluted classical Heisenberg dipoles randomly placed on the simple cubic lattice. The character of the dipolar interaction can be either ferromagnetic or antiferromagnetic depending on the spatial arrangements of the interacting dipoles. In dipolar systems on fully occupied lattices, the character of a long-range ordered phase depends on the lattice geometry. For example, a system of dipoles placed on the body centered cubic or on the face centered cubic lattice orders ferromagnetically, while the ground state of dipoles on the simple cubic lattice is antiferromagnetic. In either case, in the ground-state configuration, both ferromagnetically and antiferromagnetically coupled dipole pairs are present; hence, some of the interactions are frustrated. If the spatial arrangement of the dipoles is random, ferromagnetic and antiferromagnetic bonds occur randomly. Thus, a spatially disordered dipolar system is randomly frustrated, and, if the amount of disorder is sufficient, the spin-glass phase occurs.

Systems with magnetic order induced by dipolar interactions alone are somewhat rare in nature. In typical magnets, the interaction that is responsible for formation of a long-range order is usually the short-range exchange interaction. A low temperature phase, that is induced by the dipolar interaction, can occur when the nearest-neighbour exchange is geometrically frustrated, and as such does not produce long-range order;

hence, at the temperatures much lower that the exchange interaction energy scale, weak interactions such as the dipolar interaction induce ordering. Another way in which ordering can be controlled by the dipolar interactions is to dilute the system such that there are few pairs of spins separated by the nearest-neighbour distance. As the spatially disordered dipolar system is randomly frustrated, a diluted lattice system of magnetic dipoles can either have a tendency to long-range order, in the case of weak disorder, or may enter the spin-glass phase, if the amount of randomness is large. One can also think of systems of interacting macroscopic magnetic dipoles, each one corresponding to a magnetic nanoparticle that consist of a single magnetic domain, where quantum effects such as exchange interaction are not present at the considered length scale.

Some dipolar Ising spin-glass systems were studied experimentally and numerically. Experimental studies of magnetic nanoparticles, both ferromagnetic [114, 190] and antiferromagnetic [191], indicate a spin-glass-like behaviour. In Ref. [114] and Ref. [190] ferromagnetic magnetite, Fe_3O_4, nanoparticles of average size around 5nm have been studied. A magnetic moment of such particles is around $3000\mu_B$. Such a large magnetic moment brings the temperature scale from miliKelvin, as in the case of interactions of single ion dipoles, to the order of several Kelvin [192]. Each nanoparticle consists of a single magnetic domain and develops an easy axis due to anisotropy in the shape of the particle. The nanoparticles are dispersed in a liquid solvent. When the solvent freezes, the directions of the easy axes are frozen randomly. Numerically, a spin-glass freezing in a system of random easy-axis Ising dipoles has been found in local mean-field studies [192] and in equilibrium Monte Carlo simulations [115, 116]. The Monte Carlo studies in Ref. [115] and in Ref. [116] pertain to systems of random easy-axis Ising dipoles placed on a fully unoccupied simple cubic lattice and on a diluted simple cubic lattice, respectively.

A well studied example of a diluted dipolar Ising SG in a crystalline system is $LiHo_xY_{1-x}F_4$. Ho^{3+} ions in the crystalline environment of $LiHoF_4$ constitute strongly uniaxial, Ising-like, magnetic dipoles. Numerous experimental studies [7, 8, 118, 119] show that, at sufficiently high dilution, $LiHo_xY_{1-x}F_4$ exhibits a spin-glass phase, but other experiments suggested that the spin-glass transition is absent [21, 193]. In Chapter 3, the diluted magnetic material $LiHo_xY_{1-x}F_4$ has been studied numerically using local mean-field theory. The first Monte Carlo studies of diluted dipolar Ising model

suggested that there is no spin-glass transition in this system [121, 122], but recent large-scale Monte Carlo simulations [120], using the parallel tempering technique and a finite-size scaling analysis of the spin-glass correlation length, ξ_L, show compelling evidence of an equilibrium transition to the spin-glass phase.

Both experimental and numerical studies of the diluted dipolar Heisenberg spin glass are still missing. Similarly to the Ising-like material $LiHo_xY_{1-x}F_4$, Heisenberg-like magnetic materials with relatively strong dipolar interactions, can be diluted to diminish the effect of the exchange interaction and to generate random frustration. Examples of candidate materials are diluted variants of geometrically frustrated gadolinium compounds such as $(Gd_xY_{1-x})_2Ti_2O_7$ and $(Gd_xY_{1-x})_2Sn_2O_7$ or $(Gd_xY_{1-x})_3Ga_5O_{12}$ that were introduced in Section 1.2.1 and 1.2.3, respectively. With a half-filled 5f electronic shell Gd^{3+} ion is almost an ideal realisation of an isotropic, Heisenberg-like, magnetic dipole.

It is interesting to compare diluted dipolar Heisenberg spin glasses, where the interaction is anisotropic, with extensively studied canonical spin glasses [41, 42], where Heisenberg-like spins are interacting via isotropic RKKY coupling [43–45]. A comparison of diluted dipolar Heisenberg spin glass with Ising spin glass, either interacting via short-range exchange interaction like $Fe_{0.5}Mn_{0.5}TiO_3$ [108, 109], or with diluted dipolar Ising spin glass like $LiHo_xY_{1-x}F_4$[7, 8, 118] is also of interest. Numerically, results of simulations of a diluted dipolar a Heisenberg spin glass can be compared with numerical studies of the Heisenberg Edwards-Anderson model [99, 101, 102, 104–107], Ising Edwards-Anderson model [92–96, 194], or with the recent study of a diluted dipolar Ising SG [120].

At high dilution, the lattice structure should be irrelevant and data obtained for different systems should be directly comparable. Here we consider the simplest possible geometry - we study dipoles randomly placed in the sites of the simple cubic lattice. We provide Monte Carlo data that supports the scenario that in the low dipole concentration regime, of the diluted dipolar Heisenberg model there is an equilibrium phase transition to a spin-glass phase. We calculate the critical exponents ν and η for the spin-glass transition in the model studied. Unfortunately, the exponents we obtained do not agree with those in the literature for Heisenberg or Ising spin glasses studied experimentally [42] and by simulations [94, 96, 105, 107]. This may be due to significant scaling corrections. Effects of significant scaling corrections were

also observed in simulations of Heisenberg EA SG [99, 101, 102, 104–107]. Here the problem of scaling correction is exacerbated by the severe restriction of the system sizes we are able to study that is due to the computationally expensive summation of the long-range interaction and the very slow equilibration of the system studied.

The rest of this chapter is organised as follows. In Section 5.1, we define the model and MC method employed. In Section 5.2, we introduce the observables calculated in the simulation. In Section 5.3, we present and discuss our results. Our conclusions are presented in Section 5.4. Some auxiliary data and technical details of the simulations are discussed in Appendices. In Appendix B, magnetization and staggered magnetization are discussed. In Appendix C, we discuss the issue of a self-interaction term that must be taken into account when periodic boundary conditions are used in a long-range interacting system. And finally, in Appendix D, we discuss the Ewald summation technique. The parallel tempering technique is explained very briefly in the text of this chapter; for a more complete introduction to Monte Carlo methods and the parallel tempering technique, the reader should refer to Chapter 2.

5.1 Model and method

We consider a system that consist of classical three-component (n=3) Heisenberg dipoles, that are free to point in any direction. The dipoles are randomly distributed on the sites of 3D simple cubic (SC) lattice. The Hamiltonian is of the form

$$\mathcal{H} = \frac{1}{2}\epsilon_d \sum_{i,j,\mu,\nu} \frac{\delta^{\mu\nu} r_{ij}^2 - 3 r_{ij}^{\mu} r_{ij}^{\nu}}{r_{ij}^5} S^{\mu}(\boldsymbol{r}_i) S^{\nu}(\boldsymbol{r}_j). \tag{5.1}$$

$S^{\mu}(\boldsymbol{r}_i)$ denotes a Cartesian component of a classical spin vector, $\boldsymbol{S}(\boldsymbol{r}_i)$, that is of unit length, $|\boldsymbol{S}(\boldsymbol{r}_i)| = 1$. The energy scale of dipolar interactions is set by $\epsilon_d = \frac{\mu_0 \mu^2}{4\pi a^3}$, where μ is the magnetic moment of the spin $\boldsymbol{S}(\boldsymbol{r}_i)$, a is the lattice constant and μ_0 denotes vacuum permeability. In this chapter, the temperature is expressed in units of ϵ_d. The summation is carried over all occupied lattice site pairs and over the vector components of the spin, $\mu, \nu = x$, y and z. The factor $1/2$ is included to avoid double counting. $\boldsymbol{r}_i$ and $\boldsymbol{r}_j$ are the positions of ions labeled i and j, respectively and their distance, $|\boldsymbol{r}_{ij}| = |\boldsymbol{r}_j - \boldsymbol{r}_i|$, is measured in the units of nearest-neighbour distance, a.

We impose periodic boundary conditions. In the case of long-range interactions, it means that to calculate pairwise interaction we sum over an infinite array or dipole images replicated with a periodicity set by the dimensions of the simulation box. It is convenient to consider the interaction constant for spins i and j as a 3 by 3 matrix, $\hat{L}_{ij}$. Matrix elements of $\hat{L}_{ij}$ are denoted $L_{ij}^{\mu\nu}$, and for dipoles separated by a vector $\boldsymbol{r}_{ij}$, are given by the sum,

$$L_{ij}^{\mu\nu} = \sum_{\boldsymbol{n}} \frac{\delta^{\mu\nu} \left|\boldsymbol{r}_{ij} + \boldsymbol{n}\right|^2 - 3 \left(\boldsymbol{r}_{ij} + \boldsymbol{n}\right)^{\mu} \left(\boldsymbol{r}_{ij} + \boldsymbol{n}\right)^{\nu}}{\left|\boldsymbol{r}_{ij} + \boldsymbol{n}\right|^5}, \tag{5.2}$$

over vectors $\boldsymbol{n}$ of the SC lattice with the unit cell being the size of a cubic simulation box, L; L is an integer expressing the size of the simulation cell in units of the lattice constant, a. Vectors $\boldsymbol{n}$ are of the form $\boldsymbol{n} = kL\hat{x} + lL\hat{y} + mL\hat{z}$, where k, l, m are integers and $\hat{x}$, $\hat{y}$ and $\hat{z}$ are unit vectors of the SC lattice. Note that in the simulation, care must be taken to correctly include the self-interaction terms (see Appendix C). The self-interaction terms originate from the interaction of a spin with its periodic images replicated outside the simulation cell. The lattice summation (5.2) is performed using the Ewald technique [76–79]; the details of which are given in Appendix D. The calculated Ewald sums correspond to a summation over a long cylinder, such that the demagnetization field is zero. Using interaction constants defined in Eq. (5.2), the Hamiltonian can be written in the form

$$\mathcal{H} = \frac{1}{2}\epsilon_d \sum_{i,j} \boldsymbol{S}(\boldsymbol{r}_i)\hat{L}_{ij}\boldsymbol{S}(\boldsymbol{r}_j). \tag{5.3}$$

The summation in Hamiltonian (5.3) includes only the spins enclosed in the simulation cell, while the presence of spins outside the simulation box is approximated by periodic images of the spin in the simulation cell, and this effect is included in the interaction constants, given by matrices $\hat{L}_{ij}$.

Our simulation follows the standard single spin-flip Metropolis Monte Carlo algorithm with parallel tempering (PT) [153, 154] (see Section 2.2). PT was reported to significantly speed up the equilibration in slowly relaxing systems [153, 154]. In this technique, we simultaneously simulate N_T thermal replicas - the copies of the system with the same spatial disorder, at different temperatures. In each thermal replica,

the simulation begins from a different random initial spin configuration. At every 10 local update sweeps, a configuration swap among thermal replicas is attempted with acceptance probability preserving the detailed balance condition. The frequency of tempering is chosen to balance the two factors. As thermal tempering is computationally inexpensive, it is desirable to perform replica swap attempts often, to promote traveling of the replicas along the temperature axis. But, on the other side, after a configuration exchange, a sufficient number of local moves have to be performed to let the new configuration evolve at given temperature; in the case of higher temperature - to overcome free energy barriers. If the subsequent tempering is attempted to soon, the two configurations can be swapped back, and in that case no evolution of a trapped state out of local energy minimum would be made. The number of thermal replicas, N_{T}, and simulated temperatures, T_α, where $\alpha = 1, \ldots, N_{\mathrm{T}}$, are chosen to yield a sufficiently high and temperature independent PT configuration swap acceptance rate, i. e. not less than 50%. This is achieved by choosing T_α to satisfy the formula [104] (see Section 2.2.2)

$$(T_\alpha - T_{\alpha-1})/T_\alpha = 1/\sqrt{C_V\, N}, \tag{5.4}$$

were N denotes the number of dipoles. The specific heat per spin, C_V, used in Eq. (5.4) was measured in a preliminary simulation of the smallest system size, with uniformly distributed temperatures.

The Metropolis single-spin moves are attempted within a temperature-dependent solid angle, where the angle is self-consistently chosen such that the acceptance rate is close to 50%. To carry out a spin move we choose a coordinate system with the $\hat{z}$ axis along the current spin direction, and randomly choose a polar angle, θ, and azimuthal angle, ϕ. In order to obtain a uniform distribution of random points on a unit sphere, one needs to draw ϕ and $z = \cos(\theta)$ from a uniform probability distribution, such that $\phi \in (0, 2\pi)$ and $z \in (-1, 1)$. Here, to maintain the desired acceptance rate, the move is restricted to a limiting angle, $\theta_{\max}$, relative to the initial spin direction; hence, the choice of z is restricted to $z \in (1 - z_{\max}, 1)$, where $z_{\max} = \cos(\theta_{\max})$. To obtain $z_{\max}$ such that the acceptance rate, p_{acc}, is 50%, during each 100 MCS p_{acc} is measured, and afterwards $z_{\max}$ is adjusted. If p_{acc} is lower than 0.5, $z_{\max}$ should be decreased; in the opposite case, when $p_{\mathrm{acc}} > 0.5$, $z_{\max}$ should be increased, while, formally, for $p_{\mathrm{acc}} = 0.5$ $z_{\max}$ does not change. Such update of $z_{\max}$ can be obtained when multiplying

the current value of $z_{\max}$, $z_{\max}^{(\mathrm{old})}$, by $2p_{\mathrm{acc}}$; hence, a new value of $z_{\max}$ is calculated according to the formula $z_{\max}^{(\mathrm{new})} = 2p_{\mathrm{acc}} z_{\max}^{(\mathrm{old})}$, with the restriction $z_{\max}^{(\mathrm{new})} \in (0.001, 2)$. After choosing ϕ and θ, that is a new spin direction in the coordinates relative to the initial spin direction, a transformation to the global coordinate system is performed.

We simulated two dipole concentrations, x=0.0625 and x=0.125, and for each concentration we consider 4 system sizes varying between around 30 and 200 dipoles, which is the largest size that we were able to equilibrate. To perform the necessary disorder average (see Section 5.2), we considered at least 1000 disorder samples. The parameters of the simulations are collected in Table 5.1. To generate results reported here, we used in total around $3 \cdot 10^5$ hours (∼35 years) of CPU time on AMD Opteron, 2.6 GHz. The statistical error is based on disorder sampling fluctuation and is calculated using standard jackknife method [150, 195, 196].

L	N_{dip}	N_{samp}	N_{eq}	N_{prod}	N_{T}	$T_{\min}$	$T_{\max}$
x=0.0625							
8	32	5000	$5{\cdot}10^5$	$5{\cdot}10^5$	16	0.05	0.1763
10	62,63	2000, 2000	$2{\cdot}10^6$	10^6	16	0.05	0.1763
12	108	1200	10^7	10^6	16	0.05	0.1763
14	172	1000	10^7	10^6	16	0.05	0.1763
x=0.125							
6	27	3000	$5{\cdot}10^5$	$5{\cdot}10^5$	16	0.0750	0.2869
8	64	2000	$2{\cdot}10^6$	10^6	16	0.0750	0.2869
10	125	1500	$2{\cdot}10^6$	10^6	16	0.0800	0.2811
12	216	1000(+200)	$5{\cdot}10^6(2{\cdot}10^7)$	10^6	16	0.0850	0.2787

Table 5.1: Parameters of the Monte Carlo simulations for two dipole concentrations, x. L is the linear size of the simulation box; N_{dip} is the number of spins, and N_{samp} denotes number of disorder samples. N_{eq} and N_{prod} are the number of MCS in the equilibration and measurement phase of the simulation, respectively. N_{T} is the number of thermal replica and $T_{\min}$, $T_{\max}$ are the lowest and highest temperatures in PT scheme. For L=10, x=0.0625, to obtain desired x, two numbers of dipoles were simulated, and the disorder average was taken over the results for both $N_{\mathrm{dip}} = 62$ and $N_{\mathrm{dip}} = 63$. For L=12, x=0.125 the numbers given in round brackets pertain to a subset of disorder replicas simulated longer, to monitor equilibration; the long equilibration time results for these replicas were included in the disorder averaging.

To reduce the number of performed lattice sums, for each lattice site k we calculated

the local interaction field,

$$\boldsymbol{H}_k = \sum_{j \neq k} \hat{L}_{kj} \boldsymbol{S}_j, \tag{5.5}$$

and update it only when the spin change is accepted. Having $\boldsymbol{H}_k$ available, the computational cost of calculating the energy from Hamiltonian (5.3) is of order of N, and not N^2, and the computational cost of calculating the energy change after a single spin move is $\mathcal{O}(1)$; hence, rejected Metropolis updates are computationally inexpensive.

In was reported that the autocorrelation time can be substantially decreased in simulations of Heisenberg SG by performing computationally inexpensive overrelaxation (microcanonical) spin updates [155, 156]. Here, in the case of long-range interaction, computational cost of overrelaxation moves would not be less then the cost of Metropolis spin flips, as most of the time is spent on updating the local interaction field (5.5), and the local interaction field has to be updated both after a Metropolis spin flip and after an overrelaxation move. Furthermore, it is worth to note that, in a general case of non-cubic geometry, in the case of periodic boundary condition, where the self-interaction term is present (see Appendix C), an overrelaxation move does not preserve the energy (see Section 2.2.3).

In the case of the nearest neighbour Heisenberg SG model, it is more efficient to use the heatbath algorithm [157–159] for local spin updates. In the heatbath algorithm, the computational cost of rejected spin moves is avoided. Here the benefit of using the heatbath algorithm would not be high because the computational cost of rejected spin update attempts is negligible in comparison with the computational cost of accepted updates which require calculating the lattice sums in Eq. (5.5). Also, similarly to the case of overrelaxation moves, if the geometry of the simulation cell is not cubic, the self-interaction term in the Hamiltonian introduced by the periodic boundary conditions makes heatbath algorithm impractical (see Appendix C and Section 2.2.4). To keep our method general and to obtain results that are the easiest to compare with possible future simulation with different lattice geometries, we decided to not use the heatbath algorithm nor overrelaxation moves in this work.

5.2 Physical Quantities

In glassy systems, the order parameter can be defined as an overlap between two independent, identical copies of the system. In the case of 3D Heisenberg spins, the overlap can be calculated for 9 combinations of vector components μ and ν, where $\mu, \nu = x, y, z$. We write

$$q^{\mu\nu}(\boldsymbol{k}) = \frac{1}{N} \sum_{\boldsymbol{r}} S_{\mu}^{(\alpha)}(\boldsymbol{r}) S_{\nu}^{(\beta)}(\boldsymbol{r}) \exp(i\boldsymbol{k} \cdot \boldsymbol{r}), \tag{5.6}$$

where α and β denote different *real* replicas that are simulated independently copies of the system with the same random disorder. The wave-vector-dependent SG order parameter is

$$q(\boldsymbol{k}) = \sqrt{\sum_{\mu,\nu} |q^{\mu\nu}(\boldsymbol{k})|^2}. \tag{5.7}$$

Traditionally the finite size scaling (FSS) analysis of SG simulation data is based on calculation of Binder ratios [151, 197, 198], which for an n=3 Heisenberg SG is defined as [105, 107]:

$$U_L = \frac{1}{2} \left(11 - 9 \frac{[\langle q(0)^4 \rangle]}{[\langle q(0)^2 \rangle]^2} \right), \tag{5.8}$$

where $\langle \ldots \rangle$ denotes thermal averaging and $[\ldots]$ is a disorder average. The numerical factors in Eq. (5.8) are chosen such that at $T = \infty$, assuming Gaussian distribution of $q(0)$, $U_L = 0$, and at $T = 0$, where $q(0)$ is not fluctuating, U_L is 0. Being dimensionless, the quantity U_L is expected to display finite-size scaling (FSS) properties described by [95]

$$U_L = \tilde{X}(L^{1/\nu}(T - T_g)), \tag{5.9}$$

where scaling function $\tilde{X}$ is an analytic function of its argument, [1] and ν is the universal correlation length exponent, such that there is no system size dependence outside the the argument of the scaling function. Many recent works report that in the case of disordered systems, a FSS analysis can be achieved when considering finite

[1] We do not call the function $\tilde{X}$ universal because it implicitly contains a non-universal factor, as opposite to the case when a scaling formula is written as $U_L = \tilde{X}'(AL^{1/\nu}(T - T_g))$, with a non-universal constant, A, given explicitly and $\tilde{X}'$ being a universal scaling function [95, 199].

size correlation length [94, 104, 120, 200], ξ_L, while U_L may not cross due to a lack of unique ground state [200] or because it is too noisy [94], being a quantity that requires evaluation of a four-point correlation function, as opposite to ξ_L, that is defined using a two-point correlation function. We define the SG susceptibility [41, 94, 104] as

$$\chi_{\mathrm{SG}}(\boldsymbol{k}) = N\left[\left\langle q(\boldsymbol{k})^2\right\rangle\right]. \tag{5.10}$$

Assuming an Ornstein-Zernike form for the SG susceptibility [201],

$$\chi_{\mathrm{SG}}(\boldsymbol{k}) \propto 1/(|\boldsymbol{k}|^2 + \xi^{-2}), \tag{5.11}$$

where $|\boldsymbol{k}| \ll 1/\xi$, we define a finite-size SG correlation length [94, 202], ξ_L, via

$$\xi_L = \frac{1}{2\sin(k_{\mathrm{min}}/2)}\left(\frac{\chi_{\mathrm{SG}}(0)}{\chi_{\mathrm{SG}}(\mathbf{k}_{\mathrm{min}})} - 1\right)^{1/2}. \tag{5.12}$$

The correlation length divided by the system dimension, ξ_L/L, similarly to the Binder ratio, is a dimensionless quantity and is expected to scale according to the relation [94, 95, 104, 107]

$$\xi_L/L = \tilde{Y}(L^{1/\nu}(T - T_g)), \tag{5.13}$$

where $\tilde{Y}$ is a scaling function. Hence, at a putative SG transition temperature, T_g, ξ_L/L is expected to be size independent.

5.3 Monte Carlo Results

A system of dipoles in a fully occupied SC lattice orders antiferromagnetically [52]. To rule out a long-range order in the simulated diluted systems, we calculated magnetization, M, and staggered magnetization, M_{stag}. Both M and M_{stag} are small and decrease with increasing system size. This indicates that their nonzero value is a finite-size effect and not a result of long-range ordering. More detailed discussion of M and M_{stag} is given in Appendix B.

We plot in Fig. 5.1 the temperature dependence of the Binder ratio, U_L, for x=0.125 and x=0.0625, for different system sizes. The Binder ratio curves do not

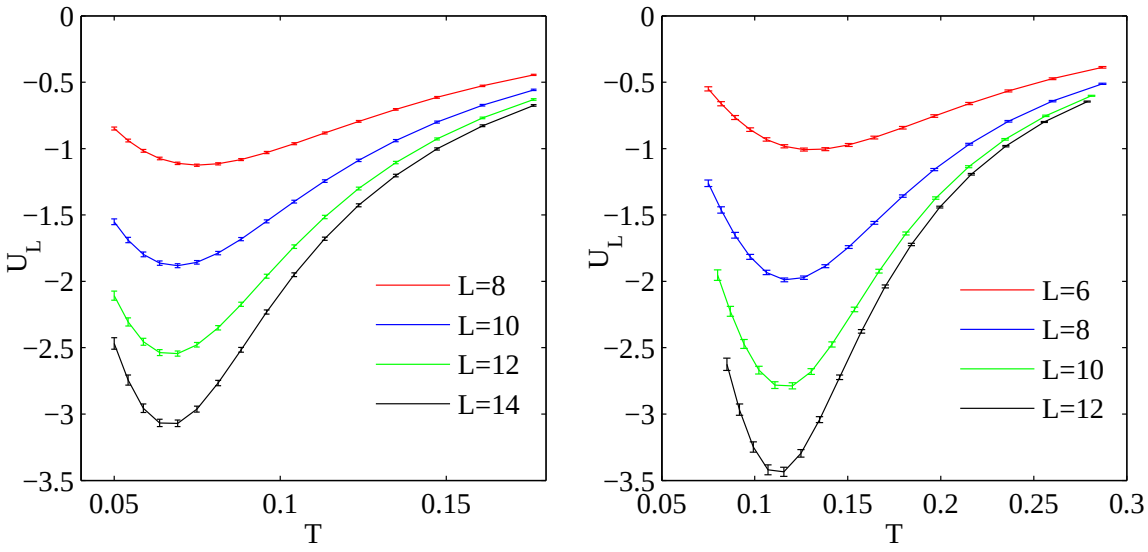

Figure 5.1: Binder ratios for x=0.0625 (left) and x=0.125 (right) as a function of temperature.

cross; hence, they do not provide indication of phase transition. Also, in some studies of other models, a crossing of the Binder ratios was not found, while the scaling invariance of the finite size correlation length was established, indicating a transition to a SG phase. The magnitude of scaling corrections is different for different observables and it is larger for binder ratio than for correlation length. In the simulation of Ising EA SG [94, 95] U_L do cross, but the scaling correction are larger for U_L than for ξ_L/L [94]. In the case of site diluted EA Ising SG [194], where scaling corrections are large in comparison with other Ising SG models, while ξ_L/L plots are crossing with large shifts between system sizes, the U_L plots do not cross, but merge at low temperature. A similar effect can be seen in the studies of diluted dipolar SG [120] - U_L plots do not cross, but they have a tendency to merge at low T, while ξ_L/L plots intersect. In the case of Heisenberg EA SG [105–107], the behaviour of spin and chirality Binder ratios differs, but both do not cross, while in correlation length shifts between system sizes shows that scaling corrections are large. It is worthwhile to note that the form of Binder ratio plots, characterized by a dip to a negative value in the proximity of T_g, resembles the Binder ratio plots for chirality (and not spin) in the Heisenberg EA model [105, 107], or the Binder ratio plots for spin in Heisenberg SG

models in the presence of random anisotropy in 3 [203] and 4 [204] dimensions.

In Figs. 5.2 and 5.3, we show the plots of ξ_L/L vs T for various system sizes. The curves do cross; but, for both concentrations, there are large shifts between the intersection points for different system sizes. Due to a narrow range of available system sizes, the separation between the curves in the crossing region is small in comparison with errorbars. An attempt to locate the intersection points would be hampered by a large statistical uncertainty. Also, the number of intersection points is small. Thus, it is not possible to systematically analyze the scaling corrections shifts of the crossing points versus system size. Neither would it be helpful to use FSS techniques that include scaling corrections. Similarly, large scaling corrections are found in studies of Heisenberg EA SG model [105–107]. In the case of Heisenberg EA SG a broad range of system sizes were studied and the data could be analysed with scaling corrections taken into account [105–107].

The scaling equation (5.13) is expected to be satisfied only in close proximity of T_g. To better describe the data at a larger distance from the critical point, Campbell *et al.* proposed a heuristic extended scaling scheme (ESS) [205]. They suggested a scaling equation for ξ_L/L of the form:

$$\xi_L/L = \tilde{Y}\left((TL)^{1/\nu}\left(1-\frac{T_g}{T}\right)\right), \tag{5.14}$$

and showed the improvement of the accuracy it provides in the case of 2D Ising ferromagnet. Based on the assumption of a symmetric interaction distribution they proposed, and tested numerically, an alternative scaling formula for the Ising EA spin glass, where T_g/T in Eq. (5.14) is replaced with $(T_g/T)^2$. Here we use the scaling formula of Eq. (5.14) because the bond distribution in the case of diluted dipoles is not symmetric. In a recent MC simulation of a diluted dipolar Ising SG, an ESS as given by (5.14) was found to describe the scaling of ξ_L/L better than if $(T_g/T)^2$ was used [120].

We fit our data for ξ_L/L to the scaling function (5.14) over the whole simulated temperature range, shown in Table I. The scaling function, $\tilde{Y}$, is approximated with a 6th order polynomial,

$$F(z) = \sum_{m=0}^{6} a_m z^m, \tag{5.15}$$

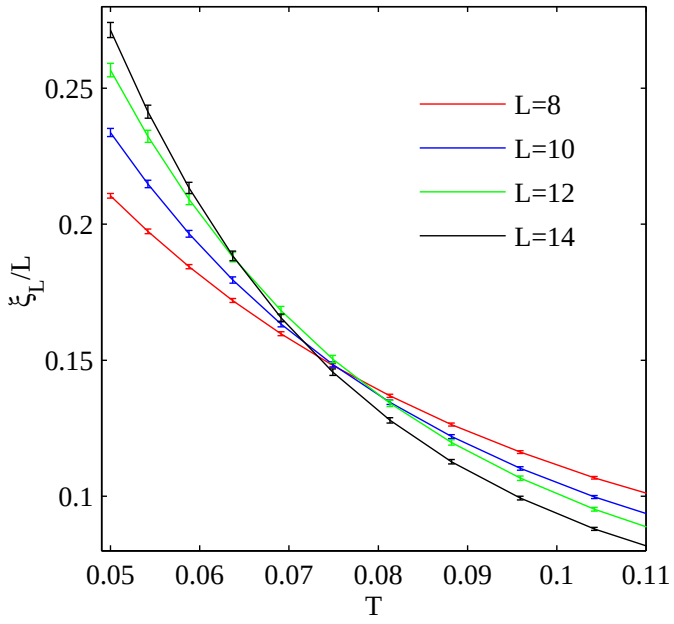

Figure 5.2: SG correlation length as a function of temperature, x=0.0625.

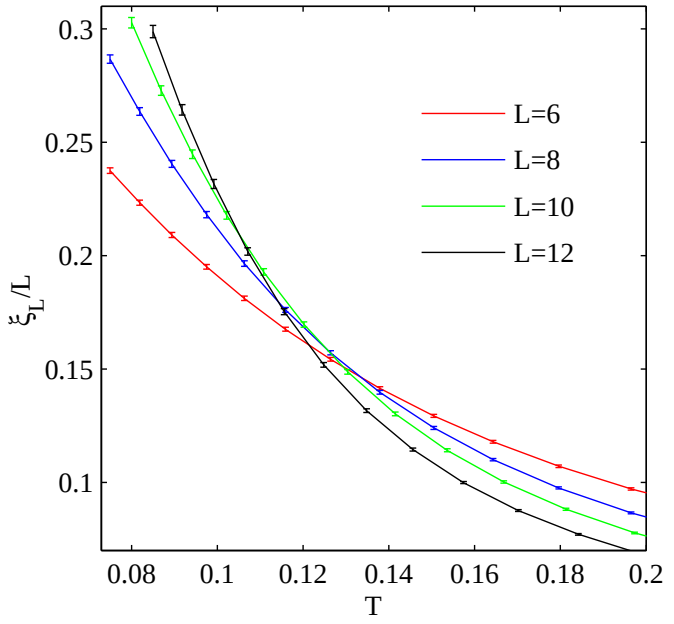

Figure 5.3: SG correlation length as a function of temperature, x=0.125.

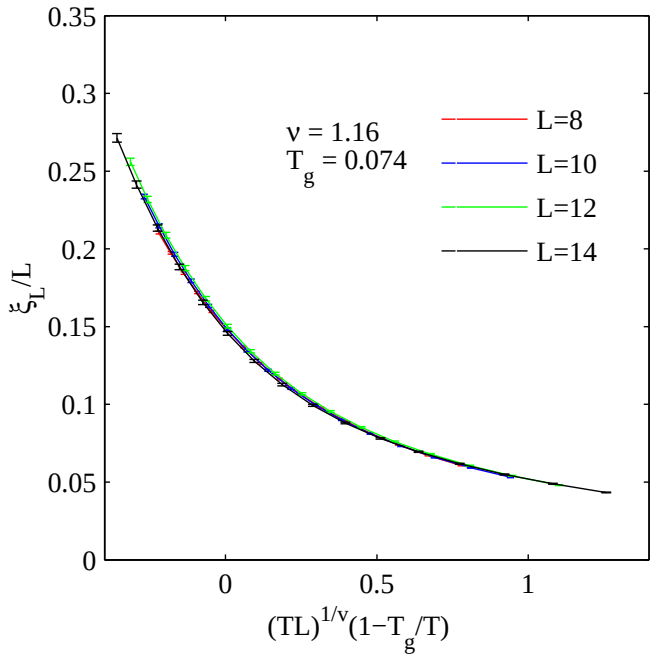

Figure 5.4: Extended scaling of ξ_L/L at x=0.0625

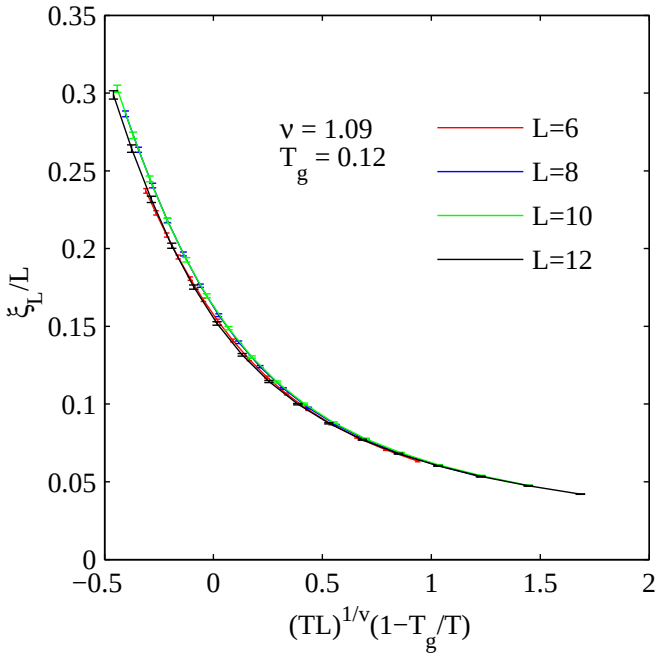

Figure 5.5: Extended scaling of ξ_L/L at x=0.125

where $z = (TL)^{1/\nu}\,(1 - {}^{T_g}/_{T})$. We define the penalty function,

$$D = \sum_{\text{MC data}} \left(F(z)L/\xi_L - 1\right)^2, \tag{5.16}$$

that is minimized with respect to the parameters $\{a_m\}$, T_c and ν. We obtain the values of the critical exponent ν =1.16, ν =1.09, and the transition temperatures T_g=0.074, T_g=0.12 for x=0.0625 and x=0.125, respectively. The scaling collapse of the simulation data is shown in Fig. 5.4 and Fig. 5.5.

In Figs. 5.6 and 5.7, just for comparison, we present the results of the fitting to the conventional formula (5.13) and ESS with $({}^{T_g}/_{T})^2$. The fitting to the conventional formula (5.13), shown in Fig. 5.6, gives quite similar results to the ESS of Eq. (5.14). Apparently, the inaccuracy due to the small system sizes studied is larger here than the correction made by replacing Eq. (5.13) with Eq. (5.17).

In the case of fitting to Eq. (5.17) with $({}^{T_g}/_{T})^2$, we obtained visibly worse data collapse than when ${}^{T_g}/_{T}$ was used; the result of this fit is shown in Fig. 5.7.

In Figs. 5.8 and 5.9, we plot the SG susceptibility of Eq. (5.10) for x=0.0625 and x=0.125, respectively.

The SG susceptibility is expected to scale according to the ESS formula [205]

$$\chi_{\text{SG}} = (TL)^{2-\eta}\,\tilde{Z}\left((TL)^{1/\nu}\left(1 - \frac{T_g}{T}\right)\right), \tag{5.17}$$

We performed a fit following a procedure similar to the method used for the scaling fit of ξ_L/L, described in Eqs. (5.15) and (5.16). For x=0.0625 we obtain T_g= 0.078, ν=1.25 and η=1.45. For x=0.125 we got T_g= 0.12, ν=1.18 and η=1.35. The critical temperatures are consistent with those obtained from FSS of ξ_L/L. The values of a critical exponent ν obtained here are slightly larger than ν obtained from scaling of ξ_L/L. The scaling collapse of χ_{SG} is plotted in Fig. 5.10 and 5.11 for x=0.0625 and x=0.125, respectively.

In the dipolar Hamiltonian (5.1) off-diagonal terms, that couple different vector components of the dipolar moment are present. The off-diagonal terms destroy the rotational (O(3)) symmetry in an otherwise isotropic vector spin system, and only the Z_2 Ising symmetry remains. It was suggested that such spatially disordered dipolar systems belong to the Ising universality class [123, 206]. Due to spatial disorder,

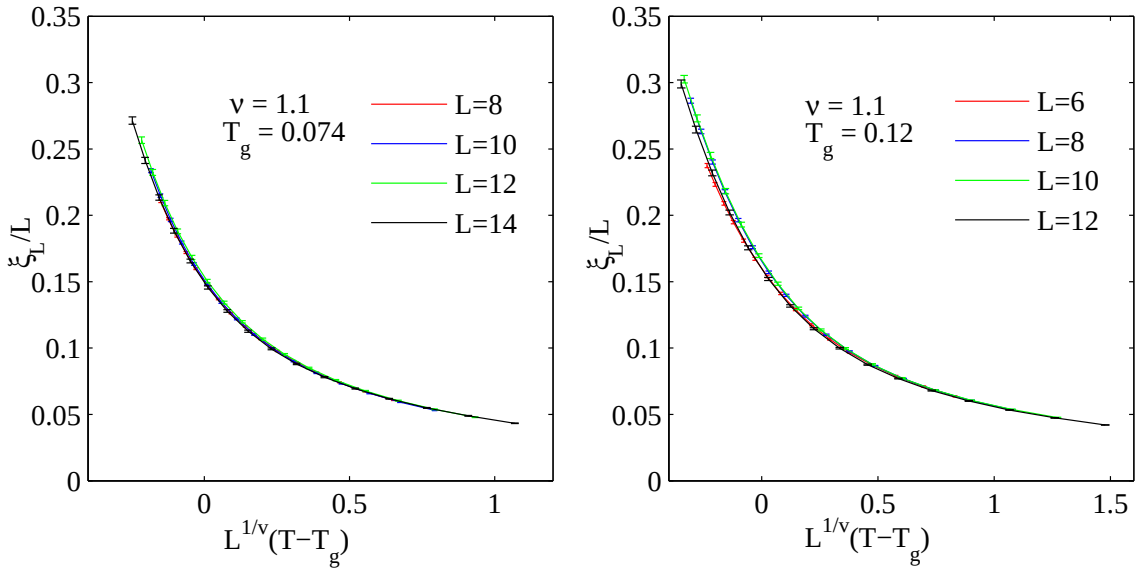

Figure 5.6: Conventional scaling of ξ_L/L with $L^{1/\nu}(T-T_g)$; x=0.0625 (left) and x=0.125 (right).

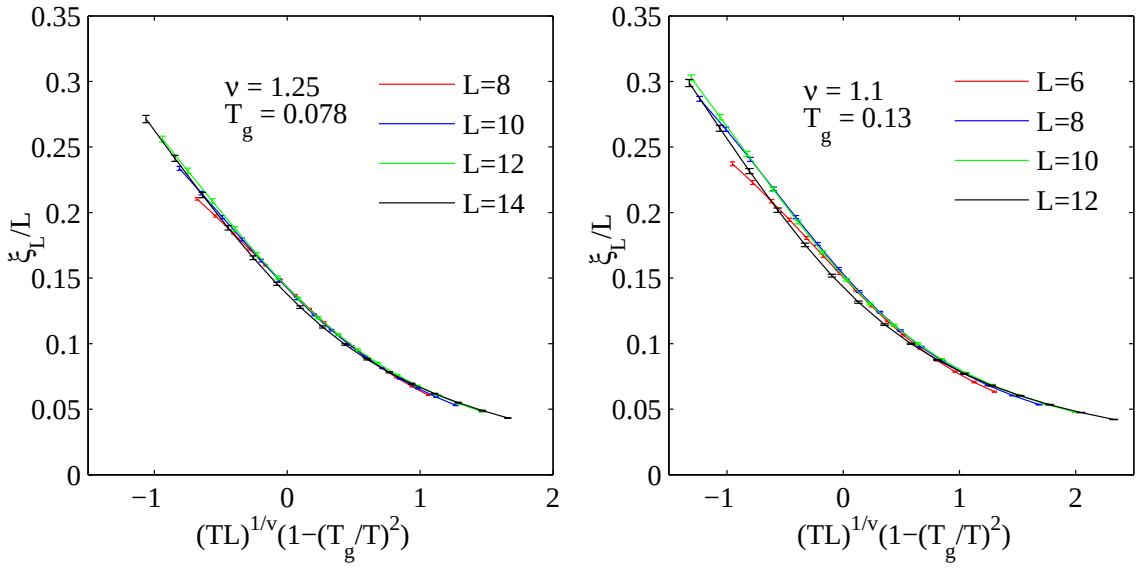

Figure 5.7: Extended scaling of ξ_L/L with $(TL)^{1/\nu}\left(1-(T_g/T)^2\right)$; x=0.0625 (left) and x=0.125 (right).

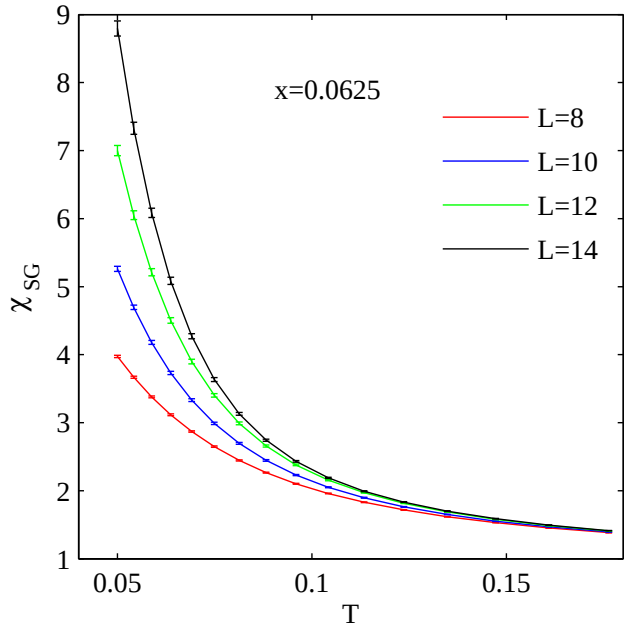

Figure 5.8: Spin-glass susceptibility, x=0.0625

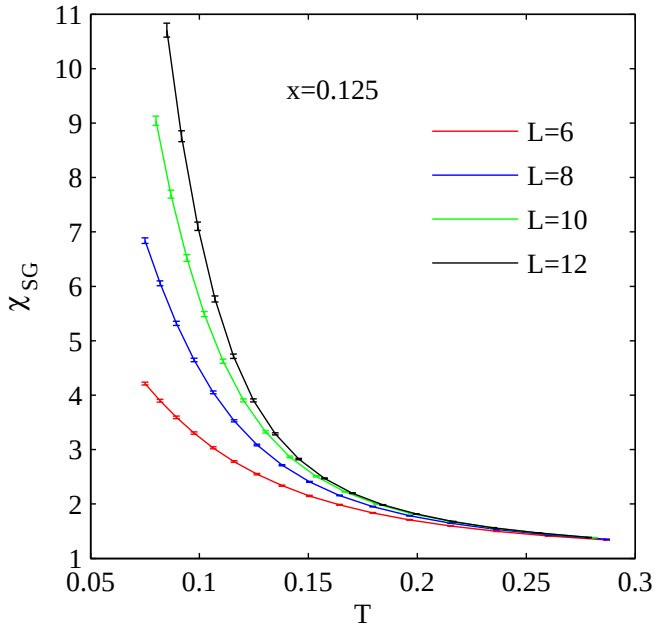

Figure 5.9: Spin-glass susceptibility, x=0.125

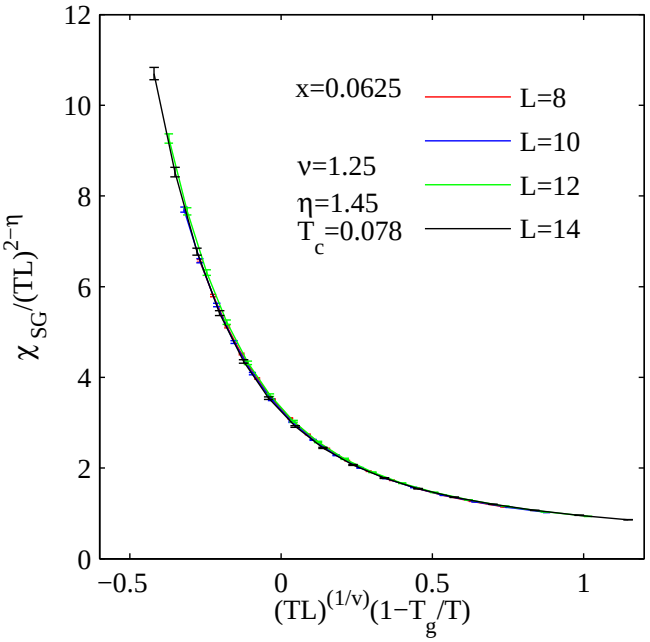

Figure 5.10: Spin-glass susceptibility scaling, x=0.0625

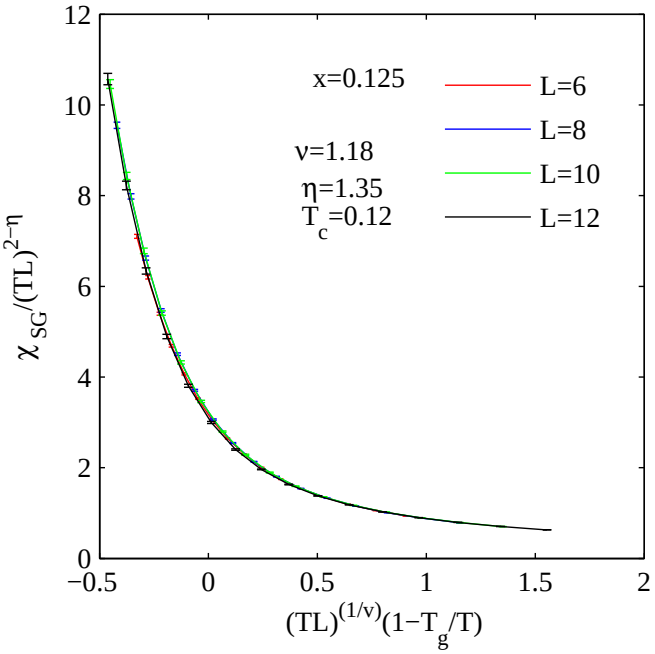

Figure 5.11: Spin-glass susceptibility scaling, x=0.125

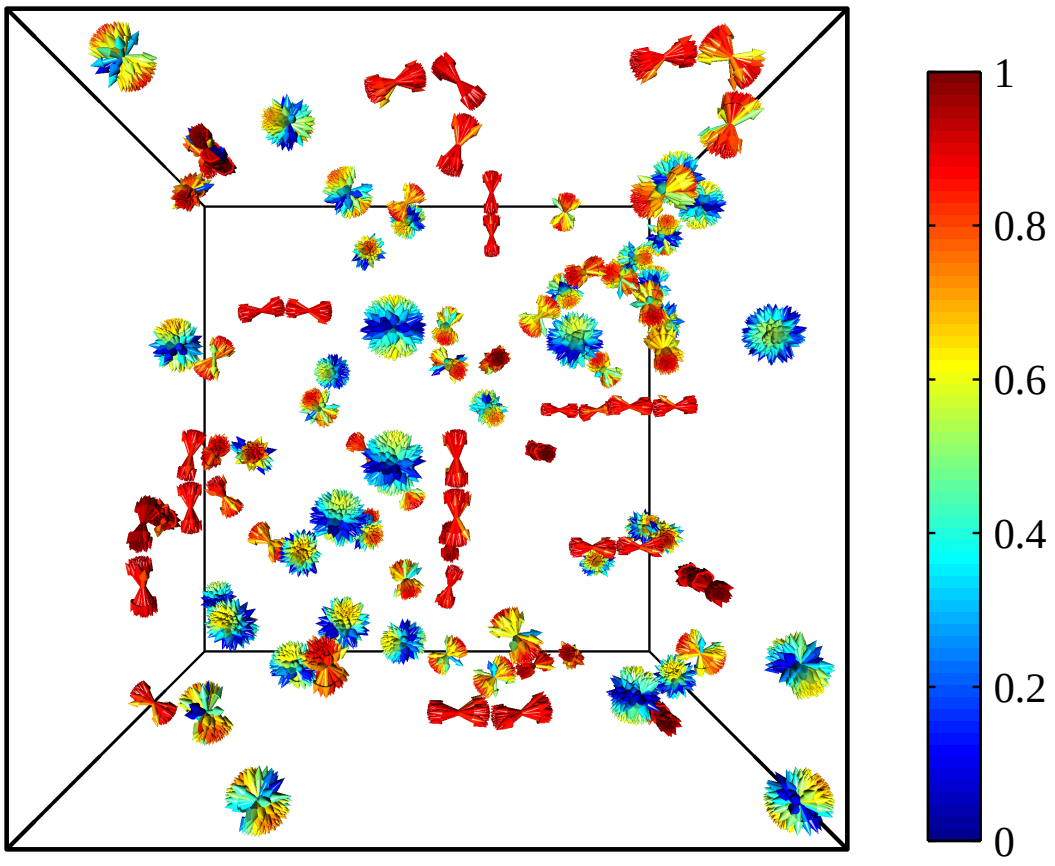

Figure 5.12: Snapshot of 200 equilibrated independently spin configurations for L=12, at T=0.05 and x=0.0625. The alignment, i.e the dot product, of the spins with the local freezing axes is indicated by the colors of arrows.

the couplings, including the off-diagonal terms, are random, and the distribution of local freezing direction in the SG phase remains uniform, unlike in a system with a global single-ion anisotropy (e.g. $-DS_z^2$ term in the Hamiltonian). With a uniform distribution of local freezing directions, a system is said to have a statistical rotational symmetry [206].

The values of the critical exponents found in this work do not agree with either those from simulations of Ising SG, $\nu = 2.45$, $\eta = -0.375$ [96], nor Heisenberg SG, $\nu = 1.49$, $\eta = -0.19$ [107]. It is possible that our exponent ν is in agreement with $\nu = 1.3$ obtained for Ising diluted dipolar SG [120]. Extracting SG critical exponents from simulations is difficult. Critical exponents for Ising SG were discussed for a long time [92–96], and proposed values were changing much with progress in development of simulation algorithms and computer hardware. Similarly to the early simulations of the Ising SG [92, 93], our data suffer from large scaling corrections. As our system sizes are small, one may want to compare our exponent ν with the results of simulations of the Ising SG performed for small system sizes, e.g. these in Ref. [92] ($\nu = 1.2$) or Ref. [93] ($\nu = 1.3$). There is a reasonably good agreement in ν but not in η. The value of the exponent η, from simulation [94–96, 107] and experiments [42, 109, 110] on many different materials, both Ising and Heisenberg, is a small number, either positive or negative but not exceeding 0.5 in absolute value. Surprisingly, the value of η we obtained for diluted dipolar Heisenberg SG, $\eta = 1.4$, is much larger.

Having discussed the question of universality class and commented on the expectation that, for diluted n=3 component dipoles, it should be Ising, it is interesting to ask whether such Ising structure is explicitly physically manifest in the low temperature regime of the systems studied above. We show in Fig. 5.12 a number of super imposed snapshots of the spin configurations for one disorder realization, in the low temperature phase, at T=0.05, and dipole concentration x=0.0625. To obtain the graph presented, we independently simulated 200 copies of a system with the same spatial disorder realisation, starting from a different random initial spin configuration and using a different pseudorandom number stream. A final spin configuration was recorded at the end of each of the simulations. We considered the system size L=12, and for x=0.0625 we have 108 occupied lattice sites, out of the total number of $12^3 = 1728$. The parameters of the simulations, such as parallel tempering temperature ranges and numbers of Monte Carlo sweeps, are given in Table 5.1, i.e. they are the same as in the

simulations where disorder averages were taken. At each of the occupied lattice sites, 200 arrows are drawn, showing the spin directions obtained from 200 independent simulations, as described above. In the case of isotropic Heisenberg model, the Hamiltonian has O(3) rotational symmetry, and one expects the spin directions obtained from the procedure explained above to be uniformly distributed at all the lattice sites considered. Here, due to the anisotropic character of the dipolar interactions, a subset of the dipoles is characterized by a unique Ising local freezing direction. It is indicated by the fact that in the snapshots some dipoles have a strong tendency to point along a particular local random direction, i.e the arrows can be enclosed by a circular conical surface with a small opening angle. For clarity, the alignment of spins with the local freezing directions, which is measured as an absolute value of the scalar product of a spin and the local freezing direction, is indicated by the color of the arrows. The local freezing direction vector is computed by summing all the spin vectors in the following way. Starting from the second element in the sum, it is checked if adding another vector to the existing sum will increase or decrease the magnitude of the new sum. If adding the new element is to decrease the magnitude of the sum, the spin vector is added with a minus sign, such that the magnitude of the sum always increases. In this way we always obtain a vector that is pointing along the unoriented local freezing axis, but the orientation of the vector obtained, which is irrelevant, depends on the order of summation, precisely on the choice of the first vector in the summation. Not all the sites are characterised by a local freezing direction. The arrows on the sites that do not have a local freezing direction create spherical structures. These dipoles have freedom to point in any direction in the low temperature phase. That means that these dipoles are strongly frustrated and decoupled from the other dipoles. Such inhomogeneous "random Ising structures" have also been observed in a model of diluted two-component 2D quadrupoles [207]. Furthermore, it is interesting to note that this behavior resembles the presence of "protected degrees of freedom" observed in gadolinium gallium garnet (GGG) [55], a material that, when magnetically diluted, is likely to be an experimental realization of the dipolar SG.

In the simulations of a SG system, it is of paramount importance to ensure equilibration of the system before the statistics for the measured observables is collected. As the quantity of foremost interest here is the correlation length, we assume that the system is equilibrated when the correlation length reaches a stationary state. In

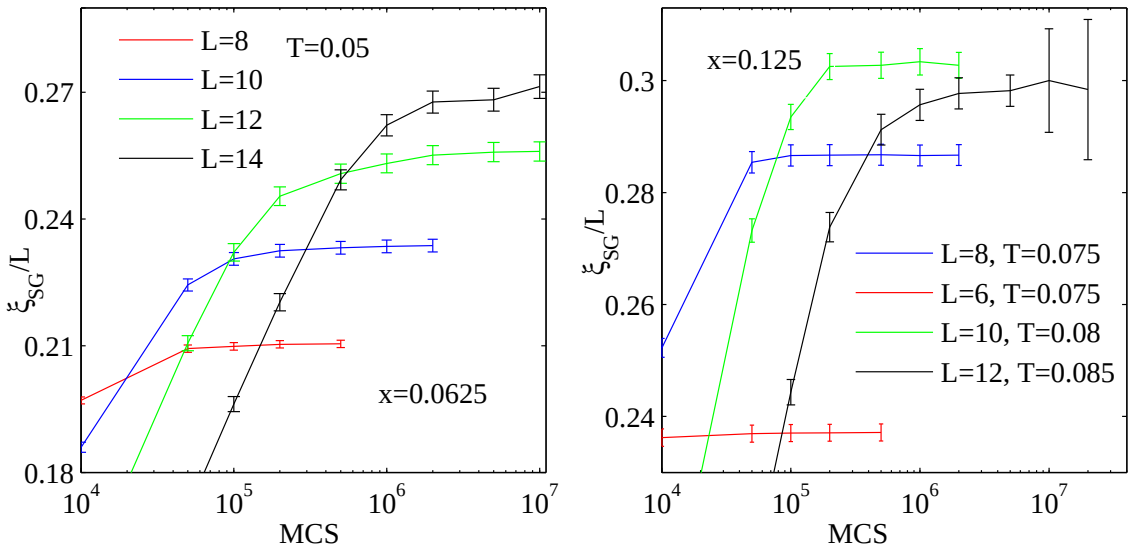

Figure 5.13: Equilibration, x=0.0625 (left) and x=0.125 (right).

Fig. 5.13 we plot ξ_L/L vs. the number of the equilibration steps performed before the measurement was taken. The number of necessary equilibration steps increases very fast with the system size and, because of this, we were only able to equilibrate system sizes up to around 200 dipoles.

We observe that the long-range Heisenberg SG takes longer time to equilibrate that its short range counterpart [105, 107]. A similar fact has been observed in the case of dipolar Ising SG [120].

5.4 Summary

In conclusion, we studied the spin-glass (SG) transition in a diluted dipolar Heisenberg model. From an analysis of the finite size scaling of the SG correlation length, ξ_L, we found an indication of a SG transition at a temperature T_g=0.074, T_g=0.12, and critical exponent ν =1.16, ν =1.09 for dipole concentrations x=0.0625 and x=0.125, respectively. From finite size scaling of SG susceptibility, $\chi_{\rm SG}$, we obtained T_g= 0.078, ν=1.25, η=1.45, and T_g= 0.12, ν=1.18, η=1.35 for x=0.0625 and x=0.125, respectively. As in the isotropic Heisenberg SG, the Binder ratio, U_L, does not exhibit crossing for different system sizes.

Because long-range interactions and hence a large number of interacting spin pairs gives rise to larger magnitude of frustration than in short range (nearest neighbour) SG, diluted dipolar SG seems to be more difficult to equilibrate than nearest-neighbour models. We perform 10^7Monte Carlo sweeps to equilibrate a system of around 200 dipoles. To compare, in the the case of the Heisenberg Edwards-Anderson spin glass around 10^7 Monte Carlo sweeps, with both overrelaxation and heatbath sweeps are counted as a Monte Carlo sweep, were used to equilibrate a system of 32,768 spins [106]. In simulations of the Ising Edwards-Anderson spin glass around $6.5 \cdot 10^6$ Monte Carlo sweeps was used to equilibrate a system of 8000 spins [94].

In the next chapter we study the easy-plane pyrochlore antiferromagnet with weak dipolar interactions. The phenomenology observed in the easy-plane pyrochlore antiferromagnet is different than that of a spin glass. Without the dipolar interaction the system is geometrically frustrated and a long-range ordered configuration is selected by the order-by-disorder mechanism. The dipolar interaction lifts the degeneracy of the ground-state manifold. Surprisingly, the technical difficulty of simulating such model turns out to be similar to that of long-range spin glass discussed above. For moderate system sizes, the system does not equilibrate even with a very large number of Monte Carlo sweeps and only very small system sizes can be simulated.

Chapter 6

Monte Carlo Studies of The Pyrochlore Easy-Plane Antiferromagnet

In this chapter, Monte Carlo studies of the pyrochlore easy-plane antiferromagnet with dipolar interactions are reported. These studies are motivated by the physics of the pyrochlore antiferromagnet $Er_2Ti_2O_7$. The magnetic moments of Er^{3+} ions in the crystalline environment of $Er_2Ti_2O_7$ are found to be characterised by a strong planar anisotropy [36], such that, effectively, they can be approximated by magnetic moments of magnitude $\sim 3\mu_B$ that are confined to the local XY planes tangential to the tetrahedra of the pyrochlore lattice [37, 61]. The Curie-Weiss temperature of $Er_2Ti_2O_7$ is $\theta_{\rm CW} = -22$ K [37, 83], with the negative sign of $\theta_{\rm CW}$ indicating an overall antiferromagnetic character of the interactions. While the Curie-Weiss temperature is quite large, the magnetic ordering is postponed down to $T_N \sim 1.2$ K [37, 61, 83, 84, 208]; which suggests a significant degree of frustration. The magnetic order in $Er_2Ti_2O_7$ was studied using neutron scattering [37, 84, 208]. It was found that the phase transition at $T_N \sim 1.2$ K is continuous. The system orders with propagation vector $\boldsymbol{q}$=0; that is, with the periodicity of the lattice, such that there is the same spin arrangement on each tetrahedron. The configuration of the spins was found to be the ψ_2 state, in the notation of Refs. [37, 84, 208]. In this thesis this configuration will be referred to as the Champion-Holdsworth state [37, 60, 61].

The ground state of the isotropic easy-plane pyrochlore antiferromagnet with nearest-neighbour exchange interactions is macroscopically degenerate; it contains a continuously degenerate manifold with propagation vector $\boldsymbol{q}$=0, and a macroscopic number of disordered configurations [60, 61]. In Monte Carlo simulations, it was found that, despite the degeneracy, the system undergoes a first order phase transition at the temperature $\sim 0.1J$, where J is the exchange constant, to a long-range ordered state with propagation vector $\boldsymbol{q}$=0 [59]. In subsequent numerical studies, it was established that the spin configuration is the Champion-Holdsworth state [60, 61] - the same configuration that was found in the neutron scattering experiments on $Er_2Ti_2O_7$ [37, 84, 208]. But, as it was already pointed out by the authors of Ref. [37] that this agreement cannot provide the explanation of the physics of $Er_2Ti_2O_7$. It has to be noted that there is a continuous phase transition in $Er_2Ti_2O_7$, while in the simulations of the easy-plane pyrochlore antiferromagnet, the transition appears to be strongly first order. Another inconsistency, that will be discussed later, and which is investigated in this chapter, is the effect of the dipolar interactions that are present in $Er_2Ti_2O_7$ and have not been considered in the aforementioned numerical studies.

The first order phase transition in the easy-plane pyrochlore antiferromagnet is an example of a so-called order-by-disorder selection [58]. This phenomenon has been extensively discussed in the context of the Heisenberg antiferromagnet on the kagome lattice [209]. In an order-by-disorder transition, while the ground state is macroscopically degenerate the entropic contribution to the free energy selects particular configurations. In the presence of thermal or quantum fluctuations, the states that are characterised by the largest number of soft modes are selected. Champion *et al.* [37, 60, 61] studied the spin wave excitations in the easy-plane pyrochlore antiferromagnet. To prove that indeed the order-by-disorder selection is responsible for ordering in the model studied, they showed that in the Champion-Holdsworth state, in reciprocal space, there are planes of soft modes, which do not occur in other $\boldsymbol{q}$=0 configurations. A related approach is to consider the zero-point energy. It was found that the minimum of zero-point energy is in the Champion-Holdsworth state [210], confirming that there is a quantum-fluctuation-driven order-by-disorder selection of the Champion-Holdsworth state.

In $Er_2Ti_2O_7$, in addition to the antiferromagnetic exchange interactions, dipolar interactions of significant magnitude are present. For example, in the Champion-

Holdsworth state the energy of the dipolar interactions per spin is ∼0.6 K [37]. The theoretical model discussed so far [37, 59–61], i.e. the pyrochlore easy-plane antiferromagnet, does not include the dipolar interactions. The dipolar interactions lift the degeneracy of the ground state. The ground state selected by the dipolar interactions is a configuration that belongs to the ground-state manifold of the exchange-only model, but it is not the configuration selected by the order-by-disorder mechanism. This ground state will be called the Palmer-Chalker state [67].

It was suggested that, in addition to thermal fluctuations, quantum fluctuations may play a role in stabilising the entropic selection of the Champion-Holdsworth state [37, 61]. The free ion magnetic moment of Er^{3+} in the crystalline environment of $Er_2Ti_2O_7$ is $3.8\mu_B$ [37] while the ordered moment, at 50 mK, was found to be $\sim 3\mu_B$ [37]. In antiferromagnets, quantum fluctuations reduce the ordered magnetic moment from the single ion value [37]; and the reduction in the magnetic moment observed in $Er_2Ti_2O_7$ might be an indication that quantum fluctuations are at play [37]. But, it is also possible that the selection of the Champion-Holdsworth state in $Er_2Ti_2O_7$ can be explained without considering quantum effects.

While for any nonzero dipolar interaction the ground state is the Palmer-Chalker state[1], it is plausible that, if the dipolar interaction is sufficiently weak, over some temperature range, the order-by-disorder selection of the Champion-Holdsworth state still takes place. While at T=0 the energetic ground state is selected, it is possible that over the intermediate temperature range, between the energetic selection of the ground state and the paramagnetic phase, the entropic contribution to the free energy prevails and order-by-disorder selection takes place. A situation where a thermal selection prevails over an energetic selection was observed in the so-called $J - J'$ model [211]. The $J - J'$ model is a generalisation that combines the properties of the Heisenberg face centered cubic (FCC) and pyrochlore antiferromagnets, such that for $J < 0$ (antiferromagnetic) and $J' = 0$ we have the pyrochlore antiferromagnet and for $J = J' < 0$ the Hamiltonian describes the FCC antiferromagnet [211]. In the case of the FCC antiferromagnet, there is an order-by-disorder selection of the $\boldsymbol{q}_0 = (\pi/a, 0, 0)$ ordered state from the degenerate $\frac{\pi}{a}(1, q, 0)$ ground-state manifold [212–215]. On the other hand, the pyrochlore antiferromagnet does not order down to $T = 0$ [38–40].

[1]Strictly speaking, the Palmer-Chalker state is the ground state of the easy-plane pyrochlore antiferromagnet for the dipolar, D, and exchange, J, coupling such that $D/J < 5.7$ [67].

For $0 < \alpha < \alpha_c \simeq 0.21$, where $\alpha = J'/J$, there is an unique incommensurate ground state [211]. Nevertheless, it was shown in Monte Carlo simulations that, for $0 < \alpha < \alpha_c$, the thermal selection of the collinear $\boldsymbol{q}_0$ state and not the energetic selection of the incommensurate ground state takes place [211].

The main goal of this study of the easy-plane Heisenberg antiferromagnet with dipolar interactions is to determine the range of the ratio of the strength of the dipolar interaction, D, and the exchange interaction, J, hence D/J, that separates the regime where, upon cooling from paramagnetic phase, a thermal selection of the Champion-Holdsworth state takes place, and the regime where the Palmer-Chalker ground state is selected directly upon cooling from the paramagnetic phase. We find that the D/J that suppresses the selection of the Champion-Holdsworth state is very small, $D/J \simeq 2 \cdot 10^{-4}$; which is much smaller than the dipolar interaction strength in $Er_2Ti_2O_7$.

This chapter is organized as follows. In Section 6.2, we start by reviewing the previous numerical studies of the easy-plane pyrochlore antiferromagnet. In Section 6.3, we discuss the geometry of the pyrochlore lattice, the ground state manifold of the easy-plane pyrochlore antiferromagnet and some particular states of the ground-state manifold, i.e the Champion-Holdsworth state that is selected in order-by-disorder mechanism and the Palmer-Chalker state that is the ground state when the degeneracy is lifted by the dipolar interactions. In Section 6.4, the Monte Carlo method that is used and the observables that are computed in the simulations are described. And finally, in Section 6.5, we present our results; we discuss the case of zero dipolar interactions at first, and then we proceed to investigate the effect of nonzero dipolar interactions. The chapter is concluded with a brief summary.

6.1 The Hamiltonian and the relative strength of the dipolar interactions in $Er_2Ti_2O_7$

The Hamiltonian for $Er_2Ti_2O_7$ can be written in the form

$$\mathcal{H} = \sum_i \mathcal{H}_{\text{cf}}(\boldsymbol{J}_i) + \frac{1}{2} \sum_{ij} \sum_{\mu\nu} D_{ij}^{\mu\nu} J_{i,\mu} J_{j,\nu} - \mathcal{J}_{\text{ex}} \sum_{i,j} \boldsymbol{J}_i \cdot \boldsymbol{J}_j, \tag{6.1}$$

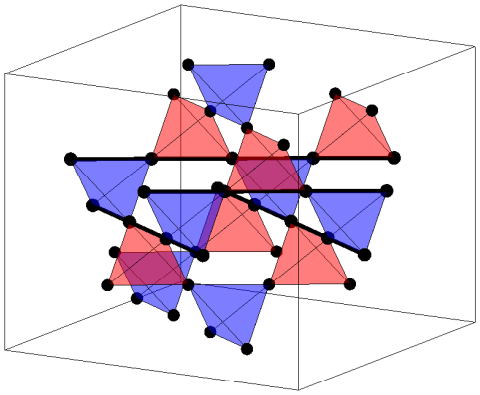

Figure 6.1: The pyrochlore lattice. Some lines of spins that can be collectively flipped in $\boldsymbol{q}$=0 state, without violating $\boldsymbol{L}$=0 condition, are indicated by thick lines.

where $\mathcal{H}_{\rm cf}(\boldsymbol{J}_i)$ is the crystal field Hamiltonian and the subsequent terms describe the dipolar and the nearest-neighbour exchange interaction. The crystal field Hamiltonian is of the form

$$\mathcal{H}_{\rm cf}(\boldsymbol{J}_i) = \sum_{nm} B_n^m O_n^m, \tag{6.2}$$

where B_n^m are the crystal field parameters and O_n^m are Stevens' "operator equivalents" [171, 172]. The crystal field parameters for $Er_2Ti_2O_7$ can be found in Ref. [216]. The dipolar interaction tensor, $D_{ij}^{\mu\nu}$, is of the form

$$D_{ij}^{\mu\nu} = \frac{\mu_0 (g_J \mu_{\rm B})^2}{4\pi a^3} \frac{\delta^{\mu\nu} \left|\boldsymbol{r}_{ij}\right|^2 - 3\left(\boldsymbol{r}_{ij}\right)^{\mu}\left(\boldsymbol{r}_{ij}\right)^{\nu}}{\left|\boldsymbol{r}_{ij}\right|^5}, \tag{6.3}$$

where $\boldsymbol{r}_{ij}$ is a vector connecting spins i and j expressed in the units of the lattice constant, a. We calculate the dipolar coupling coefficient

$$D_a = \frac{\mu_0 (g_J \mu_{\rm B})^2}{4\pi a^3} = 0.0008868\,{\rm K}, \tag{6.4}$$

where the Landé g-factor for Er^{3+} is $g_J = 6/5$ and the lattice constant is $a = 10.04$ Å. For the nearest-neighbour distance, $r_{\rm nn} = \frac{\sqrt{2}}{4}a$, one gets

$$D_{\rm nn} = \frac{\mu_0 (g_J \mu_{\rm B})^2}{4\pi r_{\rm nn}^3} = 0.02\,{\rm K}. \tag{6.5}$$

The exact value of the exchange constant, $J_{\rm ex}$, is not known. To have an estimation of the order of magnitude we use the molecular field components obtained by Cao *et al.* in polarized neutron diffraction experiments [216]. In the $Fd\bar{3}m$ symmetry that characterize $Er_2Ti_2O_7$, the susceptibility tensor, $\boldsymbol{\chi}$, has only two independent matrix elements, thus only parallel and perpendicular components to the local anisotropy axis, $\chi_{||}$ and $\chi_{\perp}$, are considered. The magnetic moment, $\boldsymbol{m}$, induced by applied field $\boldsymbol{H}$, consist of $m_{||} = \chi_{||} H_{||}$ and $m_{\perp} = \chi_{\perp} H_{\perp}$. The susceptibility data are fitted [216] to a mean-field calculations with two anisotropic molecular field tensor components as free parameters. The anisotropic molecular field tensor components can be treated as an estimation of the total inter-spin interaction. The mean-field expression for local magnetization is

$$m_\mu = -g_J \mu_B \left\langle J_\mu (H_\mu^{\rm eff}, T) \right\rangle, \tag{6.6}$$

where μ denote the perpendicular or parallel component, $||$ or $\perp$. $H_\mu^{\rm eff}$ consist of the applied magnetic field, H, and the local molecular field,

$$H_\mu^{\rm eff} = H - \lambda_\mu m_\mu, \tag{6.7}$$

where λ_μ is the anisotropic molecular field tensor component that describes the effect of the exchange and dipolar coupling. $J_\mu(H_\mu^{\rm eff}, T)$ is computed by diagonalising the mean-field Hamiltonian, similarly to the method outlined in Chapter 4 for rare earth hydroxides. The values of the molecular field tensor components obtained for $Er_2Ti_2O_7$ are $\lambda_{||} = -0.15\ {\rm T}/\mu_B = -0.1452$ K and $\lambda_{\perp} = -0.45\ {\rm T}/\mu_B = -0.4355$ K [216]. That means that the dipolar coupling, $D_{\rm nn} = 0.02$ K, is around one order of magnitude weaker than the exchange coupling. We will compare this estimation with that obtained from Monte Carlo simulations. In our simulations we estimate the range of the dipolar and exchange coupling ratio, D/J, for which there is order-by-disorder selection of the Champion-Holdsworth state.

In this section the dipolar coupling, $D_{\rm nn}$ and the molecular field tensor components are obtained for the crystal field Hamiltonian (6.1). In the simulation we use an effective Hamiltonian describing the ground-state doublet. In that effective Hamiltonian both the exchange and dipolar interaction constants, J and D, are rescaled by the same factor; hence, the ratio of the dipolar coupling and the exchange coupling obtained in this section can be directly compared with D/J from the simulations.

6.2 Previous numerical studies of the easy-plane pyrochlore antiferromagnet

We start by discussing previous studies of the Heisenberg pyrochlore antiferromagnet with a strong planar anisotropy [59] and the Heisenberg pyrochlore easy-plane antiferromagnet [60, 61]. Previously studied models did not include the dipolar interaction. For completeness, we begin our calculations by considering the already studied case of zero dipolar coupling. But the main goal of this work is to investigate the case when the dipolar interaction is present. We will consider a range of dipolar coupling strengths relative to the exchange interaction to locate the boundary between the entropic selection of the Champion-Holdsworth state [60, 61] that was established to take place in the zero dipolar interaction case, and the energetic selection of the Palmer-Chalker state [67] that is the ground state of the model with a dipolar interaction included, for the dipolar to exchange ratio $D/|J| < 5.7$.

6.2.1 The Heisenberg pyrochlore antiferromagnet with a strong planar anisotropy

The Heisenberg pyrochlore antiferromagnet with a strong planar anisotropy was studied by Bramwell *et al.* [59]. They considered the Hamiltonian

$$\mathcal{H} = -J \sum_{<i,j>} \boldsymbol{S}_i \cdot \boldsymbol{S}_j - A \sum_{i=1}^{N} (\boldsymbol{\delta} \cdot \boldsymbol{S}_i)^2 \,, \tag{6.8}$$

where $\boldsymbol{S}_i$ are classical Heisenberg spins placed on the sites of the pyrochlore lattice (see Fig. 6.1), and $J < 0$ denotes the nearest-neighbour antiferromagnetic exchange inter-

action constant. The summation runs over all the nearest-neighbour spin pairs, which are denoted by $\langle i, j \rangle$. The second term implements a local easy plane anisotropy; $\boldsymbol{\delta}$ is a unit vector in the the local $\langle 111 \rangle$ easy-axis direction, and $A < 0$ is the anisotropy constant. The negative value of A, which is the case considered here, promotes configurations with spins perpendicular to the local $\langle 111 \rangle$ direction, $\boldsymbol{\delta}$; in the opposite situation, where $A > 0$, configurations with spins oriented along the local $\langle 111 \rangle$ direction are energetically favourable. A model with $A > 0$ is often referred to as the soft spin ice model [217]. In the limiting case of infinite anisotropy, $A \to -\infty$, the Hamiltonian (6.10) reduces to the easy-plane XY pyrochlore antiferromagnet. While, in the other limit, $A \to \infty$, the Hamiltonian (6.10) would describe Ising spins.

A Monte Carlo simulation was performed for $A = -5J$. The system sizes from $L = 2$ up to L=6 were simulated, which corresponds to N=128 and N=3456 spins, respectively. The root-square-averaged four-sublattice magnetization, M_4, was calculated [59];

$$M_4 = \frac{1}{4}\sqrt{M_\alpha^2 + M_\beta^2 + M_\gamma^2 + M_\delta^2}, \tag{6.9}$$

where α, β, γ and δ denote the four sublattices. Upon simulated cooling, a sharp increase of M_4 was observed at the critical temperature $T_c/J \simeq 0.1$. A nonzero value of M_4 indicates a $q = 0$ long-range ordered state. A steep increase of the order parameter is a characteristic feature of a first order phase transition. The discontinuous character of the transition was confirmed by analysing the finite-size dependence of the maximum specific heat, $C_{\max}$; where one expects at a first order phase transition the relation, $C_{\max} \propto L^3$, where L is a linear size of the system, which was observed in this case.

A 12-fold degenerate ground state of a single tetrahedron that simultaneously satisfies the anisotropy and $\boldsymbol{L}$=0 conditions was proposed [59]. These 12 configurations consist of coplanar spin arrangements composed of two pairs of antiparallel spins. There are 3 such arrangements generated by the threefold tetrahedral symmetry. When combined with the 4 possible inversions of the antiparallel spin pairs, they give 12 ground-state configurations. One of such configurations, the Palmer-Chalker state is shown in Fig. 6.4, and another one is illustrated in Fig. 6.5. The pyrochlore lattice can be seen as composed of two perpendicular sets of lines (see Fig. 6.1). Any configura-

tion such that each line consist of antiparallel spins, while the direction of the spins in the line is independent of the direction of the spins in other lines, satisfies the ground state condition. There is a large ($\propto L^2$) number of the ground states constructed that way (see also the discussion in Sec. 6.3.6). The Monte Carlo simulations [59] showed that, despite the ground state degeneracy, a long-range ordered configuration is selected, demonstrating that a thermal order-by-disorder selection mechanism is at play [58].

6.2.2 The easy-plane pyrochlore antiferromagnet

Champion *et al.* [60, 61] studied the model with infinite anisotropy, that is given by the Hamiltonian

$$\mathcal{H} = -J \sum_{<i,j>} \boldsymbol{S}_i \cdot \boldsymbol{S}_j, \tag{6.10}$$

with the spin vectors, $\boldsymbol{S}_i$, confined to the easy planes perpendicular to the local easy axes. The local easy planes on a tetrahedron are shown in Fig. 6.2. This is a limiting case of the Hamiltonian (6.8) with $A \to -\infty$. It was recognized [60, 61] that the degeneracy of the ground state of a single tetrahedron is continuous [60, 61], and that the discrete set of ground states that was proposed by Bramwell *et al.* [59] is just a subset of this continuous ground state manifold. The equations minimizing the energy of a spin configuration on a single tetrahedron were solved analytically [60, 61] and a rather complicated system of solutions, describing the $q = 0$ ground state manifold, parametrized by a continuous free variable was obtained [60, 61].

From Monte Carlo simulations, was found [60, 61] that the a set of six symmetry related long-range ordered configurations is thermally selected. One of such configurations is shown in Fig. 6.3. This set of configurations will be referred to as the Champion-Holdsworth state [60, 61]. The Champion-Holdsworth state is discussed in more detail in Section 6.3.4. The sublattice magnetization, M_4 of Eq. (6.9), was calculated. Consistently with the results of Bramwell *et al.* [59], a sharp increase of M_4, that indicates a first order phase transition, was seen. The critical temperature was estimated to be $T_c = 0.125J$. As might be expected, the T_c for the infinite anisotropy model is higher than $T_c = 0.1J$ obtained in Ref. [59], where a finite anisotropy, $A = -5J$, was considered (see Section 6.2.1). Monte Carlo results for his-

tograms of the energies of bonds between individual spins were analysed. Two peaks were observed at $-2J/3$ and $J/3$. These are the values corresponding to the bond energies in the Champion-Holdsworth state.

In a spin wave calculation, was found that only in the spin configurations of the Champion-Holdsworth state there are two continuous planes of soft modes in k-space, while in other spin configurations soft modes occur only for a discrete number of wave-vectors, k. This confirms the order-by-disorder selection scenario, i.e. from the ground state manifold a configuration having the largest number of soft modes is selected. The specific heat calculated from the mode counting argument [60, 61, 218] compares fairly well with the specific heat calculated from low temperature Monte Carlo simulation in the Champion-Holdsworth state.

6.3 The pyrochlore lattice and the ground state of the XY pyrochlore antiferromagnet

6.3.1 The lattice structure and the local coordinate system

The pyrochlore lattice of corner-sharing tetrahedra is depicted in Fig. 6.1. The pyrochlore lattice is a non-Bravais lattice; it consist of 4 face centered cubic (FCC) sublattices. It can be viewed as an FCC lattice with a four atom tetrahedral basis, constituting together a 16 ion cubic unit cell. In Cartesian coordinates the FCC lattice vectors are: $a_1 = \frac{a}{2}(1,1,0)$, $a_2 = \frac{a}{2}(1,0,1)$ and $a_3 = \frac{a}{2}(0,1,1)$, where a is the lattice constant for the 16 ion unit cell. The tetrahedral basis consist of four sites given by the vectors: $b_1 = \frac{a}{4}(0,0,0)$, $b_2 = \frac{a}{4}(1,1,0)$, $b_3 = \frac{a}{4}(1,0,1)$ and $b_4 = \frac{a}{4}(0,1,1)$.

For each sublattice the local easy axis is parallel to the local $\langle 111 \rangle$ direction, that is, it points from the vertex to the centre of the tetrahedron. The unit vectors pointing in the local $\langle 111 \rangle$ direction are: $\hat{n}_1 = \frac{1}{\sqrt{3}}(1,1,1)$, $\hat{n}_2 = \frac{1}{\sqrt{3}}(-1,-1,1)$, $\hat{n}_3 = \frac{1}{\sqrt{3}}(-1,1,-1)$ and $\hat{n}_4 = \frac{1}{\sqrt{3}}(-1,1,1)$. It is convenient to define a local coordinate system with $\hat{k}$ direction corresponding to the local easy-axis direction. We choose the $\hat{x}$ axis to point in the direction of one of the edges of the triangle opposite to the considered vertex. We choose the unit vectors of such a local coordinate system to be those given in Table 6.1 and shown in Figure 6.2.

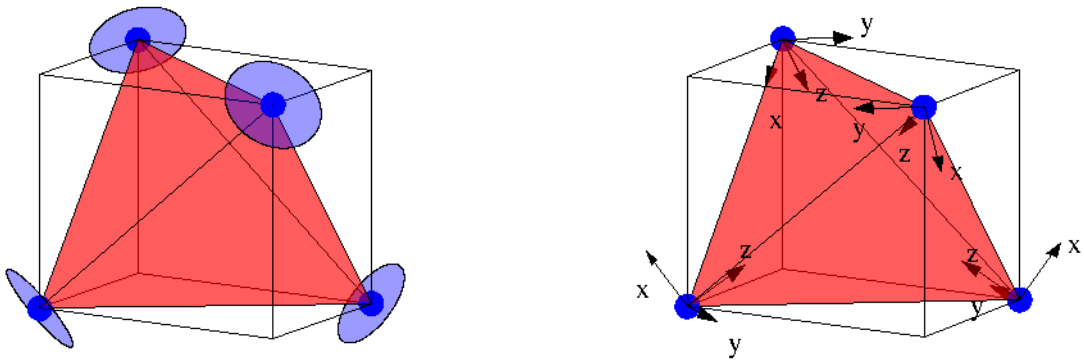

Figure 6.2: Easy planes (left) and local coordinate system (right). The local ($\hat{x}_\alpha$,$\hat{y}_\alpha$,$\hat{z}_\alpha$) unit vectors, in terms of the global coordinates, are given in Table 6.1.

α	1	2	3	4
$\hat{x}_\alpha$	$\left(-\frac{1}{\sqrt{6}}, -\frac{1}{\sqrt{6}}, \frac{2}{\sqrt{6}}\right)$	$\left(\frac{1}{\sqrt{6}}, \frac{1}{\sqrt{6}}, \frac{2}{\sqrt{6}}\right)$	$\left(\frac{1}{\sqrt{6}}, -\frac{1}{\sqrt{6}}, -\frac{2}{\sqrt{6}}\right)$	$\left(-\frac{1}{\sqrt{6}}, \frac{1}{\sqrt{6}}, -\frac{2}{\sqrt{6}}\right)$
$\hat{y}_\alpha$	$\left(\frac{1}{\sqrt{2}}, -\frac{1}{\sqrt{2}}, 0\right)$	$\left(-\frac{1}{\sqrt{2}}, \frac{1}{\sqrt{2}}, 0\right)$	$\left(-\frac{1}{\sqrt{2}}, -\frac{1}{\sqrt{2}}, 0\right)$	$\left(\frac{1}{\sqrt{2}}, \frac{1}{\sqrt{2}}, 0\right)$
$\hat{z}_\alpha$	$\left(\frac{1}{\sqrt{3}}, \frac{1}{\sqrt{3}}, \frac{1}{\sqrt{3}}\right)$	$\left(-\frac{1}{\sqrt{3}}, -\frac{1}{\sqrt{3}}, \frac{1}{\sqrt{3}}\right)$	$\left(-\frac{1}{\sqrt{3}}, \frac{1}{\sqrt{3}}, -\frac{1}{\sqrt{3}}\right)$	$\left(\frac{1}{\sqrt{3}}, -\frac{1}{\sqrt{3}}, -\frac{1}{\sqrt{3}}\right)$

Table 6.1: The local ($\hat{x}_\alpha$,$\hat{y}_\alpha$,$\hat{z}_\alpha$) unit vectors on the pyrochlore lattice. These vectors are shown in the right panel of Fig. 6.2.

Using the unit vectors from Table 6.1, it is easy to write the transformation matrices for converting a vector expressed in local coordinates to global coordinates. Let $\boldsymbol{S}'_i$ be the spin vector at site i, expressed in terms of the local coordinates,

$$\boldsymbol{S}'_i = (S_i'^{(x)}, S_i'^{(y)}, S_i'^{(z)}). \tag{6.11}$$

Then, in the global coordinates, the spin vector is:

$$\boldsymbol{S}_i = S_i'^{(x)}\hat{x}_{\alpha(i)} + S_i'^{(y)}\hat{y}_{\alpha(i)} + S_i'^{(z)}\hat{z}_{\alpha(i)}, \tag{6.12}$$

where $\alpha(i)$ denote one of the four sublattices, the one that contain the site i. The

vectors $\hat{x}_{\alpha(i)}$, $\hat{y}_{\alpha(i)}$, $\hat{z}_{\alpha(i)}$ are the local coordinate vectors given in Table 6.1. This transformation can be written in matrix notation,

$$\boldsymbol{S}_i = M_{\alpha(i)} \boldsymbol{S}'_i, \tag{6.13}$$

where the matrices M_α are constructed from the local coordinate vectors given in Table 6.1. We have

$$M_1 = \begin{pmatrix} -\frac{1}{\sqrt{6}} & \frac{1}{\sqrt{2}} & \frac{1}{\sqrt{3}} \\ -\frac{1}{\sqrt{6}} & -\frac{1}{\sqrt{2}} & \frac{1}{\sqrt{3}} \\ \frac{2}{\sqrt{6}} & 0 & \frac{1}{\sqrt{3}} \end{pmatrix}, \quad M_2 = \begin{pmatrix} \frac{1}{\sqrt{6}} & -\frac{1}{\sqrt{2}} & -\frac{1}{\sqrt{3}} \\ \frac{1}{\sqrt{6}} & \frac{1}{\sqrt{2}} & -\frac{1}{\sqrt{3}} \\ \frac{2}{\sqrt{6}} & 0 & \frac{1}{\sqrt{3}} \end{pmatrix},$$

$$M_3 = \begin{pmatrix} \frac{1}{\sqrt{6}} & -\frac{1}{\sqrt{2}} & -\frac{1}{\sqrt{3}} \\ -\frac{1}{\sqrt{6}} & -\frac{1}{\sqrt{2}} & \frac{1}{\sqrt{3}} \\ -\frac{2}{\sqrt{6}} & 0 & -\frac{1}{\sqrt{3}} \end{pmatrix}, \quad M_4 = \begin{pmatrix} -\frac{1}{\sqrt{6}} & \frac{1}{\sqrt{2}} & \frac{1}{\sqrt{3}} \\ \frac{1}{\sqrt{6}} & \frac{1}{\sqrt{2}} & -\frac{1}{\sqrt{3}} \\ -\frac{2}{\sqrt{6}} & 0 & -\frac{1}{\sqrt{3}} \end{pmatrix}.$$

6.3.2 Hamiltonian in the local coordinate system

Consider Hamiltonian of the form

$$\mathcal{H} = -\frac{1}{2} \sum_{(i,j)} \boldsymbol{S}_i \hat{L}_{ij} \boldsymbol{S}_j, \tag{6.14}$$

where tensor $\hat{L}_{ij}$ describes both dipolar and exchange interaction. $\boldsymbol{S}_i$ denote spin vectors expressed in the global coordinate system. In the simulation with local anisotropy, it is more convenient to operate on the spin vectors expressed in local coordinates. We would like to find a transformation of $\hat{L}_{ij}$ to $\hat{L}'_{ij}$ such that we write the Hamiltonian in the form

$$\mathcal{H} = -\frac{1}{2} \sum_{(i,j)} \boldsymbol{S}'_i \hat{L}'_{ij} \boldsymbol{S}'_j, \tag{6.15}$$

where $\mathbf{S}'_i$ denote spin $\mathbf{S}_i$ expressed in the local coordinates. We use Eq. (6.13) and write

$$\mathcal{H} = -\frac{1}{2} \sum_{(i,j)} \boldsymbol{S}'_i \hat{M}^T_{\alpha(i)} \hat{L}_{ij} \hat{M}_{\alpha(ij)} \boldsymbol{S}'_j. \tag{6.16}$$

This gives

$$\hat{L}'_{ij} = \hat{M}^T_{\alpha(i)} \hat{L}_{ij} \hat{M}_{\alpha(j)} \tag{6.17}$$

or

$$L'^{\mu\nu}_{ij} = \sum_{l,k} M^{l\mu}_{\alpha(i)} L^{lk}_{ij} M^{k\nu}_{\alpha(j)}. \tag{6.18}$$

6.3.3 The ground-state manifold

As discussed in Sec. 1.1.7, the condition for the $\boldsymbol{q} = 0$ ground state is that the total magnetic moment on each tetrahedron, $\boldsymbol{L}$, is zero,

$$\boldsymbol{L} = \boldsymbol{S}_1 + \boldsymbol{S}_2 + \boldsymbol{S}_3 + \boldsymbol{S}_4 = 0. \tag{6.19}$$

Additionally, the spins are confined to easy planes, and it narrows down the number of degrees of freedom compared to the case of Heisenberg spins, but as will be shown below, there is still a continuously degenerate ground-state manifold. In addition to the three equations implementing the condition $\boldsymbol{L}$=0, for each of the spins on the vertices of a tetrahedron or on the four sublattices there is a further equation that imposes the requirement that the spin is confined to its easy plane. Further, for each spin there is a normalization requirement. That gives, in total, $3+4+4 = 11$ equations with $4 \cdot 3 = 12$ unknowns, that is 4 spins with 3 vector components each. The solution to these equations was obtained by Champion *et al.* [61] with the aid of a computer algebra system. Here we will use a different approach. We will not present a rigorous solution but the merit of our method is that the ground-state manifold is described by relatively simple formulae.

As the spins are confined to the XY planes, the direction of each spin, i, can be specified by a single angle θ_i, relative to the local $\hat{x}_{\alpha(i)}$ axis. The configuration of the spins on a single tetrahedron, or in a $q = 0$ ordered state, is specified by 4 angles: θ_1, θ_2, θ_3 and θ_4. To find the ground-state configuration one needs to solve a system of 3 equations (6.19) with 4 unknowns θ_1, θ_2, θ_3 and θ_4. The spin vectors in the local coordinate system can be easily expressed in terms of the angles θ_i, where $i = 1, \ldots, 4$,

$$\boldsymbol{S}'_i = (\cos(\theta_i), \sin(\theta_i), 0). \tag{6.20}$$

Transforming $\boldsymbol{S}'_i$ to the global coordinate system, we rewrite Eq. (6.19) as

$$\boldsymbol{L} = M_1\boldsymbol{S}'_1 + M_2\boldsymbol{S}'_2 + M_3\boldsymbol{S}'_3 + M_4\boldsymbol{S}'_4 = 0, \tag{6.21}$$

which, after expanding, gives

$$\begin{gathered}
-\cos(\theta_1) + \sqrt{3}\sin(\theta_1) + \cos(\theta_2) - \sqrt{3}\sin(\theta_2) + \cos(\theta_3) - \sqrt{3}\sin(\theta_3) \\
-\cos(\theta_4) + \sqrt{3}\sin(\theta_4) = 0 \\
-\cos(\theta_1) - \sqrt{3}\sin(\theta_1) + \cos(\theta_2) + \sqrt{3}\sin(\theta_2) - \cos(\theta_3) - \sqrt{3}\sin(\theta_3) \\
+\cos(\theta_4) + \sqrt{3}\sin(\theta_4) = 0 \\
\cos(\theta_1) + \cos(\theta_2) - \cos(\theta_3) - \cos(\theta_4) = 0.
\end{gathered} \tag{6.22}$$

It can be converted to a simpler form:

$$\begin{gathered}
-\cos(60-\theta_1) + \cos(60-\theta_2) + \cos(60-\theta_3) - \cos(60-\theta_4) = 0 \\
-\cos(60+\theta_1) + \cos(60+\theta_2) - \cos(60+\theta_3) + \cos(60+\theta_4) = 0 \\
\cos(\theta_1) + \cos(\theta_2) - \cos(\theta_3) - \cos(\theta_4) = 0
\end{gathered} . \tag{6.23}$$

To find the solution of Eq (6.23) we make a heuristic assumption that the angles appear in equal pairs. We consider 3 cases:

1. The case where $\theta_1 = \theta_2 = \theta$.

   The first two equation are reduced to

   $$\begin{gathered}
   \cos(60-\theta_3) = \cos(60-\theta_4) \\
   \cos(60+\theta_3) = \cos(60+\theta_4)
   \end{gathered} ,$$

   and the only solution is

   $$\theta_3 = \theta_4.$$

   The third equation gives

   $$\theta_4 = \pm\theta,$$

   and finally we have two solutions:

   $$\begin{gathered}
   \theta_1 = \theta, \quad \theta_2 = \theta, \quad \theta_3 = \theta, \quad \theta_4 = \theta \\
   \theta_1 = \theta, \quad \theta_2 = \theta, \quad \theta_3 = -\theta, \quad \theta_4 = -\theta
   \end{gathered} .$$

2. For $\theta_1 = \theta_3 = \theta$, in similar way, we obtain

$$\begin{array}{cccc} \theta_1 = \theta & \theta_2 = \theta & \theta_3 = \theta & \theta_4 = \theta \\ \theta_1 = \theta & \theta_2 = -120 - \theta & \theta_3 = \theta & \theta_4 = -120 - \theta \end{array} .$$

3. And for the last case: $\theta_1 = \theta_4 = \theta$, we get

$$\begin{array}{cccc} \theta_1 = \theta & \theta_2 = \theta & \theta_3 = \theta & \theta_4 = \theta \\ \theta_1 = \theta & \theta_2 = 120 - \theta & \theta_3 = 120 - \theta & \theta_4 = \theta \end{array} .$$

Combining these results, the solution to Eqs. (6.23) are four sets of angles θ_1, θ_2, θ_3 and θ_4:

θ_1	θ_2	θ_3	θ_4
θ	θ	θ	θ
θ	θ	$-\theta$	$-\theta$
θ	$-120 - \theta$	θ	$-120 - \theta$
θ	$120 - \theta$	$120 - \theta$	θ

(6.24)

The energy of the ground state of the whole lattice cannot be less than the energy of the configuration where the spin arrangements on all the tetrahedra are optimized independently. Hence, the configurations such that all tetrahedra are in one of the configurations described by Eq. (6.24) belong to the ground state manifold of the whole lattice. Nevertheless, ground states other than the $\boldsymbol{q} = 0$ states described here can also exist. Examples of such configurations will be given in Section 6.3.6.

The ground state manifold given by Eq. (6.24) is fully connected. There are 6 high symmetry configurations where different branches of solutions to Eq. (6.19) intersect with the first branch, i.e. $\theta_1 = \theta_2 = \theta_3 = \theta_4 = \theta$. These 6 configurations are such that the all four angles are equal, $\theta_1 = \theta_2 = \theta_3 = \theta_4 = \theta$, and θ =0, 60, 120, 180, 240 and 300 degrees. As will be described later, these 6 particular states are selected from the ground-state manifold by thermal fluctuations. We refer to these configurations as the Champion-Holdsworth configurations[60, 61].

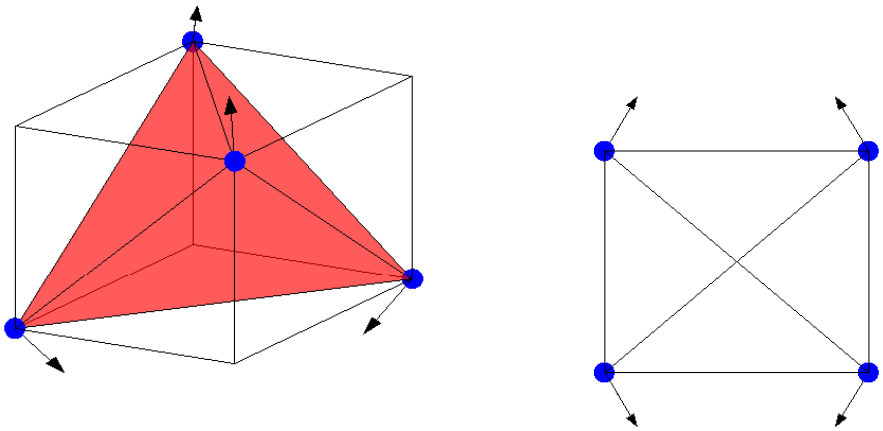

Figure 6.3: One of the Champion-Holdsworth configurations. The right panel shows a projection onto xz plane.

6.3.4 The Champion-Holdsworth configurations

In the presence of thermal or quantum fluctuation a frustrated system[2] has a tendency to choose the configurations of its ground-state manifold that are characterized by the largest number of soft modes. Such states for the easy-plane pyrochlore antiferromagnet were identified by Champion *et al.* One of the six possible Champion-Holdsworth spin arrangements is illustrated in Fig. 6.3. The angles in the Champion-Holdsworth state, in the notation introduced in Section 6.3.3 are given in Table 6.2. Each of

	θ_1	θ_2	θ_3	θ_4
1	0	0	0	0
2	60	60	60	60
3	120	120	120	120
4	180	180	180	180
5	240	240	240	240
6	300	300	300	300

Table 6.2: Champion-Holdsworth states .

these six states consist of two pairs of spins that are coplanar with the edge of the

[2]Precisely, we mean here systems with non-global degeneracy of the ground state, i.e. where there are local degrees of freedom in the ground-state manifold.

tetrahedron connecting them. To list all the possible six Champion-Holdsworth configurations one can imagine that one spin can be coplanar with one of the three edges of the tetrahedron that meet in the vertex, and for each edge, the spin can have two opposite directions, giving two configurations related by the inversion of all the spins.

6.3.5 The ground state of the easy-plane pyrochlore antiferromagnet with dipolar interaction

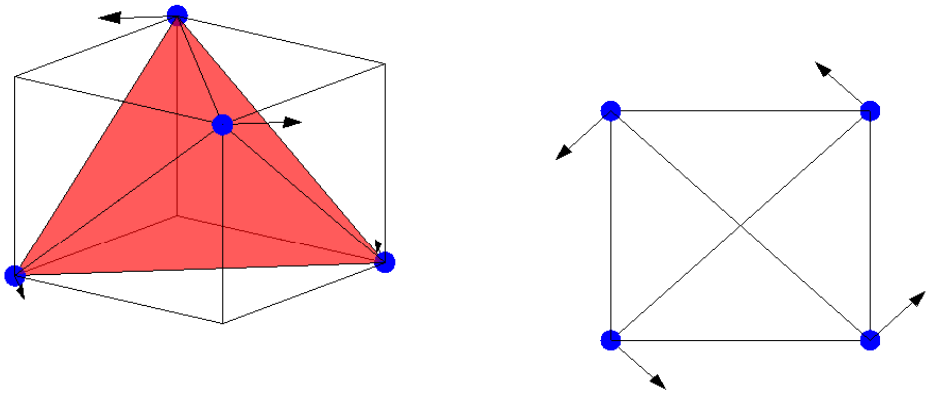

Figure 6.4: One of the Palmer-Chalker configurations. The right panel shows a projection onto xy plane.

In this section, the ground state of the easy-plane pyrochlore magnet with nearest-neighbour antiferromagnetic exchange and dipolar interaction is discussed. In Section 6.3.3 it was shown that the q = 0 ground state of the easy-plane pyrochlore nearest-neighbour antiferromagnet consists of a continuous manifold described by Eqs. (6.24). Adding dipolar interaction lifts the degeneracy of the ground state manifold and a six-fold degenerate ground state is selected [67]. One of the ground-state configurations is illustrated in Fig. 6.4. This is a coplanar arrangement that consists of two antiparallel pairs of spins. The antiparallel spins are perpendicular to the edge of the tetrahedron connecting them and oriented along the direction of the opposite edge. There are six such configurations - a particular spin in a tetrahedron can be antiparallel to one of its three neighbours, and in each of these three possibilities there

are two configurations related by reversing all the spins. This six configurations are given in Table 6.3, using the notation described in Section 6.3.3. The Palmer-Chalker state belongs to the ground-state manifold of the easy-plane pyrochlore antiferromagnet. It is worthwhile to note that Palmer-Chalker state is also a ground state of the Heisenberg pyrochlore antiferromagnet [67].

	θ_1	θ_2	θ_3	θ_4
1	90	90	270	270
2	270	270	90	90
3	30	210	210	30
4	210	30	30	210
5	150	330	150	330
6	330	150	330	150

Table 6.3: Palmer-Chalker states.

6.3.6 Line defects and macroscopic number of disordered ground states

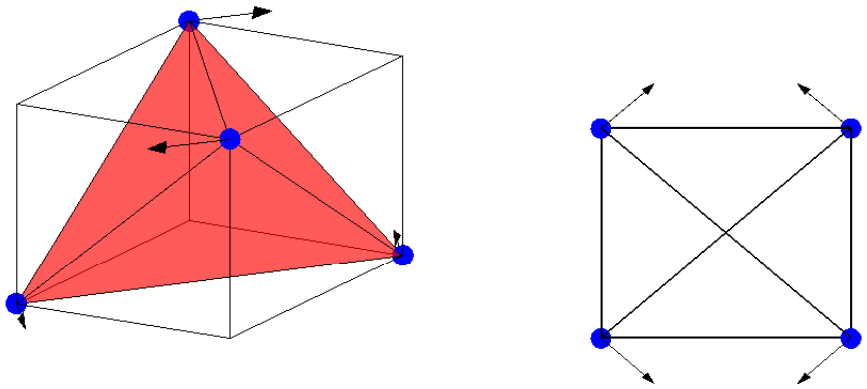

Figure 6.5: A "defected" Palmer-Chalker configuration obtained by flipping two spins in a Palmer-Chalker configuration. The right panel shows a projection onto xy plane.

A possible ground-state configuration for the whole lattice is such that all tetrahedra have the same spin arrangement, such that the condition of zero magnetic

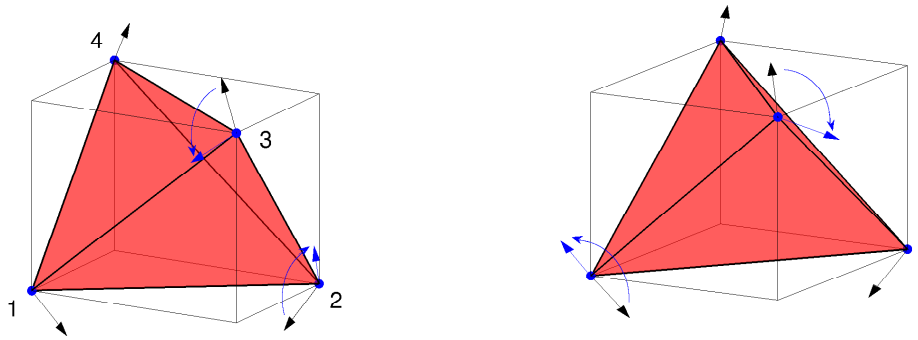

Figure 6.6: Two ways of flipping a pair of spins in a Champion-Holdsworth configuration that preserve the $\boldsymbol{L}$=0 condition. In the left panel, spin 3 is flipped by 120 degrees and spin 2 is flipped by 120 degrees. In the right panel, spin 3 is flipped by -120 degrees and spin 1 is flipped by -120 degrees.

moment ($\boldsymbol{L} = 0$ (Eq. 6.19)) on each tetrahedron is satisfied. Here we will show that besides these long-range ordered spin arrangements, other, disordered, ground states are possible. Let us imagine that all tetrahedra are in the Palmer-Chalker arrangement illustrated in Fig. 6.4. Two antiparallel spins (one of the two such pairs) can be reversed by 180 degrees and the new configuration still satisfies the condition of zero magnetic moment on each tetrahedron. Such a spin arrangement is illustrated in Fig. 6.5. In the infinite lattice, an infinite chain (see Fig. 6.1) of such antiparallel spins can be reversed, creating a line defect [61]. A similar argument can be provided for the Champion-Holdsworth state (see Fig. 6.3), but in the case of the Champion-Holdsworth state two spin modifications are possible. These two possibilities are illustrated in Fig. 6.6. In the case of a Palmer-Chalker state (Fig. 6.4) a pair of antiparallel spins is flipped (Fig. 6.5), so for each spin there is only one antiparallel and only one such modification. In the Champion-Holdsworth state, a spin can be flipped together with one of the two other spins, that are not coplanar with the first spin and the edge of the tetrahedron that connects the spins. Consider flipping the

spin 3 in Fig. 6.6 by 120 degrees or by -120 degrees. If spin 3 is flipped by 120 degrees, spin 2 has to by flipped by 120 degrees. This is shown in the left panel of Fig. 6.6. If spin 3 is flipped by -120 degrees spin 1 has to by flipped by -120 degrees, as shown in the right panel of Fig. 6.6. Again, an infinite line of spins can be flipped on a lattice without violating the $\boldsymbol{L}$=0 condition for any tetrahedron. In the described way, a macroscopic number of ground states can be generated [59]. The number of such a ground states is of the order of L^2, where L is the linear size of the system [59].

6.4 The model and the Monte Carlo method

6.4.1 The model and calculated observables

We consider a system consisting of classical XY spins restricted to the easy planes of the pyrochlore lattice (see Fig. 6.2). The spins interact via the antiferromagnetic nearest-neighbour exchange interaction and the dipolar interaction. The results presented here were obtained with the dipolar interaction truncated beyond the nearest-neighbour distance, to speed up the calculations. The nearest-neighbour model also has the Palmer-Chalker ground state; hence, such a model still captures the competition between the energetic selection of the Palmer-Chalker state and thermal selection of the Champion-Holdsworth state. The nearest-neighbour Hamiltonian is of the form

$$\mathcal{H} = -J \sum_{\langle i,j \rangle} \boldsymbol{S}_i \cdot \boldsymbol{S}_j + D \sum_{\langle i,j \rangle} \frac{\delta^{\mu\nu} r_{ij}^2 - 3 r_{ij}^{\mu} r_{ij}^{\nu}}{r_{ij}^5} S_i^{\mu} S_j^{\nu}, \tag{6.25}$$

where $\langle i,j \rangle$ denotes summation over the nearest-neighbour pairs. The exchange interaction is antiferromagnetic and in the convention used above , the interaction constant is negative, J<0. We measure the inter-spin distance in units of the lattice constant, a, that is the size of a cubic unit cell that contains 16 spins; thus, the nearest-neighbour distance is $d_{\mathrm{NN}} = \frac{\sqrt{2}}{4} a$. The dipolar interaction constant is of the form $D = \frac{\mu_0}{4\pi} \frac{\mu^2}{a^3}$, where μ is the effective dipolar moment of the classical spins, $\boldsymbol{S}_i$, and μ_0 is the vacuum permeability. Below, for convenience, when presenting the results of our simulations, we will express both the temperature and the dipolar coupling, D, in units of the exchange constant, J. To avoid confusion we will write $D/\left|J\right|$ rather than just D, but

the temperature in units of J will be denoted just T.

The exchange term in the Hamiltonian is minimised by the requirement of zero magnetic moment on all tetrahedra, $\boldsymbol{L} = 0$, (see Sec. 1.1.7). If, in addition to that, the spins are confined to the local easy planes, the ground state is given by the fully connected manifold described in Sec. 6.3.3. As discussed earlier, at $T>0$, from the ground-state manifold, in the exchange-only case, $D = 0$, the set of symmetry-related Champion-Holdsworth configurations is selected [60, 61] by an order-by-disorder mechanism (see Sec. 6.2.2). The dipolar term lifts the degeneracy of the ground-state manifold, giving the six-fold degenerate Palmer-Chalker ground state [67]. With a relatively weak dipolar interaction a competition between the entropic selection of the Champion-Holdsworth state and the energetic selection of the Palmer-Chalker state occurs. In the course of the simulations we attempted to establish the value of the relative strength of the dipolar interaction separating the entropic selection of the Champion-Holdsworth and the energetic selection of the Palmer-Chalker state at the phase transition from the paramagnetic state.

The pyrochlore lattice consists of four face-centered cubic sublattices. A direct measure of $\boldsymbol{q} = 0$ order is the sublattice magnetization

$$M_4 = \sqrt{\frac{1}{4}\sum_{\alpha=1}^{4}\left(\frac{1}{N_\alpha}\sum_{i}^{N_\alpha}\boldsymbol{S}_{i,\alpha}\right)^2}, \tag{6.26}$$

where α denotes the sublattices or vertices of tetrahedron and N_α is the number of sites in each sublattice (i.e. number of primitive tetrahedra).

To distinguish the type of $\boldsymbol{q}$=0 ordering in the simulations, for each kind of order, i.e. the Champion-Holdsworth and Palmer-Chalker states, we consider an order parameter that is a projection of the spin configuration onto the spin directions in the fully ordered state. Both for the Champion-Holdsworth and Palmer-Chalker states there are six possible spin directions and all these arrangements have to be included in the definition of the order parameter. Let $\hat{\mathbf{e}}_\alpha$ be the unit vector pointing in the direction of the spins on the sublattice α in a particular ordered state. The vectors $\hat{\mathbf{e}}_\alpha$

lie in the easy planes of the pyrochlore lattice . For a given set of $\hat{\mathbf{e}}_\alpha^{(\gamma)}$ we write

$$\Psi_\gamma = \frac{1}{N}\sum_{i=1}^{N_\alpha}\sum_{\alpha=1}^{4} \boldsymbol{S}_{i,\alpha}\cdot\hat{\mathbf{e}}_\alpha^{(\gamma)}, \tag{6.27}$$

where γ labels the set of spin directions and $\hat{\mathbf{e}}_\alpha^{(\gamma)}$ denotes the set of 4 vectors for a chosen ground-state configuration, γ. Vectors $\hat{\mathbf{e}}_\alpha^{(\gamma)}$ can be also specified in polar coordinates, as angles, φ_α relative to the axis $\hat{x}_\alpha$ in the XY plane. The angles φ_α are given in Tables 6.2 and 6.3 for the Champion-Holdsworth and Palmer-Chalker states, respectively[3]. Using angles $\theta_{i,\alpha}$, that, in the same coordinate system, express the directions of the individual spins, we write

$$\Psi_\gamma = \frac{1}{N}\sum_{i=1}^{N_\alpha}\sum_{\alpha=1}^{4} \cos(\varphi_\alpha^{(\gamma)} - \theta_{i,\alpha}). \tag{6.28}$$

We consider here two particular ordered states: Palmer-Chalker state and Champion-Holdsworth state. For both of them there are 3 different configurations plus another 3 given by inversion of all spins; hence, to account for all 3 possibilities, we define the Palmer-Chalker or Champion-Holdsworth order parameter,

$$q_{\mathrm{PC/CH}} = \left\langle \sum_{\gamma=1}^{3} \Psi_\gamma^2 \right\rangle, \tag{6.29}$$

where $\hat{\mathbf{e}}_\alpha^{(\gamma)}$ in the definition of Ψ_γ corresponds to the directions of the spins in the Palmer-Chalker or Champion-Holdsworth states, and $\langle\ldots\rangle$ denotes thermal average.

6.4.2 Monte Carlo simulation

We use parallel tempering Monte Carlo simulation technique. The details of this method were given in Section 2.2. Parallel tempering was reported to significantly speed up the equilibration in slowly relaxing systems [153, 154]. It was also shown to be useful in simulation of systems undergoing a first order phase transition [219].

[3]Note that the angles in Tables 6.2 and 6.3 were denoted θ_α, because they were denoting spin directions. Here those angles are denoted φ_α, while $\theta_{i,\alpha}$ denotes the direction of individual spins.

In the parallel tempering Monte Carlo method, one simultaneously simulates N_T thermal replicas, copies of the system with the same spatial disorder, at different temperatures. Each thermal replica is simulated independently, using different pseudo-random number stream. In the simulations where random initial configurations are used, for each replica the simulation begins from a different random initial configuration. In addition to standard Metropolis spin moves, at every 100 local update sweeps, a configuration swap among thermal replicas is attempted with acceptance probability preserving the detailed balance condition. Conventionally, a local update sweep consist of N Metropolis attempts to move a spin, with N being the number of spins in the system. In the simulations described in this chapter, we use a relatively large number of thermal replicas, $N_T = 64$, with uniformly increasing temperatures. The choice of equidistant temperature points is rationalized below. To ensure uniform acceptance rate for the parallel tempering configuration swaps, the optimal selection of the temperatures would be such that the largest density of temperature points is where the specific heat is the largest. The system considered here undergoes a first order phase transition. In a finite-size simulation, at a first order phase transition, there is a peak of specific heat, C_V. The location, that is the effective transition temperature, and the magnitude of the peak of C_V depends on the system size and, in the problem considered here, it also varies with the strength of dipolar interaction. Hence, the selections of the temperatures would have to be done self-consistently for each simulation. In the simulations discussed below, the equilibration is very slow and self-consistently adjusting the temperatures is impractical, if not impossible.

The spins are confined to their easy planes and each spin in simulation can be represented by a single angle θ_i. Local moves consist of rotating a spin by a random angle drawn from uniform probability distribution, within a particular range of angles, $\Delta\theta_{\max}$, chosen to obtain 50% acceptance rate. A Monte Carlo sweep consist of N local spin update attempts, that are accepted or rejected with Metropolis probability. The local updates are performed on randomly selected spins. The spin move range is self-consistently adjusted every 100 Monte Carlo sweeps. When the acceptance rate, τ, measured over 100 Monte Carlo sweeps, is larger than 0.5 the range $\Delta\theta_{\max}$ is increased, and if $\tau < 0.5$, $\Delta\theta_{\max}$ is decreased. Such adjustment of $\Delta\theta_{\max}$ is achieved if the new angle update range $\Delta\theta'_{\max}$ is calculated according to the formula

$$\Delta\theta'_{\max} = 0.5(\Delta\theta_{\max})\tau. \tag{6.30}$$

The statistics is collected every 100 Monte Carlo sweeps, after the local sweeps and before the parallel tempering swaps.

The simulations of first order transitions are difficult due to the presence of an energy barrier between the ordered and paramagnetic phase. While in the thermodynamical limit the energy barrier has a character of a discontinuous jump, in a finite-size system the the singularity is smeared off due to the fluctuations, and the transition between an ordered and disordered phase happens over a finite interval of temperatures. If the fluctuations are of order of the the energy gap the transition between the ordered and disordered state in the simulation is likely to happen. The fluctuations decrease with increasing the system size, N, like $1/\sqrt{N}$. In consequence, equilibrating a simulation at a first order transition regime gets more difficult as the system size increases, or when, due to a change of simulation parameters, the energy barrier increases.

To ensure equilibration, we ran our simulations starting from different initial configurations - either random initial configuration or ordered configurations (i.e. the Champion-Holdsworth or Palmer-Chalker state), and we compared the results. If the simulation is not equilibrated a hysteresis-like effect is observed; the effective transition temperature is higher when the simulation was started from ordered configuration and lower for simulation started from random initial configuration. The evolution of observables, i.e. order parameters and energy, with Monte Carlo time was also monitored. Further discussion of equilibration issues is presented in Appendix E.

6.5 Monte Carlo results

6.5.1 Order-by-disorder selection of the Champion-Holdsworth state in the easy-plane pyrochlore antiferromagnet

Before we present our results on the effect of dipolar interaction on the easy-plane pyrochlore antiferromagnet, we consider the case with zero dipolar interaction, described

by the Hamiltonian

$$\mathcal{H} = -J \sum_{\langle i,j \rangle} \boldsymbol{S}_i \cdot \boldsymbol{S}_j. \tag{6.31}$$

It was shown in Sec. 6.3.3 that the ground-state manifold of the easy-plane pyrochlore antiferromagnet is degenerate and contains a $\boldsymbol{q}$=0 sub-manifold consisting of 4 connected branches parametrized by one continuous variable. It was established by carrying out Monte Carlo simulations that from the ground state manifold a $\boldsymbol{q}$=0 ordered state is thermally selected [59–61]. The set of 6 thermally selected configurations is the Champion-Holdsworth [60, 61] state described in Section 6.3.4.

The usage of the parallel tempering method allows us to obtain more accurate data at the first order phase transition than the data reported in Ref. [60, 61]. Furthermore, we use a direct method of analysing spin configurations such as plotting angle histograms and computing order parameter which distinguishes the Champion-Holdsworth state from other $\boldsymbol{q} = 0$ configurations. But, the main goal in considering the zero-dipolar-interaction case first is to establish a consistent reference for comparison with the cases when the dipolar interaction is included.

We report here data for 4 system sizes L=2, 3, 4 and 5. To equilibrate the system, we run the simulation for $5 \cdot 10^6$ Monte Carlo sweeps per spin and the statistics is collected over another $5 \cdot 10^6$ Monte Carlo sweeps per spin. The number of parallel tempering swaps and the number of measurements corresponding to $5 \cdot 10^6$ Monte Carlo sweeps per spin is $5 \cdot 10^4$. We also tried to simulate the larger system size, L=6, but we could not reach equilibrium. For any set of simulation parameters, two simulations were run. One simulations was started from a random initial configuration, and, to ensure equilibration, the results were compared with the results from another simulation that was started from the Champion-Holdsworth state as an initial configuration. The evolution of the measured quantities with the Monte Carlo time, i.e. with an increasing number of Monte Carlo sweeps, was also examined (see Appendix E).

In Fig. 6.7, we show the sublattice magnetization, M_4 of Eq. (6.26), vs temperature. There is a sharp increase of M_4 at the temperature $T \simeq 0.127$. This indicates a first order phase transition to a $\boldsymbol{q} = 0$ ordered state. The finite-size effects are very significant for L=2 and 3 and they considerably smear the signature of the first order transition. M_4 indicates that there is long-range order in each of the four sublattices but it does not provide any information about the orientation of the spins in each sub-

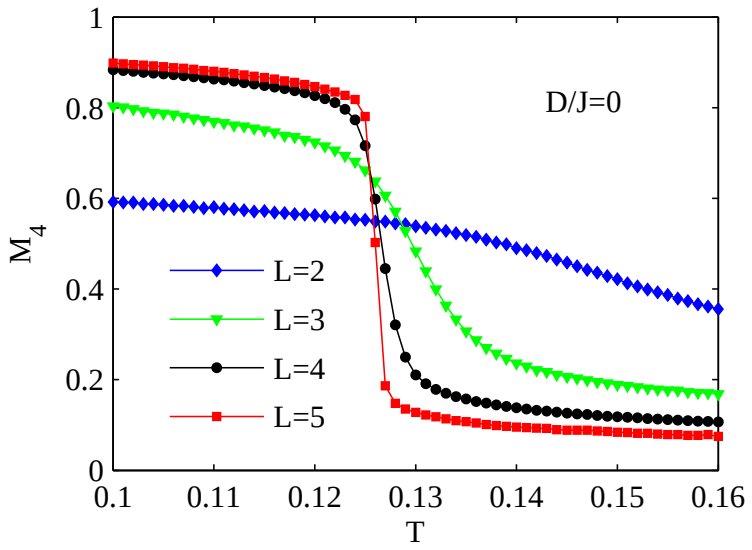

Figure 6.7: The sublattice magnetization, M_4, for D/J=0 and 4 system sizes L=2,3,4 and 5.

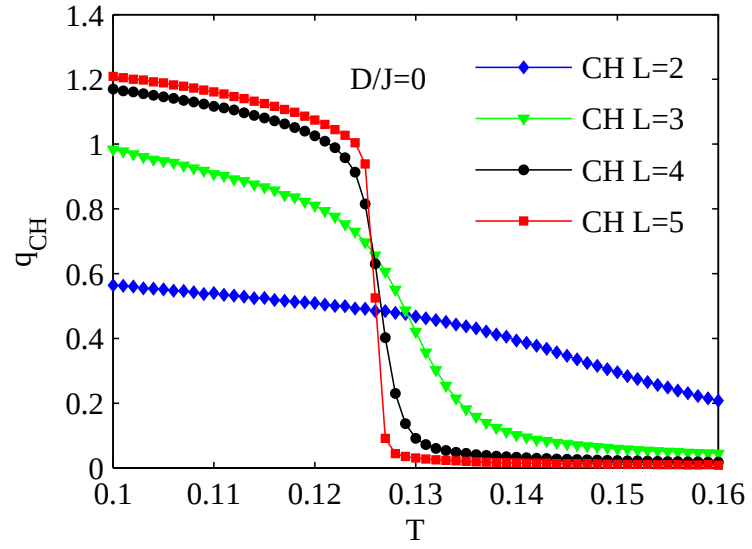

Figure 6.8: The Champion-Holdsworth order parameter, $q_{\rm CH}$, of Eq. (6.29) for D/J=0 and 4 system sizes L=2,3,4 and 5.

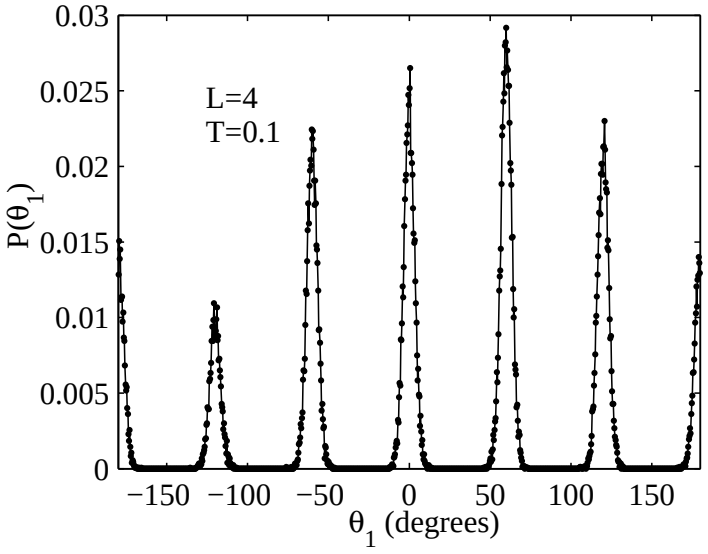

Figure 6.9: Normalized histogram of angle θ_1 for L=4 and T=0.1.

lattice. To distinguish ordering into the Champion-Holdsworth state from any other $\boldsymbol{q} = 0$ order, $q_{\rm CH}$ of Eq. (6.29) is calculated. $q_{\rm CH}$ vs T plots are shown in Fig. 6.8. Similarly to M_4 in Fig. 6.7, $q_{\rm CH}$ vs T plot has a step shape that is characteristic to a first order transition.

The XY spin orientations are described by an angle, θ_i. The most direct way to analyze the spin configuration is to plot a histogram of their directions, θ_i. In Fig. 6.9 we show a histogram of spin angles, θ_i, for L=4 at T=0.1. The histogram includes the angles for spins in all four sublattices, collected along with other observables every 100 Monte Carlo sweeps, i.e. $5 \cdot 10^4$ configuration snapshots. In the histogram there are 6 peaks corresponding to the 6 possible Champion-Holdsworth configurations. The presence of the peaks at all 6 angles indicates that during the simulation the system was switching between different configurations in the Champion-Holdsworth state.

In Fig. 6.10 we plot specific heat, C_V. In the thermodynamic limit, at a first order phase transition the specific heat is divergent. The finite-size effects smears the divergence. Upon increasing the system size the peaks in C_V plots become sharper and higher.

To confirm that the transition is first order, in Fig. 6.11, we show an energy histogram for L=4 at T=0.127. The double-peaked form of the histogram at the

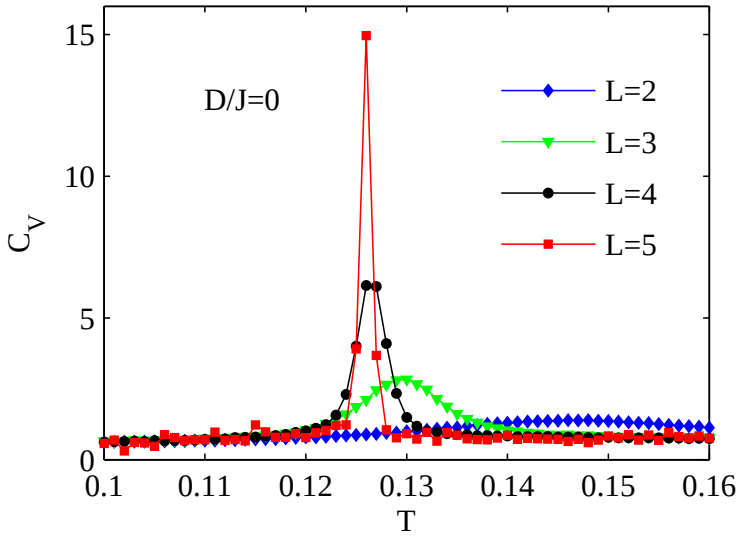

Figure 6.10: Specific heat, C_V, for D/J=0 and 4 system sizes L=2,3,4 and 5.

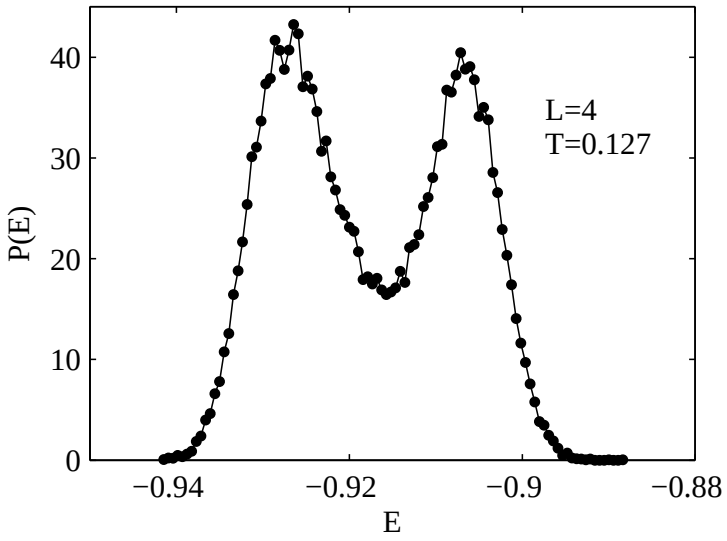

Figure 6.11: Normalized energy histogram for L=4 and T=0.127.

tentative transition temperature indicates a first order phase transition.

6.5.2 Competition between the entropic selection of the Champion-Holdsworth state and the energetic selection of the Palmer-Chalker state in the easy-plane pyrochlore antiferromagnet with dipolar interaction

The ultimate aim of this work was to study the XY pyrochlore antiferromagnet in the presence of the dipolar interaction. In the case of the exchange interaction only, there is a degenerate, fully connected ground-state manifold. From the continuous ground-state manifold the Champion-Holdsworth state is selected by an order-by-disorder mechanism. The thermally-driven order-by-disorder first order phase transition to the Champion-Holdsworth state in the easy-plane pyrochlore antiferromagnet was described in the previous section. When the dipolar interactions are included, the continuous degeneracy of the ground-state manifold is energetically lifted. The lowest energy configuration is the Palmer-Chalker state [67], that was discussed in Section 6.3.5. In this section, we show that the order-by-disorder selection of the Champion-Holdsworth state persist up to some strength of the dipolar interaction relative to the exchange interaction.

In the case of zero dipolar interaction, the equilibration of simulations for large system sizes was difficult due to the strongly first order character of the phase transition. It turns out that equilibrating our simulations becomes even harder when dipolar interactions are included and the Palmer-Chalker state is selected. We were unable to equilibrate the simulation for L=4 in the regime where the Palmer-Chalker state is selected and in this regime we present only the results obtained from simulations for system size L=3. For the very low values of D/J where the Champion-Holdsworth state is selected, we report data up to L=5. To obtain the data reported in this section, we run the simulations for 10^8 Monte Carlo sweeps, and the thermal averages of observables are obtained from the last 10^7 Monte Carlo sweeps. The equilibration issues are discussed in detail in Appendix E. We do not present results for L=2 because for such a small system size, finite-size effects smear the transition so much that it would be impossible to recognize whether the long-range order appearing in the system is

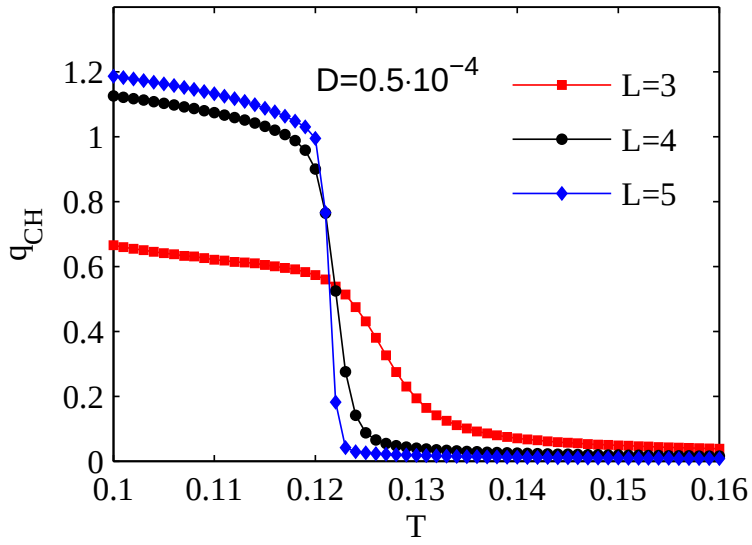

Figure 6.12: q_{CH} vs T for L=3, L=4 and L=5. $D/J = 0.5 \cdot 10^{-4}$.

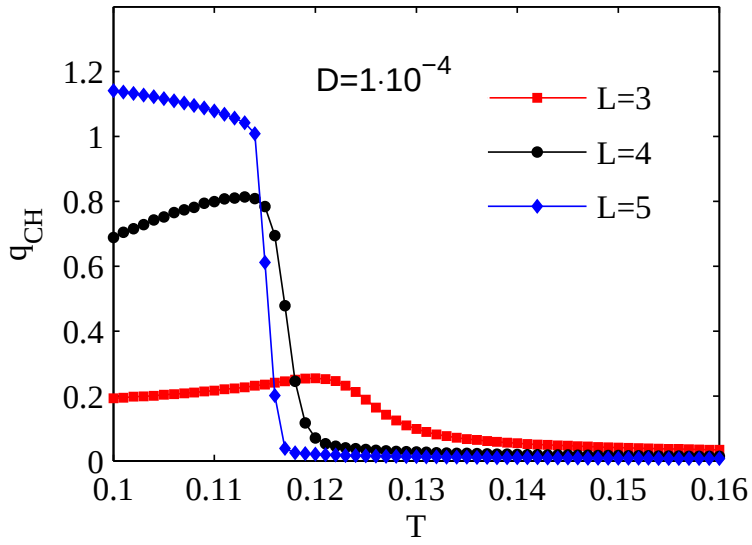

Figure 6.13: q_{CH} vs T for L=3, L=4 and L=5. $D/J = 1 \cdot 10^{-4}$.

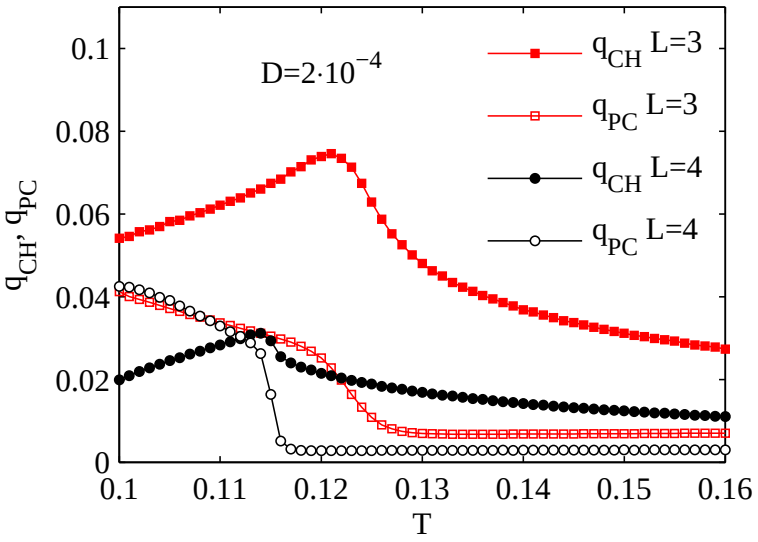

Figure 6.14: $q_{\rm CH}$ and $q_{\rm PC}$ vs T for L=3 and L=4. $D/J = 2 \cdot 10^{-4}$.

Palmer-Chalker or Champion-Holdsworth ordering. Even for L=3, the details of the low temperature spin configuration are obscured by large fluctuations that occur in such a small system.

We consider the Hamiltonian (6.25), i.e.

$$\mathcal{H} = -J \sum_{\langle i,j \rangle} \boldsymbol{S}_i \cdot \boldsymbol{S}_j + D \sum_{\langle i,j \rangle} \frac{\delta^{\mu\nu} r_{ij}^2 - 3 r_{ij}^{\mu} r_{ij}^{\nu}}{r_{ij}^5} S_i^{\mu} S_j^{\nu}.$$

It contains the antiferromagnetic nearest-neighbour exchange interaction and the dipolar interaction truncated at the nearest-neighbour distance.

In Figs. 6.12 and 6.13 we plot the $q_{\rm CH}$ order parameter vs temperature for $D/J = 0.5 \cdot 10^{-4}$ and $D/J = 1 \cdot 10^{-4}$, respectively, for L=3, L=4 and L=5. For these values of D/J an entropic selection of the Champion-Holdsworth state takes place. $q_{\rm PC}$ was also calculated and it was found to be very small. The fluctuations of the local angles, θ, are larger than in the D=0 case; hence, the value of $q_{\rm CH}$ is lower.

At $D/J = 2 \cdot 10^{-4}$ there is a strong competition between the ordering into the Champion-Holdsworth state and ordering into the Palmer-Chalker state. In Fig. 6.14 we plot both $q_{\rm CH}$ and $q_{\rm PC}$ for L=3 and L=4. Both $q_{\rm CH}$ and $q_{\rm PC}$ have very small and comparable values for both system sizes. To get some insight into the type of ordering

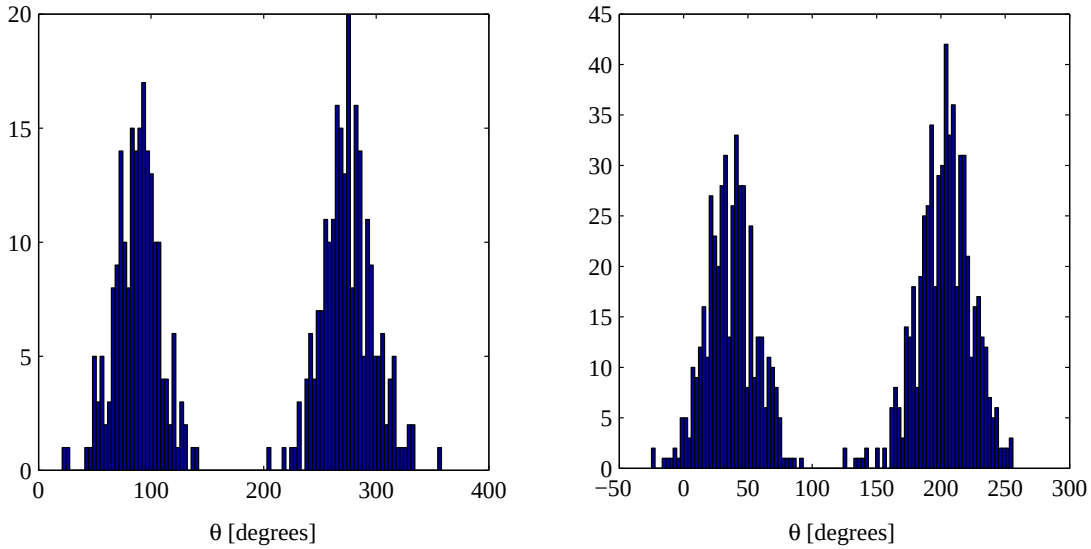

Figure 6.15: The histograms of all angles, θ_i, in one configuration snapshot for $D/J = 2 \cdot 10^{-4}$ at T=0.1. Data for L=3 and L=4 is shown in the left and right panel, respectively.

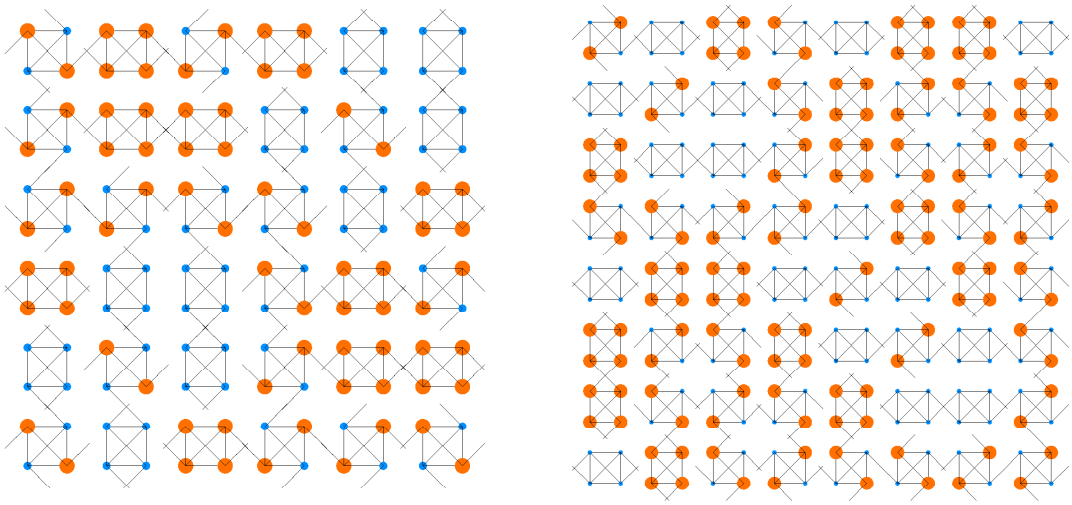

Figure 6.16: The snapshots of spin configurations for $D/J = 2 \cdot 10^{-4}$ at T=0.1. Data for L=3 and L=4 is shown in the left and right panel, respectively. Only one layer of tetrahedra is shown. The direction of the projection is chosen to be consistent with Figs. 6.3, 6.4 and 6.5. The angles, θ_i, are indicated by lines showing a spin direction, by color and by symbol size. The angles rounded for clarity.

in the system in this crossover from the thermally-selected Champion-Holdsworth state and the energetically-selected of Palmer-Chalker state, we analyze a snapshot of a spin configuration for $D/J = 2 \cdot 10^{-4}$ at T=0.1. The histograms of local angles, θ_i, in one spin configuration snapshot are shown in Figure 6.15. The histograms contain N=432 and N=1024 data points, i. e. equal to the number of spins for L=3 and L=4, respectively. The angle distributions are clearly concentrated around two values: 90 and 270 degrees for L=3, and 30 and 210 degrees for L=4. Each of these angle pairs corresponds to one of the Palmer-Chalker states (see Table 6.3). The peaks in the angle distributions are very broad. The histograms of spin angles for individual sublattices were also constructed. They all have two-peak structure, similar to those in Fig. 6.15, and not just one peak that would indicate the same angle on all the sites of the considered sublattice. This means that there is no $\boldsymbol{q}$=0 ordering, not only that the distribution of angles is broad.

To visualize the spin configurations, we create projections of one layer of the cubic unit cells; that is 9 cells for L=3 and 16 cells for L=4, respectively. Each cell contains 4 tetrahedra and 16 spins. The distribution of angles is very broad and analyzing the configuration would not be possible, if exact values of all angles were shown. To clarify the image we round each angle to the closest "Palmer-Chalker angle" from the pair of the "Palmer-Chalker angles" that were obtained for the data set considered, i.e. 90 or 270 degrees for L=3 and 30 or 210 degrees for L=4 respectively (as in the the histograms in Fig. 6.15). This spin projections are shown in Fig. 6.16. The spin direction is indicated both by a line and by a color and size of a lattice site. The projection planes were chosen separately for L=3 and L=4, to provide a view consistent with the 2D projections in Fig. 6.4 and Fig. 6.5. The general character of the spin configurations for L=3 and L=4 is quite similar. Let us focus on the L=4 case here, to simplify the discussion by referring to a single set of angles, the one that was obtained for L=4. There are two types of single tetrahedron spin arrangements present in Fig. 6.16. Roughly half of the tetrahedra have the Palmer-Chalker spin arrangement, either (30, 210, 30, 120) or (210, 30, 30, 210) degrees, which are two configurations given by spin inversion. Another half of the tetrahedra are in the "defected Palmer-Chalker" states, like that in Figure 6.5. Such arrangements are created by flipping a pair of parallel spins in the Palmer-Chalker state. Note that in this "defected Palmer-Chalker" state all angles are equal, as in the Champion-Holdsworth state. Because of

this configuration of angles, one can say that this configuration is "more similar" to the Champion-Holdsworth state than is the Palmer-Chalker state - to transform the "defected Palmer-Chalker" state into the Champion-Holdsworth state a rotation of all spin by 30 degrees is required, while to transform the Palmer-Chalker" state into the Champion-Holdsworth state two spins have to be rotated by 150 degrees.

One can ask if this partialy ordered state which was obtained here for $D/J = 2 \cdot 10^{-4}$ is somehow similar in origin to the partially ordered phase which was found by Chern *et al.* [220] in the pyrochlore Heisenberg antiferromagnet with first-, J_1, and second-nearest-neighbour, J_2, intearctions. To answer this question, to look for some spatial correlations between the type of local order on the tetrahedra, i.e. the Palmer-Chalker and the "defected Palmer-Chalker" state, a more systematic analysis of spin configuration snapshots is needed.

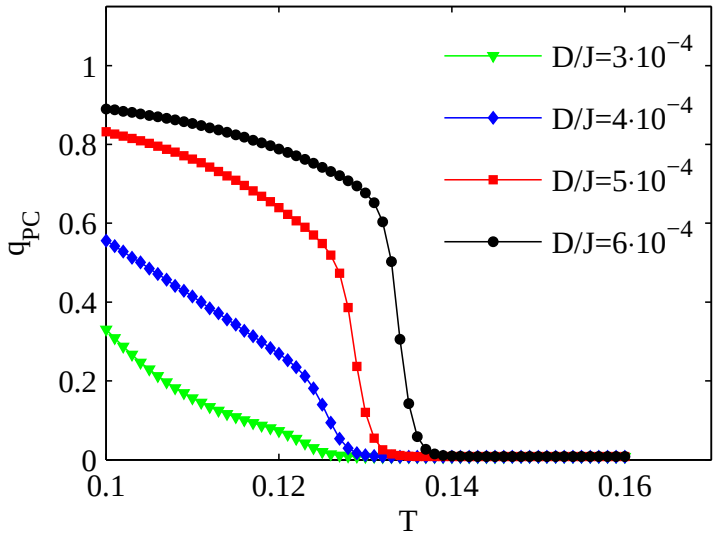

Figure 6.17: q_{PC} vs T for $D/J = 3 \cdot 10^{-4}$, $4 \cdot 10^{-4}$, $5 \cdot 10^{-4}$ and $6 \cdot 10^{-4}$, L=3.

Upon further increase of D/J, the value of q_{PC} increases while q_{CH} vanishes. In Figure 6.17 we plot q_{PC} for $D = 3 \cdot 10^{-4}$, $4 \cdot 10^{-4}$, $5 \cdot 10^{-4}$ and $6 \cdot 10^{-4}$. In this regime we show only data for L=3 because equilibrating L=4 was not possible (see Appendix E). Clearly q_{PC} increases with an increase of D/J.

It is difficult to establish the exact value of D/J separating the entropic selection of the Champion-Holdsworth state and energetic selection of the ground state - the

Palmer-Chalker state. Based on the data presented here it can be estimated to be around $D/J = 2 \cdot 10^{-4}$.

6.6 Summary

In this chapter, Monte Carlo studies of the easy-plane pyrochlore antiferromagnet with dipolar interactions were presented. The model was studied in the context of the XY-like pyrochlore antiferromagnet $Er_2Ti_2O_7$. In the neutron scattering experiments [37, 61, 84, 208] it was found that $Er_2Ti_2O_7$ undergoes a second order transition to the Champion-Holdsworth state. This result was compared with Monte Carlo studies of the easy-plane pyrochlore antiferromagnet [37, 60, 61]. The easy-plane pyrochlore antiferromagnet undergoes an order-by-disorder first order transition to the Champion-Holdsworth state. It was already recognized by the authors or Refs. [37, 61] that the thermal selection of the Champion-Holdsworth state that was observed in Monte Carlo simulations of the easy-plane pyrochlore antiferromagnet is not a likely explanation of the physics of $Er_2Ti_2O_7$. One of the reasons is that the dipolar interaction that is present in $Er_2Ti_2O_7$ lifts the degeneracy of the ground-state manifold of the easy-plane pyrochlore antiferromagnet and selects the Palmer-Chalker configuration as the ground state [67].

In our work we simulated the easy-plane pyrochlore antiferromagnet with dipolar interactions. Our aim was to check at what relative value of the dipolar coupling strength compared to the exchange interaction the energetic selection of the Palmer-Chalker suppresses the entropic selection of the Champion-Holdsworth state. We found that the boundary value of the relative strength of the dipolar coupling is $D/J \simeq 2 \cdot 10^{-4}$. The dipolar coupling constant, D, that was used in the simulation is corresponding to the distances measured in units of the lattice constant, a, and the nearest-neighbour dipolar coupling is $D_{\mathrm{nn}} = D/r_{\mathrm{nn}} = D/\left(\sqrt{2}/4\right)^3$. Hence, we got $D_{\mathrm{nn}}/J \simeq 0.005$. This is significantly lower value than the ratio of the dipolar coupling and exchange coupling for $Er_2Ti_2O_7$, that we estimated to be of order of $D_{\mathrm{nn}}/J \simeq 0.2$ (see Section 6.1). Hence, the model studied does not explain the physics of $Er_2Ti_2O_7$. It is possible that some other types of interactions can be at play, which, by destabilising the energetic selection of the Palmer-Chalker state, may promote entropic selection

of the Champion-Holdsworth state. It was also suggested that quantum fluctuations can stabilize the order-by-disorder selection in $Er_2Ti_2O_7$ [37, 61].

Simulations of first order phase transitions are difficult due to the energy barrier between an ordered state and the paramagnetic phase. In the zero dipolar coupling case, D=0 and for $D > 0$, where the Champion-Holdsworth state is selected, we were able to simulate system sizes up to L=5. In the regime were the Palmer-Chalker state is selected, performing unusually large number, 10^8, of Monte Carlo sweeps, we managed to equilibrate only the simulations for L=3. This peculiar behaviour may be a topic of a future studies. Can the slow dynamics be attributed to the competition of order-by-disorder and energetic selection? Or, maybe, it just originates in the specific features of the easy-plane pyrochlore antiferromagnet?

Chapter 7

Conclusion

In this work we considered four theoretical problems motivated by or related to experimental studies of magnetic materials. In Chapter 3, we investigated the effect of transverse-field-induced longitudinal random field [25] in the diluted dipolar Ising material $LiHo_xY_{1-x}F_4$. Using a local mean-field theory applied to an effective spin-1/2 Hamiltonian we mapped a phase diagram in the parameter space of temperature, T, transverse magnetic field, B_x, and concentration of magnetic ions, x. The temperature, T, vs Ho^{3+} concentration, x, phase diagram obtained for zero transverse field, B_x=0, is in quasi-quantitative agreement with the experimental phase diagram proposed by Reich *et al.* Ref. [117], with the distinction that the spin-glass phase extends down to $x = 0$. This is in agreement with earlier mean-field studies predicting that either spin-glass or ferromagnetic ordering persist down to x=0 [136, 166]. This is also in agreement with recent experimental studies [119, 135] that found a spin-glass transition in experiments on $LiHo_{0.045}Y_{0.955}F_4$, contradicting earlier studies [13, 14, 117] suggesting a novel anti-glass state and not a spin-glass phase for this concentration of magnetic ions.

The experimental studies show that in the low dilution regime the rate of depressing the critical temperature, T_c, by the transverse field, B_x, is larger than basic mean-field theory predicts. It was shown that this effect can be accounted for in a local mean-field calculation that includes the effect of transverse-field-induced longitudinal random field [25]. But the phase boundary, T_c vs B_x calculated in Ref. [25] is restricted to low values of magnetic field B_x. We recognized that this restriction is due to the

effect of finite-size tail in magnetization plots and the geometry of the problem in the parameter space (T ,B_x ,x). By looking for a signature of a phase transition when concentration, x, and not T or B_x is varied, we were able to identify the phase boundaries in the broad range of transverse field, B_x.

The main accomplishment of our local mean-field studies, is using local free energy minima counting as a method to recognise a spin-glass phase. Using this method, we were able to obtain the spin-glass phase boundary at $B_x = 0$ and to show that for $B_x > 0$ the spin-glass phase is suppressed by a formation of a state with spins aligned along the longitudinal random field.

The technique used in Chapter 3 to study $LiHo_xY_{1-x}F_4$, i.e. the local mean-field theory applied to an effective spin-1/2 Hamiltonian suffers from two sources of systematic error. First of them is neglecting the effect of thermal fluctuations, which is inherent to mean-field method. While the classical, i.e. $B_x = 0$, case can be studied by classical Monte Carlo simulations and the pure case, $x = 1$, in transverse field can be simulated using quantum Monte Carlo methods [1, 127], Monte Carlo studies of the effect of transverse field and dilution simultaneously are difficult, if not impossible. Hence, this source of inaccuracy is difficult to eliminate. The second factor limiting the accuracy of our calculation is neglecting the hyperfine interaction, which was shown to have a significant effect in the strong transverse field, i.e. close to the quantum phase transition [10, 127]. Including hyperfine interaction requires diagonalising 136×136 matrices. The local mean-field method is computationally intensive due to considering a large number of local magnetizations, performing disorder averages and repeating the calculations for multiple random initial conditions in order to count the local free energy minima in the glassy state. Adding hyperfine interaction will increase the computational complexity, but, in principle, performing such calculation, for limited number of points in the parameter space should, be possible.

In Chapter 4 we studied $Ho(OH)_3$, $Dy(OH)_3$ and $Tb(OH)_3$ magnetic materials to assess their suitability for experimental studies of quantum criticality and, in their diluted form: $Ho_xY_{1-x}(OH)_3$, $Dy_xY_{1-x}(OH)_3$ and $Tb_xY_{1-x}(OH)_3$, effects of transverse-field-induced longitudinal random field. We used mean field theory to estimate the value of transverse magnetic field, B_x^c, that, at zero temperature, destroys ferromagnetic order and brings the system to quantum paramagnetic phase. We obtained B_x^c =4.35 T, B_x^c =5.03 T and B_x^c =54.81 T for $Ho(OH)_3$, $Dy(OH)_3$ and $Tb(OH)_3$,

respectively. B_x^c for $Tb(OH)_3$ is too large to be obtained in a laboratory. $Ho(OH)_3$ was found to be very similar to $LiHoF_4$ in its low-temperature magnetic properties, and $Ho(OH)_3$ seems to be a good candidate to exhibit the phenomena observed in $LiHoF_4$. In the case of $Dy(OH)_3$ we found that for the values of B_x close to B_x^c, the phase transition between the ferromagnetic and paramagnetic phases is first order. This effect is strongly dependent on the parameters of the model, e.g. on the crystal field parameters which are not known with very high level of accuracy; hence, a first order transition may, or may not occur in the real material.

In Chapter 5, we provided a compelling evidence that in a system of spatially disordered Heisenberg dipoles there is a thermodynamical phase transition to a spin-glass phase. A diluted dipolar Heisenberg spin glass have not been yet observed experimentally, but there do exist magnetic materials that are likely to be a realisation of a diluted dipolar Heisenberg spin glass. Good candidates are diluted gadolinium compounds $(Gd_xY_{1-x})_2Ti_2O_7$, $(Gd_xY_{1-x})_2Sn_2O_7$ and $(Gd_xY_{1-x})_3Ga_5O_{12}$. We studied the systems of Heisenberg dipoles randomly placed on the simple cubic lattice at concentrations x=0.0625 and x=0.125. We performed a finite-size scaling analysis of the spin-glass correlation length, ξ_L, and the spin-glass susceptibility, χ_{SG}. We calculated the critical exponents ν and η. From our calculations, for both concentrations and considering both ξ_L and χ_{SG}, we obtained ν between 1.1 and 1.25. The values obtained for the exponent η are 1.35 and 1.45, for $x = 0.125$ and $x = 0.0625$, respectively. Due to a slow equilibration and computationally expensive summation of long-range interactions, we were able to study only a small number of relatively small system sizes. Because of that limitation, the accuracy of our data is relatively low, and we were not able to include scaling corrections in out finite-size scaling analysis.

In Chapter 6, we studied the pyrochlore easy-plane antiferromagnet with dipolar interaction in the context of frustrated magnetic material $Er_2Ti_2O_7$. Er^{3+} ions in the crystalline environment of $Er_2Ti_2O_7$ are found to be a good realisation of local-easy-plane XY spins [36]. Neutron scattering studies reveal that $Er_2Ti_2O_7$ undergoes a continuous phase transition and orders in the so-called Champion-Holdsworth state [37, 84, 208]. This is in disagreement with the fact that the ground state of the easy-plane pyrochlore antiferromagnet with dipolar interaction is not the Champion-Holdsworth state but the so-called Palmer-Chalker state [67]. It was demonstrated that without considering dipolar interaction the easy-plane pyrochlore antiferromag-

net has a continuously degenerate ground-state manifold and undergoes the order-by-disorder transition to the Champion-Holdsworth state [37, 60, 61]. Using Monte Carlo simulations we showed that, even though the the ground state of the easy-plane pyrochlore antiferromagnet with dipolar interaction is the Palmer-Chalker state, the order-by-disorder selection of the Champion-Holdsworth state, for some range of temperatures, persist for small values of dipolar coupling strength. Nevertheless, the upper bound of dipolar to exchange coupling ratio where the thermal selection of the Champion-Holdsworth state persist, which was found in our simulations, is significantly lower than the ratio of the dipolar to exchange coupling strength we estimated for $Er_2Ti_2O_7$. This indicates that other possibilities have to be considered in order to explain the physics of $Er_2Ti_2O_7$. One of the them is including other types of interactions that would destabilise energetic selection of the Palmer-Chalker state and that way promote entropic selection of the Champion-Holdsworth state. Another possibility is that quantum fluctuations are stabilising the order-by-disorder selection of the Champion-Holdsworth state.

We hope that out work will stimulate interest in experimental studies of such materials like $Ho_xY_{1-x}(OH)_3$ and $Dy_xY_{1-x}(OH)_3$ in the context of quantum criticality, dipolar diluted Ising spin glass and physics of transverse field Ising model, or the mentioned above diluted gadolinium compounds, in the context of a diluted dipolar Heisenberg spin glass.

Theoretically, the local mean-field studies of transverse field diluted dipolar Ising system, $LiHo_xY_{1-x}F_4$, with counting of local free energy minima turned out to be a useful technique for studies of competition of random frustration and random field effects in this material. It might become valuable theoretical tool complementing eventual experimental studies of $Ho_xY_{1-x}(OH)_3$. The accuracy of local mean-field studies for diluted holmium compounds in a transverse magnetic field can be improved by including the hyperfine interaction. The problem of $Er_2Ti_2O_7$ still remains unsolved. We showed that there is a regime where the order-by-disorder selection wins the competition with energetic selection of the ground state, but, in the model studied, the tendency to select the Palmer-Chalker ground state is strong even with very weak dipolar coupling. A likely avenue that may lead to understanding the physics of $Er_2Ti_2O_7$ is to search for possible factors that may destabilise the selection of the Palmer-Chalker ground state.

APPENDICES

Appendix A

Perturbative calculation of the phase diagram in $Dy(OH)_3$

To investigate the role of the J_z matrix elements between the two lowest states and the first excited levels on the magnetic behaviour of $Dy(OH)_3$, we calculate the critical temperature for a second order transition using second order perturbation theory. This method is exact in the second order phase transition regime, where B_x is less than the tricritical field value, B_x^{TCP} ($B_x^{\mathrm{TCP}} = 4.85$ T when using the CFP of Scott *et al.*).

For a given value of the transverse field, B_x, and the corresponding value of average magnetization in transverse direction, $\langle J_x \rangle$, we consider $\mathcal{L}_{zz} J_z \langle J_z \rangle$ term as a perturbation to the reference mean-field Hamiltonian,

$$\mathcal{H}_0 = \mathcal{H}_{\mathrm{cf}}(\boldsymbol{J}_i) - g\mu_{\mathrm{B}} B_x J_x + \mathcal{L}_{xx} J_x \langle J_x \rangle , \tag{A.1}$$

describing the PM phase at a temperature $T > T_c(B_x)$ as in Eq. 4.6 Here too, we have dropped the constant terms. The eigenvalues, E_p, and eigenstates, $|p\rangle$, of the perturbed Hamiltonian,

$$\mathcal{H} = \mathcal{H}_0 + \mathcal{L}_{zz} J_z \langle J_z \rangle , \tag{A.2}$$

are written in terms of eigenvalues, $E_p^{(0)}$, and eigenstates, $\left|p^{(0)}\right\rangle$, of the unperturbed Hamiltonian, $\mathcal{H}_0$, of Eq. (A.1),

$$E_p = E_p^{(0)} + \langle J_z \rangle E_p^{(1)} + \langle J_z \rangle^2 E_p^{(2)}, \tag{A.3}$$

$$|p\rangle = |p^{(0)}\rangle + \langle J_z\rangle \sum_{k\neq p} c^{(1)}_{p,k}|k^{(0)}\rangle. \tag{A.4}$$

The coefficients of the perturbative expansion are given by

$$E^{(1)}_p = \mathcal{L}_{zz} J^z_{pp}, \tag{A.5}$$

$$E^{(2)}_p = \sum_{k\neq p} \frac{\mathcal{L}^2_{zz}|J^z_{kp}|^2}{E^{(0)}_p - E^{(0)}_k} \tag{A.6}$$

and

$$c^{(1)}_{pk} = \frac{\mathcal{L}_{zz} J^z_{kp}}{E^{(0)}_p - E^{(0)}_k}, \tag{A.7}$$

where $J^z_{kp} = \left\langle k^{(0)}\right| J_z \left|p^{(0)}\right\rangle$ are the matrix elements of the J_z operator in the basis of eigenvectors of the unperturbed Hamiltonian, $\mathcal{H}_0$. The applied magnetic field, B_x, lifts the degeneracy of the Kramers doublets, thus we can use the non-degenerate perturbation method. The diagonal elements of the J_z operator vanish, hence, the first order correction to energy vanish, $E^{(1)}_p = J^z_{pp} = 0$.

We calculate the thermal average of the J_z operator,

$$\langle J_z\rangle = \sum_p \langle p| J_z |p\rangle \, e^{-E_p/T}/Z, \tag{A.8}$$

using the perturbed eigenstates, $|p\rangle$, and eigenvalues, E_p, and where $Z = \sum_p e^{-E_p/T}$. Keeping only terms up to third order in $\langle J_z\rangle$ in the expansion of Eq. (A.8), we find

$$\frac{1}{Z} e^{-E_p/T} = n^{(0)}_p \left(1 + K_p \langle J_z\rangle^2\right) \tag{A.9}$$

and

$$\langle p| J_z |p\rangle = 2\mathcal{L}_{zz} \langle J_z\rangle \sum_{k\neq p} \frac{|J^z_{pk}|^2}{E^{(0)}_p - E^{(0)}_k}, \tag{A.10}$$

where, for convenience, we write $n^{(0)}_p = e^{-E^{(0)}_p/T}/Z^{(0)}$, $Z^{(0)} = \sum_p e^{-E^{(0)}_p/T}$ and $K_p = \frac{1}{T}\left(\sum_k n^{(0)}_k E^{(2)}_k - E^{(2)}_p\right)$. Thus, we can write

$$\langle J_z\rangle = 2\langle J_z\rangle \sum_p n^{(0)}_p \left(1 + K_p \langle J_z\rangle^2\right) \sum_{k\neq p} \frac{\mathcal{L}_{zz}|J^z_{pk}|^2}{E^{(0)}_p - E^{(0)}_k}, \tag{A.11}$$

and finally, we get

$$\langle J_z \rangle^2 = \frac{1 - 2\sum_{p,k\neq p} n_p^{(0)} \frac{\mathcal{L}_{zz}|J_{pk}^z|^2}{E_p^{(0)} - E_k^{(0)}}}{2\sum_{p,k\neq p} n_p^{(0)} K_p \frac{\mathcal{L}_{zz}|J_{pk}^z|^2}{E_p^{(0)} - E_k^{(0)}}}. \tag{A.12}$$

Putting $\langle J_z \rangle = 0$ in Eq. (A.12) we obtain the condition for the critical temperature T_c:

$$2\sum_{p,k\neq p} \frac{\mathcal{L}_{zz}|J_{pk}^z|^2}{E_p^{(0)} - E_k^{(0)}} e^{\frac{-E_p^{(0)}}{T_c}} = 1. \tag{A.13}$$

In solving Eq. (A.13) for T_c, we have to self-consistently update the value of $\langle J_x \rangle$ in order to diagonalize $\mathcal{H}_0$ in Eq. (A.1) and to find $E_p^{(0)}$. Solving Eq. (A.13) with only the 4 lowest energy eigenstates (after diagonalizing the full transverse field Hamiltonian of Eq. (4.3)), yields a phase diagram that is in good agreement for $B_x < B_x^{\rm TCP}$ with the phase boundary obtained with all crystal field eigenstates (or equivalently from Eq. (4.7)). Estimating the values of the elements of the sum in Eq. (A.13), one can see that the matrix elements of the J_z operator, mixing the two lowest states with the excited states, may bring a substantial correction to the value of the critical temperature obtained when only the two lowest eigenstates are considered. In the low temperature regime, one could omit the matrix elements between the states of the excited doublet, but we have to keep the matrix elements between the states of the ground doublet and first excited doublet. The contribution from the further exited states is quite small because of the increasing value of the energy gap present in the denominator in Eq. (A.13).

At T=0, Eq. (A.10) leads to the equation for the critical transverse field, B_x^c:

$$2\sum_{k\neq 1} \frac{\mathcal{L}_{zz}|J_{1k}^z(B_x^c)|^2}{E_1^{(0)}(B_x^c) - E_k^{(0)}(B_x^c)} = 1. \tag{A.14}$$

Again, we see that the matrix elements of J^z operator, admixing the ground state with excited levels, have to be considered. Note that since Eq. (A.14) pertains to the case of zero temperature, this equation is only valid in a regime where the transition is second order (i.e. when $J_{\rm ex} > J_{\rm ex}^{\rm 2nd}$).

Appendix B

Magnetization and staggered magnetization

To rule out the presence of a long range order we calculate the magnetization and staggered magnetisation. The thermal and disorder averaged magnitude of magnetization is defined as

$$M = \left[\left\langle \left| \frac{1}{N} \sum_{i=1}^{N} \boldsymbol{S}_i \right| \right\rangle \right], \tag{B.1}$$

where $\langle \ldots \rangle$ denotes thermal averaging and $[\ldots]$ is a disorder average.

A system of dipoles in fully occupied SC lattice orders antiferromagnetically [52]. The ground state (GS) of such antiferromagnet is described by a spin vector with the following components: [52, 221]

$$\begin{aligned} S_i^x &= \tau_i^x \sin\theta \cos\phi, \\ S_i^y &= \tau_i^y \sin\theta \sin\phi \quad , \\ S_i^z &= \tau_i^z \cos\theta, \end{aligned} \tag{B.2}$$

Such GS has two rotational degrees of freedom: polar angle, θ, and azimuthal angle, ϕ. $\boldsymbol{\tau}_i \equiv [\tau_i^x, \tau_i^y, \tau_i^z]$ is given by

$$\boldsymbol{\tau}_i = [(-1)^{r_i^y + r_i^z}, (-1)^{r_i^x + r_i^z}, (-1)^{r_i^x + r_i^y}]. \tag{B.3}$$

$\boldsymbol{r}_i$ is the position of site i, measured in units of lattice constant, and its vector com-

ponents, r_i^x, r_i^y and r_i^y, on SC lattice, are all integers. The staggered magnetization, which is indicating ordering described by Eqs. (B.2), is given by

$$M_{\text{stag}} = \left[\left\langle \left| \frac{1}{N} \sum_{i=1}^{N} \boldsymbol{S}_i \boldsymbol{\tau}_i \right| \right\rangle \right] . \tag{B.4}$$

In Figs. B.1 and B.2 we plot the magnetization, M, and the staggered magnetization, M_{stag}, for x=0.0625 and x=0.125, respectively. M has a small value that decreases with system size, L; this indicates that nonzero magnetization is just a finite-size effect and not an indication of long-range order. Furthermore, M remains constant at all temperatures and does not increase below T_g. The fairy large magnetization indicates that the finite-size effects are large, and thus the scaling corrections are expected to be large. The staggered magnetization, M_{stag}, is smaller than the magnetization, M. M_{stag}, similarly to M, decreases with increasing system size, L, and there are no features indicating ordering transition.

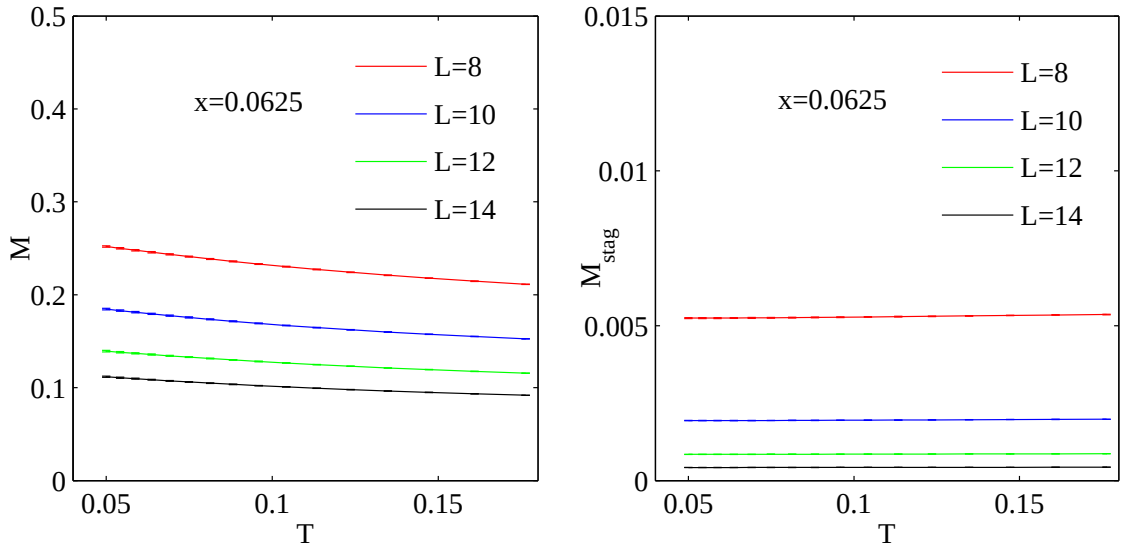

Figure B.1: Magnetization, M, and staggered magnetization, M_{stag}, x=0.0625.

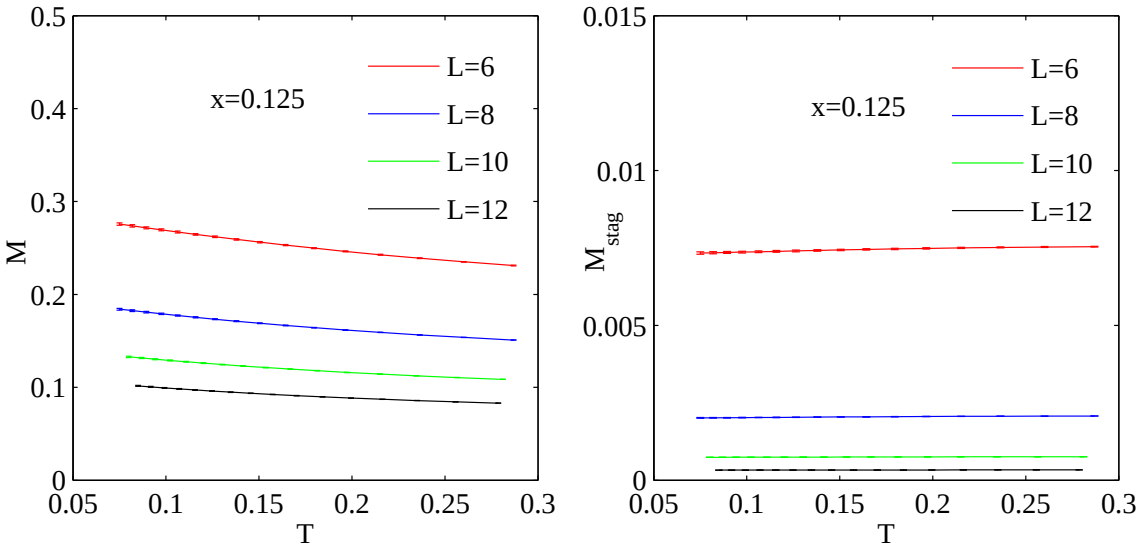

Figure B.2: Magnetization, M, and staggered magnetization, M_{stag}, x=0.125.

Appendix C

Periodic boundary conditions and self-interaction

We consider a dipolar Hamiltonian of the form

$$\mathcal{H} = \frac{1}{2}\epsilon_d \sum_{i,j,\mu,\nu} \frac{\delta^{\mu\nu} r_{ij}^2 - 3r_{ij}^\mu r_{ij}^\nu}{r_{ij}^5} S^\mu(\boldsymbol{r}_i) S^\nu(\boldsymbol{r}_j), \tag{C.1}$$

where μ and ν are vector components, μ,ν=x, y or z. It can be written as

$$\mathcal{H} = \frac{1}{2}\epsilon_d \sum_{i,j,\mu.\nu} \mathcal{L}_{ij}^{\mu\nu} S_i^\mu S_j^\nu, \tag{C.2}$$

or shorter

$$\mathcal{H} = \frac{1}{2}\epsilon_d \sum_{i,j} \boldsymbol{S}_i \hat{\mathcal{L}}_{ij} \boldsymbol{S}_j, \tag{C.3}$$

where

$$\mathcal{L}_{ij} = \mathcal{L}(\boldsymbol{r}_{ij}) = \frac{\delta_{ij} |\boldsymbol{r}_{ij}|^2 - 3r_{ij}^\mu r_{ij}^\nu}{|\boldsymbol{r}_{ij}|^5}. \tag{C.4}$$

To impose periodic boundary conditions, we replace the coupling tensor, $\mathcal{L}_{ij}$, with

$$L_{ij}^{\mu\nu} = {\sum_{\boldsymbol{n}}}' \frac{\delta_{ij} |\boldsymbol{r}_{ij} + \boldsymbol{n}|^2 - 3(\boldsymbol{r}_{ij} + \boldsymbol{n})^\mu (\boldsymbol{r}_{ij} + \boldsymbol{n})^\nu}{|\boldsymbol{r}_{ij} + \boldsymbol{n}|^5}, \tag{C.5}$$

where $\boldsymbol{n} = kL\hat{x} + lL\hat{y} + mL\hat{z}$; k, l, m are integers and $\hat{x}$, $\hat{y}$ and $\hat{z}$ are unit vectors. L is the linear dimension of the cubic simulation box. $\sum_{\boldsymbol{n}}{}'$ means that the summation does not include the $\boldsymbol{n}$=0 term for $i = j$, where $\boldsymbol{r}_{ij} = 0$. One must be aware of the presence of the self-interaction term

$$L_{ii}^{\mu\nu} = \sum_{\boldsymbol{n}\neq\boldsymbol{0}} \frac{\delta_{ij} \left|\boldsymbol{n}\right|^2 - 3\boldsymbol{n}^{\mu}\boldsymbol{n}^{\nu}}{\left|\boldsymbol{n}\right|^5}. \tag{C.6}$$

The self-interaction term describes the interaction of a dipole with its own periodic images replicated outside the simulation box. For a cubic simulation box it reduces to a simple form $L_{ii}^{\mu\nu} = L_{ii}\delta_{\mu\nu}$. To show that the off-diagonal terms are zero, for $\mu \neq \nu$ we write

$$L_{ii}^{\mu\nu} = -3 \sum_{\boldsymbol{n}\neq\boldsymbol{0},\boldsymbol{n}^{\mu}>\boldsymbol{0}} \frac{\boldsymbol{n}^{\mu}\boldsymbol{n}^{\nu} + \left(-\boldsymbol{n}^{\mu}\right)\boldsymbol{n}^{\nu}}{\left|\boldsymbol{n}\right|^5} = 0. \tag{C.7}$$

And further, in cubic symmetry, all three directions $\hat{x}$, $\hat{y}$ and $\hat{z}$ are equivalent; hence, $L_{ii}^{xx} = L_{ii}^{yy} = L_{ii}^{zz}$.

Appendix D

Ewald summation

We wish to calculate the lattice sum

$$L_{ij}^{\mu\nu} = \sum_{\boldsymbol{n}}{}' \frac{\delta_{ij} \left|\boldsymbol{r}_{ij}+\boldsymbol{n}\right|^2 - 3(\boldsymbol{r}_{ij}+\boldsymbol{n})^{\mu}(\boldsymbol{r}_{ij}+\boldsymbol{n})^{\nu}}{\left|\boldsymbol{r}_{ij}+\boldsymbol{n}\right|^5}. \tag{D.1}$$

The prime with the summation sign means that for $i = j$ the sum does not include the $\boldsymbol{n}$=0 term. Noting that

$$-\nabla_{\mu}\nabla_{\nu}\frac{1}{\boldsymbol{r}} = \frac{\delta_{\mu\nu}r^2 - 3r_{\mu}r_{\nu}}{r^5}, \tag{D.2}$$

we write

$$L_{ij}^{\mu\nu} = -\nabla_{\mu}\nabla_{\nu}\sum_{\boldsymbol{n}}{}' \frac{1}{\left|\boldsymbol{r}_{ij}+\boldsymbol{n}\right|}; \tag{D.3}$$

hence, we may calculate the lattice summation for Coulomb potential and obtain the sums for dipolar interactions by taking derivatives afterwards.

The infinite sum (D.3) is conditionally convergent, that means that the result depends on the asymptotic order of summation. The Coulomb or dipolar potential is slowly decaying at large distances; hence, with direct summation it converges slowly. To alleviate these problems, the summation is to be performed by the method introduced by Ewald [76–79]. In Ewald technique, we separate the summation into two rapidly convergent sums: one performed in the direct (real) space and the other sum performed in the reciprocal space. Here we show only simplified derivation, rigorous

mathematical proofs and detailed discussions can be found in Ref. [78].

Using the relation

$$\frac{1}{r} = \frac{2}{\sqrt{\pi}} \int_0^\infty e^{-r^2\rho^2} d\rho, \tag{D.4}$$

we write

$$\frac{1}{r} = \frac{2}{\sqrt{\pi}} \int_0^\alpha e^{-r^2\rho^2} d\rho + \frac{\mathrm{erfc}(\alpha r)}{r}, \tag{D.5}$$

where

$$\mathrm{erfc}(x) = 1 - \mathrm{erf}(x) = \frac{2}{\sqrt{\pi}} \int_x^\infty e^{-y^2} dy \tag{D.6}$$

is the complementary error function. The second term in Eq. (D.5), for large α, is decreasing fast with increasing r; hence, converges rapidly in the summation over $\boldsymbol{n}$. The first term falls to zero slowly with increasing r, but it converges rapidly in a reciprocal space summation formulation. The splitting parameter α is chosen such that both real space and reciprocal space sums are converging fast. To obtain the reciprocal space summation term we use the relation

$$\frac{2}{\sqrt{\pi}} \sum_{\boldsymbol{n}} e^{-(\boldsymbol{r}+\boldsymbol{n})^2\rho^2} = \frac{2\pi}{L^3} \sum_{\boldsymbol{K}} \rho^{-3} e^{-K^2/4\rho^2} e^{i\boldsymbol{K}\boldsymbol{r}}, \tag{D.7}$$

where $\boldsymbol{K}$ are the reciprocal lattice vectors associated to the simulation cell, $\boldsymbol{n} = kL\hat{x} + lL\hat{y} + mL\hat{z}$; k, l, m are integers and $\hat{x}$, $\hat{y}$ and $\hat{z}$ are unit vectors. Some care must be taken to account for the particular case of r=0 that is corresponding to self-interaction (C.6). In that case, n=0 should be excluded from the summation (D.3) and we write

$$\frac{2}{\sqrt{\pi}} \sum_{\boldsymbol{n}\neq 0} e^{-(\boldsymbol{r}+\boldsymbol{n})^2\rho^2} = \frac{2\pi}{L^3} \sum_{\boldsymbol{K}} \rho^{-3} e^{-K^2/4\rho^2} e^{i\boldsymbol{K}\boldsymbol{r}} - \frac{2}{\sqrt{\pi}} e^{-\boldsymbol{r}^2\rho^2}. \tag{D.8}$$

Noting that

$$\int_0^\alpha d\rho\, \rho^{-3} e^{-K^2/4\rho^2} = \frac{2}{K^2} e^{-K^2/4\alpha^2}, \tag{D.9}$$

we can write

$$\sum_{\boldsymbol{n}}{}' \frac{1}{|\boldsymbol{r}_{ij}+\boldsymbol{n}|} = \sum_{\boldsymbol{n}}{}' \frac{\mathrm{erfc}(\alpha\,|\boldsymbol{r}_{ij}+\boldsymbol{n}|)}{|\boldsymbol{r}_{ij}+\boldsymbol{n}|} + \sum_{\boldsymbol{K}\neq 0} \frac{4\pi}{L^3K^2} e^{-K^2/4\alpha^2} e^{i\boldsymbol{K}\boldsymbol{r}_{ij}} - \frac{2\alpha}{\sqrt{\pi}}\delta_{ij}. \tag{D.10}$$

The divergent, $\boldsymbol{K}$=0 term in reciprocal lattice summation is omitted.

To calculate dipolar the sum in (D.3), we need to take derivative of expression (D.8). To start, we compute

$$-\nabla_\mu\nabla_\nu \frac{\mathrm{erfc}(\alpha r)}{r} = \frac{\delta_{\mu\nu}B(r)r^2 - C(r)r_\mu r_\nu}{r^5}, \tag{D.11}$$

where

$$B(r) = \mathrm{erfc}(r) + \frac{2\alpha r}{\sqrt{\pi}} e^{-\alpha^2 r^2}, \tag{D.12}$$

and

$$C(r) = 3\mathrm{erfc}(r) + \frac{2\alpha r(3+2\alpha^2 r^2)}{\sqrt{\pi}} e^{-\alpha^2 r^2}. \tag{D.13}$$

For the reciprocal space part we compute

$$-\nabla_\mu\nabla_\nu e^{i\boldsymbol{K}\boldsymbol{r}} = K_\mu K_\nu e^{i\boldsymbol{K}\boldsymbol{r}},$$

and to obtain the self term

$$-\nabla_\mu\nabla_\nu e^{-\boldsymbol{r}^2\rho^2} = 2\rho^2\left(\delta_{\mu\nu} - 2\rho^2 r_\mu r_\nu\right) e^{-r^2\rho^2}. \tag{D.14}$$

Finally, we have

$$L_{ij}^{\mu\nu} = \sum_{\boldsymbol{n}}{}' \frac{\delta_{\mu\nu}B(r_{ij})r_{ij}^2 - C(r_{ij})r_{ij}^\mu r_{ij}^\nu}{r^5} \tag{D.15}$$

$$+\frac{4\pi}{L^3}\sum_{\boldsymbol{K}\neq 0}\frac{K_\mu K_\nu}{K^2}e^{-K^2/4\alpha^2}e^{i\boldsymbol{K}\boldsymbol{r_{ij}}} \tag{D.16}$$

$$-\frac{4\alpha^3}{3\sqrt{\pi}}\delta_{\mu\nu}\delta_{ij}. \tag{D.17}$$

Similarly to Coulomb case (D.10), in the reciprocal space summation, divergent $\boldsymbol{K}$=0 term is omitted.

The effect of the magnetic polarization of the surface does not vanish in the thermodynamic limit. In the case of a spherical sample, or a summation over a series of spherical shells, the surface contribution to the total energy is [79]

$$U^{(\mathrm{surf})} = \frac{2\pi}{(2\epsilon'+1)L^3}\sum_{i,j}\boldsymbol{\mu}_i\boldsymbol{\mu}_j,$$

where ϵ' is the magnetic permeability of the surrounding medium. In the case of a long cylindrical shape the surface term is zero. In our simulations we set the surface term to zero; hence, we are implicitly considering a long, cylindrical sample, or we put $\epsilon' = \infty$, infinite magnetic permeability outside the considered system, so called "metallic boundary conditions", by analogy to the physical situation with electric, as opposed to magnetic dipoles.

Appendix E

Slow equilibration in simulations of the easy-plane pyrochlore antiferromagnet

In Monte Carlo simulations a certain number of Monte Carlo sweeps have to be carried out before the simulation equilibrates, i.e. reaches a steady state, where the configurations are sampled with the Boltzmann probability distribution that is corresponding to the simulated temperature. There is no universal way to find out how many Monte Carlo sweeps need to be carried out before equilibrium is reached. It depends on the simulated model, temperature and system size. Some systems equilibrate quite quickly; e.g. in simulations of unfrustrated Ising or Heisenberg ferromagnets usually an order of magnitude larger number of Monte Carlo sweeps is performed to obtain a good statistics for the measured observables than to equilibrate the system. On the opposite side, some systems are very hard to equilibrate. It happens in the situations when high energy barriers are present. An example of such systems are spin glasses. Another example of models difficult to equilibrate are system undergoing a first order phase transition. In the case of spin glasses, there is a large number of local energy minima in the phase space that are separated by high energy barriers. In the case of a first order phase transition, the energy barrier occurs between the ordered phase and paramagnetic phase.

It turns out that the simulations of the easy-plane pyrochlore antiferromagnet are

very difficult to equilibrate. One reason for that is that the transition is strongly first order. The difficulty of equilibrating a simulation of a first order phase transition increases with increase of the system size. The energy fluctuations decrease with increase of the number of spins, N, like $1/\sqrt{N}$. For small N, the fluctuations may be sufficient to overcome the energy barrier at the effective critical temperature, and the simulated system switches between ordered and disordered configurations. For a large N, the fluctuations are insufficient for the system to overcome the energy barrier, and in the vicinity of the transition temperature a hysteresis effect occurs - over some temperature range the system stays in the initial, either ordered or disordered state.

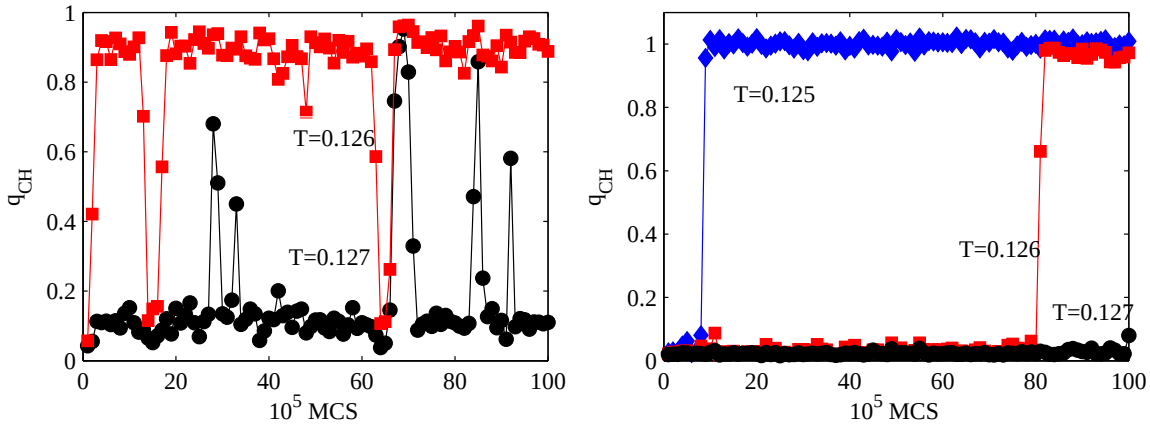

Figure E.1: Equilibration,, $q_{\rm CH}$ vs number of Monte Carlo sweeps (MCS) for D=0, L=5 (left) and L=6 (right).

For the Hamiltonian without dipolar interactions (see Section 6.5.1) we were able to equilibrate system sizes up to L=5. In Fig. E.1, we show evolution of the sublattice magnetization, M_4 of Eq. (6.26), with Monte Carlo time. The left panel shows M_4 vs number of Monte Carlo sweeps for L=5, at two temperatures: T=0.126 and T=0.127. The fact that at T=0.126 M_4 reaches a large value, that is corresponding to the ordered phase, and than switches back to the paramagnetic phase, for a short periods of Monte Carlo time, indicates that the the system just below the effective critical temperature, $T_c(L)$, and simulation is equilibrated. At T=0.127, the system is just above $T_c(L)$; it stays most of the time in the disordered state and occasionally switches to the ordered state for a short intervals of Monte Carlo time. In the right panel of Fig. E.1 equilibration for L=6 is shown for three values of temperature, T=0.125, T=0.126

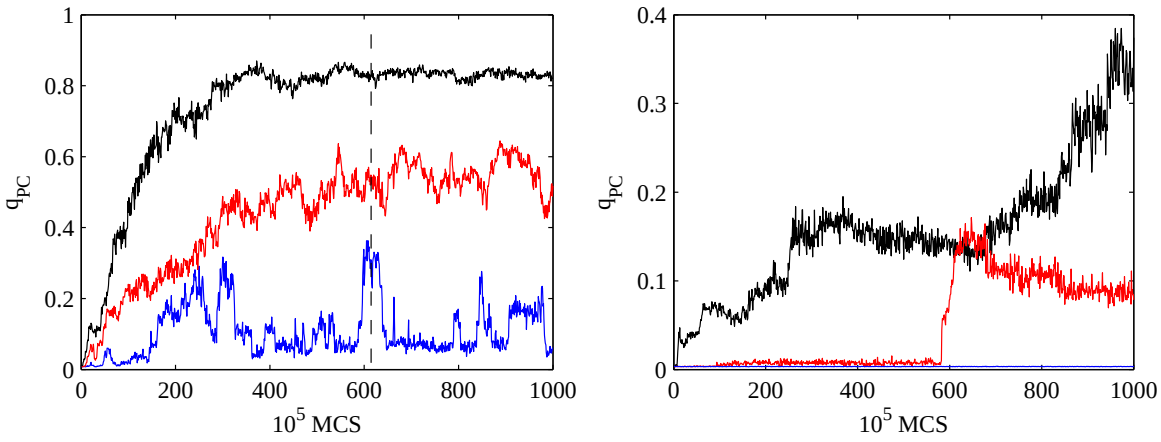

Figure E.2: Equilibration, q_{PC} vs number of Monte Carlo sweeps (MCS) for L=3 (left) and L=4 (right) with dipolar coupling $D/J = 5 \cdot 10^{-4}$.

and T=0.127. As the simulation progresses, ordered configurations are obtained at progresively higher temperatures. The simulation was started from a random initial configuration; hence, initially there is a large number of thermal replicas that are in disordered state, and because the thermal fluctuations are smaller than the energy barrier, the probability of "tunneling" from a disordered to an ordered configuration is low. There is no indication that the process of "tunneling" to the ordered configurations will not continue at higher temperatures if the simulation runs longer, i.e that the plot for T=0.127 will not exchibit a sharp increase of q_{PC}, similar to T=0.125 and T=0.126, after a sufficiently long equilibration. Hence, the simulation for L=6 is not yet equilibrated.

When a nonzero dipolar couplings are included in the Hamiltonian (see Section 6.5.2) the simulations get even more difficult to equilibrate. One reason for that can be increasing of the energy gap between the ordered and the disordered phase when strength of dipolar force increases. But the slowing down of the simulation dynamics is very large, and it is likely that there there are other reasons of this peculiar behavior - the dipolar couplings considered are very weak and thus the change of the energy barrier is expected to be small. In the regime where the dipolar coupling is large enough to induce ordering to the Palmer-Chalker state we were able to equilibrate the system sizes only up to L=3. In Fig. E.2 we show the evolution of the order parameter q_{PC} that indicates the ordering into the Palmer-Chalker state. For L=3

it clearly saturates after around $6 \cdot 10^7$ Monte Carlo sweeps. For $L = 4$, even after 10^8 Monte Carlo sweeps equilibrium is not reached yet. It seems that to equilibrate this L=4 simulation the number of Monte Carlo sweeps would have to be increased by more than one order of magnitude.

Bibliography

[1] S. M. A. Tabei, M. J. P. Gingras, Y.-J. Kao, and T. Yavors'kii, *Phys. Rev. B* **78**, 184408 (2008).

[2] C. A. Catanese and H. E. Meissner, *Phys. Rev. B* **8**, 2060 (1973).

[3] C. A. Catanese, A. T. Skjeltorp, H. E. Meissner, and W. P. Wolf, *Phys. Rev. B* **8**, 4223 (1973).

[4] E. Ising, *Z. Phys.* **31**, 253 (1925).

[5] L. Onsager, *Phys. Rev.* **65**, 1179 (1944).

[6] D. H. Reich, B. Ellman, J. Yang, T. F. Rosenbaum, G. Aeppli, and D. P. Belanger, *Phys. Rev. B* **42**, 4631 (1990).

[7] W. Wu, B. Ellman, T. F. Rosenbaum, G. Aeppli, and D. H. Reich, *Phys. Rev. Lett.* **67**, 2076 (1991).

[8] W. Wu, D. Bitko, T. F. Rosenbaum, and G. Aeppli, *Phys. Rev. Lett.* **71**, 1919 (1993).

[9] W. Wu, *Ph.D. thesis*, PhD thesis, U. of Chicago, 1992.

[10] D. Bitko, T. F. Rosenbaum, and G. Aeppli, *Phys. Rev. Lett.* **77**, 940 (1996).

[11] J. Brooke, D. Bitko, T. F. Rosenbaum, and G. Aeppli, *Science* **284**, 779 (1999).

[12] J. Brooke, *Ph.D. thesis*, PhD thesis, U. of Chicago, 2000.

[13] S. Ghosh, R. Parthasarathy, T. F. Rosenbaum, and G. Aeppli, *Science* **296**, 2195 (2002).

[14] S. Ghosh, T. F. Rosenbaum, G. Aeppli, and S. N. Coppersmith, *Nature* **425**, 48 (2003).

[15] H. M. Rønnow, R. Parthasarathy, J. Jensen, G. Aeppli, T. F. Rosenbaum, and D. F. McMorrow, *Science* **308**, 389 (2005).

[16] H. M. Rønnow, J. Jensen, R. Parthasarathy, G. Aeppli, T. F. Rosenbaum, D. F. McMorrow, and C. Kraemer, *Phys. Rev. B* **75**, 054426 (2007).

[17] D. M. Silevitch, D. Bitko, J. Brooke, S. Ghosh, G. Aeppli, and T. F. Rosenbaum, *Nature* **448**, 567 (2007).

[18] D. M. Silevitch, C. M. S. Gannarelli, A. J. Fisher, G. Aeppli, and T. F. Rosenbaum, *Phys. Rev. Lett* **99**, 057203 (2007).

[19] P. E. Jönsson, R. Mathieu, W. Wernsdorfer, A. M. Tkachuk, and B. Barbara, *Phys. Rev. Lett* **98**, 256403 (2007).

[20] C. Ancona-Torres, D. M. Silevitch, G. Aeppli, and T. F. Rosenbaum, *Phys. Rev. Lett.* **101**, 057201 (2008).

[21] P. E. Jönsson, R. Mathieu, W. Wernsdorfer, A. M. Tkachuk, and B. Barbara, *cond-mat/0803.1357* (2008).

[22] R. J. Elliott, P. Pfeuty, and C. Wood, *Phys. Rev. Lett.* **25**, 443 (1970).

[23] B. K. Chakrabarti, A. Dutta, and P. Sen, *Quantum Ising Phases and Transitions in Transverse Ising Models*, Spinger-Verlag, Heidelberg, 1996.

[24] M. Schechter and N. Laflorencie, *Phys. Rev. Lett.* **97**, 137204 (2006).

[25] S. M. A. Tabei, M. J. P. Gingras, Y.-J. Kao, P. Stasiak, and J.-Y. Fortin, *Phys. Rev. Lett.* **97**, 237203 (2006).

[26] S. M. A. Tabei, F. Vernay, and M. J. P. Gingras, *Phys. Rev. B* **77**, 014432 (2008).

[27] P. Stasiak and M. J. P. Gingras, *Phys. Rev. B* **78**, 224412 (2008).

[28] J. S. Gardner, M. J. P. Gingras, and J. E. Greedan, (to appear in Rev. Mod. Phys.).

[29] M. J. Harris, S. T. Bramwell, D. F. McMorrow, T. Zeiske, and K. W. Godfrey, *Phys. Rev. Lett.* **79**, 2554 (1997).

[30] S. T. Bramwell and M. J. P. Gingras, *Science* **294**, 495 (2001).

[31] B. C. den Hertog and M. J. P. Gingras, *Phys. Rev. Lett.* **84**, 3430 (2000).

[32] H. Kadowaki, Y. Ishii, K. Matsuhira, and Y. Hinatsu, *Phys. Rev. B* **65**, 144421 (2002).

[33] N. P. Raju, M. Dion, M. J. P. Gingras, T. E. Mason, and J. E. Greedan, *Phys. Rev. B* **59**, 14489 (1999).

[34] V. Bondah-Jagalu and S. T. Bramwell, *Can. J. Phys.* **79**, 1381 (2001).

[35] R. Siddharthan, B. S. Shastry, A. P. Ramirez, A. Hayashi, R. J. Cava, and S. Rosenkranz, *Phys. Rev. Lett.* **83**, 1854 (1999).

[36] M. J. Harris, S. T. Bramwell, T. Zeiske, D. F. McMorrow, and P. J. C. King, *J. Magn. Magn. Mater.* **177**, 757 (1998).

[37] J. D. M. Champion, M. J. Harris, P. C. W. Holdsworth, A. S. Wills, G. Balakrishnan, S. T. Bramwell, E. Čižmár, T. Fennell, J. S. Gardner, J. Lago, D. F. McMorrow, M. Orendáč, A. Orendáčová, D. M. Paul, R. I. Smith, M. T. F. Telling, and A. Wildes, *Phys. Rev. B* **68**, 020401 (2003).

[38] R. Moessner and J. T. Chalker, *Phys. Rev. Lett.* **80**, 2929 (1998).

[39] R. Moessner and J. T. Chalker, *Phys. Rev. B* **58**, 12049 (1998).

[40] J. T. Chalker, arXiv:0901.3492v1.

[41] K. Binder and A. P. Young, *Rev. Mod. Phys.* **58**, 801 (1986).

[42] K. H. Fischer and J. A. Hertz, *Spin Glasses*, Cambridge University Press, 1991.

[43] M. A. Ruderman and C. Kittel, *Phys. Rev.* **96**, 99 (1954).

[44] T. Kasuya, *Prog. Theor. Phys* **16**, 45 (1956).

[45] K. Yosida, *Phys. Rev.* **106**, 893 (1957).

[46] G. H. Wannier, *Phys. Rev.* **79**, 357 (1950).

[47] P. W. Anderson, *Phys. Rev.* **102**, 1008 (1956).

[48] L. Pauling, *J. Am. Chem. Soc.* **57**, 2680 (1935).

[49] W. F. Giauque and M. F. Ashley, *Phys. Rev.* **43**, 81 (1933).

[50] J. W. S. W. F. Giauque, *J. Am. Chem. Soc.* **58**, 1144 (1936).

[51] G. Toulouse, *Comm. Phys.* **2**, 115 (1977).

[52] J. M. Luttinger and L. Tisza, *Phys. Rev.* **70**, 954 (1946).

[53] O. A. Petrenko, C. Ritter, M. Yethiraj, and D. McK Paul, *Phys. Rev. Lett.* **80**, 4570 (1998).

[54] T. Yavors'kii, M. Enjalran, and M. J. P. Gingras, *Phys. Rev. Lett.* **97**, 267203 (2006).

[55] S. Ghosh, T. F. Rosenbaum, and G. Aeppli, *Phys. Rev. Lett.* **101**, 157205 (2008).

[56] M. J. Gingras, arXiv:0903.2772v1.

[57] A. P. Ramirez, *Annual Review of Materials Science* **24**, 453 (1994).

[58] J. Villain, R. Bidaux, J.-P. Carton, and R. Conte, *J. Phys. France* **41**, 1263 (1980).

[59] S. T. Bramwell, M. J. P. Gingras, and J. N. Reimers, *J. Appl. Phys.* **75**, 5523 (1994).

[60] J. D. M. Champion and P. C. W. Holdsworth, *J. Phys.: Cond. Matt.* **16**, S665 (2004).

[61] J. D. M. Champion, *Theoretical and Experimental Investigations of Frustrated Pyrochlore Magnets*, PhD thesis, University College London, 2001.

[62] H. T. Diep, editor, *Frustrated Spin Systems*, World Scientific, 2005.

[63] P. Bonville, J. A. Hodges, M. Ocio, J. P. Sanchez, P. Vulliet, S. Sosin, and D. Braithwaite, *Journal of Physics: Condensed Matter* **15**, 7777 (2003).

[64] R. Moessner and J. T. Chalker, *Phys. Rev. Lett.* **80**, 2929 (1998).

[65] B. Canals and C. Lacroix, *Phys. Rev. Lett.* **80**, 2933 (1998).

[66] A. S. Wills, M. E. Zhitomirsky, B. Canals, J. P. Sanchez, P. Bonville, P. D. de Reotier, and A. Yaouanc, *J. Phys.: Condens. Matter* **18**, L37 (2006).

[67] S. E. Palmer and J. T. Chalker, *Phys. Rev. B* **62**, 488 (2000).

[68] J. D. M. Champion, A. S. Wills, T. Fennell, S. T. Bramwell, J. S. Gardner, and M. A. Green, *Phys. Rev. B* **64**, 140407 (2001).

[69] J. R. Stewart, G. Ehlers, A. S. Wills, S. T. Bramwell, and J. S. Gardner, *J. Phys.: Condens. Matter* **16**, L321 (2004).

[70] A. D. Maestro and M. J. P. Gingras, *Phys. Rev. B* **76**, 064418 (2007).

[71] A. P. Ramirez1, A. Hayashi, R. J. Cava, R. Siddharthan, and B. S. Shastry, *Nature* **399**, 333 (1999).

[72] Y. M. Jana, A. Sengupta, and D. Ghosh, *Journal of Magnetism and Magnetic Materials* **248**, 7 (2002).

[73] S. Rosenkranz, A. P. Ramirez, A. Hayashi, R. J. Cava, R. Siddharthan, and B. S. Shastry, *J. Appl. Phys.* **87**, 5914 (2000).

[74] S. T. Bramwell, M. J. Harris, B. C. den Hertog, M. J. P. Gingras, J. S. Gardner, D. F. McMorrow, A. R. Wildes, A. L. Cornelius, J. D. M. Champion, R. G. Melko, and T. Fennell, *Phys. Rev. Lett.* **87**, 047205 (2001).

[75] R. Siddharthan, B. S. Shastry, and A. P. Ramirez, *Phys. Rev. B* **63**, 184412 (2001).

[76] P. Ewald, *Ann. Phys.* **64**, 253 (1921).

[77] M. T. Dove, *Introduction to Lattice Dynamics*, Cambridge University Press, 1993.

[78] S. W. De Leeuw, J. W. Perram, and E. R. Smith, *Proc. R. Soc. London* **A 373**, 27 (1980).

[79] Z. Wang and C. Holm, *J. Chem. Phys.* **115**, 6351 (2001).

[80] R. G. Melko, B. C. den Hertog, and M. J. P. Gingras, *Phys. Rev. Lett.* **87**, 067203 (2001).

[81] P. Schiffer, A. P. Ramirez, D. A. Huse, P. L. Gammel, U. Yaron, D. J. Bishop, and A. J. Valentino, *Phys. Rev. Lett.* **74**, 2379 (1995).

[82] S. T. Bramwell, M. N. Field, M. J. Harris, and I. P. Parkin, *J. Phys.: Cond. Mat.* **12**, 483 (2000).

[83] H. W. J. Blöte, R. F. Wielinga, and W. J. Huiskamp, *Physica* **43**, 549 (1969).

[84] A. Poole, A. S. Wills, and E. Lelievre-Berna, *J. Phys.: Condensed Matter* **19**, 452201 (2007).

[85] P. A. McClarty, S. H. Curnoe, and M. J. P. Gingras, *J. Phys.: Conference Series* **145**, 012032 (2009).

[86] G. Parisi, *Phys. Rev. Lett.* **43**, 1754 (1979).

[87] M. Mezard, G. Parisi, and M. A. Virasoro, *Spin Glass Theory and Beyond*, World Scientific, Singapore, 1987.

[88] D. Sherrington and S. Kirkpatrick, *Phys. Rev. Lett.* **35**, 1792 (1975).

[89] D. S. Fisher and D. A. Huse, *Phys. Rev. Lett.* **56**, 1601 (1986).

[90] T. Jörg, H. G. Katzgraber, and F. Krzakała, *Phys. Rev. Lett.* **100**, 197202 (2008).

[91] S. F. Edwards and P. W. Anderson, *J. Phys. F* **5**, 965 (1975).

[92] A. T. Ogielski and I. Morgenstern, *Phys. Rev. Lett.* **54**, 928 (1985).

[93] R. N. Bhatt and A. P. Young, *Phys. Rev. Lett.* **54**, 924 (1985).

[94] H. G. Ballesteros, A. Cruz, L. A. Fernández, V. Martín-Mayor, J. Pech, J. J. Ruiz-Lorenzo, A. Tarancón, P. Téllez, C. L. Ullod, and C. Ungil, *Phys. Rev. B* **62**, 14237 (2000).

[95] H. G. Katzgraber, M. Körner, and A. P. Young, *Phys. Rev. B* **73**, 224432 (2006).

[96] M. Hasenbusch, A. Pelissetto, and E. Vicari, *Phys. Rev. B* **78**, 214205 (2008).

[97] E. Marinari, G. Parisi, and F. Ritort, *J. Phys. A* **27**, 2687 (1994).

[98] See M. J. P. Gingras, Phys. Rev. Lett. 71, 1637 (1991) and references therein.

[99] H. Kawamura, *J. Magn. Magn. Mater.* **310**, 1487 (2007).

[100] H. Kawamura, *Phys. Rev. Lett.* **68**, 3785 (1992).

[101] H. Kawamura, *Phys. Rev. Lett.* **80**, 5421 (1998).

[102] K. Hukushima and H. Kawamura, *Phys. Rev. B* **72**, 144416 (2005).

[103] I. Campos, M. Cotallo-Aban, V. Martin-Mayor, S. Perez-Gaviro, and A. Tarancon, *Phys. Rev. Lett.* **97**, 217204 (2006).

[104] L. W. Lee and A. P. Young, *Phys. Rev. B* **76**, 024405 (2007).

[105] D. X. Viet and H. Kawamura, *Phys. Rev. Lett.* **102**, 027202 (2009).

[106] D. X. Viet and H. Kawamura, *Phys. Rev. B* **80**, 064418 (2009).

[107] L. A. Fernandez, V. Martin-Mayor, S. Perez-Gaviro, A. Tarancon, and A. P. Young, *Phys. Rev. B* **80**, 024422 (2009).

[108] A. Ito, H. Aruga, E. Torikai, M. Kikuchi, Y. Syono, and H. Takei, *Phys. Rev. Lett.* **57**, 483 (1986).

[109] K. Gunnarsson, P. Svedlindh, P. Nordblad, L. Lundgren, H. Aruga, and A. Ito, *Phys. Rev. B* **43**, 8199 (1991).

[110] S. Nair and A. K. Nigam, *Phys. Rev. B* **75**, 214415 (2007).

[111] I. S. Suzuki and M. Suzuki, *Phys. Rev. B* **68**, 094424 (2003).

[112] I. S. Suzuki and M. Suzuki, *Phys. Rev. B* **78**, 214404 (2008).

[113] H. G. Bohn, W. Zinn, B. Dorner, and A. Kollmar, *Phys. Rev. B* **22**, 5447 (1980).

[114] W. Luo, S. R. Nagel, T. F. Rosenbaum, and R. E. Rosensweig, *Phys. Rev. Lett.* **67**, 2721 (1991).

[115] J. F. Fernández, *Phys. Rev. B* **78**, 064404 (2008).

[116] J. F. Fernández and J. J. Alonso, *Phys. Rev. B* **79**, 214424 (2009).

[117] D. H. Reich, B. Ellman, J. Yang, T. F. Rosenbaum, G. Aeppli, and D. P. Belanger, *Phys. Rev. B* **42**, 4631 (1990).

[118] C. Ancona-Torres, D. M. Silevitch, G. Aeppli, and T. F. Rosenbaum, *Phys. Rev. Lett.* **101**, 057201 (2008).

[119] J. A. Quilliam, S. Meng, C. G. A. Mugford, and J. B. Kycia, *Phys. Rev. Lett.* **101**, 187204 (2008).

[120] K.-M. Tam and M. J. P. Gingras, *Phys. Rev. Lett.* **103**, 087202 (2009).

[121] J. Snider and C. C. Yu, *Phys. Rev. B* **72**, 214203 (2005).

[122] A. Biltmo and P. Henelius, *Phys. Rev. B* **78**, 054437 (2008).

[123] A. J. Bray and M. A. Moore, *J. Phys C* **15**, 3897 (1982).

[124] S. L. Sondhi, S. M. Girvin, J. P. Carini, and D. Shahar, *Rev. Mod. Phys.* **69**, 315 (1997).

[125] S. Sachdev, *Quantum Phase Transitions*, Cambridge University Press, Cambridge, 1999.

[126] P. G. de Gennes, *Solid State Commun.* **1**, 132 (1963).

[127] P. B. Chakraborty, P. Henelius, H. Kjonsberg, A. W. Sandvik, and S. M. Girvin, *Phys. Rev. B* **70**, 144411 (2004).

[128] J. A. Mydosh, *Spin Glasses: an Experimental Introduction*, Taylor & Francis, London, 1993.

[129] H. Rieger and A. P. Young, *Phys. Rev. Lett.* **72**, 4141 (1994).

[130] H. Rieger and A. P. Young, *Phys. Rev. B* **54**, 3328 (1996).

[131] M. Guo, R. N. Bhatt, and D. A. Huse, *Phys. Rev. B* **54**, 3336 (1996).

[132] R. B. Griffiths, *Phys. Rev. Lett.* **23**, 17 (1969).

[133] B. M. McCoy, *Phys. Rev. Lett.* **23**, 383 (1969).

[134] M. Schechter and P. C. E. Stamp, *Phys. Rev. Lett.* **95**, 267208 (2005).

[135] J. A. Quilliam, C. G. A. Mugford, A. Gomez, S. W. Kycia, and J. B. Kycia, *Phys. Rev. Lett* **98**, 037203 (2007).

[136] M. J. Stephen and A. Aharony, *J. Phys. C* **14**, 1665 (1981).

[137] J. Snyder and C. C. Yu, *Phys. Rev. B* **72**, 214203 (2005).

[138] A. Biltmo and P. Henelius, *Phys. Rev. B* **76**, 054423 (2007).

[139] A. Biltmo and P. Henelius, *Phys. Rev. B* **78**, 054437 (2008).

[140] R. N. Bhatt and P. A. Lee, *Phys. Rev. Lett.* **48**, 344 (1982).

[141] A. Chin and P. R. Eastham, *cond-mat/0610544* (2006).

[142] G. S. Shakurov, M. V. Vanyunin, B. Z. Malkin, B. Barbara, R. Y. Abdulsabirov, and S. L. Korableva, *Appl. Magn. Reson.* **28**, 251 (2005).

[143] S. Bertaina, B. Barbara, R. Giraud, B. Z. Malkin, M. V. Vanuynin, A. I. Pominov, A. L. Stolov, and A. M. Tkachuk, *Phys. Rev. B* **74**, 184421 (2006).

[144] N. I. Agladze, M. N. Popova, G. N. Zhizhin, V. J. Egorov, and M. A. Petrova, *Phys. Rev. Lett.* **66**, 477 (1991).

[145] J.-Y. Fortin and M. J. P. Gingras, *unpublished* (2007).

[146] J. Magarino, J. Tuchendler, P. Beauvillain, and I. Laursen, *Phys. Rev. B* **21**, 18 (1980).

[147] Z. A. Kazei, V. V. Snegirev, R. I. Chanieva, R. Y. Abdulsabirov, and S. L. Korableva, *Phys. of the Solid State* **48**, 726 (2006).

[148] G. K. Liu, J. Huang, R. L. Cone, and B. Jacquier, *Phys. Rev. B* **38**, 11061 (1988).

[149] G. Aeppli, Quantum Critical Points - Experiments, in *Proceedings of the NATO Advanced Study Institute on Dynamical Properties of Unconventional Magnetic Systems*, edited by A. T. Skjeltorp and D. Sherrington, Kluwer Academic Publishers, 1998.

[150] B. A. Berg, *Markov chain Monte Carlo simulations and their statistical analysis*, World Scientific, Singapore, 2004.

[151] D. P. Landau and K. Binder, *A Guide to Monte Carlo Simulations in Statistical Physics*, Cambridge University Press, 2000.

[152] N. Metropolis, A. W. Rosenbluth, M. N. Rosenbluth, A. H. Teller, and E. Teller, *J. Chem. Phys.* **21**, 1087 (1953).

[153] E. Marinari and G. Parisi, *Europhys. Lett.* **19**, 451 (1992).

[154] K. Hukushima and K. Nemoto, *J. Phys. Soc. Jpn* **65**, 1604 (1996).

[155] M. Creutz, *Phys. Rev. D* **36**, 515 (1987).

[156] J. L. Alonso, A. Tarancón, H. G. Ballesteros, L. A. Fernández, V. Martín-Mayor, and A. Muñoz Sudupe, *Phys. Rev. B* **53**, 2537 (1996).

[157] M. Creutz, *Phys. Rev. D* **21**, 2308 (1980).

[158] Y. Miyatake, M. Yamamoto, J. J. Kim, M. Toyonaga, and O. Nagai, *J. Phys. C* **19**, 2539 (1986).

[159] J. A. Olive, A. P. Young, and D. Sherrington, *Phys. Rev. B* **34**, 6341 (1986).

[160] A. H. Cooke, D. A. Jones, J. F. A. Silva, and M. R. Wells, *Journal of Physics C: Solid State Physics* **8**, 4083 (1975).

[161] P. Hansen, T. Johansson, and R. Nevald, *Phys. Rev. B* **12**, 5315 (1975).

[162] A. Biltmo and P. Henelius, *Europhys. Lett.* **87**, 27007 (2009).

[163] A. Aharony, *Phys. Rev. B* **8**, 3363 (1973).

[164] K. G. Wilson and J. Kogut, *Physics Reports* **12**, 75 (1974).

[165] M. Suzuki, *Prog. Theor. Phys.* **56**, 1454 (1976).

[166] H.-J. Xu, B. Bergesen, and Z. Racz, *J. Phys.: Condens. Matter* **64**, 214420 (1992).

[167] M. Guo, R. N. Bhatt, and D. A. Huse, *Phys. Rev. B* **54**, 3336 (1996).

[168] D.-H. Kim and J.-J. Kim, *Phys. Rev. B* **66**, 054432 (2002).

[169] G. Mennenga, L. J. de Jongh, and W. J. Huiskamp, *Journal of Magnetism and Magnetic Materials* **44**, 59 (1984).

[170] H. P. Christensen, *Phys. Rev. B* **19**, 6564 (1979).

[171] K. W. H. Stevens, *Proc. Phys. Soc. A* **65**, 209 (1952).

[172] M. T. Hutchings, *Point-Charge Calculations of Energy Levels of Magnetic Ions in Crystaline Electric Fields*, volume 16 of *Solid State Physics*, p. 227, Academic Press, New York and London, 1964.

[173] P. D. Scott, *Ph.D. thesis*, PhD thesis, Yale University, 1970.

[174] G. W. Beall, W. O. Milligan, and H. A. Wolcott, *J. Inorg. Nuc. Chem.* **39**, 65 (1977).

[175] G. H. Landers and T. O. Brun, *Acta Cryst.* **A29**, 684 (1973).

[176] P. D. Scott, H. E. Meissner, and H. M. Crosswhite, *Phys. Lett. A* **28**, 489 (1969).

[177] H. G. Kahle, A. Kasten, P. D. Scott, and W. P. Wolf, *J. Phys. C* **19**, 4153 (1986).

[178] S. Karmakar, M. Saha, and D. Ghosh, *J. App. Phys.* **52**, 4156 (1981).

[179] S. Karmakar, M. Saha, and D. Ghosh, *Phys. Rev. B* **26**, 7023 (1982).

[180] P. D. Scott and W. P. Wolf, *J. App. Phys.* **40**, 1031 (1969).

[181] J. M. Ziman, *Principles of the Theory of Solids*, Cambridge University Press, 1972.

[182] S. W. de Leeuw, J. W. Perram, and E. R. Smith, *Proc. Soc. Lond. A* **373**, 27 (1980).

[183] M. Born and K. Huang, *Theory of Crystal Lattices*, Oxford University Press, London, 1968.

[184] R. G. Melko and M. J. P. Gingras, *J. Phys.: Condens. Matter* **16**, R1277 (2004).

[185] C. A. Catanese, *Ph.D. thesis*, PhD thesis, Yale University, 1970.

[186] C. P. Tigges and W. P. Wolf, *Phys. Rev. Lett.* **58**, 2371 (1987).

[187] W. P. Wolf, *Bras. J. Phys.* **30**, 794 (2000).

[188] J. Jensen and A. R. Mackintosh, *Rare Earth Magnetism Theory – Structures and Excitations*, Clarendon Press, Oxford, 1991.

[189] T. I. K. Deguchi and Y. Maeno, *Rev. Sci. Instrum.* **75**, 1188 (2004).

[190] S. Mørup, F. Bødker, P. V. Hendriksen, and S. Linderoth, *Phys. Rev. B* **52**, 287 (1995).

[191] S. D. Tiwari and K. P. Rajeev, *Phys. Rev. B* **72**, 104433 (2005).

[192] M. A. Zaluska-Kotur and M. Cieplak, *Europhys. Lett.* **23**, 85 (1993).

[193] P. E. Jönsson, R. Mathieu, W. Wernsdorfer, A. M. Tkachuk, and B. Barbara, *Phys. Rev. Lett.* **98**, 256403 (2007).

[194] T. Jörg, *Phys. Rev. B* **73**, 224431 (2006).

[195] M. H. Quenouille, *Biometrika* **43**, 353 (1956).

[196] J. W. Tukey, *Ann. Math. Statist.* **29**, 614 (1958).

[197] K. Binder, *Z. Phys. B* **43**, 119 (1981).

[198] K. Binder, *Phys. Rev. Lett.* **47**, 693 (1981).

[199] V. Privman and M. E. Fisher, *Phys. Rev. B* **30**, 322 (1984).

[200] A. D. Beath and D. H. Ryan, *J. Appl. Phys.* **97**, 10A506 (2005).

[201] F. Schwabl, *Statistical mechanics*, Springer, Berlin Heidelberg New York, 2006.

[202] F. Cooper, B. Freedman, and D. Preston, *Nucl. Phys. B* **210**, 210 (1982).

[203] F. Matsubara, T. Shirakura, S. Endoh, and S. Takahashi, *Journal of Physics A: Mathematical and General* **36**, 10881 (2003).

[204] T. Shirakura and F. Matsubara, *Phys. Rev. B* **67**, 100405 (2003).

[205] I. A. Campbell, K. Hukushima, and H. Takayama, *Phys. Rev. Lett.* **97**, 117202 (2006).

[206] M. J. P. Gingras, *Phys. Rev. Lett.* **71**, 1637 (1993).

[207] P. C. W. Holdsworth, M. J. P. Gingras, B. Bergersen, and E. P. Chan, *J. Phys.: Condens. Matter* **3**, 6679 (1991).

[208] J. P. C. Ruff, J. P. Clancy, A. Bourque, M. A. White, M. Ramazanoglu, J. S. Gardner, Y. Qiu, J. R. D. Copley, M. B. Johnson, H. A. Dabkowska, and B. D. Gaulin, *Phys. Rev. Lett.* **101**, 147205 (2008).

[209] J. T. Chalker, P. C. W. Holdsworth, and E. F. Shender, *Phys. Rev. Lett.* **68**, 855 (1992).

[210] P. McClarty, Private communication.

[211] C. Pinettes, B. Canals, and C. Lacroix, *Phys. Rev. B* **66**, 024422 (2002).

[212] H. T. Diep and H. Kawamura, *Phys. Rev. B* **40**, 7019 (1989).

[213] W. Minor and T. Giebultowicz, *J. Phys. Colloques* **49**, C8 (1988).

[214] M. T. Heinilä and A. S. Oja, *Phys. Rev. B* **48**, 16514 (1993).

[215] C. L. Henley, *J. App. Phys.* **61**, 3962 (1987).

[216] H. Cao, A. Gukasov, I. Mirebeau, P. Bonville, C. Decorse, and G. Dhalenne, *Phys. Rev. Lett.* **103**, 056402 (2009).

[217] J. D. M. Champion, S. T. Bramwell, P. C. W. Holdsworth, and M. J. Harris, *Europhys. Lett.* **57**, 93 (2002).

[218] J. T. Chalker, P. C. W. Holdsworth, and E. F. Shender, *Phys. Rev. Lett.* **68**, 855 (1992).

[219] C. E. Fiore, *Phys. Rev. E* **78**, 041109 (2008).

[220] G.-W. Chern, R. Moessner, and O. Tchernyshyov, *Phys. Rev. B* **78**, 144418 (2008).

[221] J. F. Fernández and J. J. Alonso, *Phys. Rev. B* **73**, 024412 (2006).